

REPORT DOCUMENTATION PAGE

Form Approved,
OMB No. 0704-0188

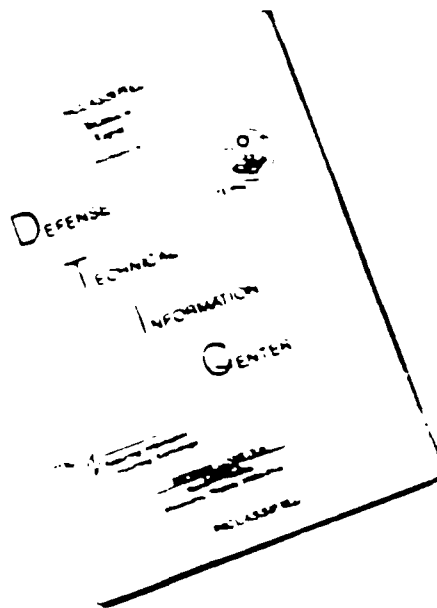
Public reporting burden for this collection of information is estimated to average 1 hour per response, including the time for reviewing instructions, searching existing data sources, gathering and maintaining the data needed, and completing and reviewing the collection of information. Send comments regarding this burden estimate or any other aspect of this collection of information, including suggestions for reducing this burden, to Washington Headquarters Services, Directorate for Information Operations and Reports, 1215 Jefferson Davis Highway, Suite 1204, Arlington, VA 22202-4302, and to the Office of Management and Budget, Paperwork Reduction Project (0704-0188), Washington, DC 20503.

1. AGENCY USE ONLY (Leave blank)		2. REPORT DATE October 1993	3. REPORT TYPE AND DATES COVERED Final 7/1/91 - 7/31/93	
4. TITLE AND SUBTITLE Multifunctional Macromolecules			5. FUNDING NUMBERS 63218C 1601 06	
6. AUTHOR(S) A. J. East, M. J. Sansone, and T. Findakly			7. PERFORMING ORGANIZATION NAME(S) AND ADDRESS(ES) H.C.C., Science & Technology Inc. 86 Morris Avenue Summit, NJ 07901-3956	
8. PERFORMING ORGANIZATION REPORT NUMBER AFOSR-TR 94 0082			9. SPONSORING/MONITORING AGENCY NAME(S) AND ADDRESS(ES) AFOSR/NC Building 410, Bolling AFB DC 20332-6448	
10. SPONSORING/MONITORING AGENCY REPORT NUMBER F49620-91-C-0062			11. SUPPLEMENTARY NOTES	
12a. DISTRIBUTION / AVAILABILITY STATEMENT APPROVED FOR PUBLIC RELEASE; DISTRIBUTION IS UNLIMITED. Approved for public release; distribution unlimited.			12b. DISTRIBUTION CODE	
13. ABSTRACT (Maximum 200 words) See Attached DTIC ELECTE MAR 24 1994 S B D				
14. SUBJECT TERMS			15. NUMBER OF PAGES 166	
16. PRICE CODE			17. SECURITY CLASSIFICATION OF REPORT UNCLASSIFIED	
18. SECURITY CLASSIFICATION OF THIS PAGE UNCLASSIFIED			19. SECURITY CLASSIFICATION OF ABSTRACT UNCLASSIFIED	
20. LIMITATION OF ABSTRACT				

AD-A277 347

94-09143

DISCLAIMER NOTICE



THIS DOCUMENT IS BEST
QUALITY AVAILABLE. THE COPY
FURNISHED TO DTIC CONTAINED
A SIGNIFICANT NUMBER OF
PAGES WHICH DO NOT
REPRODUCE LEGIBLY.

13 While numerous photorefractive polymers were synthesized by the incorporation of NLO chromophores and photoconductive components as side chains on a backbone, the most significant photorefractive behavior demonstration under this project was made in an electrooptic aminonitrostilbene methacrylate copolymer (P2ANS/MMA) without the addition of photoconductive compounds. By four wave mixing, photorefractive gratings were written in P2ANS/MMA using s-polarized and p-polarized writing beams and probed using orthogonally polarized probe beams. With probe beam orthogonally polarized to the write beams, well behaved, field dependent, stable responses ascribed to the photorefractive effect were observed. Diffraction efficiencies of 10^{-4} - 10^{-5} were obtained in 8um thick films under an applied field of 50 V/um with response times of 1.5 - 2 minutes. Increasing the sample thickness to 100um is projected to result in a diffraction efficiency of 1% - 3%. Increasing the intensity to 1 W/cm² is projected to reduce the time constant by a factor of 20. Two beam coupling experiments clearly confirmed the photorefractive nature of the gratings.

Photorefractive behavior was also observed in the tricyanovinyl-carbazole substituted siloxane polymer (TCV-CBZ/PSX) but was one order of magnitude lower than that observed in P2ANS/MMA. TCV-CBZ/PSX had much higher photoconductivity and a lower dark current than P2ANS but unfortunately also had a lower electrooptic coefficient.

Accession For	
NTIS GRA&I	<input checked="checked" type="checkbox"/>
DTIC TAB	<input type="checkbox"/>
Unannounced	<input type="checkbox"/>
Justification	
By	
Distribution/	
Availability Codes	
Dist	Avail and/or Special
A-1	

Contract # F46920-91-C-0062

**Approved for public release;
distribution unlimited.**

"MULTIFUNCTIONAL MACROMOLECULES"

Final Report Submitted to

**U.S. Air Force Office of Scientific Research
Directorate for Chemical and Atmospheric Sciences
Building 410
Bolling Air Force Base, D.C. 20332-6448**

Prepared by

A. J. East, M. J. Sansone, and T. Findakly

**HCC Science & Technology Company, Inc.
[A Subsidiary of Hoechst Celanese Corporation]
86 Morris Avenue
Summit, NJ 07901**

October 1993

**Approved for public release;
distribution unlimited.**

Table of Contents

1. Introduction	1
1.1. Objectives.....	1
1.2. Project Organization	1
1.3. Summary of Significant Results	3
2. Historical Introduction to the Photorefractive Effect.....	4
3. Synthesis of Photorefractive Polymers	6
3.1. Introduction	6
3.2. Initial Photorefractive Studies.....	6
3.3. The Grafting Reaction Catalyst.....	7
3.4. The Photoconducting Chromophore	8
3.4.1. Evaluation of Oxynitrostilbene-Carbazole Siloxane Polymer	8
3.4.2. Better Chromophores	9
3.4.3. Polymeranalogous Tricyanovinylolation Reaction	10
3.4.4. Dicyanovinylcarbazole Chromophores	10
3.4.5. Tricyanovinylcarbazole Polymers from TCV Allylcarbazole	11
3.4.6. Other Chromophores.....	12
3.5. Synthetic Experimental Detail	14
3.5.1. Cyanoethylation of Carbazole.....	14
3.5.2. Preparation of 4-(3-Cyanopropoxy)-4'-Nitrostilbene.....	14
3.5.3. 4-(4-Cyanobutoxy)-4'-Nitrostilbene.....	14
3.5.4. 4-Allyloxy-4'-Nitrostilbene	15
3.5.5. 9-Allylcarbazole by NaH/THF route	15
3.5.6. 9-Allylcarbazole by Nishi's Route	15
3.5.7. Reaction of 9-Ethylcarbazole-3-Aldehyde with Malononitrile	16
3.5.8. 9-Allylcarbazole-3-Aldehyde.....	16
3.5.9. 3-(2,2-Dicyanovinyl)-9-Allylcarbazole	17
3.5.10. 3-(1,2,2-Tricyanovinyl)-9-Allylcarbazole	17
3.5.11. Preparation of 1-Allylindoline	17
3.5.12. 1-Allylindoline-5-Aldehyde.....	18
3.5.13. 1-Allyl-5-(4-Nitrostyryl)-Indoline	18
3.5.14. 1-Allyl-5-Dicyanovinylindoline.....	19
3.5.15. 1-Allyl-5-(1,2,2-Tricyanovinyl)-Indoline	19

Table of Contents (Cont'd)

3.5.16. Reaction of 1-Allylindoline-5-Aldehyde with Diethylthiobarbituric Acid.....	19
3.5.17. Condensation of 9-Allylcarbazole-3-Aldehyde with Diethylthiobarbituric Acid	20
3.5.18. 9-Allyl-3-(2-Nitrovinyl)-Carbazole	20
3.5.19. 1-Allyl-5-(2-Nitrovinyl)-Indoline	20
3.5.20. Preparation of Platinum-Dicyclopentadiene Dichloride Catalyst	20
3.5.21. Polymeranalogous Grafting of 9-Allylcarbazole onto Polymethylhydrosiloxane.....	20
3.5.22. Co-Grafting of 4-Allyloxy-4'-Nitrostilbene and 9-Allylcarbazole onto PS122 in the Ratio 25/75	21
3.5.23. Polymeranalogous Tricyanovinylation of Poly(carbazolylpropylmethylsiloxane)	22
3.5.24. Co-Grafting of Allylcarbazole and Allyl-Dicyanovinylcarbazole onto PS122 in the Ratio 75/25	23
3.5.25. Co-Grafting of Allylcarbazole and Allyl-Tricyanovinylcarbazole onto PS122 in the Ratio 75/25	23
4. Photorefractive Characterization.....	24
4.1 Photoconductive Evaluation	24
4.2 Photorefractive Evaluation.....	35
5. Summary	63
6. References	64
7. Subcontractor Final Report (University of Leeds).....	66
8. Subcontractor Final Report (University of Bayreuth).....	80
9. Subcontractor Final Report (Cambridge University).....	109
10. Subcontractor Final Report (GEC-Marconi Research Center)	116

List of Figures

Figure 1. Photoinduced discharge curves of Kodak copier belt material.	26
Figure 2. Photoinduced discharge curves for MO3ONS and PMMA.	26
Figure 3. Photoinduced discharge curves of 10/90 ONS/CBZ/PSX.....	29
Figure 4. Photoinduced discharge with bandpass filters of 10/90 ONS/CBZ/PSX.	29
Figure 5. Photoinduced discharge curves of 10/90 ONS/CBZ/PSX with 10% TNF.....	30
Figure 6. Photoinduced discharge of 10/90 ONS/CBZ/PSX with various exposures.	30
Figure 7. Photoinduced discharge curves of 10/90 & 25/75 ONS/CBZ/PSX.	33
Figure 8. Photoinduced discharge of 10/90 ONS/CBZ/PSX, PVK and 10/90	33
Figure 9. UV/VIS spectrum of polyvinylcarbazole in cyclopentanone.	34
Figure 10. UV/VIS spectrum of 10/90 & 25/75 ONS/CBZ/PSX in cyclopentanone.	34
Figure 11. UV/VIS spectrum of 10/90 ONS/CBZ/PSX thin film.....	36
Figure 12. Four wave mixing experimental setup.....	36
Figure 13. Four wave mixing results for 10/90 ONS/CBZ/PSX.	37
Figure 14. Four wave mixing results for 10/90 ONS/CBZ/PSX with 10% TNF.	37
Figure 15. Four wave mixing results for polyvinylcarbazole with 20% TNF.	39
Figure 16. Four wave mixing results for MO3ONS/MMA with and without TNF.....	39
Figure 17. Four wave mixing results for 10/90 ONS/CBZ/PSX in air and Ar.	41
Figure 18. Photoinduced discharge curves for P2ANS and DCVHT polymers.	41
Figure 19. Photoinduced discharge for P2ANS and DCVHT polymers with surfaces charged to the same potential.	42
Figure 20. UV/VIS spectrum of carbazole-functionalized polysiloxane (CBZ/PSX).	42
Figure 21. Photoinduced discharge and derivative curves for CBZ/PSX.	44
Figure 22. Photoconductivity vs. electric field for CBZ/PSX from photoinduced discharge	44
Figure 23. Quantum efficiency vs. electric field for CBZ/PSX from photoinduced discharge ..	46
Figure 24. UV/VIS spectrum of TCV-CBZ/PSX thin film.	46
Figure 25. Photoinduced discharge curve for TCV-CBZ/PSX.	47
Figure 26. Four wave mixing results for TCV-CBZ/PSX.	47
Figure 27. UV/VIS spectrum of DCV-CBZ/PSX thin film.	49
Figure 28. Photoinduced discharge curve for DCV-CBZ/PSX.	49
Figure 29. UV/VIS spectrum of 50/50 P2ANS/MMA thin film.....	51
Figure 30. Photoinduced discharge curve for 50/50 P2ANS/MMA.	51
Figure 31. Derivative of photoinduced discharge results for 50/50 P2ANS/MMA.	52

List of Figures (Cont'd)

Figure 32. Photoconductivity vs. electric field for 50/50 P2ANS/MMA.	52
Figure 33. Quantum efficiency vs. electric field for 50/50 P2ANS/MMA.	54
Figure 34. Steady state dark and photoconductivity for P2ANS/MMA.	54
Figure 35. Diffraction efficiency vs. time for P2ANS/MMA.	56
Figure 36. Diffraction efficiency vs. time at various electric field strengths: s-write, p-probe ..	56
Figure 37. Diffraction efficiency vs. time at various field strengths	57
Figure 38. Four wave mixing using s writing beams and s & p reading beams.	57
Figure 39. Four wave mixing using s writing beams and s & p reading beams with no externally applied field.	58
Figure 40. Four wave mixing using s writing beams and s & p reading beams with external field applied opposite to the poling direction.	58
Figure 41. Four wave mixing using p writing beams and s & p reading beams.	61
Figure 42. Experimental setup for two beam coupling.	61
Figure 43. Beam geometry employed in the two beam coupling measurement.	62
Figure 44. Two beam coupling result showing energy transfer between the beams.	62

List of Tables

Table 1. Photoconductive data by the Kodak belt method	25
Table 2. Refractive indices of ONS/CBZ/PSX	31
Table 3. Pyroelectric and electrooptic data of MO3/ONS and MO6/ONS polymers	32

1. Introduction

This is the final report on contract No. F46920-91-C-0062 entitled "Multifunctional Macro-Molecules" covering the period of performance of July 1, 1991 through August 31, 1993. The report summarizes the work performed under this contract which focused on the synthesis and evaluation of photorefractive polymers.

The report is organized as follows: In this section, the project objectives, organization, and significant accomplishments are summarized. In section 2, a brief historical review of the photorefractive effect in organic and inorganic materials is given. In section 3, the synthesis of photorefractive polymers at HCC is reported. This is followed by the photorefractive evaluations and results on the synthesized polymers in section 4. The project is summarized in section 5, and references are provided in section 6. The final reports of the four subcontractors under this projects (Leeds University, Bayreuth University, Cambridge University, and GEC-Marconi) are provided in Sections 7-10.

1.1. Objectives

As an extension to the objective of incorporating several functionalities in polymeric materials, this project focused on incorporating photoconductive and electrooptic functionalities in side chain polymers in order to demonstrate, evaluate, and understand photorefractive behavior in side chain polymers. While the ultimate objective of efforts on photorefractive polymers is the realization of efficient high performance photorefractive polymers suitable for practical defense and commercial applications, this effort aimed at examining and reaching a better understanding of certain critical issues that influence the behavior of photorefractive polymers including the relationship between photoconductivity and the photorefractive behavior in novel side chain polymers to help determine the material design criteria for various applications.

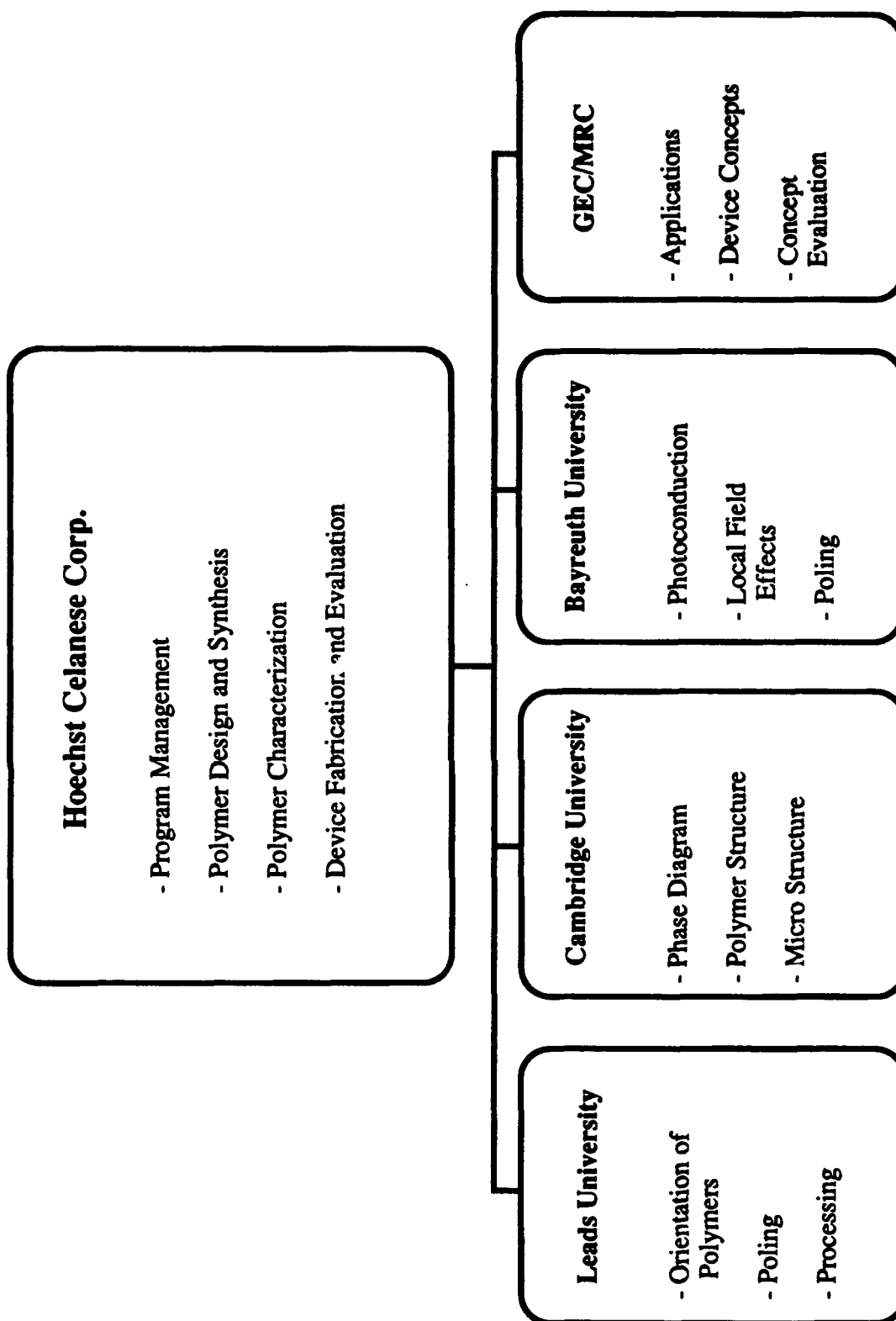
To accomplish the above, the investigation involved a considerable effort in modeling, design, synthesis, analysis, and evaluation of novel photorefractive polymers by Hoechst Celanese and its four subcontractors.

1.2. Project Organization

This project was led by Hoechst Celanese as the prime contractor in collaboration with four subcontractors: University of Leeds, University of Bayreuth, Cambridge University, and the GEC-Marconi Research Center.

Hoechst Celanese performed the synthesis and evaluation of photorefractive properties in side chain NLO polymers, and provided the project leadership and administration. The University of Leeds focused on the poling, drawing, and orientation aspects of the HCC synthesized side chain polymers. The University of Bayreuth performed an investigation of the NLO and conductive properties of the HCC synthesized polymers. Cambridge University concentrated on the structural characterization of the HCC synthesized polymers. The GEC-Marconi Research Center performed an investigation of the application areas and requirements of photorefractive polymers. The project organization is summarized on the following page.

**Multifunctional Macromolecules/Photorefractive
Polymers
Project Organization**



1.3. Summary of Significant Results

While numerous photorefractive polymers were synthesized by the incorporation of NLO chromophores and photoconductive components as side chains on a backbone, the most significant photorefractive behavior demonstration under this project was made in an electrooptic aminonitrostilbene methacrylate copolymer (P2ANS/MMA) without the addition of photoconductive compounds. By four wave mixing, photorefractive gratings were written in P2ANS/MMA using *s*-polarized and *p*-polarized writing beams and probed using orthogonally polarized probe beams. With probe beam orthogonally polarized to the write beams, well behaved, field dependent, stable responses ascribed to the photorefractive effect were observed. Diffraction efficiencies of $10^{-4} - 10^{-5}$ were obtained in 8 μm thick films under an applied field of 50 V/ μm with response times of 1.5 – 2 minutes. Increasing the sample thickness to 100 μm is projected to result in a diffraction efficiency of 1% - 3%. Increasing the intensity to 1 W/cm² is projected to reduce the time constant by a factor of 20. Two beam coupling experiments clearly confirmed the photorefractive nature of the gratings.

Photorefractive behavior was also observed in the tricyanovinyl-carbazole substituted siloxane polymer (TCV-CBZ/PSX) but was one order of magnitude lower than that observed in P2ANS/MMA. TCV-CBZ/PSX had much higher photoconductivity and a lower dark current than P2ANS but unfortunately also had a lower electrooptic coefficient.

2. Historical Introduction to the Photorefractive Effect

The photorefractive effect was first observed in LiNbO_3 in the late '60s and has since been observed in many inorganic electrooptic materials such as $\text{Bi}_{12}\text{SiO}_{20}$ (BSO-bismuth silicon oxide), BaTiO_3 , KNbO_3 , LiTaO_3 , KTN, GaAs, SBN (strontium barium niobate), etc. Such materials were found to undergo a modification of their optical properties upon illumination with intense laser beams. The effect, primarily a change in the refractive index in the illuminated regions, was first considered a nuisance and labeled "optical damage" since it caused laser beams propagating in these materials to scatter and break up through a lens-like action. During the early days of second harmonic generation research, it was observed that laser pulses incident on LiNbO_3 caused local semi-permanent changes in the refractive index of LiNbO_3 which ruined phase matching for SHG, and the crystal had to be moved around every few laser pulses to avoid "optical damage". A few years later, this phenomenon was used to advantage in the writing and storage of high quality holographic images in LiNbO_3 and LiTaO_3 .

The explanation of the photorefractive effect in crystalline materials assumes the existence of charges thought to inhabit low-lying traps formed by impurity or defect sites in the crystals. In the absence of light, these charges are frozen in place if the dark conductivity is small. In the presence of light, the trapped charges can migrate between trapping sites. This light induced migration and separation of charge in the crystal gives rise to an electrostatic field in the crystal that eventually prevents further charge separation. This electrostatic field, however, also produces a refractive index change in the crystal by the linear electrooptic (Pockels') effect, provided the crystal lacks inversion symmetry. The light induced electrostatic field can be very large (on the order of 10^5 V/cm) causing a large refractive index change (10^{-3}) in materials with large linear electrooptic coefficients, such as BaTiO_3 and KTN.

The effect described is a reversible one, albeit slow in certain cases, and can be typically reversed by light flooding. This feature of dynamic light induced refractive index change is an attractive one in a number of applications including image storage, information and signal processing, phase conjugation, wave mixing, optical amplification, photolithography, reconfigurable optical interconnections, etc. Most of these applications require materials having high photorefractive sensitivity, speed, spatial resolution, and diffraction efficiency. At present, no material exists which satisfies all of these requirements simultaneously. However, several attractive characteristics have been demonstrated in existing materials such as LiNbO_3 , KNbO_3 , BaTiO_3 , BSO, SBN, GaAs, etc. Continued improvements in materials response and nonlinearity should bring about the realization and implementation of photorefractive in numerous high technology applications in both commercial and defense areas.

The photorefractive effect is most clearly demonstrated in a holographic format, where it probably has its most useful application. When two coherent laser beams are incident in a material, a sinusoidally varying intensity (dark/bright) distribution develops as a result of interference. Absorbed photons generate electrons which move by the influence of diffusion or drift by the influence of an applied electric field until they are trapped at empty trapping sites. More electrons are trapped at empty sites in the dark regions of the light intensity pattern in the absence of an applied field, or close to the bright regions in the presence of a strong applied field. The result is a periodic spatial charge pattern which sets up an internal periodic static field distribution. The space charge field acts to modify and modulate the refractive index of the material through the linear electrooptic effect resulting in a periodic phase grating from which light can be diffracted. The formed index grating has the same spatial period as the light intensity pattern, but is shifted from it spatially by a fraction of the grating period. The written holographic grating in photorefractive materials is truly dynamic in that it follows and tracks any changes in the phases of the writing beams.

Since its first discovery, the photorefractive effect has been thoroughly investigated in inorganic materials. Activities on the development of organic and polymeric electrooptical and nonlinear optical materials during the last few years at a number of universities and industrial R&D centers has created interest to investigate the photorefractive effect in organic materials. Organic photoconductors have been used in commercial photocopiers for years. Combining these two functionalities either by blending electrooptic and photoconductive materials or by creating a bi- or tri-functional polymer has been demonstrated to result in organic photorefractive materials. In these materials, the photogeneration process tends to produce radical cations so that the resulting charge carriers are holes. In contrast to inorganic systems, there is no band structure but rather discrete quantum states. Carrier transport is believed to take place by a photon assisted hopping mechanism between these discrete states. Organic/polymeric materials possess high figures of merit, n^3r/e , because of their large electrooptic coefficients and their very low dielectric constants. They can be synthesized to tailor their properties to a given application. They also possess certain fabrication advantages such as the ability to be made into flat sheets for large area displays.

3. Synthesis of Photorefractive Polymers

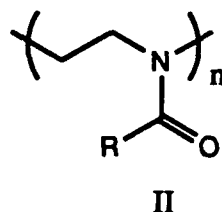
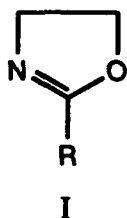
3.1. Introduction

During the first phase of this project, synthetic polymer studies at HCC focused primarily on demonstrating the fundamental principles of multifunctional macromolecules [1]. Based on HCC's experience in the polymer chemistry, it was decided to target multifunctional polymers containing piezoelectric and nonlinear optic properties as a model to prove the concept. This was successful when a regularly alternating copolymer of vinylidene dicyanide and acetoxystyrene was synthesized, methanolysed to the hydroxystyrene analog and re-esterified with NLO active acid chloride. The polymer had measurable piezoelectric, pyroelectric and electrooptic properties [2]. The integration of photoconductivity and nonlinear optical activity to produce a photorefractive polymer became the focus of the second phase of this project. Early in 1990, polymer synthesis began at HCC aimed at understanding and evaluating such materials as a natural continuation of the Multifunctional Macromolecules project [3].

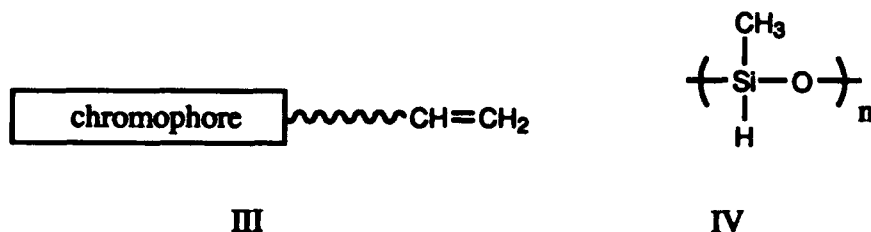
3.2. Initial Photorefractive Studies

The major issue faced early was related to the nature of the polymer backbone. In the earlier Multifunctional Macromolecules and NLO projects, the polymers were addition polymers using various methacrylate esters as monomers and were polymerized by conventional free radical initiators such as azodiisobutyronitrile at 70-90 °C. With careful purification of the monomers, very high molecular weights were achieved, sometimes exceeding 1,000,000 and often in the hundreds of thousands. Despite this, the polymers were brittle and the only polymers which gave self supporting films were those where the level of NLO active monomer was kept very low. It was shown that this effect was due to the strong dipolar interactions introduced by such chromophores. In the case of NLO active polymers with highly unsaturated chromophores, polymerization was often complicated by unwanted side reactions. Sometimes polymerization gave highly cross linked materials due to unwanted participation of unsaturated groups in the chromophore. The presence of photoconducting chromophores is an added complication. Photoconductors are electron rich and NLO chromophores have strong electron withdrawing functionalities as part of the molecule. These two types of side groups in combination lead to the formation of charge transfer complexes which can severely retard free radical polymerization and lead to very low conversion rates and low molecular weights [4,5].

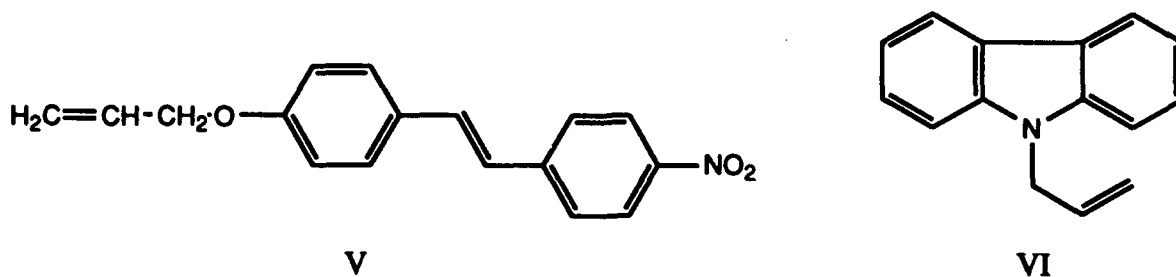
Many methacrylate monomers synthesized for various NLO activities were utilized to gain a better understanding of photorefractivity. Other routes to polymers from vinyl monomers were considered such as the anionic polymerization of methacrylates or cationic polymerization of vinyl ethers. Group Transfer Polymerization of methacrylates [6] was considered but problems were foreseen with chemical interactions, polymer reaction conditions and the necessarily complex synthetic routes. Ring opening polymerization was considered and one attractive idea was to follow the work of Hsieh and Litt [7] and Percec [8] by using polyoxazolines. Oxazolines (I) can be synthesized from various nitriles by reaction with ethanolamine and may be copolymerized under very mild cationic conditions to give a poly(N-acylethyleneimine)-(II).



A simpler route was pursued through polymeranalogous grafting of an olefine terminated chromophore (III) onto a preformed polyhydrosiloxane backbone (IV) in the presence of a platinum catalyst according to Finkelmann et. al. [9].



The starting material was commercially available poly(methylhydrosiloxane)-(IV), a viscous oil with a molecular weight around 5,000. Its one limitation was the low degree of polymerization, around 80-100 repeat units. This limited the chain length of the graft polymer. It was felt desirable to examine polymers made with lower concentrations of side groups by using copolymers of methylhydrosiloxane and dimethylsiloxane. Unfortunately, such materials are only available commercially in low molecular weight. One reason for this [10] is the difficulty of preventing cross linking at higher degrees of polymerization due to the highly reactive nature of the hydrosiloxane oligomers. The monomers prepared were 4-allyloxynitrostilbene (V) and 9-allylcarbazole (VI). These were readily prepared by a standard Williamson etherification of 4-hydroxy-4'-nitrostilbene with allyl bromide and by N-alkylation of carbazole with allyl bromide using sodium hydride in THF.



3.3. The Grafting Reaction Catalyst

The chloroplatinic acid in isopropanol (Speier's Reagent) was used to make co-grafts of 9-allylcarbazole and 4-allyloxy-4'-nitrostilbene, but the reaction failed completely with the homo grafts of 9-allylcarbazole or 9-pentenylcarbazole, both electron rich molecules. This adverse effect was overcome when a soluble organo platinum catalyst, dicyclopentadiene platinum dichloride, was used [11]. Attempts to obtain this catalyst commercially were unsuccessful. Eventually it was synthesized via Kharasch's original 1935 method [12] from chloroplatinic acid and dicyclopentadiene and isolated as a stable crystalline solid melting point 217 °C. The organo platinum catalyst was found to be readily soluble in organic solvents such as toluene and we were able to use it at levels as low as 1 part in 10,000 (molar). 9-allylcarbazole was grafted onto polymethylhydrosiloxane to make poly(carbazolylpropylmethylsiloxane) with a conversion efficiency exceeding 99%. The organometallic catalyst also worked with electron deficient NLO chromophores such as allyloxynitrostilbene. Having established a robust catalyst system, we

used it successfully for a variety of functional side groups. The reaction was run in toluene at 70 °C under Ar in strictly anhydrous conditions. It was convenient to dry the toluene over sodium benzophenone ketyl until the purple color formed in a special solvent drying apparatus and distil the anhydrous solvent into the reaction flask directly.

3.4. The Photoconducting Chromophore

For simplicity, the carbazole unit was used as the photoconducting component because it is chemically robust, easily available and easily modifiable. It is an adequate photoconductor and photo charge generator. Alternatives (e.g. aminoarylhydrazones) were considered, but were not used since they needed longer synthesis times. Both 9-allylcarbazole and 9-(4-pentenyl)-carbazole were grafted onto the hydrosiloxane backbone and 9-allylcarbazole was chosen for future work as the polymer had $T_g = 47\text{ }^{\circ}\text{C}$, whereas the T_g of the polymer from the C-5 spacer carbazole was below room temperature. Strohmreigl [11] quotes a T_g around $7\text{ }^{\circ}\text{C}$. It was difficult to isolate this polymer since it formed a sticky gum like mass. The C-3 material was a white or gray powder. Two problems arose at this point: the organic purity of the carbazole and the metals content of the polymer. Photoconductivity is badly affected by traces of trapping sites (such as polynuclear aromatics and heterocycles) and the starting material (Aldrich 99%) was shown by TLC to contain several trace organic impurities. Carbazole free from polycyclic aromatic impurities was synthesized from cyclohexanone and phenylhydrazine using the Fischer Indolization route to tetrahydrocarbazole. This is a facile and exothermic reaction [13] and the product can be catalytically dehydrogenated to pure carbazole. The dehydrogenation step is, however, not easily adaptable for large scale syntheses.

During the synthesis of 9-allylcarbazole on a large scale from commercial grade carbazole, the crude product was most easily purified by distillation under high vacuum with subsequent recrystallization from methanol. This gave a pure white product better than 99.8% pure by DSC and apparently "one spot pure" by TLC. The carbazole alkylation was adapted from [14] using sodium hydride in THF to generate the anion of carbazole and reaction with allyl bromide. Later a much more convenient route was adopted [15] in which the alkylation is done in an emulsion of aqueous sodium hydroxide and toluene using with a phase transfer catalyst, benzyltriethylammonium chloride. This method obviated reactive metal hydrides and highly flammable solvents. It was better suited to reactions involving several hundred grams of material.

By using the organo platinum catalyst at a very low level and adopting a regimen of repeated precipitations and re solutionings of the polymer during the isolation stage, trace metals content were reduced to the limits of detection. The analysis of the polymers by FTIR and NMR showed further that all the Si-H bonds had reacted and there was reasonable correlation between the calculated M_n and that measured by GPC. Co-grafting with allyloxynitrostilbene was no problem.

3.4.1. Evaluation of Oxynitrostilbene-Carbazole Siloxane Polymer

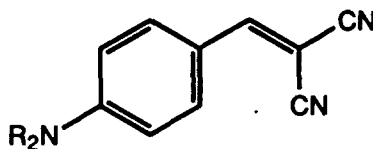
Copolymer films were spun coated from solvents such as cyclopentanone in the usual way to give films about 3-5 μm thick. Photoconductivity was measured using a Static Charge Analyser and the electrooptic coefficients measured after poling. The films were metallized with gold and poled just below T_g , the gold being subsequently removed.

It was soon shown that a 90/10 carbazole/ONS copolymer had both charge generation and photoconducting properties and an electrooptical coefficient of 1 pm/V at 633 nm. It was felt at the time that these values ought to be enough to demonstrate photorefractivity. When the first ONS/CBZ copolymers were examined, no signal could be detected. It was believed that the polymer charge generation was inadequate, so the polymer was doped with trinitrofluorenone (TNF) to form a charge transfer complex with the carbazole that would shift the UV absorption

further into the visible region. This is common practice in photoconductors based on carbazole [16]. Photorefractive measurements then gave a signal but it appeared slowly and did not vanish when the field was turned off which implied that the grating was produced not by photorefractive but by a photo bleaching process which left a permanent grating in the doped material. Further studies showed that the carbazole/TNF system alone did not bleach but that the ONS/TNF complex did. This was surprising as the oxynitrostilbene is itself an electron deficient molecule, nevertheless a charge transfer complex forms with the very strongly electron deficient TNF molecule. This is not photochemically stable as was shown at HCC [17] in an unrelated work that stilbene chromophores are susceptible to photobleaching at high light energy fluxes.

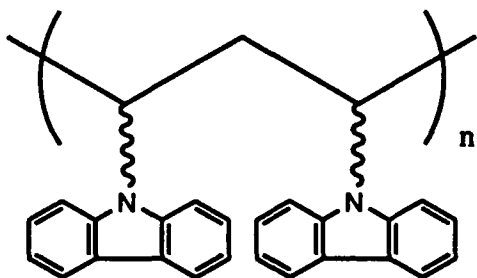
3.4.2. Better Chromophores

Unrelated research at HCC established that simple NLO chromophores with single benzene rings are much more bleach resistant than complex fused ring or highly conjugated double bond systems. A typical resistant chromophore would be a derivative of 4 aminobenzalmalononitrile such as (VII).

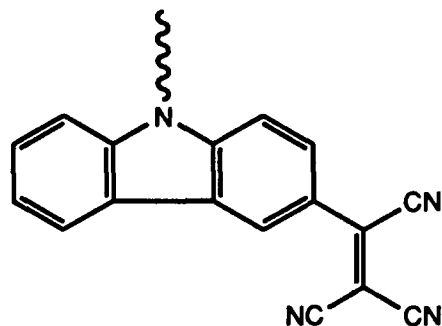


VII

Literature search revealed a Xerox Corporation Patent in 1976 [18] describing a side chain carbazole polymer (VIII) in which the carbazole rings were reacted with tetracyanoethylene (TCNE) to convert some of them into 3-tricyanovinylcarbazolyl units as in (IX). It was realized that the 3-TCV-carbazole unit is an NLO chromophore. Simultaneously it was learned that research at the University of Arizona was already pursuing the same idea [19]. The polymeranalogous tricyanovinylation was chosen to investigate our carbazolypropyl-methylsiloxane graft polymer.



VIII



IX

3.4.3. Polymeranalogous Tricyanovinylation Reaction

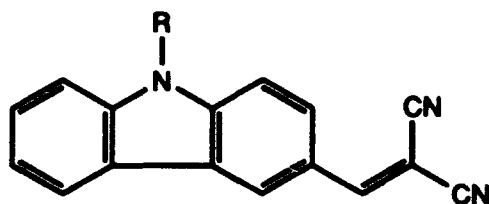
The reaction of electron rich aromatics with tetracyanoethylene (TCNE) [20] involves an electrophilic attack on the ring in which hydrogen cyanide is evolved. Carbazole would be an ideal substrate for such a reaction as it readily undergoes substitution at the 3 position by electrophiles. Accordingly, a 10 gm of purified carbazole-siloxane polymer was reacted with a large excess of TCNE in dimethyl formamide at 60 °C for four days under maximum safety guidelines. Much HCN was given off which was absorbed in trains of wash bottles full of hypochlorite bleach. The reaction took 72 hrs, but the work up with methanol as described in the literature evolved further large quantities of HCN. Despite the claim that TCNE does not react with simple primary alcohols [20], here it clearly does. The product is 1,1-dimethoxy-2,2-dicyanoethylene, produced by nucleophilic displacement of two CN groups by methanol. Thus each mole of TCNE produces in total three moles of HCN gas; one from the carbazole and two from the methanol.

The polymer was isolated as a brick red solid and elemental analysis showed that it was the desired product with about 18 moles % of the carbazole units substituted with TCV units. FTIR and NMR confirmed the presence of tricyanovinyl units. The polymer had an absorption maximum at 503 nm and films made from it were shown to be stable photochemically at 633 nm at energy densities of up to 100 watts/cm². TGA showed that the polymer was thermally stable to over 400 °C (all these polymers have similarly good thermal stabilities) and its T_g had risen to about 80 °C. It was photoconductive and after poling, at 70 V/μm it had an electrooptical coefficient of 5-6 pm/V at 633 nm. This batch had a much lower molecular weight than the starting polymer. GPC and derived absolute intrinsic viscosities showed that there was appreciable molecular weight reduction. The initial IV of the hydrosiloxane was 0.12 and that of the carbazolyated siloxane was also 0.12, showing that no degradation occurred during the grafting reaction. After the TCNE reaction, the IV fell to about 0.05. The polymer could be spun coated onto ITO glass but films had to be handled with great care to avoid cracking. The polymer was tested in by four wave mixing but the results were erratic and ambiguous. In the meantime, more runs were made using tertiary butanol in place of methanol during the workup. Much less HCN was given off at the workup stage but the IV's fell to even lower values (about 0.03) and some fractions of the isolated material remained as dark red gums which would not solidify. One possible reason for the scission of siloxane chains during this reaction is that liberated cyanide anions attack occasional SiH units left over after grafting and eliminate hydrogen via a hydride shift mechanism. The result is a cyanosilane (SiCN) unit which is easily cleaved by hydrolysis during the polymer workup.

3.4.4. Dicyanovinylcarbazole Chromophores

In view of the chain scission problem with the polymeranalogous tricyanovinylation reaction and the HCN hazards associated with it, efforts were redirected to a route in which the chromophore would be built up in a preformed state and then grafted onto the backbone. In a model experiment, 9-ethylcarbazole-3-aldehyde reacted readily with malononitrile to give 3-(2,2-dicyanovinyl)-9-ethylcarbazole (X) and this was added to a PMMA film in a guest host system. This yielded a relatively poor electrooptic coefficient of 0.8 pm/V.

The synthesis of a graftable dicyanovinylcarbazole was the pursued with 9-allyl analog (XI). The first stage involved the synthesis of 9-allylcarbazole-3-aldehyde (XII) using well known Vilsmeier Haack reaction [21] on 9-allylcarbazole yielding the desired aldehyde in 65% yield.



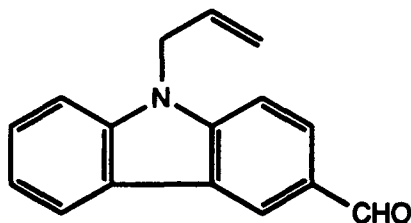
X: $R = -C_2H_5$

XI: $R = -CH_2-CH=CH_2$

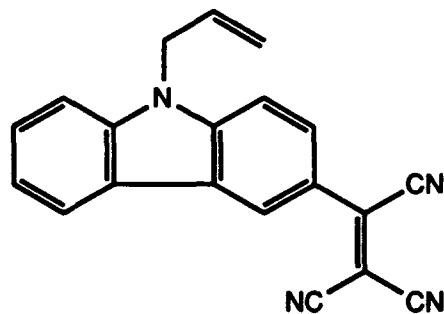
The new aldehyde (XII) reacted readily with malononitrile to give the bright yellow dicyanovinyl derivative (XI). This compound was grafted onto the siloxane backbone to give a homopolymer but the opaque yellow product was insoluble in all common solvents, possibly due to strong inter chain polar forces. It had $T_g = 75^\circ C$. Next, a copolymer was grafted using a 25/75 ratio of DCV-CBZ to plain CBZ units. This product had $T_g = 45^\circ C$ and its IV was 0.12, showing little or no chain scission had occurred. This was spun coated yielding good quality films with an electrooptical coefficient of about 0.8-1 pm/volt. Again, four wave mixing runs using poled films gave no clear unambiguous evidence of a genuine photorefractive effect.

3.4.5. Tricyanovinylcarbazole Polymers from TCV Allylcarbazole

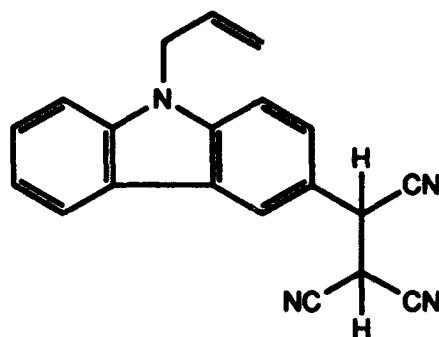
Since the tricyanovinyl group is about 5-10 times stronger as an NLO chromophore than the dicyanovinyl unit, the possibility was considered of converting the dicyanovinyl copolymers to the tricyanovinyl analogs using a series of polymeranalogous reactions [20]. The first stage was a Michael addition of HCN with sodium cyanide in DMF and this would be expected to cause backbone scission of the siloxane chain once again. The separate synthesis of 9-allyl-3-tricyanovinylcarbazole (XIII) was considered a safer route.



XII



XIII



XIV

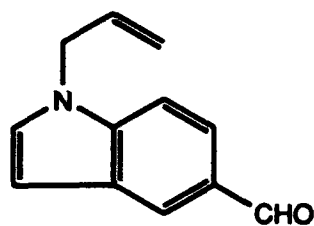
A large amount of 9-allylcarbazole-3-aldehyde (XII) and the corresponding dicyanovinylcarbazole (XI) were thus prepared and the DCV compound was reacted with cyanide in a Michael addition to give the yellow brown tricyanoethyl intermediate (XIV). This reaction was quite exothermic. The Michael product (XIV) was not isolated but oxidized in situ with lead tetra-acetate to the intense crimson tricyanovinyl compound (XIII). The desired product (XIII) formed deep crimson needles from toluene melting point 181-2 °C and its UV spectrum showed a peak at 477 nm. The structure was confirmed by NMR, FTIR in the usual way.

Using the same organo platinum catalyst, a 25/75 graft copolymer of TCV-allylcarbazole and allylcarbazole was made. GPC showed the polymer had suffered only moderate chain scission ($M_n = 14,000$, $M_w = 38,000$, $IV = 0.07$) while NMR showed that the actual level of incorporation of TCV-carbazole units was about 16% molar instead of 25 %. Some unreacted SiH units were left, which may have contributed to backbone degradation. The polymer was soluble in cyclohexanone and could be spun coated to satisfactory films. These had a maximum absorption around 500 nm and after poling at 100V/ μ m, the electrooptical coefficient at 633 nm was 7 pm/volt.

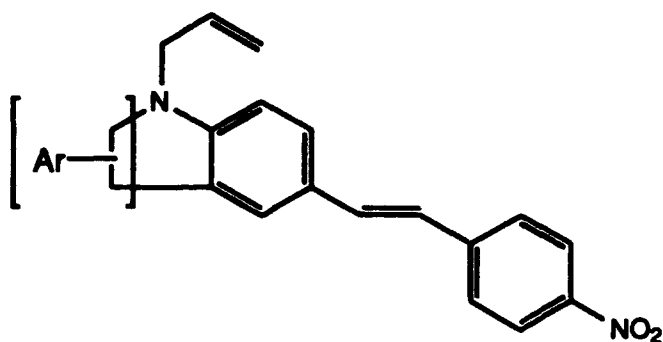
This polymer film was evaluated on the four wave mixing set up and this time a small but measurable signal was obtained which was attributed to a photorefractive effect.

3.4.6. Other Chromophores

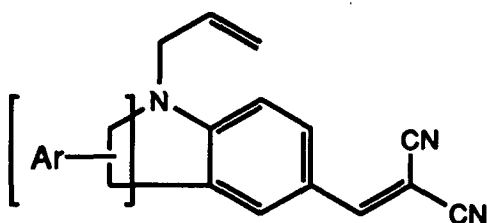
A number of alternative NLO active allyl-terminated chromophores were also synthesized, based on two starting materials: 9-allyl carbazole-3 aldehyde (XII) and 1-allylindoline-5-aldehyde (XV). Previous work at HCC [22] had shown that indoline derivatives gave electrooptic polymers with high electrooptic coefficients. The desired aldehyde was made by standard methods: indoline was reacted with allyl bromide in the presence of sodium carbonate to give 1-allylindoline and the latter converted to the 5-aldehyde (XV) by the Vilsmeier reaction. A modified Vilsmeier procedure gave better yields in this case, the difference being to run the reaction in dichloroethane as a solvent rather than in excess DMF. The aldehydes (XII) and (XV) were then reacted with 4-nitrophenylacetic acid by Hann's method [23] to give the 4'-nitrostilbenes (XVI), with malononitrile to give the dicyanovinyl compounds (XVII) from these the tricyanovinyl derivatives e.g.(XVIII) were made. The aldehydes were also reacted with 1,3-diethylthiobarbituric acid to give the benzylidene-thiobarbituric acid compounds (XIX). Finally the aldehydes were reacted with nitromethane to give the 2'-nitrostyrene derivatives [24] (XX).



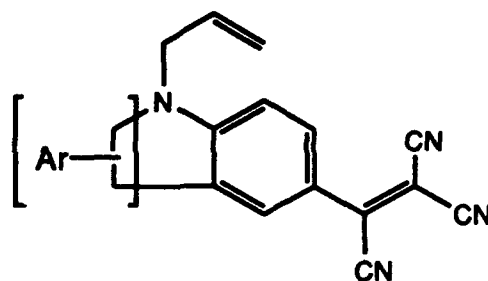
XV



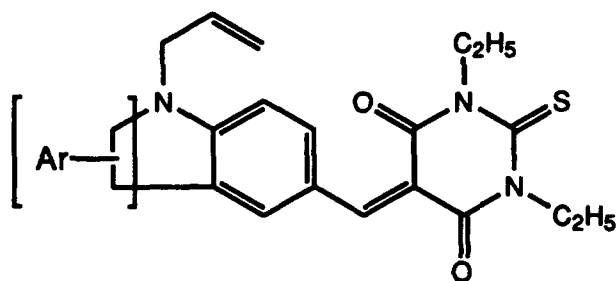
XVI



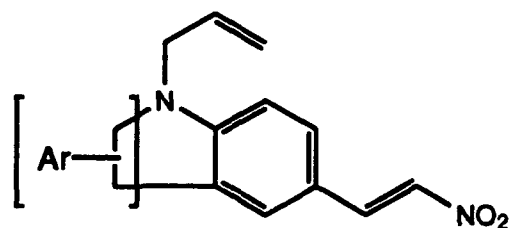
XVII



XVIII



XIX



XX

Most of this phase of the work concentrated on the nitrostilbene derived from 1-allylindoline as it bore a close resemblance to the P2ANS chromophore and a siloxane backbone polymer would provide an interesting comparison with the polymethacrylate. Attempts to graft this material onto the hydrosiloxane failed. The starting materials were recovered largely unchanged. One of the thiobarbiturates was tried and failed likewise, but in this case the low solubility of the chromophore in the reaction solvent (toluene) may have contributed. It is possible that some kind of ligand exchange complicates the Finkelmann addition of allylamines where the nitrogen is basic as in the case of 1-allylindolines. By contrast, 9-allylcarbazole reacts as desired because the nitrogen atom is neutral. Possibly N-(4-pentenyl)amines would react under Finkelmann conditions but this was never explored.

3.5. Synthetic Experimental Detail

3.5.1. Cyanoethylation of Carbazole

This reaction was run in the hood with all due precautions for handling the highly toxic acrylonitrile. Since cyanoethylations can become highly exothermic, a large 2000 ml flask was used. It was fitted with an efficient double surface reflux condenser and a large bucket of ice water ready to quench the flask in case of a reaction problems. The flask was charged with 100 gm (0.598 moles) of 99% pure carbazole (Aldrich) and 150 ml acrylonitrile. The slurry was swirled by hand and 1 ml of Triton-B catalyst (benzyltrimethylammonium hydroxide, 40% in methanol) was added. The mixture hissed with the heat of reaction and instantly darkened locally. After 2 minutes standing, the whole mass suddenly went dark and much heat was evolved, enough to make the mixture reflux briskly. About 150 ml dry toluene was added down the condenser to moderate the exotherm and the flask cooled in the ice bucket. It was let stand 40 minutes at room temperature, then refluxed gently for 1 hr to complete the reaction. The flask was chilled in ice water and brown crystals recovered. These were filtered off, washed with toluene, and then recrystallized from 600 ml boiling toluene with carbon treatment to remove the brown color. The final product formed long white needles with T_m of 156-158 °C and yield of 68 gm. after drying (52% theory). Percec [24] reported a T_m of 155.5 °C.

3.5.2. Preparation of 4-(3-Cyanopropoxy)-4'-Nitrostilbene

The reaction was run under Ar in a 5 liter 4-neck flask fitted with stirrer, reflux condenser, PE tap funnel and Ar inlet tube. A bubbler was fitted to the top of the condenser. The flask was charged with 251 gm (0.9 moles) dry blue potassium salt of 4-hydroxy-4'-nitrostilbene, 2 liters of acetonitrile (HPLC grade), 4 gm of 18-crown-6 ether, and 1 gm sodium iodide catalyst. The tap funnel was charged with 100 gm (0.97 moles) 4-chlorobutyronitrile. The mixture was stirred and refluxed gently and the chloronitrile added dropwise. The color slowly changed from blue-purple to reddish-brown. Refluxing continued for 72 hrs. After cooling overnight, yellow crystals came out which were filtered and washed with acetonitrile and placed in a very large Soxhlet thimble in a 12 liter scale Soxhlet apparatus. The crude product was extracted into 7,500 ml boiling HPLC grade toluene until no more color came out in the thimble. This took about 18 hrs. On cooling, the flask deposited a mass of long yellow needles. After filtering and drying in the vacuum oven these weighed 155 gm, (56 % theory) with a T_m of 128-129.5 °C. More material could be recovered from the toluene liquors. NMR, Mass Spec. and FTIR spectra showed the compound had the expected structure, and DSC showed its purity was 99.7 moles %, T_m = 127.1°C, ΔH = 118 j/g.

3.5.3. 4-(4-Cyanobutoxy)-4'-Nitrostilbene

This material was prepared almost exactly as in the preceding experiment from 50 gm (0.309 moles) 5-bromovaleronitrile, 78 gm (0.28 mole) blue potassium salt of hydroxynitrostilbene, 1.5 gm 18-crown-6 ether, and 500 ml acetonitrile. The product weighed 60 gm (66% theory) with a T_m of 127.5-129 °C. This melting point is very close to that of the preceding material with one less carbon but an intimate mixture of the two compounds melted at 117-127 °C, showing they were not identical. The cyanobutoxy compound ran on a TLC as one spot R_f = 0.25 (eluant: chloroform) and DSC showed it was 99.8% molar pure, T_m = 122.7 °C, ΔH = 122.5 j/g.. FTIR shows peaks at 2240 (CN); 1514,1504 and 1341 cm^{-1} (aromatic nitro). Analysis found: C = 70.58,70.67; H = 5.69, 5.71; N = 8.69, 8.47. Calculated: C = 70.81, H = 5.59, N = 8.7.

3.5.4. 4-Allyloxy-4'-Nitrostilbene

A mixture of 2000 ml acetonitrile, 111.5 gm (0.4 mole) blue potassium salt of hydroxynitrostilbene and 0.8 gm 18-crown-6 ether was refluxed under Ar while 53.23 gm (0.44 mole) allyl bromide (severe lachrymator) was added dropwise over 2-3 hrs. Since allyl halides are highly reactive, at the end of addition the purple mixture turned bright yellow. The potassium bromide was filtered from the hot acetonitrile and the filtrate left to cool overnight. The yellow product was filtered off and was substantially pure. Yield was 88 gm (78.3% theory) with a T_m of 115-6 °C. UV-vis spectrum (MeCN) showed a peak at 374 nm, $\epsilon = 30,500$.

3.5.5. 9-Allylcarbazole by NaH/THF route

The reaction was run in a 5-liter 5-neck flask fitted with a Trubore glass paddle stirrer blade, not a Teflon blade because of sodium hydride might attack Teflon. The stirrer was driven by an air motor because of the fire hazards involved. The flask was fitted with a reflux condenser, PE tap funnel, gas inlet for Ar, and a rubber septum covering the fifth neck. All glassware was dried at 110 °C overnight. The flask was charged with 23 gm 60% w/w sodium hydride dispersion in oil and 500 ml dry mixed hexanes and stirred under Ar. After 5-10 minutes the hexane was removed with a 36" #18 gauge double ended stainless steel needle through the septum into a filter flask attached to the vacuum line. As much as possible of the hexane was removed and the whole washing process repeated twice more to leave pure sodium hydride free from oil in the flask. It was kept under Ar as it may ignite in air. The hydride was covered with 250 ml dry THF from an Aldrich "Sure Seal" bottle using #18 needle via the septum and pressurizing the bottle gently with Ar. Then 97 gm (0.581 moles) 99% carbazole (Aldrich) was dissolved in 1 liter of warm anhydrous THF and added dropwise from the tap funnel to the stirred slurry of hydride. The color turned greenish-brown and hydrogen was evolved. The mixture was refluxed gently on the steam bath for 1 hr to complete the formation of the N-sodium-carbazole. Eventually a clear olive-green solution formed which was left to cool under Ar for several hrs. A mixture of 55 ml, 77 gm (0.64 mole) allyl bromide in 250 ml THF was then added dropwise from the tap funnel with stirring under Ar. There was a mildly exothermic reaction and the mixture began to go cloudy with precipitated sodium bromide. The mixture was let stand overnight at this point, then refluxed gently on the steam bath for 18 hrs. After cooling, the salt was filtered off and the clear filtrate taken down on the rotary evaporator giving a pale brown solid (120 gm, 100% theory). This was taken up in 1000 ml diethyl ether and shaken twice in a 2 liter Squibb separator funnel with 2% w/v NaOH solution to remove unreacted carbazole, then washed with water three times and dried over sodium sulfate. Filtering and removal of the solvent gave 87 gm (73%) crude product. The best way to purify it was to redistil it under high vacuum using a 24/40 short path still with a built-in Vigreux column (Kontes # K-513760-0000) and a 2-way Y-shaped Schlenk adapter with two 100 ml flasks as a receiver (Safe-Lab Ref # A-2062). After a small fore-run, the material distilled from an oil-bath at 180 °C (Ar capillary leak) as a water-white oil with a boiling point of 155 °C/0.55 mm Hg. There was almost no residue in the still pot. The solidified distillate was recrystallized from a little methanol to give glittering white plates with T_m of 56-57 °C, 99.5% pure by DSC. Final recovery was 64 gm, 53% overall. The product discolored quickly in light and air and was therefore stored under Ar in a dark brown bottle.

3.5.6. 9-Allylcarbazole by Nishi's Route

A 3000 ml 3-neck flask was charged with 250 gm sodium hydroxide and 500 ml distilled water and stirred at low rpm with a high speed Teflon stirrer until a clear solution was formed. The flask was sparged with Ar, and 100 ml toluene, 150 gm (0.898 mole) 99% carbazole and 5 gm benzyltriethylammonium chloride (PTC catalyst) added. The stirrer was run up to high speed to emulsify the organic layer and 110 ml (157 gm), 1.3 moles) allyl bromide added dropwise from a tap funnel over about 40-50 minutes. Gradually the slurry of solids became a smooth dark

colored emulsion, free from any suspended particles, over 2-3 hrs. After this time the stirrer was stopped and the mixture allowed to settle out into two layers. No solids were visible. The upper toluene layer was tested for unreacted carbazole by TLC but none was present. The flask was set up for steam distillation and dry steam blown in until about 300 ml distillate had been collected. This removed unreacted allyl bromide and some toluene. After cooling overnight, a mass of sticky brown crystals formed in the flask. The product was extracted into toluene, washed with water until neutral, dried over sodium sulfate and the solvent removed on the Rotevap. The crude product was brown and weighed 185 gm, virtually 100% theory. It was then purified by redistillation and recrystallization as described. The recovery was about 80%.

3.5.7. Reaction of 9-Ethylcarbazole-3-Aldehyde with Malononitrile

A mixture of 44.6 gm (0.2 mole) 9-ethylcarbazole-3-aldehyde (Aldrich), 13.2 gm (0.2 mole) malononitrile, and 350 ml absolute ethanol was refluxed on the steam bath until a clear solution formed and 5 drops of 4-methylpiperidine added. Within minutes the flask set solid with a mass of yellow crystals. The flask was left overnight and the product filtered, washed with ethanol and dried at 60 °C in a vacuum oven yielding 46 gm (85%) with T_m of 164-6 °C. This was recrystallized from 400 ml hot acetonitrile to give long bright yellow blades with T_m of 165-7 °C, recovery 31 gm (57%). DSC showed the material was 99.9% molar pure, T_m = 163.7 °C, ΔH = 115 j/g. NMR results were consistent with the proposed structure.

3.5.8. 9-Allylcarbazole-3-Aldehyde

This improved Vilsmeier-Haack route uses dichloroethane as a reaction medium. Consistently better yields and cleaner products were obtained by this method. A 1000 ml 3-neck flask was fitted with a sealed Teflon paddle stirrer, reflux condenser, PE tap funnel and Drierite guard tubes. All glassware was dried at 100 °C overnight. The flask was charged with 103.5 gm (0.5 mole) freshly purified 9-allylcarbazole, 600 ml dry 1,2-dichloroethane, and 55 ml, 52 gm (0.7 mole) anhydrous dimethylformamide. The tap funnel was charged with 65.3 ml and 107.3 gm (0.7 mole) phosphorus oxychloride added at 2-3 drops/second with stirring at room temperature. As soon as the chloride was added the color went orange-yellow and by the time half had been added, the color was deep wine-red. No hydrogen chloride was evolved. The addition took about 35-40 minutes. The mixture was then heated on the steam bath the gentle reflux with stirring; no HCl was evolved at first, but it began to come off slowly after 20-30 minutes. Heating continued for 6-7 hrs by which time no more HCl was evolved. The mixture was let stand overnight and solidified to a mass of yellow-brown crystals. The contents of the flask was added with stirring to a large beaker containing 550 gm sodium acetate trihydrate in 800 ml water. The mixture remained semi-solid. It was warmed to 30 °C on the steam bath to break up the pasty mass, stirred and let cool again.

The lower organic layer was run off in a Squibb separating funnel and the aqueous layer extracted twice more with dichloroethane. The combined organic layers were washed thrice with 7.5% sodium bicarbonate and once with 15% brine. All these separations took a long time to settle due to emulsion formation. The extracts were dried over magnesium sulfate overnight, then filtered and taken down on the Rotevap to give 125 gm (105% theory) of dark brown oil. Scratching and seeding caused this to crystallize. The crude product was recrystallized with carbon treatment from a minimum of methanol and pale tan-colored crystals were formed on slow cooling. These were filtered off and dried to constant weight in the vacuum oven at 45 °C. Yield was 92.6 gm, (79%), and T_m was 68-69.5 °C. The FTIR spectrum showed an aldehyde C=O at 1685 cm^{-1} , C=C vinyl band at 1645 and the characteristic aldehyde proton at 2700 cm^{-1} . The carbazole ring bands showed up clearly in the FT-Raman spectrum at 1630, 1550 cm^{-1} while proton NMR showed the structure was correct with the aldehyde proton as a sharp singlet at 10 ppm.

3.5.9. 3-(2,2-Dicyanovinyl)-9-allylcarbazole

A solution of 23 gm (0.1 mole) 9-allylcarbazole-3-aldehyde, 6.6 gm (0.1 mole) malononitrile, and 200 ml absolute ethanol was placed in a 500 ml flask and 2-3 drops of 4-methylpiperidine added. At once heat was evolved. The mixture was refluxed on the steam bath for 2 hrs as the color deepened to brown-yellow. After standing overnight a yellow solid came out which was filtered off and dried. Weight of crude product was 20.5 gm (73% theory). The solid was recrystallized from a 1/1 mixture of ethanol and acetonitrile (200 ml) to give dark yellow plates with T_m of 144-6 °C and yield of 15.4 gm (55%). TLC on silica-gel showed the product was homogeneous, $R_f = 0.2$ (eluant: chloroform-hexane 1/1) FTIR and FT-Raman showed that the product had the desired structure: CN bands at 2220 cm^{-1} and the C=C of the DCV unit showed in the Raman at 1559 cm^{-1} . NMR, both proton and C-13, confirmed the structure. DSC (van t'Hof) showed the product was 98.2% molar pure and had $T_m = 146.9$ °C, $\Delta H = 105.5$ j/g. There was a weak endotherm at 90.2 °C which may be a crystal-to-crystal transition. UV-vis spectrum (MeCN) showed a peak at 403 nm, $\epsilon = 28,930$

3.5.10. 3-(1,2,2-Tricyanovinyl)-9-Allylcarbazole

This reaction follows the route of McKusick et. al. (loc cit). The reaction was run in the hood in a 2000 ml 4-neck flask fitted with stirrer, condenser, PE tap funnel, long stem thermometer and Ar inlet. The outlet from the top of the condenser went through a train of three wash bottles; the first one empty to act as a trap, and the second and third containing Chlorox bleach to oxidize any HCN carried over to sodium cyanate. To a solution of 23.5 gm (0.083 moles), 180 ml of 3-dicyanovinyl-9-allylcarbazole dimethylformamide was added under a slow Ar sparge while stirring a solution of 5.4 gm sodium cyanide (0.11 mole) in 30 ml water. The color went from intense yellow to pale brown and heat was evolved, enough to raise the batch to nearly 40 °C. The mixture was stirred for five minutes, then 250 ml glacial acetic acid was added from the tap funnel which was then removed and replaced with a stopper. Then 36.7 gm (0.083 mole) lead tetra-acetate added in small solid portions over about 5 minutes under Ar, replacing the stopper each time as the solid was added. The reaction mixture became intense deep red and the exotherm raised the batch to 46 °C. Soon a brick-red precipitate came out. The mixture was stirred for 15 minutes then set aside at 0 °C for 48 hrs.

The red solid was filtered off, washed and dried to constant weight at 60 °C in the vacuum oven. The crude product weighed 23 gm (90% theory). It was recrystallized from 200 ml boiling toluene and filtered hot. On cooling maroon colored needles were formed. After isolation and drying, these weighed 18.5 gm (72%) with T_m of 181-2 °C. FTIR and FT-Raman spectra showed three CN bands at 2,234, 2,224 and 2,220 cm^{-1} and C=C bands at 1,645 cm^{-1} (allyl) and the tricyanovinyl C=C band at 1,500 cm^{-1} . The UV-vis spectrum showed at peak at 477 nm, $\epsilon = 22,200$. DSC purity was 98.6% molar, $T_m = 180.2$, $\Delta H = 112$ j/gm, TLC shows one spot $R_f = 0.24$ in 1/1 chloroform/hexane with a trace of impurity, $R_f = 0.0$. UV-Vis (MeCN) showed peak at 477 nm, $\epsilon = 22,200$.

3.5.11. Preparation of 1-Allylindoline

This alkylation is based on the method of Tweedie and Allabashi [26]. The reaction was conveniently run in a 5 liter 3-neck flask fitted with a steam jacket and bottom discharge valve. The flask was set up in the hood with an air motor driven paddle stirrer, reflux condenser, 500 ml PE-tap funnel, and Ar inlet with a bubble tube on top of the condenser. A mixture of 327 gm (2.75 moles) Aldrich 99% indoline, 1200 ml 190 proof denatured ethanol, 232 gm (2.2 moles) anhydrous sodium carbonate, and 500 ml distilled water was stirred in the flask and heated with steam under a slow Ar sparge until the ethanol refluxed gently. To this hot solution, 362 gm

(2.99 moles) allyl bromide was carefully added dropwise at such a rate that the heat of reaction maintained reflux with little external heating required. This took 2-3 hrs. When all the bromide had been added, the flask was steam heated and stirred under reflux for 16-20 hrs. At the end of this time the system was set for distillation and about 1000 ml ethanol distilled off.

Cold water was passed through the steam jacket for 10 minutes to reduce the batch quickly to 18-20 °C. The stirrer was stopped and the mixture allowed to settle into two layers: the upper organic one contained the product and the lower aqueous one contained the sodium bromide. The lower layer was run off carefully using the bottom discharge valve and extracted twice with 500 ml diethyl ether, the organic layers being recombined and washed with 800 ml water. The flask served as a convenient separator funnel during these operations. The organic phase was dried overnight (sodium sulfate) and taken down on the Rotevap to give a dark oil weighing 395 gm (90.4% theory). The oil was distilled under reduced pressure using a vacuum jacketed Vigreux column and came over as a water white oil at 110-115 °C/1 mm Hg. Only a small dark residue was left in the still pot. The product rapidly discolors in air and light and was stored in a dark brown bottle below 5 °C. The pure product had $n_{\text{D}}^{20} = 1.5652$

3.5.12. 1-Allylindoline-5-Aldehyde

The first three runs used the Vilsmeier reaction as described in Organic Syntheses [20] but yields were only 40-45% and there was much tarry material left after vacuum distillation. The last three runs used dichloroethane as a reaction medium (as employed for 9-allylcarbazole-3-aldehyde) and gave better yields and much less tar. The route described is the latter.

Into a 2000 ml 4-neck flask fitted with a stirrer, reflux condenser, thermometer and long stem thermometer (thoroughly dry) were placed 159 gm (1 mole) pure 1-allylindoline and 117 gm (1.7 mole) anhydrous dimethylformamide and 800 ml HPLC grade 1,2-dichloroethane. To the stirred mixture was added 245 gm (149 ml; 1.6 mole) freshly opened phosphorus oxychloride dropwise in the cold. The heat of reaction caused the batch temperature to rise to 70 °C before it fell to 55-60 °C at the end. The addition took about 1.5 hrs. The mixture was then stirred and refluxed on the steam bath (guard tubes) for 1 hr during which HCl gas was evolved and the color went an intense yellow-brown. The mixture was left to cool overnight then the flask chilled in a large ice bath while a solution of 328 gm anhydrous sodium acetate in 1000 ml water was added slowly with brisk stirring. Much heat was produced, hence the cooling bath. When the complex had been decomposed, the lower organic layer was run off in a large Squibb funnel and the aqueous layer extracted with fresh dichloroethane. The combined organic phases were washed with 7.5% sodium bicarbonate until free from acid, then with 15% brine and finally with water, then dried over anhydrous sodium sulfate. Filtering and evaporation on the RFE gave a thick brownish-green oil weighing 165 gm (88%). The crude product was distilled under high vacuum on the oil pump from an oil bath at 220 °C using a short path still with a vacuum jacketed Vigreux column. After a fore-run, the product distilled as a bright yellow vapor at 164 °C/0.25 mm condensing to an olive-green liquid which eventually solidified. The redistilled aldehyde melted at 31-2 °C. Yield was 129 gm (69%). FTIR showed an aldehyde C=O at 1660 cm^{-1} while the NMR spectrum showed the aldehydic proton as a sharp singlet at 9.7 ppm. The NMR spectrum was compatible the desired structure. TLC showed one spot $R_f = 0.10$, eluant: chloroform/hexane 1/1.

3.5.13. 1-Allyl-5-(4-Nitrostyryl)-Indoline

A mixture of 46.8 gm (0.25 mole) 1-allylindoline-5-aldehyde, 50 gm (0.28 mole) 4-nitrophenylacetic acid, 300 ml of DMF, and 25 ml morpholine were heated on the steam bath under a bubbler tube until no more carbon dioxide was evolved. This took about 6 hrs and the mixture became deep reddish-brown. Excess DMF and morpholine were removed on the Rotevap on the oil pump at 75-100 °C leaving a thick dark red oil weighing 108 gm (141 %

theory). This could not be induced to crystallize so it was left for several days in the freezer and deposited well shaped deep purple crystals which were filtered off on a sinter from the oily residue. They were recrystallized from a minimum of acetonitrile and came out as long violet-black needles (looking like iodine crystals) which were dried to constant weight at 50 °C. The yield was 14 gm and T_m was 110 °C. TLC showed one spot. Both proton and C-13 NMR showed the material had the desired structure. UV-vis spectra showed a maximum at 438 nm, $\epsilon = 25,000$.

3.5.14. 1-Allyl-5-Dicyanovinylindoline

A mixture of 52.2 gm (0.279 mole) 1-allylindoline-5-aldehyde, 18.5 gm (0.28 mole) malononitrile, 300 ml absolute ethanol were warmed on the steam bath added and the mixture stirred and refluxed for 2 hrs, then stood overnight. A mass of orange-red plates formed which were filtered off, recrystallized from 300 ml acetonitrile, then vacuum dried to constant weight at 50 °C. Yield was 47 gm (72%) and T_m was 105-107 °C. UV-Vis showed (MeCN) peak at 444 nm, $\epsilon = 68570$.

3.5.15. 1-Allyl-5-(1,2,2-Tricyanovinyl)-Indoline

This reaction was run in a 1 liter 4-neck flask in the same way as (3.5.9) above. To a mixture of 23.5 gm (0.1 mole) 1-allyl-5-dicyanovinylindoline in 260 ml DMF was added dropwise a solution of 6.5 gm sodium cyanide in 30 ml water under a slow Ar stream, the outlet passing to the hood exhaust via a train of Chlorox wash bottles. The mixture quickly warmed up to 38 °C and the yellowred color faded to a tan color. Acetic acid (300 ml) was added and the color became wine-red. Lead tetra-acetate (44.3 gm, 0.1 mole) was added slowly in small portions. The color instantly became deep purple and the exotherm warmed the mixture to 42 °C. An ice bath was used to keep the batch at about 35 °C. After stirring for 1 hr the mixture was added to 1 liter of water, stirred for 10 minutes then filtered off. The intense purple product was washed thoroughly then dried to constant weight at 60 °C for 22 hrs under high vacuum. The crude weight was 25.6 gm (99%) and the product was recrystallized from 200 ml boiling toluene to deposit deep purple needles melting point 147-9 °C. The recovery was 18.2 gm, (72% theory) and the compound ran as one spot on a TLC, $R_f = 0.87$ in chloroform/ethyl acetate (4/1). The FTIR and FT-Raman spectra were consistent with the structure (CN band at 2211 cm^{-1}) and DSC showed the material was at least 98% molar pure with $T_m = 149.4$ °C and $\Delta H = 103$ j/g. UV-vis spectrum (MeCN) showed a maximum at 542 nm, $\epsilon = 37,680$.

3.5.16. Reaction of 1-Allylindoline-5-aldehyde with Diethylthiobarbituric Acid

A mixture of 20 gm (0.1 mole) 1,3-diethylthiobarbituric acid, 18.7 gm and (0.1 mole) 1-allylindoline-5-aldehyde was dissolved with swirling in 150 ml anhydrous DMF. A mixture of 1 ml 4-methylpiperidine and 2 ml glacial acetic acid was added as catalyst. The mixture turned deep magenta and soon began to set to a mass of crystals. It was heated 30 minutes on the steam bath then left to cool overnight. Next day the mixture was heated on a heating mantle until a clear deep purple solution was formed. This was filtered hot and left to crystallize again. The product was filtered, washed with ethanol and dried at 55 °C. Yield was 16.6 gm, (45%) as very bulky purple needles having no proper melting point. The product decomposed with a sharp, reproducible exotherm at 175 °C. TLC showed one spot $R_f = 0.69$ in 4/1 chloroform/ethyl acetate. UV-Vis spectrum (MeCN) showed a peak at 511 nm, $\epsilon = 72,830$.

3.5.17. Condensation of 9-Allylcarbazole-3-Aldehyde with Diethylthiobarbituric Acid

A mixture of 10 gm (0.05 mole) diethylthiobarbituric acid, 11.8 gm (0.05 mole) allylcarbazole-aldehyde, 50 ml dry DMF, 1 ml 4-methylpiperidine, and 2 ml glacial acetic acid were swirled until they all dissolved. A mass of orange crystals soon formed and after standing overnight at room temperature these were filtered off washed with DMF then methanol and dried to constant weight at 80 °C in the vacuum oven. Yield was 9.1 gm (43%) in tiny orange needles with T_m of 248.5-249.5 °C. The solid was very sparingly soluble in all common solvents. NMR indicated it had the correct structure. UV-Vis spectrum (MeCN) showed a peak at 459 nm, $\epsilon = 37,100$.

3.5.18. 9-Allyl-3-(2-Nitrovinyl)-Carbazole

A mixture of 47 gm (0.2 mole) 9-allylcarbazole-3-aldehyde, 180 ml pure nitromethane, and 10 gm ammonium acetate was heated on the steam bath for 5 hrs and left overnight at room temperature. The orange crystals which formed were filtered, washed with ethanol, and dried at 60 °C under vacuum. Yield was 39.7 gm (72%) with T_m of 135-137 °C. Recrystallization from acetonitrile gave gold-colored needles with a purplish luster with T_m of 138.5-140 °C. FTIR-Raman showed the structure was correct, and the Raman showed nitro bands at 1,491 and 1,321 cm^{-1} and a weak C=C band (allyl?) at 1,645 cm^{-1} . UV-Vis spectrum (MeCN) showed a peak at 401 nm, $\epsilon = 17,760$.

3.5.19. 1-Allyl-5-(2-Nitrovinyl)-Indoline

A mixture of 37.4 gm (0.2 mole) 1-allylindoline-5-aldehyde, 180 ml 96% pure nitromethane and 7 gm ammonium acetate was heated on the steam bath for 5 hrs (95 °C) then left to stand in the freezer at -10 °C overnight. Next day splendid steel blue crystals had formed which were filtered, washed and dried in the vacuum oven at 56 °C. The yield was 33.3 gm (73%) with T_m of 110-2 °C. The blue crystals melted to a deep crimson liquid. A second recrystallization from ethanol gave blue prismatic needles with T_m of 110.5-111.5 °C. TLC showed one spot $R_f = 0.6$ in chloroform. UV-Vis spectrum (MeCN) showed a peak at 453 nm, $\epsilon = 29,300$.

3.5.20. Preparation of Platinum-dicyclopentadiene Dichloride Catalyst

In a 50 ml flask, 2.76 gm (6.73 millimole) chloroplatinic acid hydrate was dissolved in 6 ml glacial acetic acid and 10 ml distilled water added. The diluted solution was heated to 70 °C and 2 ml pure dicyclopentadiene was added. The mixture was stirred briskly at 70 °C for 24 hrs. It quickly changed from yellow to dark brown. At the end of the heating period the solid was filtered off, washed, then extracted with boiling tetrahydrofuran (the insoluble matter should be retained for platinum recovery since it contains significant amounts of platinum black). The solution was filtered hot and the process repeated. Much dark solid remained undissolved but on cooling a white solid came out from the THF filtrate. This was filtered and recrystallized from fresh THF. Yield was about 0.6 gm (22% theory) white solid with T_m of 217-218 °C (literature value 218 °C). The method of Drew and Doyle [27] uses dichloromethane in place of THF, but our yield was only 8% theory! The product was kept in the freezer since it deteriorates on standing.

3.5.21. Polymeranalogous Grafting of 9-Allylcarbazole onto Polymethylhydrosiloxane

The reaction was run under Ar in a 500 ml flask with condenser and septum capped side arm. All glassware was dried at 110 °C overnight. The toluene used as a reaction medium was intensively dried by refluxing over sodium metal and benzophenone in a special solvent recovery still until the final purple color of the ketyl was permanent. The toluene was then distilled into the receiver

bulb and transferred to the flask with a syringe under Ar. Strictly anerobic conditions must be maintained. The flask was charged with 8.94 gm (0.149 mole) Petrarch PS122 polymethylhydrosiloxane, 37 gm (0.178 mole) pure dry 9-allylcarbazole and 200 ml dry toluene. The mixture was heated at 60 °C in a thermostat controlled oil bath and stirred magnetically. The system was evacuated and sparged with Ar three times before adding the catalyst to remove all traces of oxygen. The dicyclopentadiene-platinum dichloride catalyst (0.006 gm; 0.0149 millimole) was added through the septum as a toluene solution (0.1 gm in 20 ml dry toluene) using a microsyringe. The reaction was run for 18-20 hrs and a sample removed with a syringe and run on a TLC to check for the presence of unreacted allylcarbazole. It was still present so another aliquot of catalyst solution was added and the reaction continued for another 20 hrs. TLC again showed starting material but the reaction was worked up at this point.

The contents of the flask was added with stirring to 1000 ml hexane in a large beaker and the product precipitated as a milky emulsion which soon settled out. The solid was filtered off and dried to give 42.3 gm (106% theory) off-white powder. TLC showed that excess starting material was still present. The product was redissolved in 300 ml of a 1/1 mixture of dichloromethane and THF and filtered through a PTFE filter membrane (0.7 µm) and reprecipitated into hexane. The product formed a gummy ball. The ball was redissolved, filtered and reprecipitated twice more until TLC showed that all unreacted allylcarbazole had been removed. By adding the polymer solution very slowly to the hexane, balling up was avoided but the solid was still sticky. After filtering and drying in vacuum at 40 °C (it puffed up into a meringue due to residual solvent) the final recovery of polymer was 19.4 gm (49 %) pale gray powder. DSC showed $T_g = 49.5$ °C; GPC in THF showed $M_w = 88,000$, $M_n = 32,000$, $MWD = 2.7$, and $IV = 0.11$. GPC in NMP/0.2% LiBr gave $M_w = 65,000$, $M_n = 32,000$, $MWD = 2.0$, and $IV = 0.11$. NMR showed only a trace of unreacted Si-H and was consistent with the desired structure. Analysis showed Pt content = 78 ppm, chloride = 21 ppm. Analysis found: C = 71.70, 71.67, H = 6.47, 6.37, N = 5.08, 5.06, Si = 11.03%. Calculated for $C_{16}H_{17}NOSi$: C = 71.87; H = 6.41, N = 5.24, Si = 10.50%

3.5.22. Co-Grafting of 4-Allyloxy-4'-nitrostilbene and 9-Allylcarbazole onto PS122 In the ratio 25/75

The reaction was run under the same conditions and anerobic conditions as in the previous experiment. A mixture of 18 gm (0.3 mole) PS122 poly(methylhydrosiloxane), 55.95 gm (0.27 mole) 9-allylcarbazole, 25.4 gm (0.09 mole) 4-allyloxy 4'-nitrostilbene, and 400 ml dry toluene was stirred at 70 °C, degassed and sparged with Ar. A clear orange solution resulted. The DCPD-platinum catalyst (0.012 gm) was added dissolved in toluene with a microsyringe and the reaction run for 2 days at 70 °C under Ar. Within 1 hr the solution had gone yellow and cloudy, at the end of two days the mixture had formed a slurry which settled out on standing. The supernatant toluene layer was discarded and the lower yellow solid dissolved in THF and reprecipitated twice into methanol and once into hexane. The third solution was filtered through a 0.5 µm PTFE membrane before precipitation. After drying to constant weight at 50 °C, the yellow powder weighed 64 gm (94%). DSC gave $T_g = 58$ °C. TGA showed onset of decomposition at 380 °C in nitrogen. GPC in THF gave $M_w = 200,000$, $M_n = 82,000$, $MWD = 2.4$, and $IV = 0.08$. Analysis found: C = 69.43, 69.72, H = 6.95, 6.90, N = 4.29, 4.32, Si = 8.65, 8.88. Calculated for a 27/75 copolymer: C = 70.80, H = 6.31, N = 5.09, Si = 10.22. NMR showed the material had the correct structure and the ratio of carbazole to nitrostilbene units was approximately 3:1. FTIR also confirmed the structure with carbazole ring bands (750 cm^{-1}) and aromatic nitro bands ($1,340\text{ cm}^{-1}$) both present. The absence of Si-H bands at $2,150\text{ cm}^{-1}$ suggested the extent of the grafting reaction was almost 100%. The polymer readily spun coated to give clear yellow films.

3.5.23. Polymeranalogous Tricyanovinylolation of Poly(carbazolylpropylmethylsiloxane)

This reaction evolves large amounts of HCN gas and uses the highly toxic reagent tetracyanoethylene, TCNE. It was set up in the special Toxics Lab hood which is fitted with an alarm set to ring if the vent gases contain more than 4 ppm HCN. The method was taken from Limburg's US Patent #3,978,029. An elaborate safety review was undertaken first and the main feature was to remove all HCN before it could escape into the hood by passing all the outlet gases through a train of alkaline hypochlorite wash bottles. This converts the highly toxic HCN into relatively harmless sodium cyanate. Draege tube "sniffers" were used inside the hood to detect traces of HCN and full personal protective gear including fresh air breathing apparatus and cyanide emergency kits were available.

The reactor vessel was a 1000 ml 3-neck flask with a reflux condenser, 250 ml PE tap funnel and gas inlet tube heated by a temperature controlled oil bath and stirred magnetically. The outlet from the top of the condenser went through a silica-gel drying tower, then into a wash bottle as an anti suck back trap, then through a 2 liter flask half full of full strength "Chlorox" bleach, next into a similar 1 liter flask of "Chlorox", then into another wash bottle as a safety trap and finally out to the hood vent via a bubbler. The reactor flask was dried at 110 °C first and then sparged in a stream of Ar.

The cool dry reactor flask was charged with 10 gm (0.0375 moles) poly(methyl-carbazolylpropylsiloxane) dissolved in 200 ml anhydrous DMF (Aldrich "Sure Seal" bottles) and stirred and sparged with Ar. Into the tap funnel were placed 25 gm (large excess) tetracyanoethylene (highly toxic) and 150 ml dry DMF and the mixture shaken until a clear blue solution formed. The reaction mixture was heated to 62 °C and 50 ml TCNE solution added dropwise to the reactor. The exit gases from the bubbler were monitored periodically with the Draege sniffer. No significant amounts of HCN were detected. The reaction proceeded at 62 °C for 17 hrs then 25 ml more TCNE solution was added. After 30 hrs the rest of the TCNE was added and the reaction ran for a total of 48 hrs. At the end of this time no HCN was detectable, so the apparatus was taken down, all glassware being decontaminated with dilute Chlorox to remove traces of cyanide or TCNE. The reaction solution was a red-brown color.

Up to this point no significant amounts of HCN had been detected. The Chlorox traps had done their job well. The next phase was to quench the reaction mixture into excess methanol in a Waring Blender and this caused problems. The Blender was charged with 3 liters methanol and the motor started at low speed while the reaction mixture was slowly poured into it. A precautionary check with the Draeger tube revealed considerable amounts of HCN gas were present, 40-80 ppm. The Blender was stopped and the contents left to stand in the hood, being periodically monitored but the HCN content in the air above the Blender remained in the 60-120 ppm range for several hrs. Clearly the large amount of HCN present was not coming from the reaction mixture but from reaction of residual TCNE with the methanol. The contents of the Blender were transferred carefully to a large 5 liter 3-neck flask fitted with a stirrer, gas inlet and long condenser and stirred under a stream of Ar. The exit gases were vented through the Chlorox train. By using the Draege tubes directly at the exit from the condenser we could monitor the HCN evolution but after stirring overnight at room temperature the level of HCN in the flask was still 80-100 ppm. The Chlorox had to be replaced several times in the washing train as it became exhausted. Eventually the 5-liter flask was heated to gentle reflux to complete the reaction and expel the final traces of HCN. The mixture was refluxed four hrs then left under Ar to cool. Next day the level of HCN was about 35 ppm. The solid product was filtered from the methanol in the hood wearing breathing apparatus, and the vacuum line from the filter was passed through a Chlorox wash train to prevent HCN being drawn down the works vacuum line. The solid on the filter was washed with methanol and checked with the Draege tube ; this time the HCN level was down to 1 ppm. The liquid wastes from this procedure were all placed in glass carboys and labeled as cyanide waste for special disposal.

The brick-red product was dried at 40 °C on the house vacuum line overnight: by now no HCN was detectable. It was redissolved in DMF and reprecipitated into methanol twice, finally it was dissolved in THF, filtered through a 0.5 µm PTFE filter membrane and finally precipitated into methanol. The dried red powder weighed 8.79 gm. DSC showed $T_g = 80$ °C. TGA showed decomposition starts in nitrogen at about 400 °C. GPC in THF showed $M_w = 42,00$, $M_n = 6,200$, MWD = 6.8, and IV = 0.05. FTIR showed CN bands at 2,228 and 2,221 cm^{-1} . Comparison with FTIR spectrum of starting polymer indicates that the degree of substitution is low. C-13 NMR detected the presence of the CN unit. Analysis found: C = 70.64, 70.57, H = 5.84, 5.86, N = 7.56, 7.54, Si = 9.11, 8.95. This corresponds with about 18 moles percent carbazole units substituted with TCV units. UV-vis spectrum showed a peak at 490 nm.

3.5.24. Co-Grafting of Allylcarbazole and Allyl-Dicyanovinylcarbazole onto PS122 in the ratio 75/25

This reaction was run under the conditions used in experiments (3.5.22-23). A 1 liter 2-neck flask with a reflux condenser and septum side neck and charged with 11.32 gm (0.04 mole) 3-dicyanovinyl-9-allylcarbazole, 24.84 gm (0.12 mole) 9-allylcarbazole, 9.62 gm (0.16 mole) polymethylhydrosiloxane (PS122) and 400 ml freshly dried toluene. The mixture was stirred under Ar at 60 °C after degassing and Ar sparging and the catalyst (0.1 gm DCPD-platinum dichloride) added as an aliquot in toluene. The reaction was run for 18-20 hrs; a TLC sample was withdrawn but there was still starting material present. After 24 hrs, more catalyst (0.005 gm) was added and the reaction run for 36 hrs; this time it went cloudy. TLC still showed s.m. after 36 hrs. The reaction suspension was quenched into 2 liters of methanol and let stand after which an orange gummy solid settled out. This was filtered off, redissolved in THF, filtered and reprecipitated into methanol. Again it was a yellow gum but a third sequence in THF and methanol gave a brittle yellow powder. TLC showed this was now free from allylcarbazole but some DCV-carbazole was still present. A fourth sequence in THF, filtering through a fine filter and reprecipitation into methanol gave after drying a yellow powder weighing 25 gm (55% theory). This cast as clear yellow films from THF solution. DSC showed $T_g = 48.5$ °C. TGA showed decomposition starts at 410 °C in nitrogen. GPC in THF showed $M_w = 115,000$, $M_n = 26,000$, MWD = 4.5, and IV = 0.12.

3.5.25. Co-Grafting of Allylcarbazole and Allyl-Tricyanovinylcarbazole onto PS122 in the ratio 75/25

Again this was run as in previous examples. The reactor flask was charged with 6 gm (0.1 mole) PS122, 15.5 gm (0.075 mole) 9-allylcarbazole, 7.7 gm (0.025 mole) 9-allyl-3-tricyanovinylcarbazole and 500 ml freshly dried toluene. The solution was stirred, degassed and sparged with Ar. After 30 minutes at 80 °C, a clear yellow red solution formed. The catalyst was 0.01 DCPD-platinum complex added as an aliquot in toluene. The reaction was left to run for 24 hrs and another aliquot of catalyst added. After 36 hrs the reaction was ended and quenched into methanol. The product came out as a gummy red solid. This was dissolved in THF and reprecipitated several times into methanol to remove unreacted starting material. The final solution in THF was filtered through a 0.5 µm PTFE membrane before final precipitation. After drying at 50 °C to constant weight, the product was a reddish brown powder weighing 18 gm (62 %). The polymer spun cast to clear red films from THF. GPC in THF showed $M_w = 38,000$; $M_n = 14,000$; MWD = 2.7, IV = 0.07. DSC showed $T_g = 54$ °C. TGA showed decomposition starts in nitrogen at 400 °C. FTIR showed the structure has significant unreacted Si-H bonds left, about 8 moles %. The incorporation of allylcarbazole is 75% (i.e. virtually complete) but by difference only 16 moles % of the silicons carry TCV-carbazole units. UV-Vis spectrum showed a peak at 503 nm.

4. Photorefractive Characterization

4.1 Photoconductive Evaluation

A Monroe Static Charge Analyzer model 276A was used for the characterization of materials by the photoinduced discharge (PID) method. This instrument is widely used for characterization of photoconductors in the photocopier industry. The materials to be measured are cut into one inch diameter discs and two samples are placed into a revolving turntable. The samples are spun at 600 rpm over two corona charging stations 120° apart. The corona charging can be positive or negative. The samples are charged in the corona field. An AC electrometer consisting of three electrodes, placed 120° apart, measures the average surface potential on the samples by capacitive coupling. A sixth port allows light to impinge on the rotating sample for photocurrent measurement. This method is a fast screening tool which provides qualitative and semi-quantitative information on the photoconductive properties of a material.

A second principal method for measuring the photoconductive behavior of materials is the time of flight measurement. This method is preferred because it is easier to analyze mathematically and yields carrier mobilities and transit times. In comparison, the PID method simulates the xerographic process and is experimentally easier to implement but not as readily analyzed. The time of flight measurements on HCC materials were performed at the University of Bayreuth.

After the samples are corona charged, photocharge generation is induced with a broadband light source (GE 1076 bulb, 25 ft-candles at 2810 K color temperature). The peak lamp intensity occurs at about 1 μm . The rate of change of sample voltage with time, dV/dt , both with and without illumination is recorded on a strip chart recorder. An IEEE board was used to interface the Monroe instrument with a personal computer for data acquisition.

As a first calibration test, a Kodak belt from a photocopying machine was used to gather data for comparison with HCC materials. The results are shown in Figure 1. The corona charging time was 40 seconds followed by 90 seconds of dark decay and 90 seconds of photodecay. Three curves were made using a positive corona at three different levels of corona current: 30, 50, and 90 mA. The coating thickness was not determined and the composition is not known. When subjected to a negative corona, the Kodak material was unable to accept a large amount of charge and the discharge characteristics were quite different. There was no evidence of photodecay. The explanation lies in the fact that the mobile charge carriers are positively charged (holes), which holds true for most polymeric materials as well.

The discharge behavior of MO3ONS/MMA copolymers was compared with the homopolymers. The results are shown in Figure 2. PMMA exhibits slow decay after charging and no photodecay as expected. A 10/90 copolymer of MO3ONS /PMMA has a steeper discharge curve but there is no appreciable photodecay. The 70/30 copolymer and the MO3ONS homopolymer both exhibit photodecay. The initial decay rates are less than half of the Kodak belt decay rates but, without knowing the thickness of the Kodak belt material, meaningful comparison is not possible.

The photoconductive data by the Kodak belt are listed in Table 1. Except as noted in Table 1, all data were taken with a positive corona and 50 mA corona current. The results of the static charge analysis for some miscellaneous materials are compared in Figure 3. All three samples exhibit a substantial photodecay compared with the Kodak material. The dark decay of P2ANS/PMMA 50/50 was quite high while the photodecay leveled off quickly compared with the Kodak material. The presence of the oxynitrostilbene and the aminonitrostilbene, both NLO active chromophores, makes these side chain polymers photoconductive, albeit not very good ones. The question is whether or not the polymers are also photorefractive. This will be discussed later in this report.

Table 1. Photoconductive Data by the Kodak Belt Method

Sample	Number †	-dV/dt dark decay	-dV/dt photodecay
Figure 1		(volts/sec)	(volts/sec)
Kodak belt	81101 (50 mA)	15	15
Kodak belt	81002 (90 mA)	15	16
Kodak belt	81003 (30 mA)	15	12
Kodak belt	81004 (30 mA) neg. corona	0.6	0.2*
Figure 2			
PMO3	80701	7.5	6
MO3ONS/MMA 70/30	80601	3.2	8.7
MO3ONS/MMA 10/90	80501	2.5	1.6*
PMMA	80401	0.36	0.25*
Figure 3			
PMO6	81001	4.4	8.7
MO3ONS/MMA 70/30	80601	3.2	8.7
P2ANS/PMMA50/50	80301	11	8

† Positive corona charging except where noted.

* No abrupt change in slope. Photodecay minimal or zero.

This preliminary work established the utility of the static charge analyzer for characterizing photoconductivity, one of the properties required for photorefraction. It also allowed the comparison of HCC materials with commercial photoconductors.

Because of the difficulty in interpreting experimental results from guest/host systems to functionalized polymers, it was decided to concentrate on synthesizing a bifunctional polymer. The incorporated functionalities were photoconductivity and electrooptic activities in an effort to achieve photorefractivity in a single polymeric material.

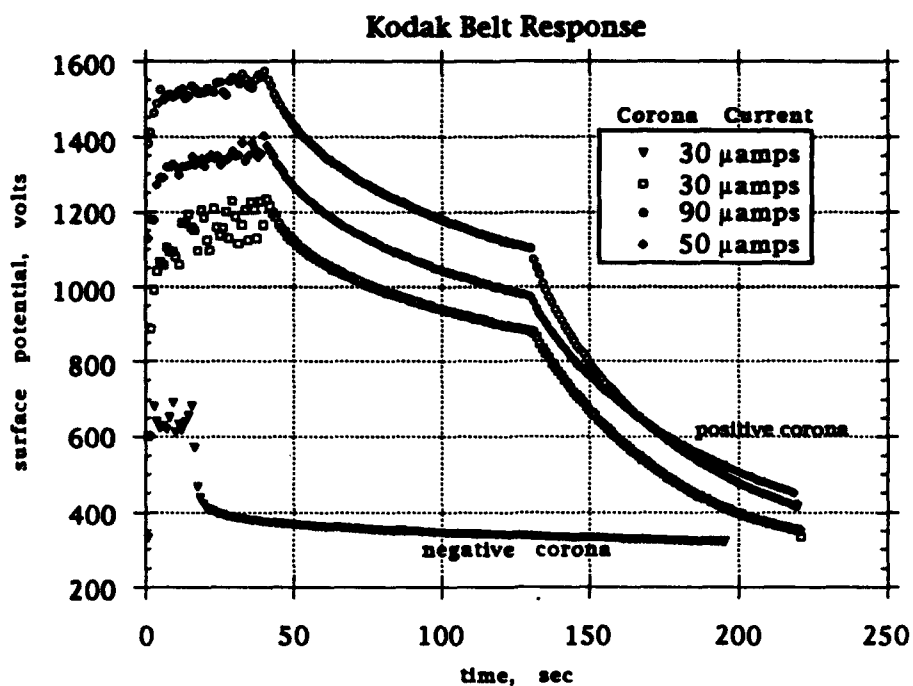


Figure 1. Photoinduced discharge curves of Kodak copier belt material.

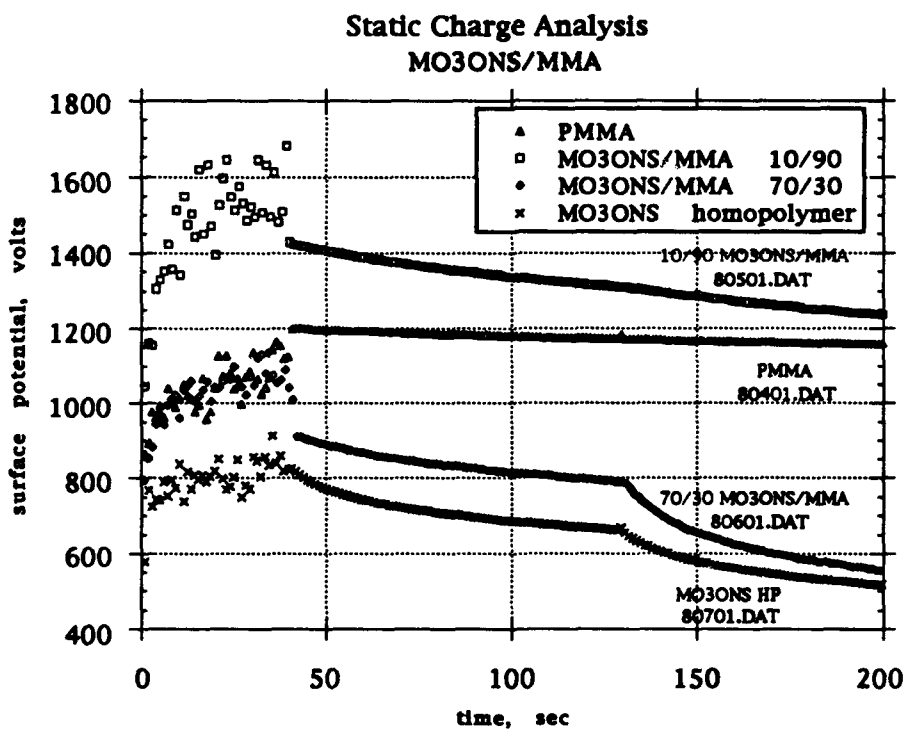
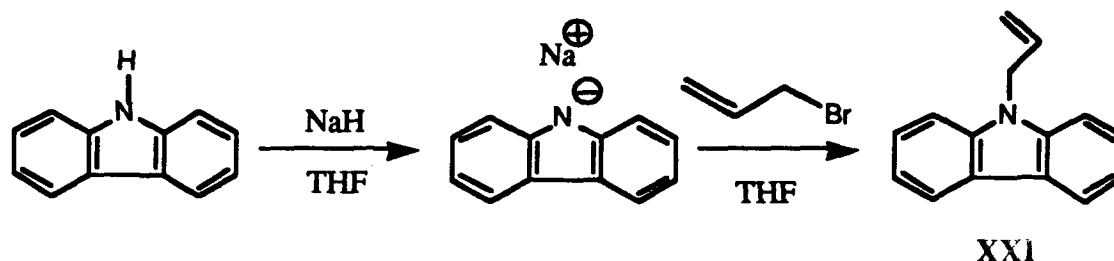
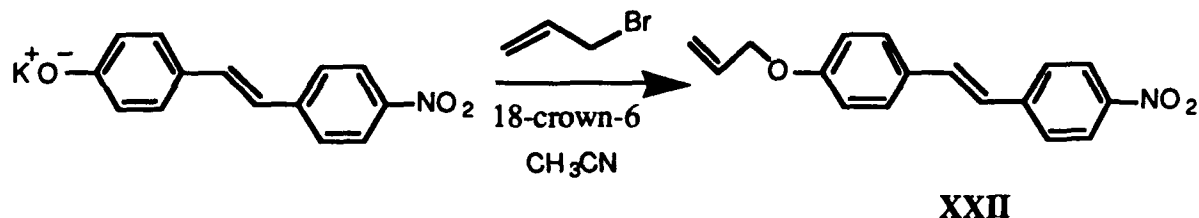


Figure 2. Photoinduced discharge curves for MO3ONS and PMMA.

Polymethylhydrosiloxane is an easily functionalized polymer. Substitution via hydrosilylation across a terminal alkenyl group is a well known reaction that offers wide flexibility in the choice of side chain substituents. Side chain polysiloxanes containing carbazole units isolated from the backbone by different length alkyl spacer groups have been studied for their photoconductive properties at the University of Bayreuth, one of the subcontractors on this project. Because of our extensive experience with oxynitrostilbene, it was selected to provide the electrooptic function. Carbazole, a well known organic photoconductor, was chosen to provide the photoconductive role. Preparation of N-propenyl carbazole was accomplished by first reacting carbazole with sodium hydride in THF to form the anion. This was subsequently reacted with allyl bromide to afford the desired carbazole with a terminal alkenyl group.

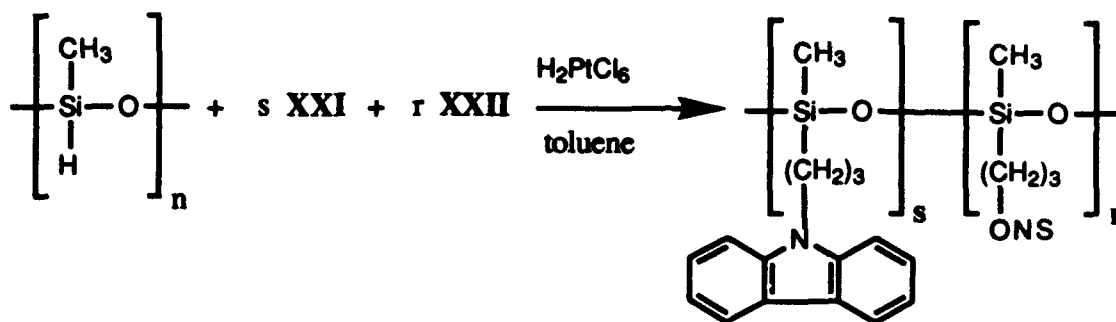


The propenyl oxynitrostilbene is prepared by reacting the potassium salt of oxynitrostilbene with allyl bromide in acetonitrile using 18-crown-6 to sequester potassium.



These two substituents are then mixed together in the desired ratio and reacted with the polymethylhydrosiloxane in toluene. The reaction is catalyzed by chloroplatinic acid.

Addition of the side groups was better than 99%. The ratio of carbazole units to ONS units in the first polymer prepared was 9/1. The T_g was found to be 57°C by DSC. A second polymer with a 3/1 ratio and a T_g of 62°C was also prepared. Confirmation of the degree of substitution and the relative ratio of the substituents was obtained by NMR.



The 10/90 carbazole/oxynitrostilbene/polymethylsiloxane polymer (ONS/CBZ/PMS) was dissolved in cyclohexanone and spin coated on ITO coated. A positive corona current of 50 mA was used to charge the surface to 540 V for 10 seconds. This was followed by a 30 second dark decay period and then 30 seconds of photoinduced decay (Figure 3). It is clear that the oxynitrostilbene is responsible for charge generation. The strong photo decay is due to the presence of the carbazole which, although not generating charge, is a good organic charge transport material.

Figure 4 shows the PID curves generated by filtering the output of the tungsten lamp on the static charge analyzer. The 452 nm filter with a 65 nm pass band gave the only photoresponse. It should be remembered that the spectral output of the tungsten lamp peaks at about 1 μm so that the 334 nm filter, which has a passband of only 2 nm, is receiving too little radiation to observe a photoresponse. In fact, a very strong photoresponse is expected in the UV due to charge generation by carbazole. In our system, charge is being generated by the oxynitrostilbene and transported by carbazole.

TNF (trinitrofluorenone) is known to form a charge transfer complex with PVK (polyvinylcarbazole). This complex absorbs in the visible region of the spectrum allowing the use of PVK and similar molecules at more suitable frequencies. When 10 wt% TNF was added to 10/90 ONS/CBZ/PMS, the PID curves (Figure 5) showed clearly that the absorption band had been considerably broadened out as far as 645 nm.

Figure 6 is a comparison of a standard PID curve with a dark decay curve and a composite photo and dark decay curve. It is clear that the photodecay portion of the standard curve is the difference between the other two curves. In order to obtain this data, it was necessary to make a standard run before the three shown in Figure 5 to condition the sample. The data was then collected with about 20 seconds between runs. These systems require a significant amount of time to revert to their initial states, so the data must either be collected quickly as was done in this case, or with long time intervals between data sets to insure adequate reproducibility.

The PID curves for 10/90 and 25/75 ONS/CBZ/PSX polymers are compared in Figure 7. The surface potential accommodated by the 25/75 composition at the same corona current setting is higher because of the increased oxynitrostilbene content while the photodecay rate is lower because of the smaller amount of charge transporting carbazole.

The refractive indices on substituted polysiloxane samples were measured using a prism coupling at two wavelengths, 632.8 and 1289 nm. The results are given in Table 2.

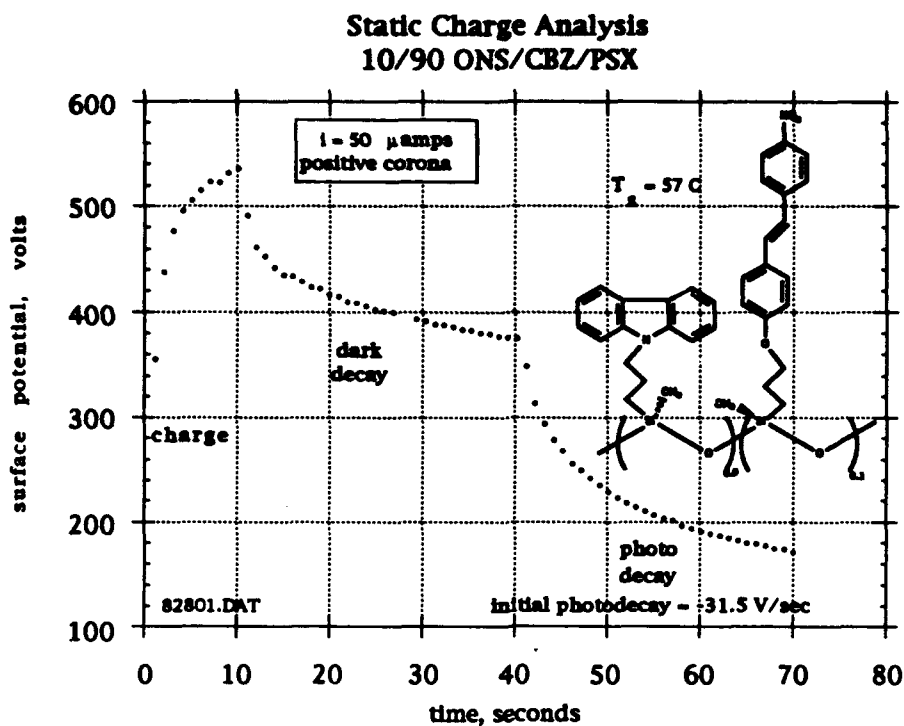


Figure 3. Photoinduced discharge curves of 10/90 ONS/CBZ/PSX.

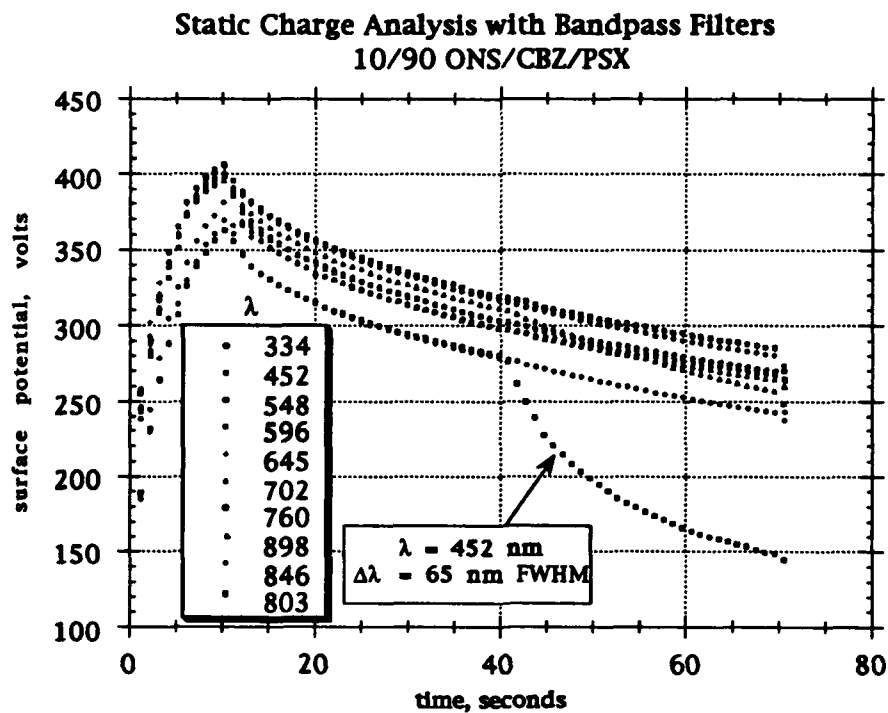


Figure 4. Photoinduced discharge with bandpass filters of 10/90 ONS/CBZ/PSX.

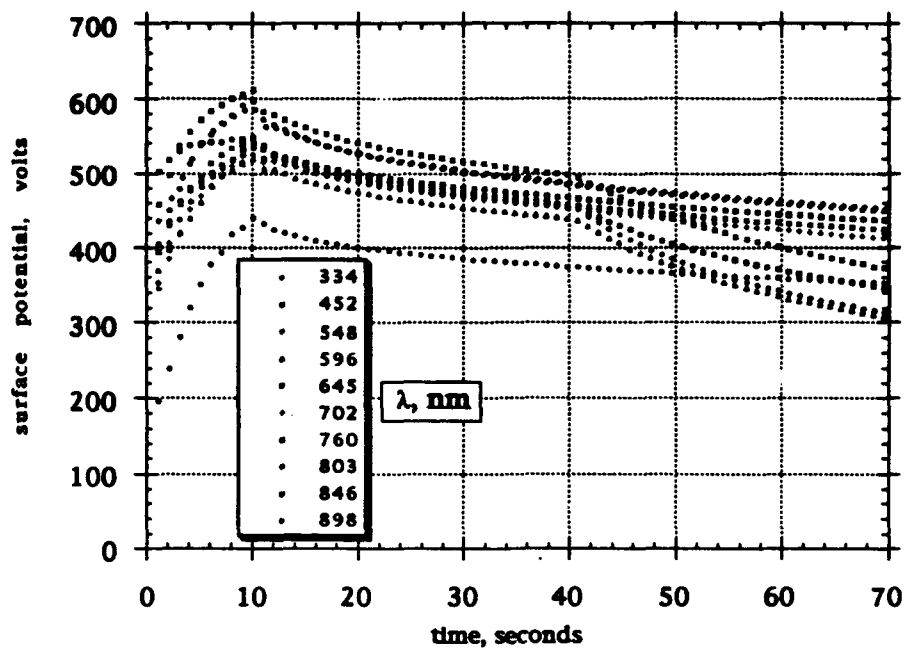


Figure 5. Photoinduced discharge curves of 10/90 ONS/CBZ/PSX with 10% TNF.

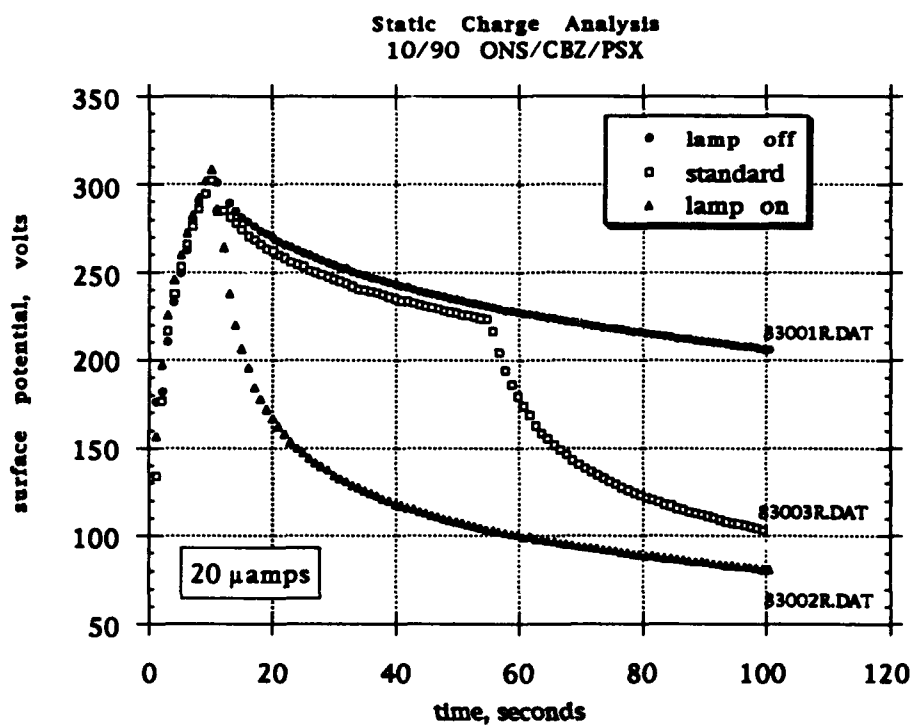


Figure 6. Photoinduced discharge of 10/90 ONS/CBZ/PSX with various exposures.

Table 2. Refractive Indices of ONS/CBZ/PSX

Wavelength	10/90 ONS/CBZ/PSX		25/75 ONS/CBZ/PSX	
(nm)	n _{TE}	n _{TM}	n _{TE}	n _{TM}
632.8	1.6422	1.6427	1.6498	1.6497
1289	1.6122	1.6122	1.6152	1.6145

These samples were poled at 100 V/ μ m and Their electrooptic coefficients were also measured. Measurements were made on both 10/90 and 25/75 samples. Table 3 compares this data with some earlier data on MO3/ONS and MO6/ONS obtained in the first phase of the Multifunctional Macromolecules program. The pyro and electrooptic coefficients have been divided by the volume fraction of ONS in the polymer for comparative purposes. In Table 3, the volume percent of oxynitrostilbene in various polymers developed within this project has been calculated using the group contribution method from Van Krevelen's book "Properties of Polymers". The method yields the Vander Waals' volume which correlates quite well with the molar volume. Both the pyroelectric and electrooptic coefficients for the 25/75 polymer are lower than expected. The cause of this result is not known yet.

Figure 8 shows the PID curves for three polymeric materials. The curve for PVK (polyvinyl carbazole) shows that the positive corona generated surface charge has a substantial dark decay, i.e., positive charges are conducted in this material. There is no photodecay because the light source contains no UV radiation which is necessary for absorption and exciton formation in PVK. The 10/90 MO3ONS/MMA curve shows that this material exhibits very low conductivity. However, when carbazole and ONS units are both present as they are in 10/90 ONS/CBZ/PMS, both dark decay and photo decay are observed. It is clear that exciton formation is due to the presence of oxynitrostilbene while charge transport is provided by the carbazole units.

The UV/visible spectrum for PVK (polyvinyl carbazole) in cyclopentanone is shown in Figure 9. Major peaks occur at 335 and 345 nm. The UV/visible spectrum for ONS/CBZ/PMS for both 10/90 and 25/75 compositions is shown in Figure 10. The spectra were run in cyclopentanone against a cyclopentanone reference. In addition to the carbazole absorptions at 336 and 347 nm, there is an absorption maximum at 380 nm due to the oxynitrostilbene chromophore. As expected, the height of the ONS peak compared with the carbazole peak increases with increasing ONS substitution. As indicated on the spectrum, the T_g also increases from 57° to 62°C with increasing ONS substitution. There is considerable absorption by all these polymers in the UV which cannot be recorded in cyclopentanone because it also absorbs in that region. A spectrum of a 0.18 μ m film of 10/90 ONS/CBZ/PSX is given in Figure 11 for comparison.

Table 3. Pyroelectric and Electrooptic Data of MO3/ONS and MO6/ONS Polymers

Sample	vol. % ONS	pyro coeff. $\mu\text{cm}^{-2}\text{K}^{-2}$	$\frac{\text{pyro}}{\text{vol\%}}$ x 100	EO coeff (633 nm) pm/V	$\frac{\text{EO}}{\text{vol\%}}$ x 100
10/90 MO3ONS	17.8	2.23	12.5	2.86	16.1
5/95 MO6ONS	9.7	1.75	18.0	1.8	18.6
10/90 MO6ONS	17.1	2.00	11.7	2.6	15.2
10/90 ONS/K/PMS	7.9	1.56	19.7	1.2	15.2
25/75 ONS/K/PMS	19.1	1.85	9.7	2.2	11.5

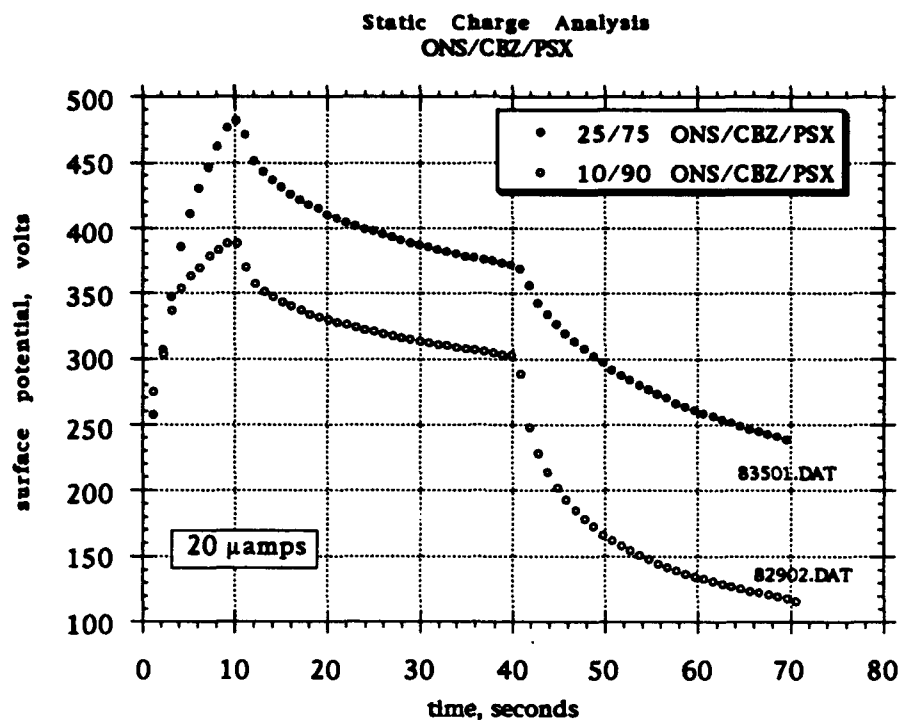


Figure 7. Photoinduced discharge curves of 10/90 & 25/75 ONS/CBZ/PSX.

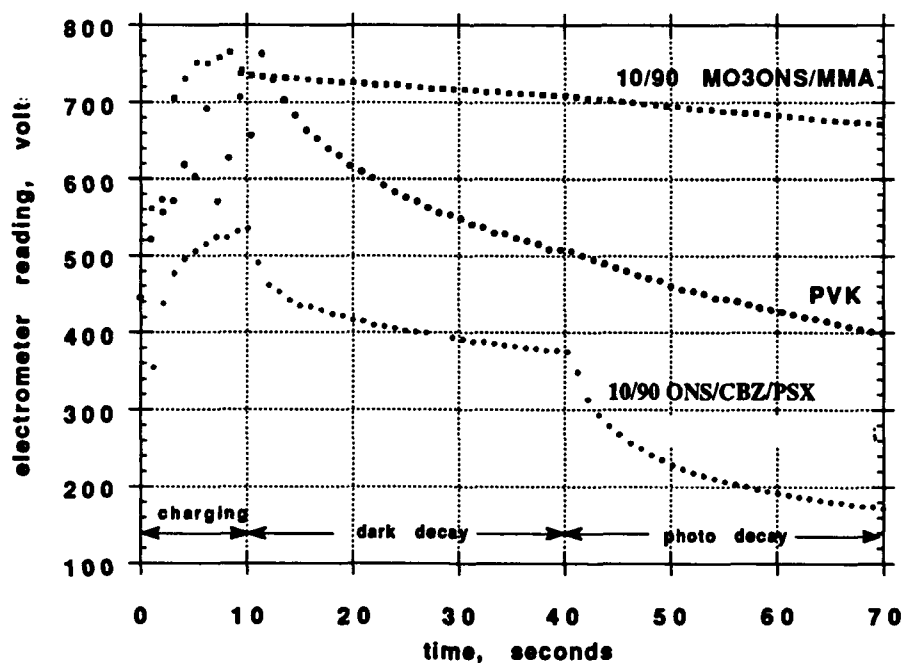


Figure 8. Photoinduced discharge of 10/90 ONS/CBZ/PSX, PVK and 10/90

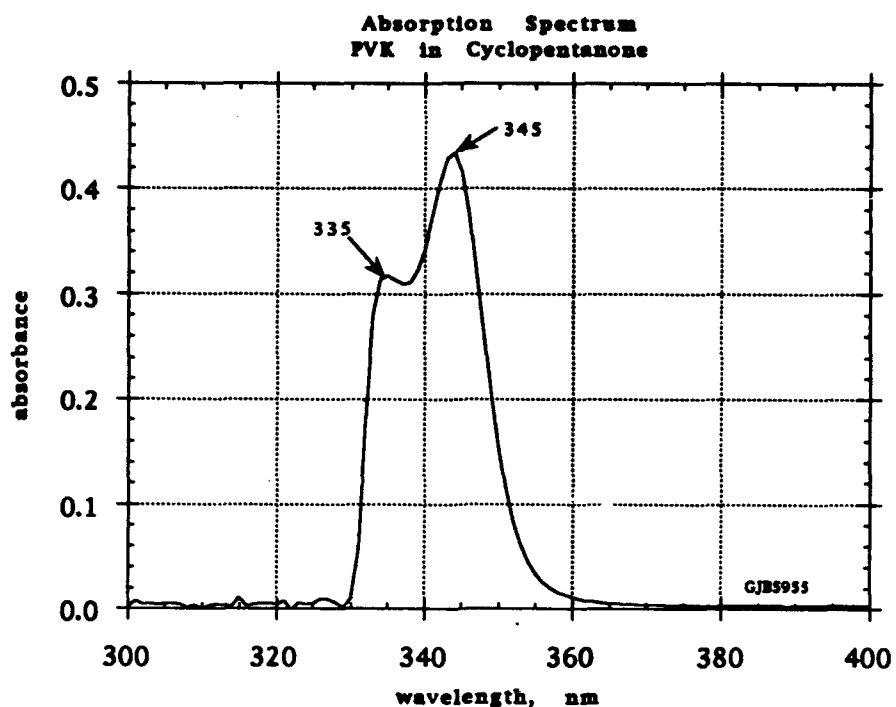


Figure 9. UV/VIS spectrum of polyvinylcarbazole in cyclopentanone.

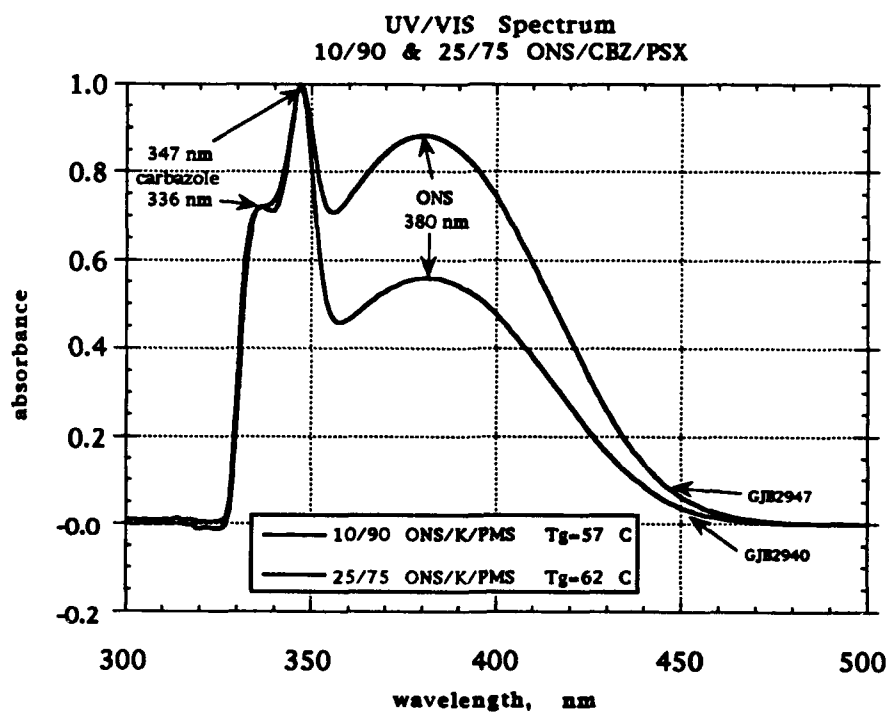


Figure 10. UV/VIS spectrum of 10/90 & 25/75 ONS/CBZ/PSX in cyclopentanone.

4.2. Photorefractive Evaluation

A number of experimental methods have been described for measuring the photorefractive. Four wave mixing was employed in the initial attempts to characterize HCC materials as shown in Figure 12. A 35 mW HeNe laser, aligned so that the beam polarization is vertical (*s*-wave), is passed through a 50/50 beam splitter. One of these beams (beam # 2) is reflected from two mirrors entering the sample from the back. The other beam is passed through a glass slide at approximately 45°. The *s*-wave reflection is about 18%, 9% from each surface. This beam is passed through a half wave plate which rotates the polarization by 90° (*p*-polarization). The beam is then chopped at 100 Hz and enters the sample as the second beam (# 1). Finally, the beam which is transmitted through the glass slide enters a polarizing beam splitter which transmits *p*-waves and reflects *s*-waves. This reflected probe beam (#3) enters the sample. In the usual four wave mixing geometry, a total of three diffraction gratings are formed by the pairwise interaction of the three incident beams. Because one of the beams in our set up is orthogonally polarized to the other two, only one such grating is formed between beams #2 and #3. It is from this grating that the phase conjugate beam is reflected back along the probe beam direction (beam #3). Clearly if no grating is formed in the material, there will be no phase conjugate beam. (This is one of the main advantages of this technique: it is run against a null background.) Because beam #1 is *p*-polarized, it will be transmitted through the polarizing beam splitter. Because it has been chopped, it can be detected using a lock-in amplifier at the chopping frequency. The grating spacing of the induced diffraction grating is given by:

$$\Lambda = \frac{\lambda}{2n \sin(\theta/2)} \quad (1)$$

where Λ is the grating spacing, λ the free space wavelength, n is the refractive index, and θ is the angle between the beams forming the grating. In our apparatus, $\theta = 159.4^\circ$. In this geometry, grating spacing of about 200 nm are achieved. The Bragg condition for reflection of the conjugate beam off this grating is automatically satisfied. The grating direction in the sample is about 10° off the vertical along the long dimension. This is important because the poling direction of the photorefractive polymers should be transverse to the grating direction in order to achieve the desired refractive index modulation through the electrooptic effect.

Initial attempts to look for photorefraction in the 4-wave mixing geometry were performed on 10/90 ONS/CBZ/PMS using Ar-ion laser at 488 nm. The sample was unpoled with 10% TNF added as a sensitizer. Grating formation as recorded are shown in Figure 13. The grating was permanent, probably due to bleaching. The laser source was thus changed to 633 nm to move away from the absorption peak. Samples of 10/90 ONS/CBZ/PSX with TNF added to sensitize absorption to 633 nm were prepared by spin coating the polymer onto TCO coated glass. A gold electrode was evaporated on part of the sample and the sample was poled at 95 V/ μ m. Figure 14 shows the 4-wave mixing results on the 10/90 polymer on both poled and unpoled sections. Grating formation was observed clearly. The recording times, however, were quite long and when exposure was stopped at the peak signal times, the gratings persisted. It is believed that the material was photobleached. The subsequent loss of signal at longer times may be due to loss of the grating due to vibration, thermal fluctuations, or scattering. Because of the experimental uncertainties in the measurement, the longer time and smaller signal for the poled section may not be real. It could be rationalized by the smaller absorption cross section that the poled sample would be expected to present to the incident radiation.

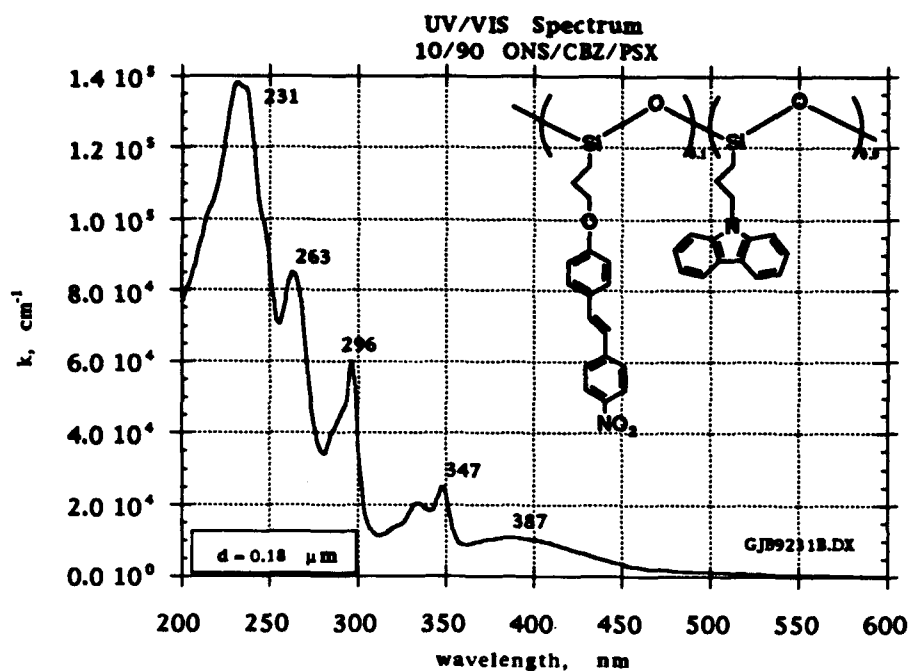


Figure 11. UV/VIS spectrum of 10/90 ONS/CBZ/PSX thin film.

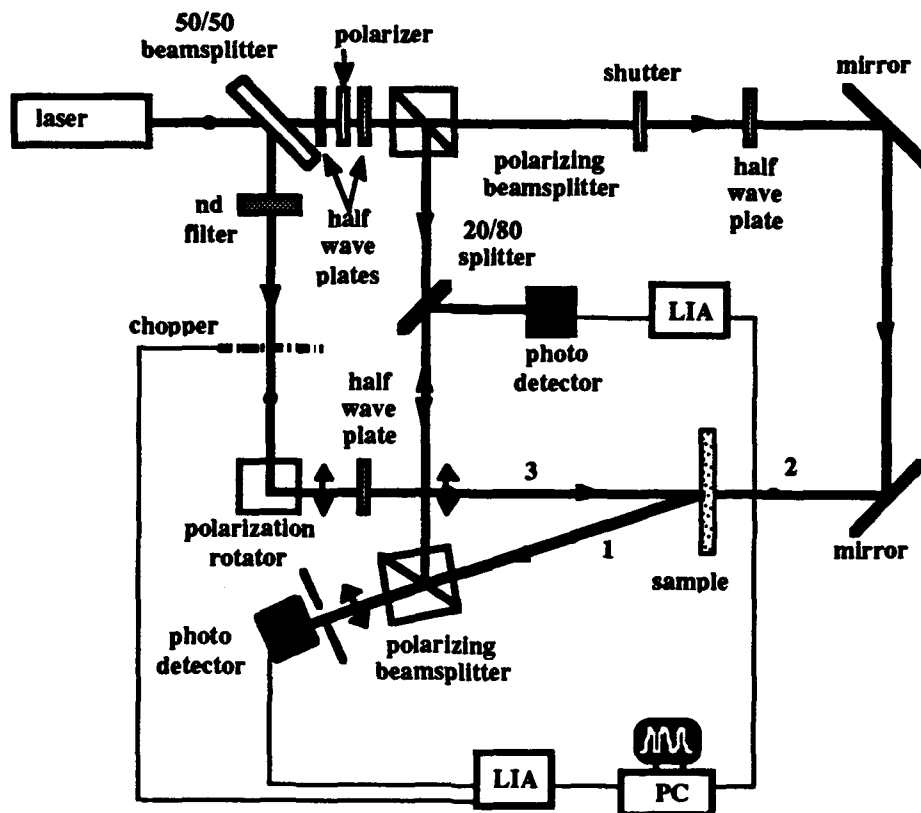


Figure 12. Four wave mixing experimental setup.

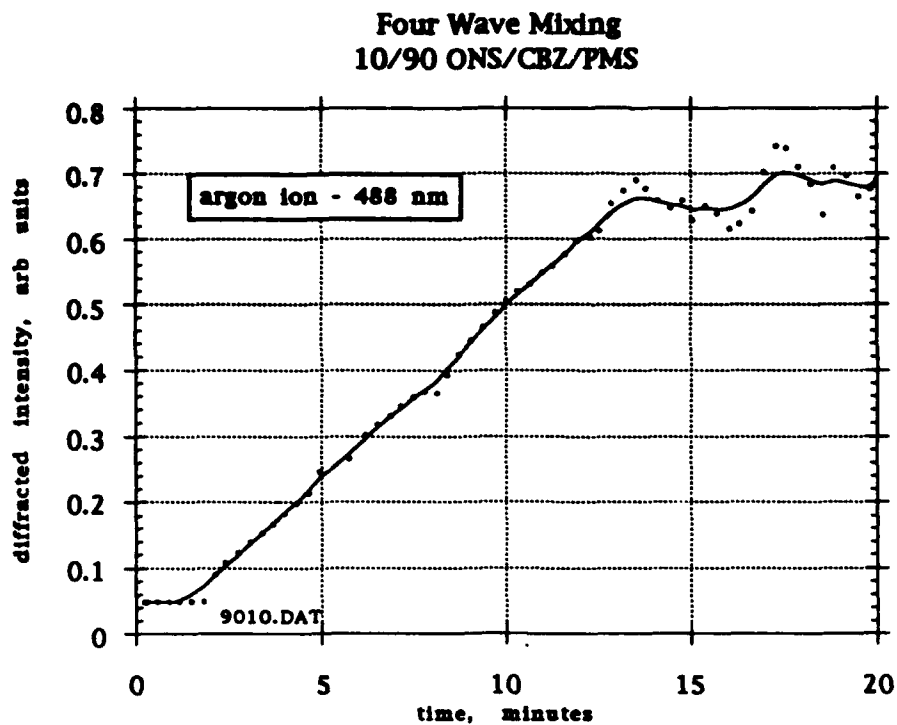


Figure 13. Four wave mixing results for 10/90 ONS/CBZ/PSX.

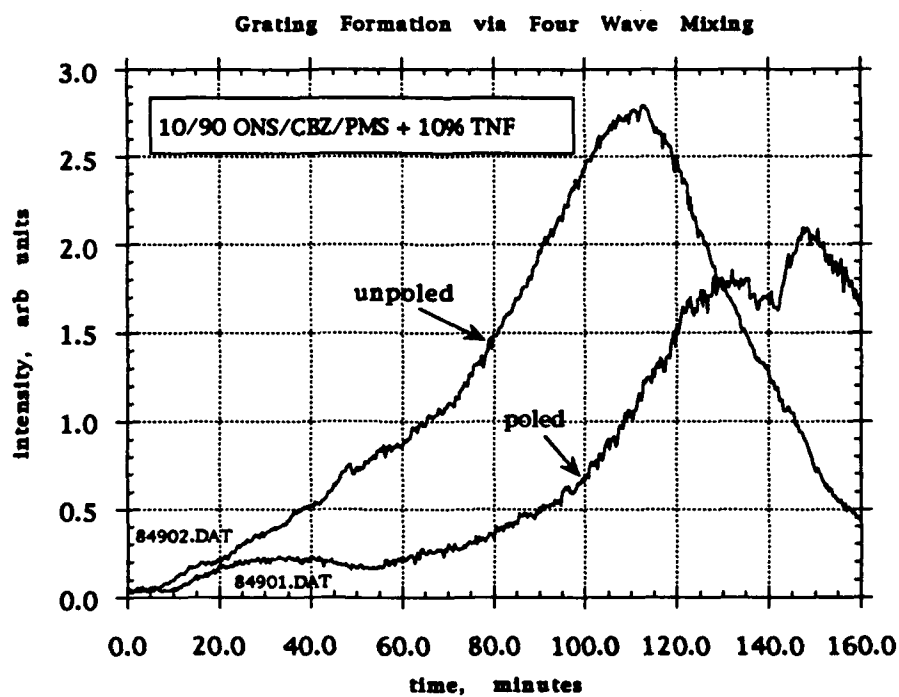
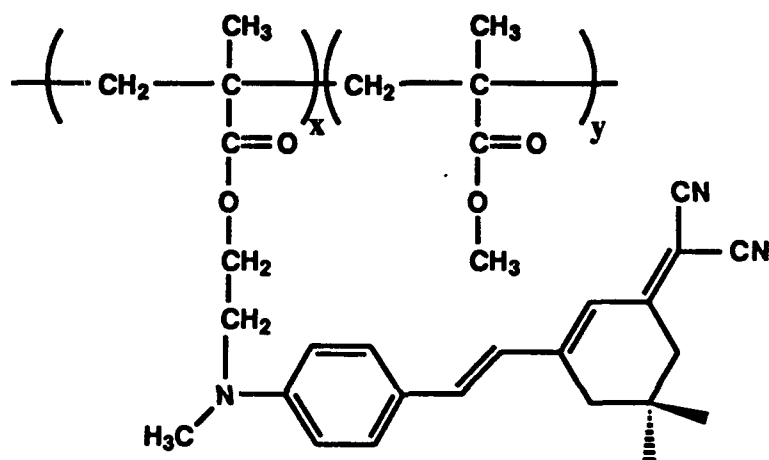


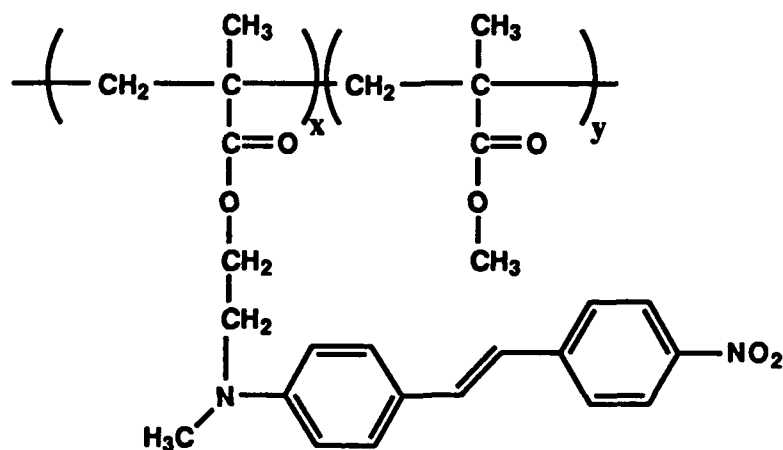
Figure 14. Four wave mixing results for 10/90 ONS/CBZ/PSX with 10% TNF.

In order to establish the cause of photobleaching, a sample of TNF sensitized PVK (polyvinyl carbazole) was tested. As shown in Figure 15, no signal was detected by the lock-in amplifier. It is thus reasonable to assume that the carbazole/TNF complex does not bleach at 633 nm. A sample of MO3ONS/MMA with 20% TNF was then tested and compared with a sample of MO3ONS/MMA without TNF. The results in Figure 16 show that the sensitized oxynitrostilbene is bleaching which points to the bleaching cause of 10/90 ONS/K/PMS .

In order to exclude oxygen from the system, a box with a beam port was built to house the sample during measurement. The box has a port to admit an inert gas. Argon was used to purge the system for twenty minutes and the measurement was performed as described earlier. It was found to be necessary to shut off the supply of Ar to the box during the run to avoid erratic results. Results are shown in Figure 17. The results indicate that oxygen plays a significant role in the photobleaching process. Similar findings have been found in the NLO program with DANS copolymers in waveguide devices where the light intensities are quite high.



XXIII: dicyanovinyl hexatriene copolymer - DCVHT



XXIV: aminonitrostilbene copolymer - P2ANS

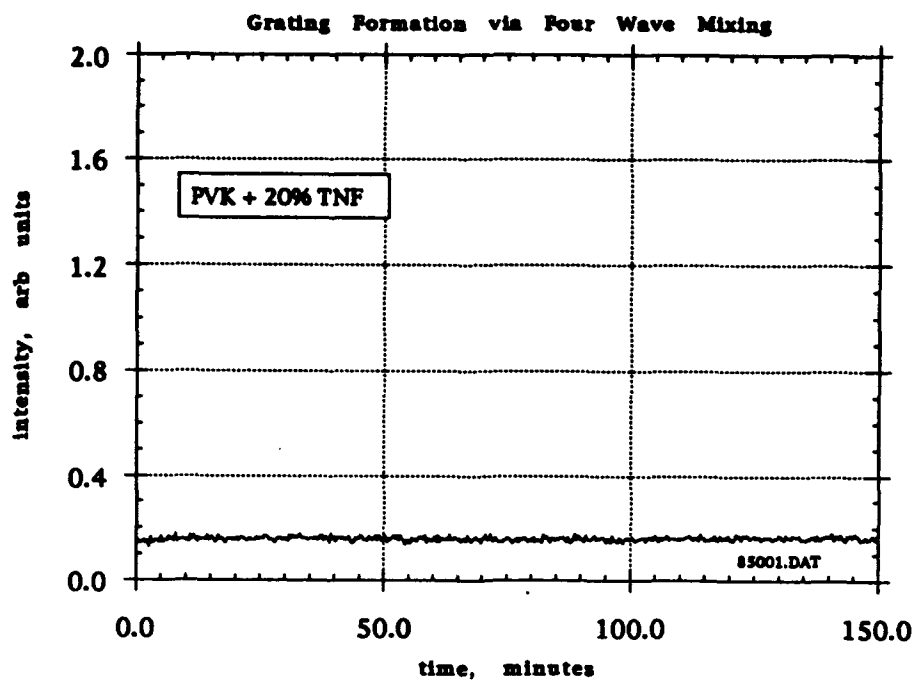


Figure 15. Four wave mixing results for polyvinylcarbazole with 20% TNF.

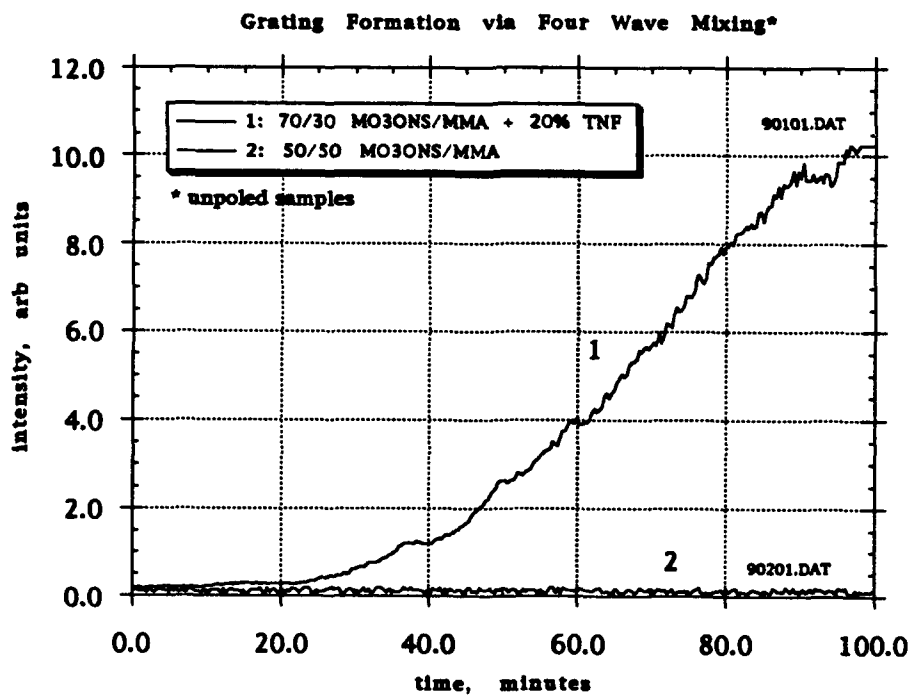


Figure 16. Four wave mixing results for MO3ONS/MMA with and without TNF.

The static charge analyzer was used to compare the charge transport characteristics of dicyanovinylhexatriene (DCVHT) polymer with P2ANS, both of which are NLO polymers with high electrooptic coefficients. Samples were spin coated from cyclohexanone and were of comparable thicknesses (about 4 μm). Figure 18 shows the result when the positive corona current in both samples was 50 mA. The P2ANS sample was charged to a higher potential than the DCVHT sample. The charges in the DCVHT are apparently quite mobile which explains the low surface potential and the high dark current decay rates. Also, no evidence for photo decay for DCVHT was observed. The samples were then run again with each surface charged to the same potential so that the charges were subjected to comparable electric fields (Figure 19). The dark decay for the DCVHT is 4 - 5 times higher than that of P2ANS. The photo decay for P2ANS is almost nonexistent because, at this low potential, geminate recombination is probably high.

A sample of poly[3-(9-carbazolyl)-propyl methyl siloxane], CBZ/PSX, was spin coated onto an ITO coated slide and its photoinduced discharge curve was measured on the static charge analyzer. The sample was 8.04 μm thick. The absorption spectrum of a 4 μm sample of this material is shown in Figure 20. The discharge curve is shown in Figure 21. The sample was charged for 5 seconds and allowed to dark decay for 90 seconds. During this time the surface potential decreased by 22%. The photodecay began at a surface potential of 800 volts and was quite rapid, decaying to half its final value of 93 volts in 5 seconds and to 90% in 25 seconds.

The data from Figure 21 was further analyzed in an attempt to quantify the photoconductivity and the quantum efficiency. It is possible to relate the photconductivity, σ , to the photodischarge rate, dV/dt , as follows:

$$j = \frac{i}{A} = \frac{1}{A} \frac{dq}{dt} = \frac{C}{A} \frac{dV}{dt} = \sigma E = \sigma \frac{V}{d} \quad (2)$$

where j = current density in amp/ m^2 , i = current in amps, A = cross sectional area in m^2 , q = charge in coulombs, C = the capacitance in farads, V = surface potential in volts, σ = conductivity in ohm-meters, E = electric field in volts/meter, d = film thickness in meters. The capacitance of a parallel plate capacitor is:

$$C = \frac{\epsilon_r \epsilon_0 A}{d} \quad (3)$$

where ϵ_r = relative permittivity (dielectric constant) and ϵ_0 = permittivity in farads/meter. Substituting equation (3) into (2) and solving for σ yields the following expression:

$$\sigma = \epsilon_r \epsilon_0 \frac{1}{V} \frac{dV}{dt} \quad (4)$$

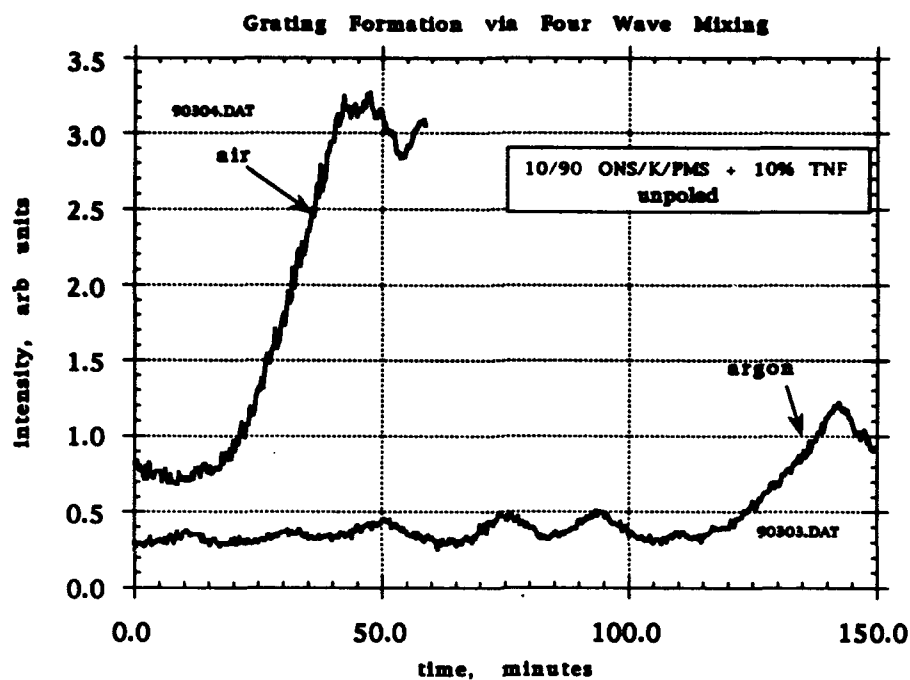


Figure 17. Four wave mixing results for 10/90 ONS/CBZ/PSX in air and Ar.

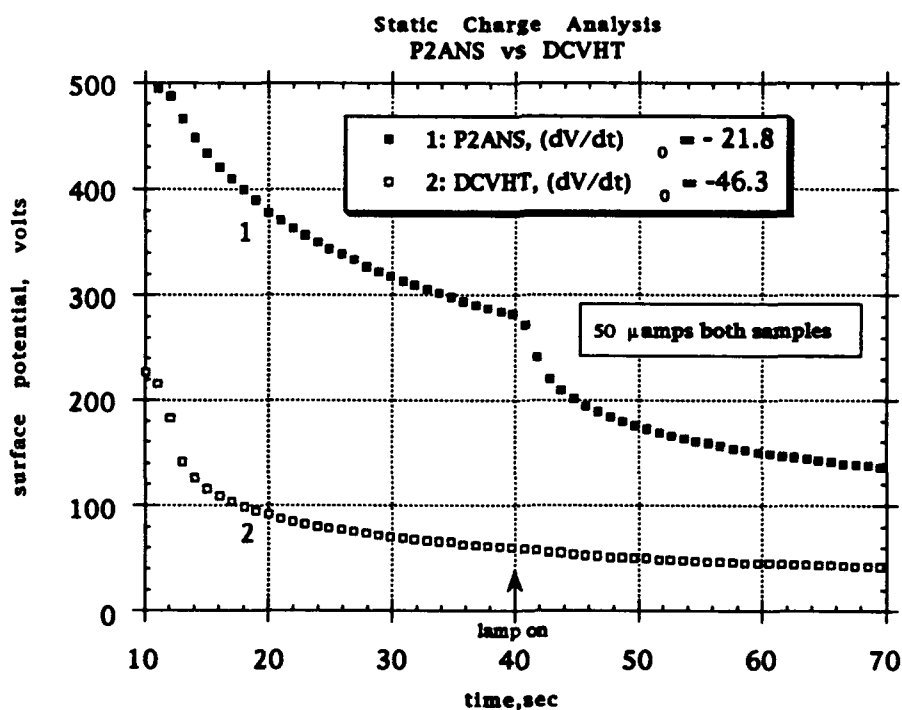


Figure 18. Photoinduced discharge curves for P2ANS and DCVHT polymers.

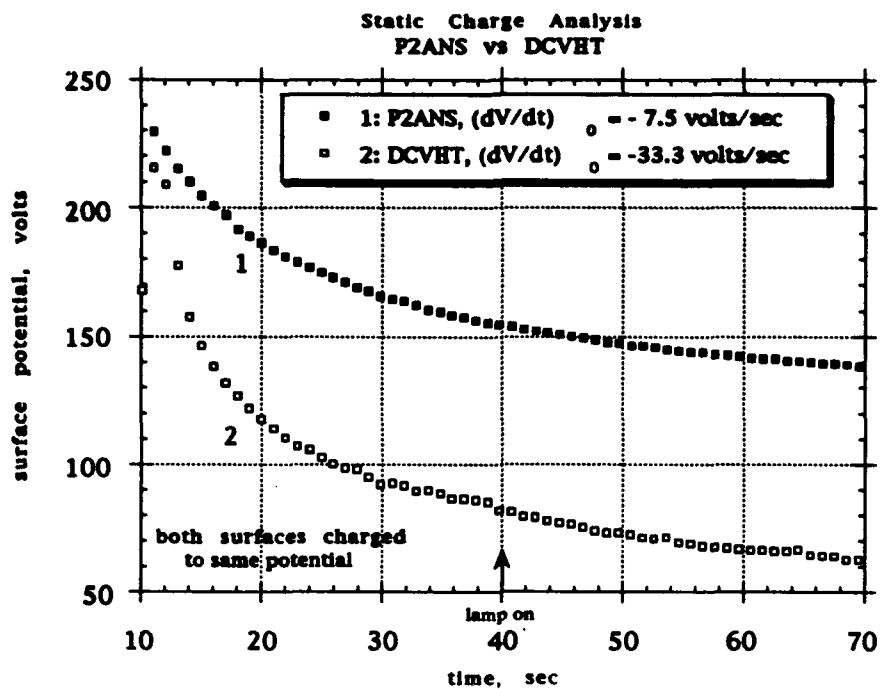


Figure 19. Photoinduced discharge for P2ANS and DCVHT polymers with surfaces charged to the same potential.

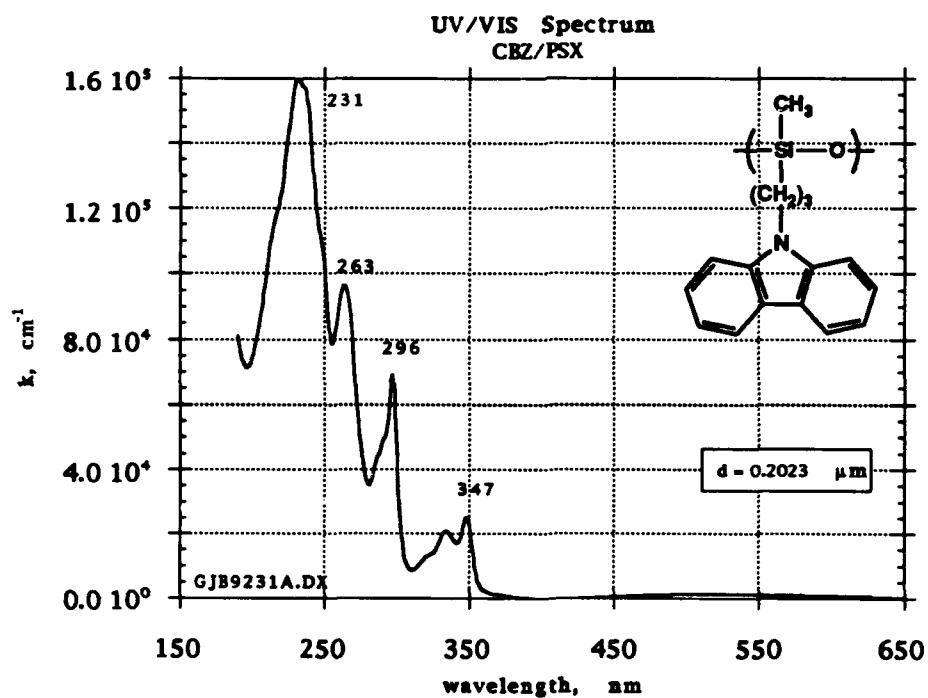


Figure 20. UV/VIS spectrum of carbazole-functionalized polysiloxane (CBZ/PSX).

If the dark conductivity is significant, it should be subtracted out as follows:

$$\sigma = \frac{\epsilon_0 \epsilon_r}{V} \left[\left(\frac{dV}{dt} \right)_{light} - \left(\frac{dV}{dt} \right)_{dark} \right] \quad (5)$$

It is a known characteristic of charge transport in disordered systems that the electrical conductivity is field dependent (dispersive transport). This may be written as:

$$\sigma = \sigma_0 E^{m-1} \quad (6)$$

where σ_0 = low field conductivity. If $m = 1$, then charge transport in the system is nondispersive. Because polymer systems are disordered, it can be expected that the conductivity is field dependent. Calculating σ according to (5) using the data of Figure 21 and plotting $\log \sigma$ vs. $\log E$ yields a straight line, as shown in Figure 22. Note that $m = 2.84$ so that the current is given by:

$$j = \sigma_0 E^{2.84} \quad (7)$$

The quantum efficiency is difficult to calculate for this system since a broadband light source was used. However, reasonable approximation can be made by assuming that all the light from 210 to 350 nm is absorbed and the average wavelength is 350 nm. The spectral output curve of a 200 W XeHg arc lamp used to irradiate the sample was integrated from 210 to 350 nm. The total power in this range was calculated to be about 500 mW. Assuming $\lambda = 350$ nm which is equivalent to 3.54 eV/photon, a photon flux of 880×10^{15} photons/second is calculated. The quantum efficiency η is defined as the number of charge carriers generated per absorbed photon.

$$\eta = \frac{\text{photocurrent}}{\text{photon flux}} = \frac{dq/dt}{\Phi} = \frac{C dV/dt}{\Phi} \quad (8)$$

Calculating η according to (8) and plotting $\ln \eta$ vs. $\ln E$ again yields a straight line (Figure 23).

The dependence of η on field is expected because the probability that light induced electron-hole pairs (excitons) will separate increases with field strength. At high field strengths, quantum efficiencies between 0.01 and 0.001 are observed.

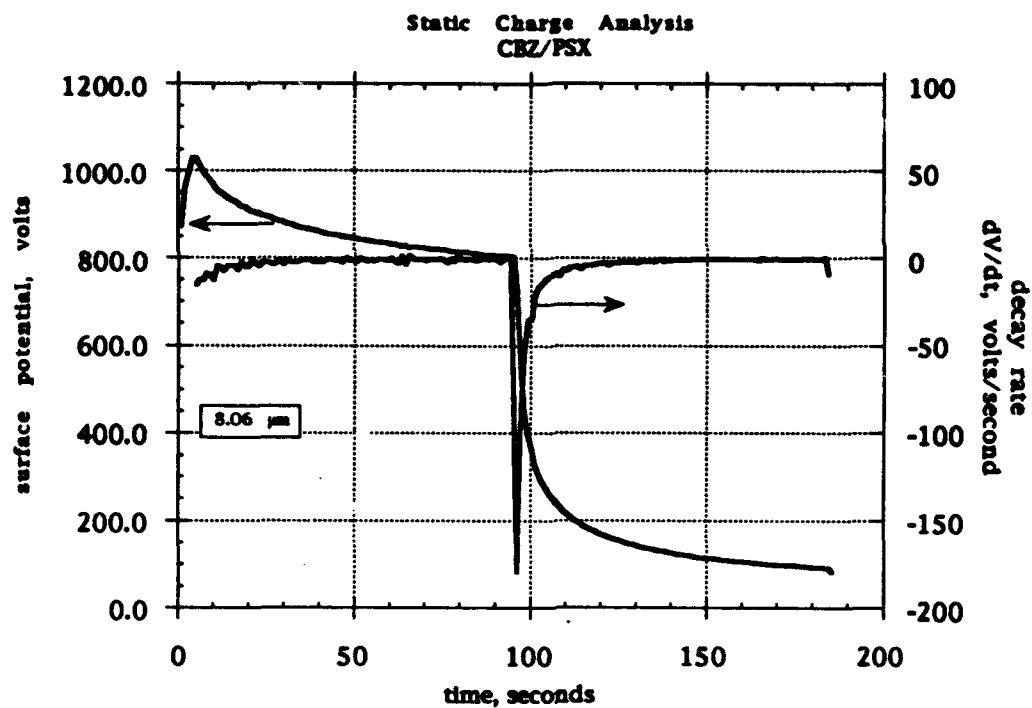


Figure 21. Photoinduced discharge and derivative curves for CBZ/PSX.

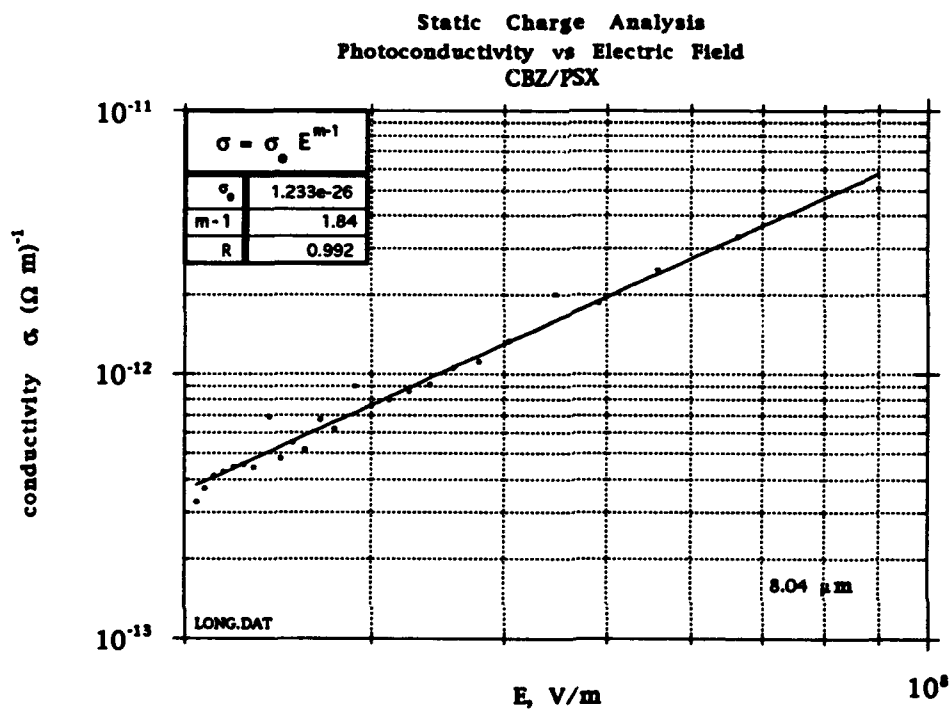


Figure 22. Photoconductivity vs. electric field for CBZ/PSX from photoinduced discharge.

The above analysis is useful for the determination of the conductivity and its field dependence as well as the quantum efficiency from easily performed experiments. Unfortunately, it does not allow calculation of the charge carrier mobility. The mobility is related to the conductivity by:

$$\sigma = ne\mu \quad (9)$$

where n = charge carrier density in cm^{-3} , $e = 1.602 \times 10^{-19}$ coulombs (electronic charge), and μ = carrier mobility in $\text{cm}^2/\text{V}\cdot\text{sec}$. The field dependence of the conductivity arises from the fact that both the mobility and the carrier density are field dependent.

Tricyanovinylated carbazole/siloxane polymer was prepared by reacting CBZ/PSX with tetracyanoethylene. The UV/visible spectrum of a thin film of this polymer is given in Figure 24. The percent substitution of tricyanovinyl groups on the carbazole rings is about 18%. TGA showed that the polymer was thermally stable to over 400°C and its T_g had risen to about 80°C . The absorption peak of the tricyanovinyl group occurs at 503 nm. The combination of the tricyanovinyl acceptor group conjugated with the carbazole nitrogen donor suggests that this polymer will be electrooptic. A spin coated sample was poled at $70 \text{ V}/\mu\text{m}$ and the electrooptic coefficient was measured to be 2.2 pm/V at $1.3 \mu\text{m}$ and 6.7 pm/V at 633 nm. Bleaching experiments at 633 nm and at 514 nm indicate that this material is robust when compared with the 10/90 ONS/CBZ/PSX polymers which bleached readily at 633 nm due to the ONS (oxynitrostilbene) chromophore. This is surprising because the ONS peak absorption at 380 nm occurs at a much shorter wavelength than the TCV absorption. The TCV-CBZ/PSX polymer was spin coated onto ITO coated glass and tested on the static charge analyzer using a 200 watt XeHg lamp. The photodecay was quite steep indicating that the substitution has not diminished the photoconductivity of the carbazole units (Figure 25). Four wave mixing indicated that this material was weakly photorefractive, about one order of magnitude smaller than P2ANS after accounting for thickness, electrooptic coefficient, and applied voltage. The results are shown in Figure 26 comparing the signal obtained from both of these materials.

The tricyanovinylated derivative had a much lower molecular weight than the starting material. GPC and derived absolute intrinsic viscosities showed that there was significant random chain scission. The initial intrinsic viscosity of the siloxane backbone was 0.12 and that of the carbazolylated siloxane was also 0.12, showing that little or no degradation to the backbone occurred during the grafting reaction. After the tricyanovinylation reaction, the intrinsic viscosity fell to about 0.05. The polymer could be spin coated onto ITO glass but films had to be handled with great care to avoid cracking. Two more runs tests were made using *t*-butanol rather than methanol for the workup. Much less HCN was released at the workup stage but the intrinsic viscosity fell to even lower values (about 0.03) and some fractions of the isolated material remained as sticky dark red gums and would not solidify. It is not yet known why the TCNE reaction attacks the polymer backbone but it clearly does so. One idea is that the cyanide ion which is a strong nucleophile may attack the siloxane chain at the site of any remaining Si-H units and cause some sort of nucleophilic unzipping reaction.

In view of the chain-scission problem with the TCV reaction and the HCN hazard involved, the dicyanovinyl analog was chosen as a more viable alternative. The 3-aldehyde of 9-allyl carbazole (XXV) was synthesized via a Vilsmeier-Haack reaction, the aldehyde being isolated in 65% yield. The aldehyde reacted readily with malononitrile giving a bright yellow DCV derivative as shown below (XXVI). This was grafted onto a siloxane backbone as a homopolymer but the opaque yellow product was insoluble in all common solvents. It had $T_g = 75^\circ\text{C}$.

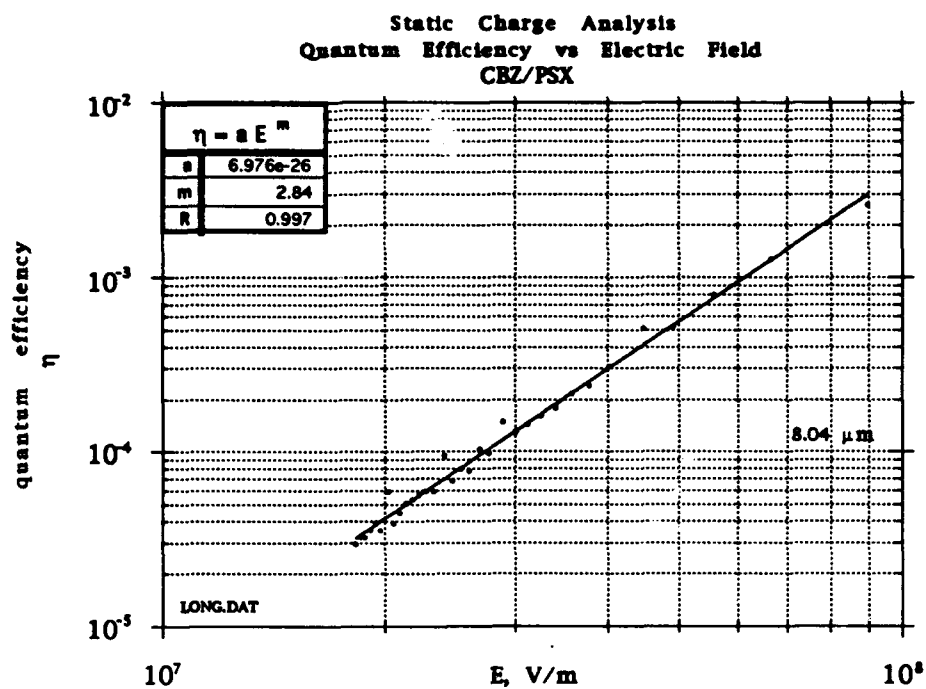


Figure 23. Quantum efficiency vs. electric field for CBZ/PSX from photoinduced discharge.

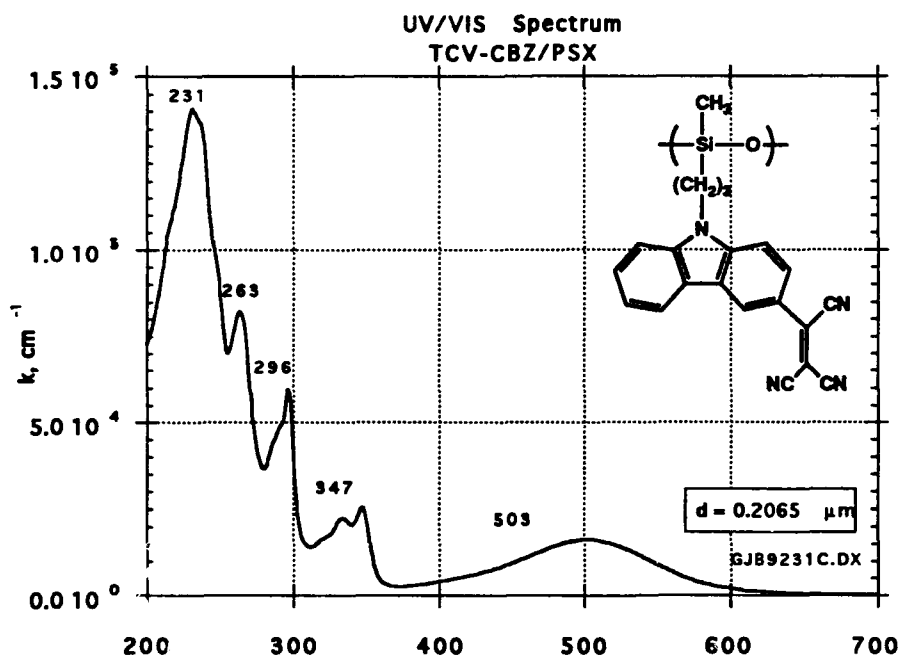


Figure 24. UV/VIS spectrum of TCV-CBZ/PSX thin film.

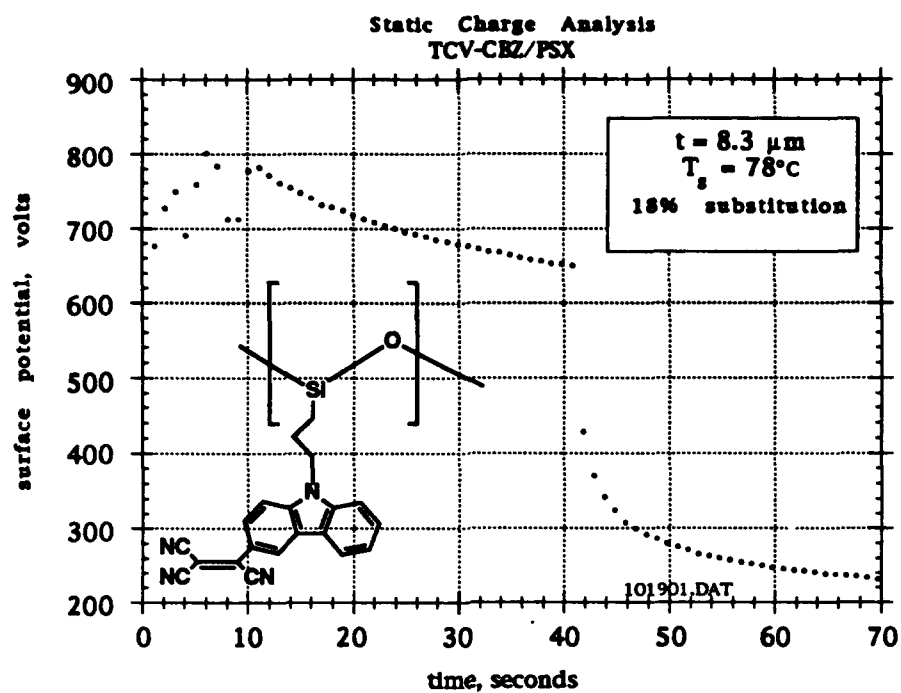


Figure 25. Photoinduced discharge curve for TCV-CBZ/PSX.

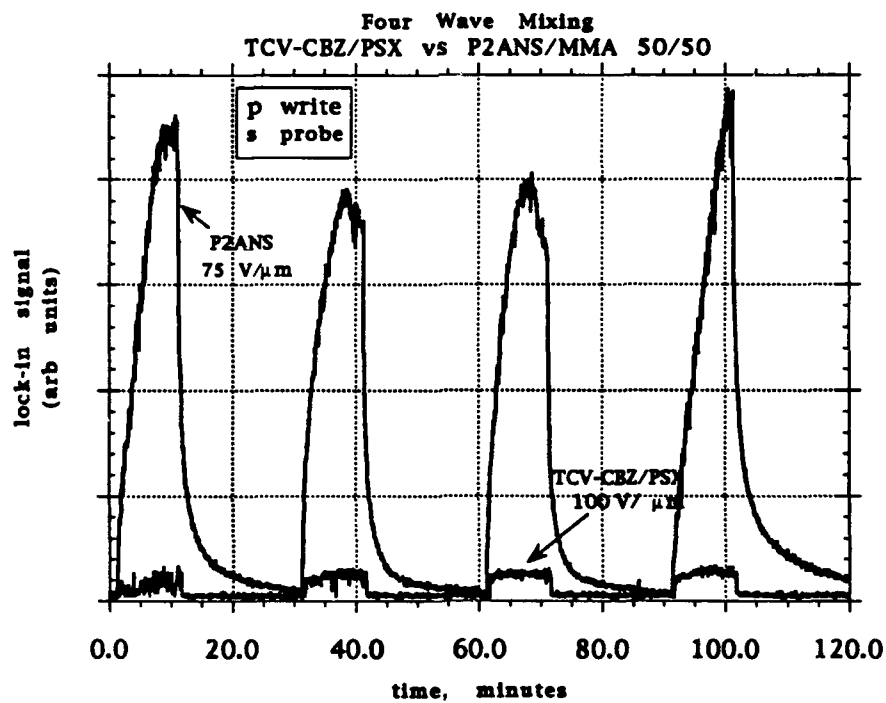
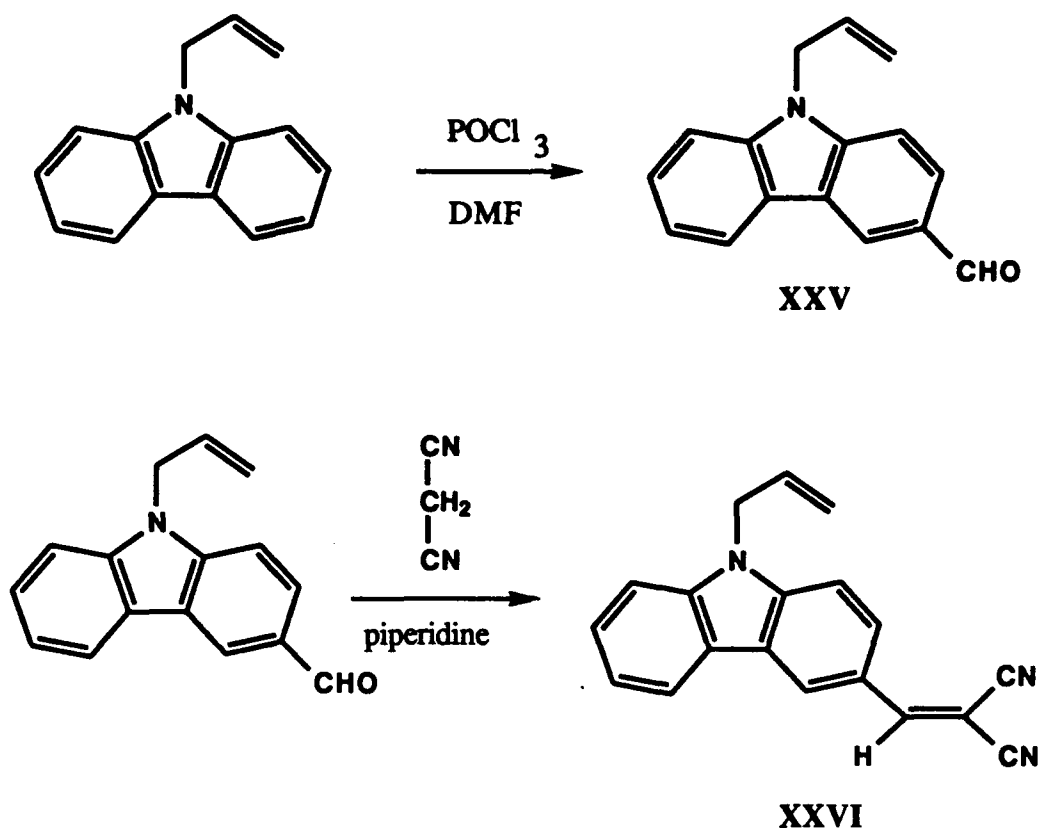


Figure 26. Four wave mixing results for TCV-CBZ/PSX.



Next a copolymer graft was made using a 25/75 ratio of DCV-CBZ to plain CBZ units. The product had $T_g = 45^\circ\text{C}$ and its IV was 0.12, showing no chain-scission had occurred. Poled films had an electrooptic coefficient of 2.5 pm/V at 633 nm. Figure 27 shows the UV/visible spectrum of the DCV-CBZ/PSX. The absorption maximum of the DCV chromophore occurs at 423 nm. Static charge analysis indicates that the material is photoconductive as shown in Figure 28. The data were collected at 452 nm and at 645 nm, the latter being close to the 633 HeNe wavelength where four wave mixing is done. Four wave mixing did not reveal the presence of a grating despite the material's photoconductivity at 633 nm and has an electrooptic coefficient of 2.5 pm/V at that wavelength. Since it was shown that the TCV-CBZ/PSX is weakly photorefractive, it is likely that this is also the case for the DCV-CBZ/PSX. Because its electrooptic coefficient is smaller and the sample is thinner, the diffracted signal was probably below the detection limits.

P2ANS/MMA is a copolymer of methyl methacrylate with a dialkylaminonitrostilbene methacrylate comonomer as shown in (X). The refractive indices for the 50/50 material are 1.63 and 1.72 at 1300 nm and 633 nm, respectively. The linear electrooptic coefficient depends on poling and has been measured up to 38 pm/V at 1300 nm. Differential Scanning Calorimetry yields a T_g of $\approx 138^\circ\text{C}$. The presence of the amino nitrogen group, a structural feature common to many organic photoconductors, gives rise to a low level of photoconductivity which, as will be shown later, is sufficient to allow the polymer to exhibit photorefractive behavior without the incorporation of separate photoconductive units. The UV/visible spectrum for a 0.2 μm film of this polymer is given in Figure 29. Absorption maximum occurs at 427 nm with an absorption coefficient $k = \alpha/2.303 = 59,600\text{ cm}^{-1}$. Because of the presence of the nitro group, there is considerable tailing of the absorption peak with subsequent significant absorption at 633 nm.

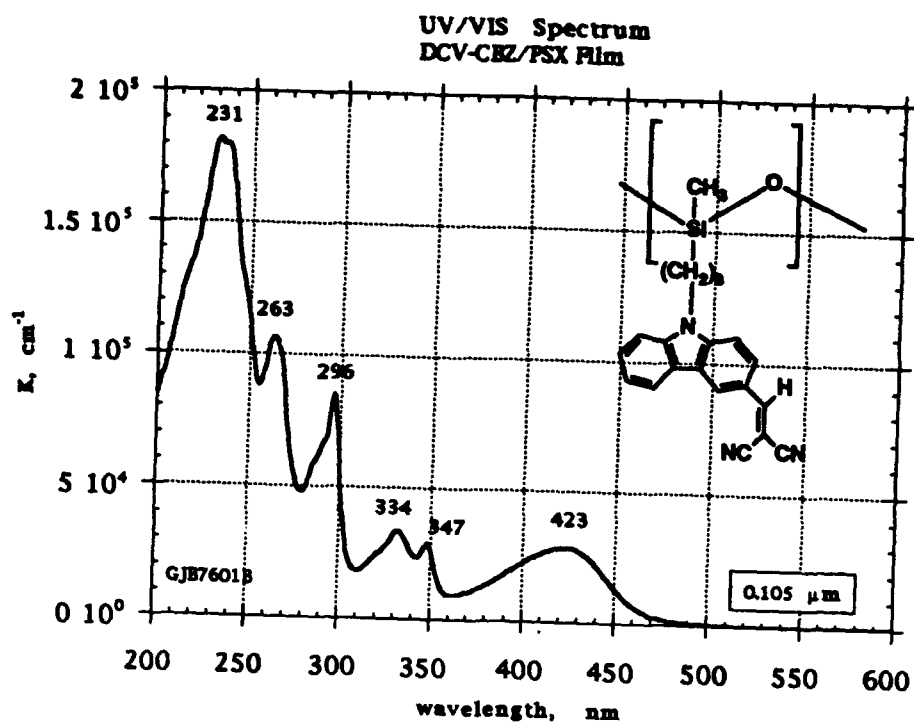


Figure 27. UV/VIS spectrum of DCV-CBZ/PSX thin film.

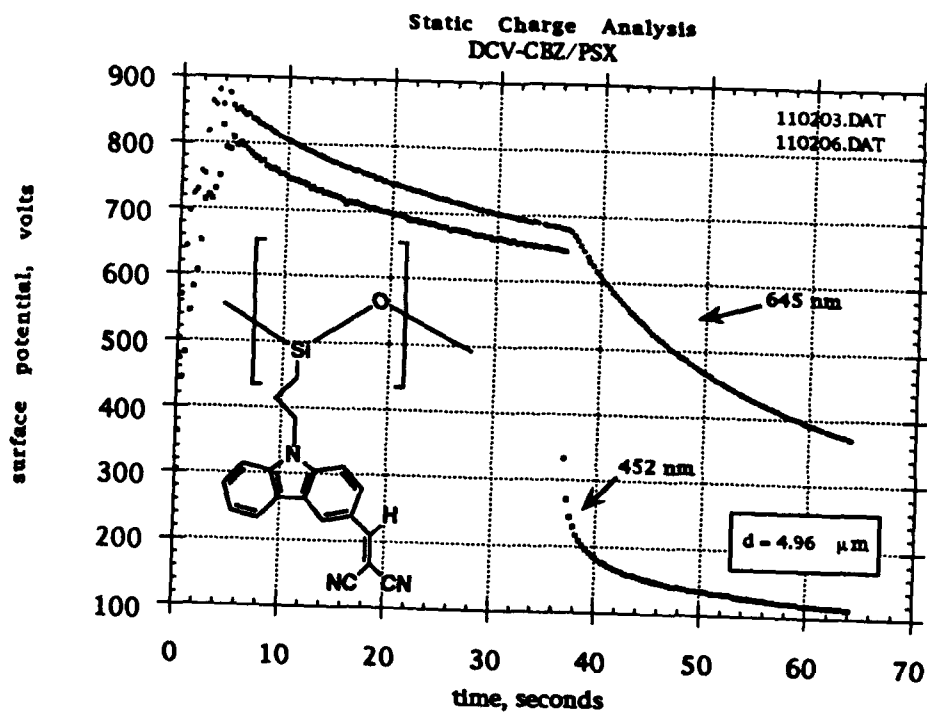


Figure 28. Photoinduced discharge curve for DCV-CBZ/PSX.

A solution of 50/50 P2ANS/MMA copolymer was spin coated onto a glass slide with a resulting thickness of 3.56 μm . The static charge analyzer was used to corona charge the surface for 5 seconds to a surface potential of 600 volts. The decay of the surface potential was monitored for 30 seconds in the dark and then for 30 seconds with exposure to light. Because the samples are rotated during measurement, the 30 second exposure consisted of cycles of 8 msec of exposure to light followed by 92 msec in the dark. The light source was a 200 watt Hg(Xe) lamp with an 80 nm bandpass filter centered at 645 nm. The results are shown in Figure 30. The data was differentiated numerically and a plot of decay rate vs. surface potential was constructed (Figure 31). The dark decay rate at a potential of 193 volts was 3 V/s and jumped to 21 V/s upon irradiation.

The data in Figure 31 was further analyzed in order to quantify the photoconductivity and the quantum efficiency. The photoconductivity, σ , is related to the photodischarge rate, dV/dt , by equation (5) above. The field dependent electrical conductivity is again given by equation (6) where $m = 1$ for nondispersive transport. Calculating σ according to (2) using the data of Figure 4 and plotting $\log \sigma$ vs. $\log E$ yields a straight line. This result is shown in Figure 32. Note that $m-1 = 2.22$ so that the field dependent current is given by:

$$j = \sigma_0 E^{3.22} \quad (10)$$

This strong dependence on the field is common in organic materials and a characteristic of dispersive transport.

An approximate value for the overall quantum efficiency can be calculated from the data in Figure 31. The incident power was 850 mW/cm². A 645 nm filter with a passband of 80 nm was used to get as close to 633 nm as possible. Taking the center frequency of the filter at $\lambda = 645$ nm (equivalent to 1.92 eV/photon) and an illuminated sample area of 3.24 cm², a photon flux, ϕ , of 8.94×10^{15} photons/second was calculated. The quantum efficiency Φ is defined as the number of charge carriers generated per absorbed photon.

$$\Phi = \frac{dq/dt}{\phi} = \frac{C dV/dt}{\phi} \quad (11)$$

Calculating Φ according to (5) and plotting $\log \Phi$ vs. $\log E$ again yields a straight line (Figure 33). Quantum efficiencies between 10^{-3} and 10^{-5} were observed. The strong dependence of quantum efficiency on field is expected because the probability that light induced electron-hole pairs will separate increases with field strength. A theory relating the overall charge generation to the electric field strength and other parameters has been developed by Onsager. Our data did not fit the Onsager model but this may be in part due to the small range of electric field strengths employed in our measurements and to experimental error.

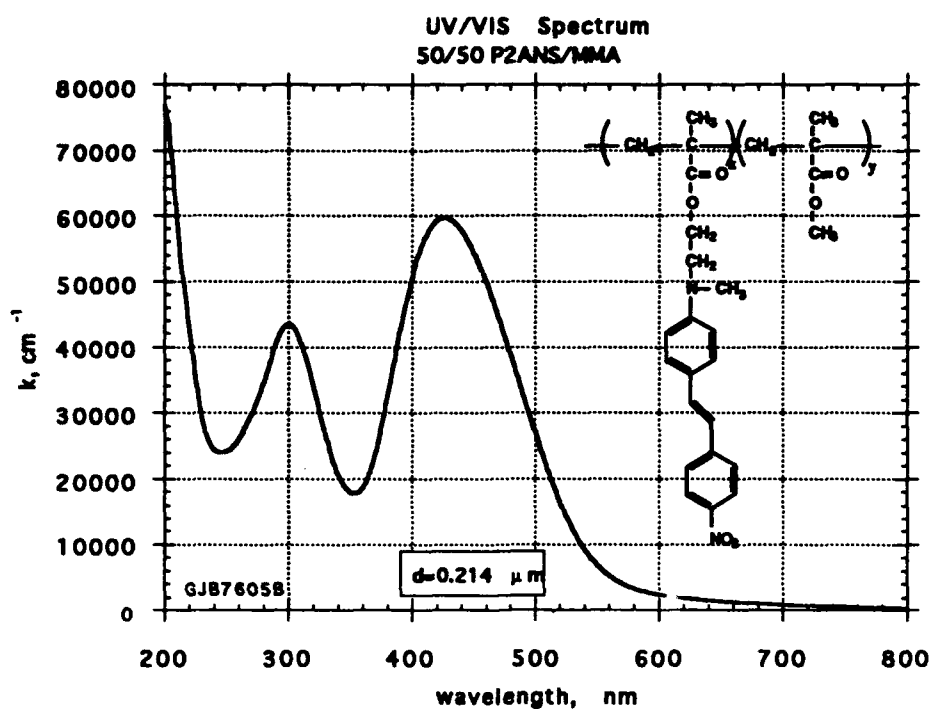


Figure 29. UV/VIS spectrum of 50/50 P2ANS/MMA thin film.

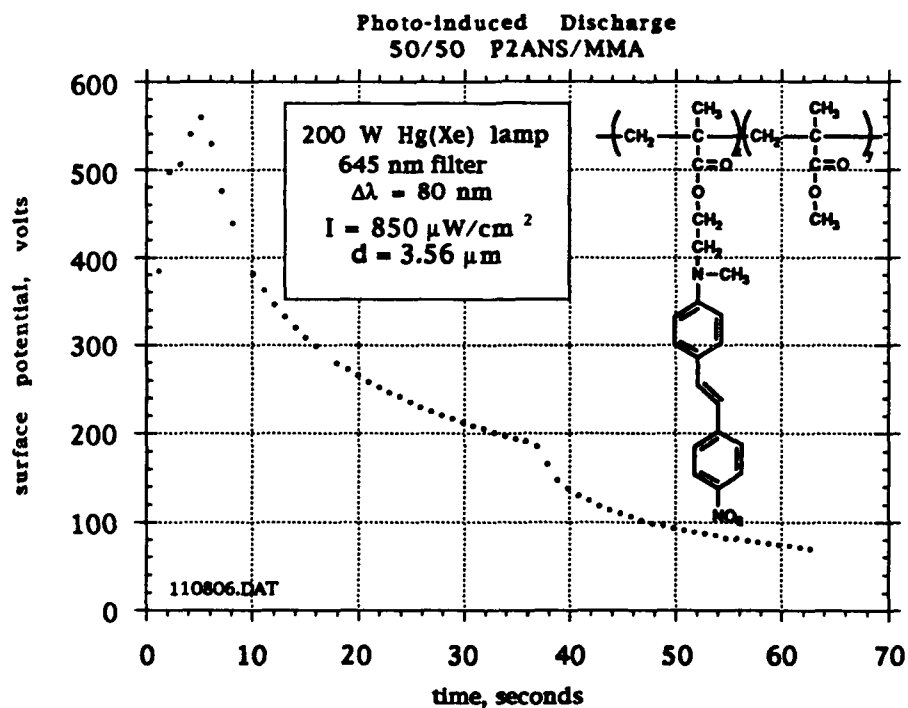


Figure 30. Photoinduced discharge curve for 50/50 P2ANS/MMA.

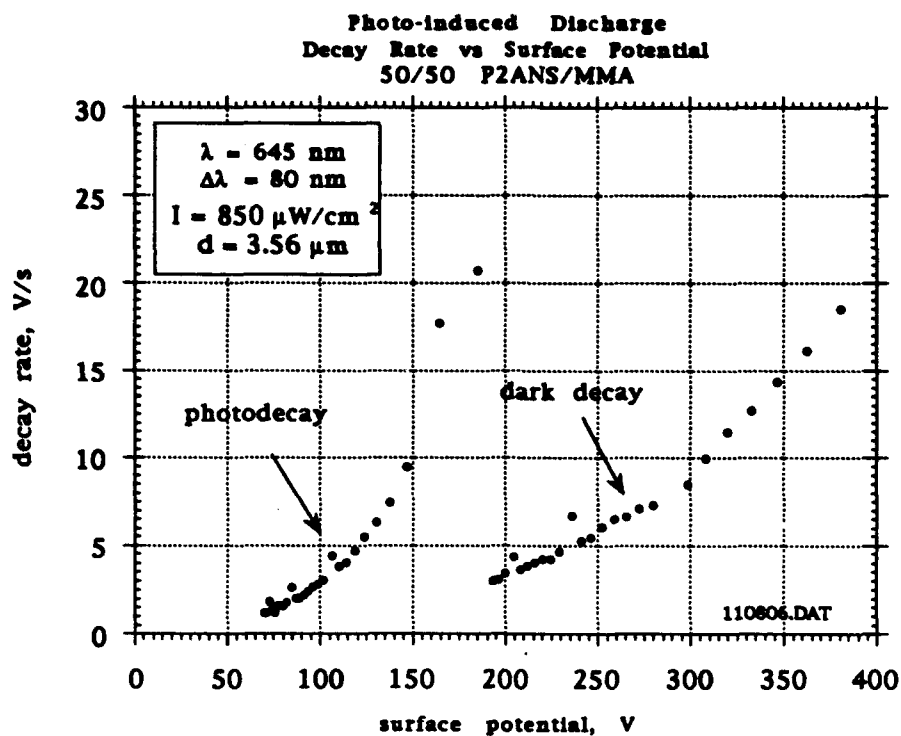


Figure 31. Derivative of photoinduced discharge results for 50/50 P2ANS/MMA.

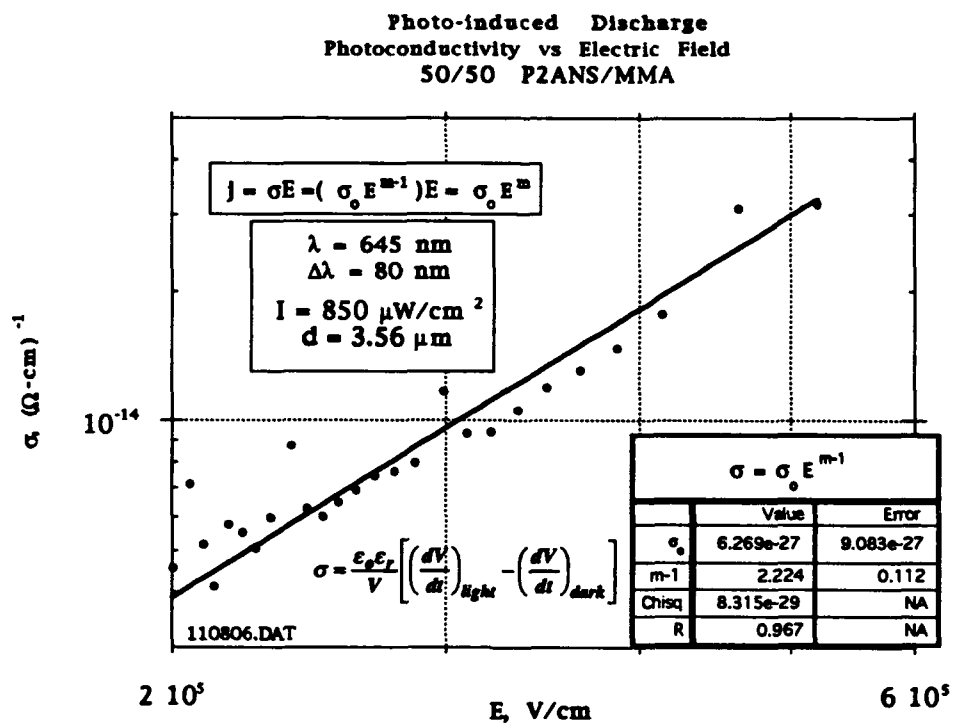


Figure 32. Photoconductivity vs. electric field for 50/50 P2ANS/MMA.

A solution of 50/50 P2ANS/MMA copolymer was spin coated onto ITO coated glass to a thickness of 4 μm and metallized with a 100 nm thick gold electrode. Using a dc power supply and a picoammeter, steady state photoconduction measurements were performed with a 5 mW HeNe laser as the source of illumination. The dark conductivity was measured to be $10^{-15} - 10^{-14} (\text{W.cm})^{-1}$ at $10^5 - 10^6 \text{ V/cm}$, as shown in Figure 34. This was 1-2 orders of magnitude smaller than the measured photoconductivity which, depending on intensity, ranged from 10^{-14} to $10^{-12} (\text{W.cm})^{-1}$. The current density j is related to the electric field by $j = \sigma E = \sigma_0 E^m$, with the field dependent conductivity given by $\sigma = \sigma_0 E^{m-1}$, where σ_0 is a constant. If $m=1$, the conductivity is field independent and Ohm's law is obeyed. From the measurements shown in Figure 34, the exponent m is estimated to be about 3 indicating a strong dependence on the field. This agrees with the results obtained above using the photoinduced discharge technique. The photosensitivity, defined as the photoconductivity per unit intensity, was found to be constant at fixed field strengths below saturation as expected and ranged with field from $4 \times 10^{-12} - 1 \times 10^{-10} (\text{W.cm})^{-1}/(\text{W/cm}^2)$. These measurements indicate that the photoconductivity of P2ANS/MMA is significant enough to account for the observation of photorefraction in this electrooptic polymer.

A sample of 50/50 P2ANS/MMA was spin coated onto ITO coated glass to a thickness of 8 μm . The sample was metallized with a 100 nm gold electrode and poled at 100 V/ μm . This resulted in an electrooptic coefficient of 20 pm/V and a refractive index of 1.72 at 633 nm. The poling electrode was stripped and replaced with a 5 nm layer of gold to enable light transmission. The writing beams were balanced at an intensity of 55 mW/cm² each and an external electric field of 50 V/ μm was applied. The angle between the two writing beams was 84° giving rise to a grating period of 184 nm. This resulted in approximately 40 grating periods across the sample thickness. The diffraction efficiency was recorded over a period of 60 minutes with 10 minute write and 5 minute erase cycles to demonstrate reversibility. The erasure was accomplished by blocking one of the write beams, thus flooding the grating region with uniform illumination. The results are shown in Figure 35 for a *p*-polarized probe beam.

While the material responds initially within seconds, the rise and fall time constants were 1.5 – 2.5 minutes and 2 – 3 minutes respectively as approximated from curve fitting. It should be noted that the response time is inversely proportional to the writing beam intensity. Increasing the intensity to 1 W/cm² (a typical value) could reduce the time constant by a factor of 20. The measured diffraction efficiencies were on the order of 10^{-5} . The diffraction efficiency of a lossless reflection index grating is given by:

$$\eta = \tanh^2(\pi \Delta n d / \lambda \cos \theta) \quad (12)$$

where λ is the free space wavelength, θ is the Bragg angle, d is the thickness, and Δn is the refractive index change. For the sample used, $\lambda = 0.633$, $d = 8.0$, $\theta = 6.1^\circ$, and $\eta = 4 \times 10^{-5}$, Δn is calculated to be 1.6×10^{-4} . From this, the space charge field can be calculated from the relationship $\Delta n = 1/2 n^3 r E_{SC}$ where r is the electrooptic coefficient, n is the refractive index, and E_{SC} is the space charge field. The electrooptic coefficient was 20 pm/V resulting in a space charge field of 3.1 V/ μm assuming no losses. This represents only 6% of the applied field.

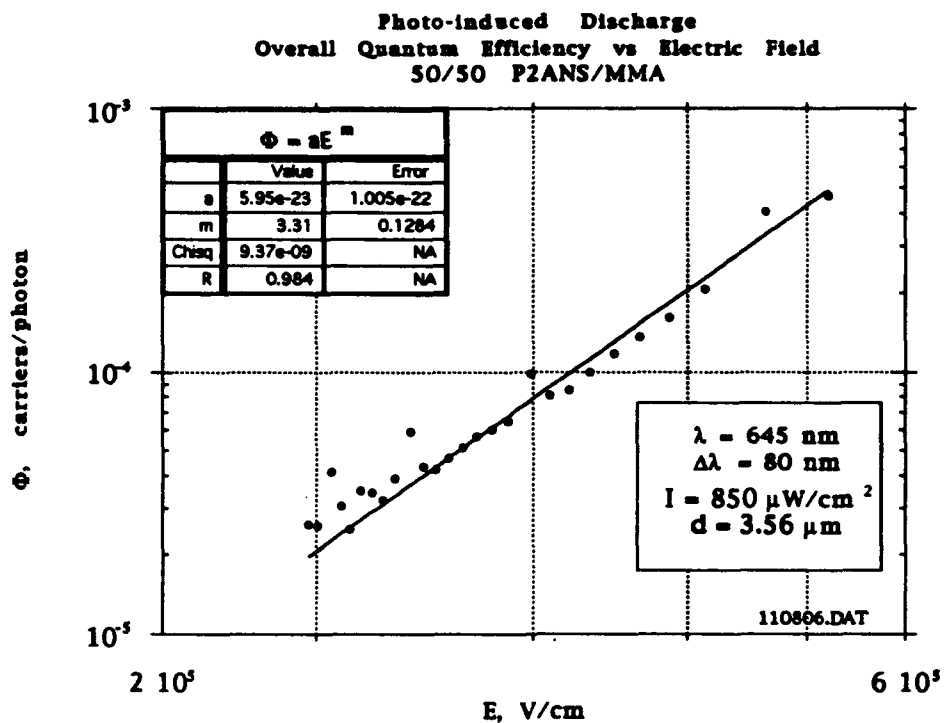


Figure 33. Quantum efficiency vs. electric field for 50/50 P2ANS/MMA.

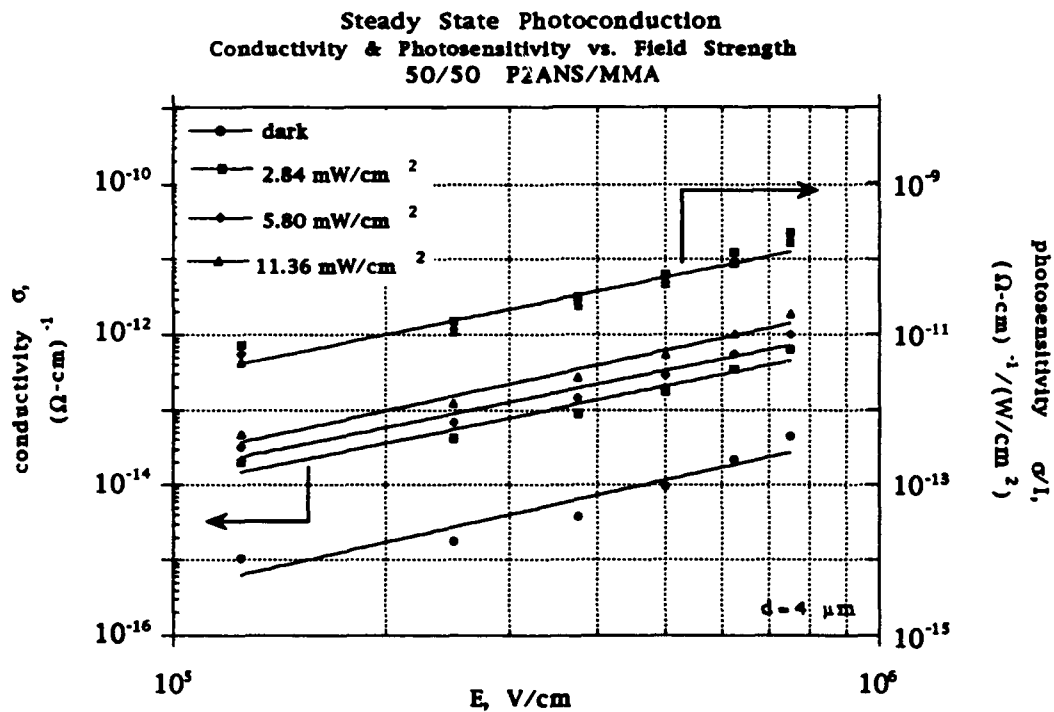


Figure 34. Steady state dark and photoconductivity for P2ANS/MMA.

Taking absorption into account ($\alpha = 3823 \text{ cm}^{-1}$ at 633 nm) and applying Kogelnik's formulation for reflection gratings [28], a more realistic space charge field of $19.6 \text{ V}/\mu\text{m}$ is calculated. It is important to note that various processes which lead to grating formation can contribute to the detected signal. Thus, electrochromic and photochromic effects, among others, may contribute to the measured diffraction. Even small perturbations of the absorption coefficient on the order of a few percent of the background absorption can account for some of the observed diffraction.

The photorefractive effect in polymeric materials is strongly field dependent due to the lower probability of geminate recombination of the separated charges in the presence of an external field. The field dependence of the diffraction efficiency is shown in Figure 36 for a grating written with *s*-polarized beams and probed with a *p*-polarized beam. It can be seen that the signal grows with the applied field as expected. While the basic theory predicts a quadratic dependence of the diffraction efficiency on the field at low diffraction efficiencies, the dependence observed in this case is sublinear. Under no field, no measurable signal was detected, as expected.

Measurements were also performed using *p*-writing waves. This required a slight modification of the setup shown in Figure 37. Figure 37 shows the results for the *s*-polarized component of the probe beam at three different applied fields. The results are similar to those obtained using *s*-polarized beams to write the grating. The diffraction efficiencies are one order of magnitude higher than those shown in Figures 35 and 36. The sample thickness was $11.4 \mu\text{m}$ which accounts for a factor of two increase. The polymer was also from a different, much higher molecular weight batch which might affect poling efficiency and relaxation. The fact that the diffraction efficiency is field dependent is a strong indication that the material is photorefractive.

The four 4-mixing apparatus was modified so that the probe beam had both *s*- and *p*-components. An additional lock-in amplifier was employed to detect the added component. The results for P2ANS are shown in Figure 38. The writing time is 10 minutes followed by a 20 minute erase cycle during which one of the writing beams is blocked by a shutter. An external field of $50 \text{ V}/\mu\text{m}$ was applied to the sample in the poling direction. The *p*-wave behavior was as expected. The diffracted *s*-wave was stronger and not as well behaved. This suggests the possibility of a competing reversible process such as *cis-trans* isomerization which might be superimposed on top of a photorefractive contribution. Because the writing beams are *s*-polarized, they would interact with side chains that are properly aligned. This selected subset of molecules could undergo isomerization forming a reversible absorption grating detectable by an *s* polarized probe.

In the next experiment, no external field was applied to the sample. The photorefractive effect in polymeric materials is strongly field dependent due to geminate recombination of the separated charges. As can be seen from Figure 39, the *p*-wave is practically gone. The *s*-wave signal is still present and is accordingly not caused by the photorefractive effect.

If external field is applied in opposition to the poling direction, the *s*-wave signal is reduced by 35 to 50% and the *p*-wave is small and highly fluctuating. Photorefraction is not expected in this case because sample depoling by the external field. The results are shown in Figure 40. When the same experiment was conducted on unpoled samples, the *p*-wave signals were quite small. The *s*-wave signal was always present. The *p*-wave signal is ascribed to a photorefractive response.

These experiments were repeated using *p*-waves instead of *s*-waves to write the grating. This required minor modifications to the optical setup. In this case, the diffracted signal from the *s*-polarized probe beam is comparable in strength to that observed for the *p*-component in the original set up. However, the *p*-component in this case is significantly smaller and more stable than in the previous experiments (Figure 41). This could be an important clue to understanding the P2ANS system but further experimental work is required. When we attempted to write a grating in the material using beams of opposite polarity, no grating was detected as expected.

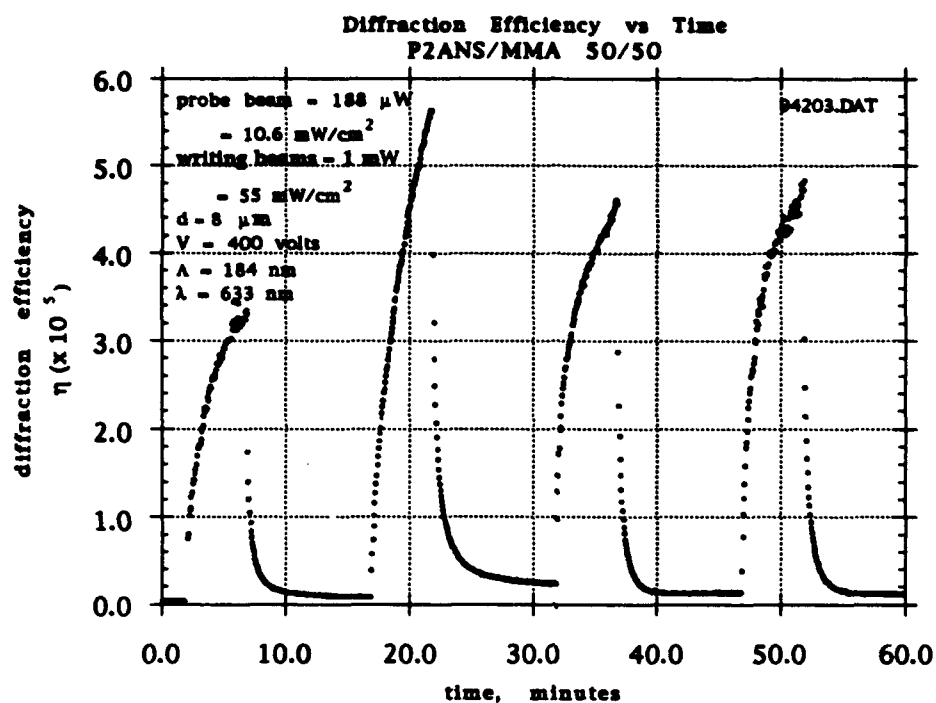


Figure 35. Diffraction efficiency vs. time for P2ANS/MMA.

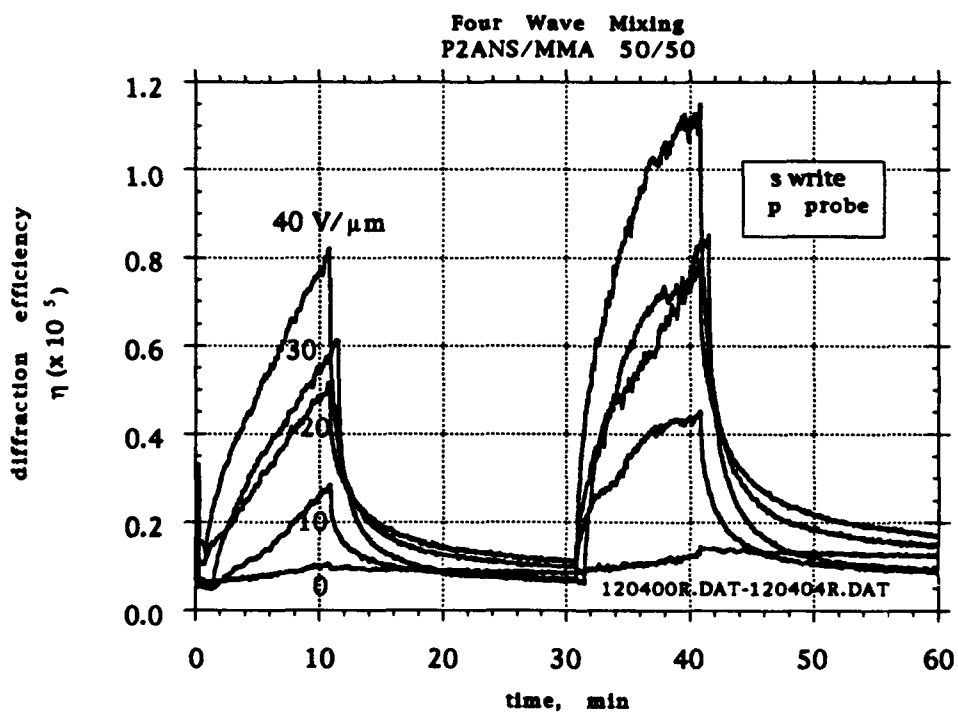


Figure 36. Diffraction efficiency vs. time at various electric field strengths - s write, p probe.

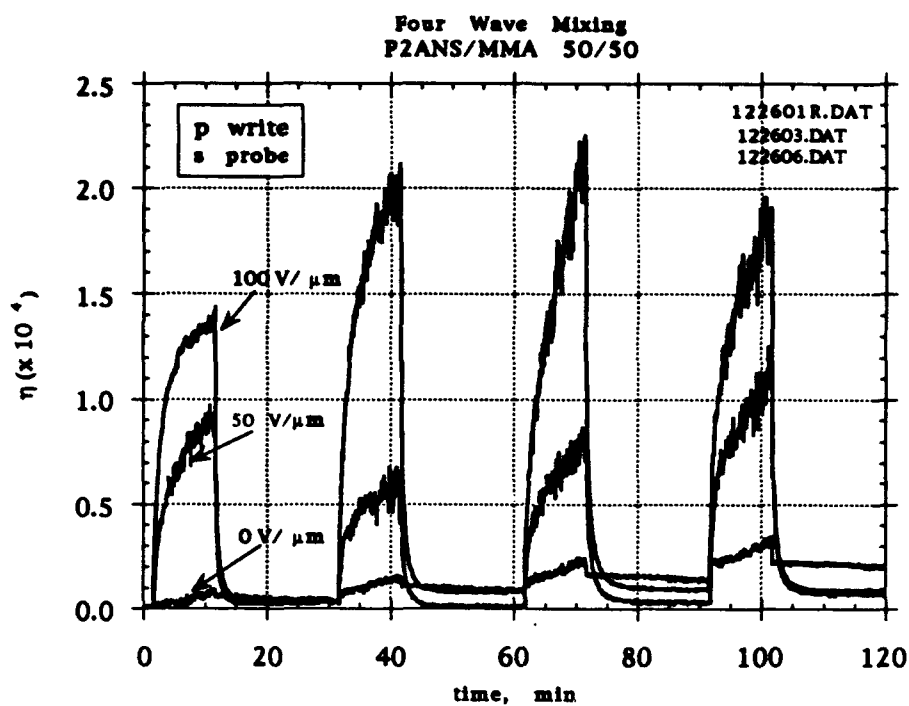


Figure 37. Diffraction efficiency vs. time at various field strengths: *p* write, *s* probe.

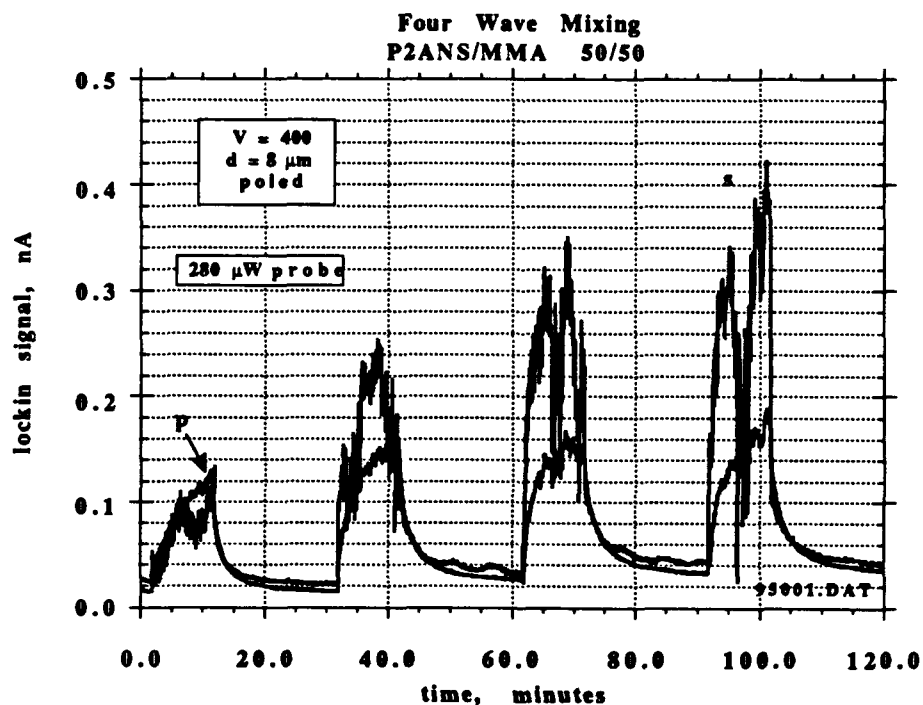


Figure 38. Four wave mixing using *s* writing beams and *s* & *p* reading beams.

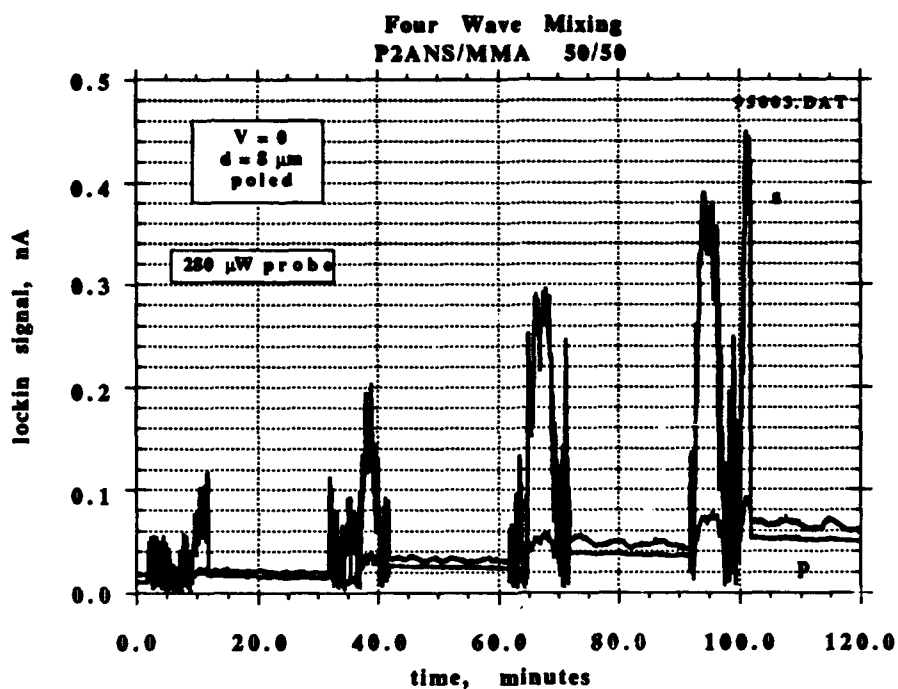


Figure 39. Four wave mixing using *s* writing beams and *s* & *p* reading beams with no externally applied field.

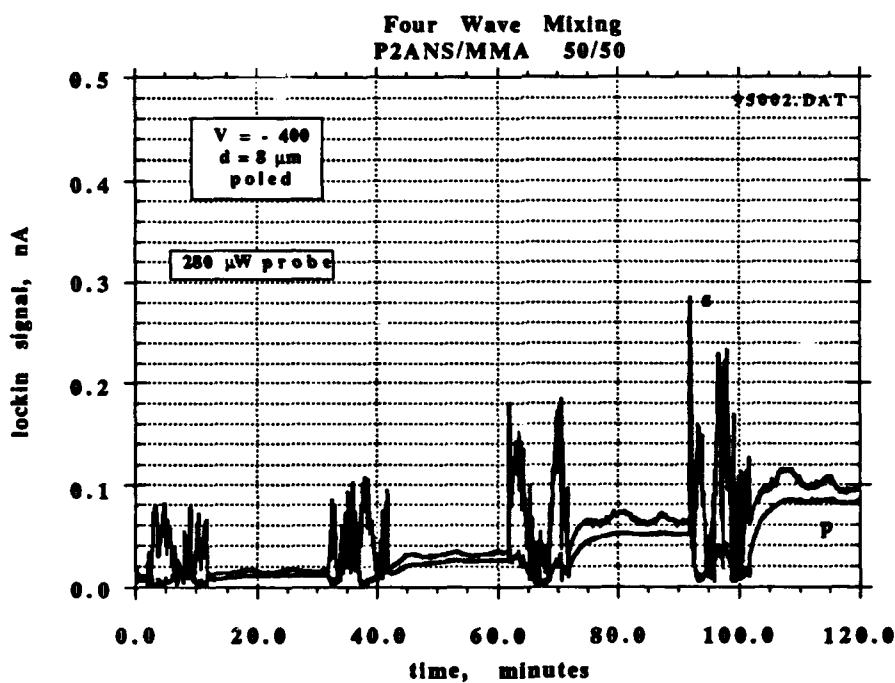


Figure 40. Four wave mixing using *s* writing beams and *s* & *p* reading beams with external field applied opposite to the poling direction.

According to the tests and results discussed above, it is believed that P2ANS exhibits photorefractive behavior but that other effects are occurring simultaneously and contributing to the overall signal. The *p*-polarized probe beam when used to read a grating written by *s*-polarized writing beams appears to be measuring primarily a photorefractive effect. A two beam coupling experiment can discriminate between photorefractive gratings and absorption gratings by allowing detection of energy transfer between two beams caused by the phase shift between the intensity distribution and the electrooptic index grating in the sample.

Two beam coupling is the best method for determining the grating formation mechanism in potential photorefractive systems. Two coherent beams are interfered in the material forming a grating. If the grating is due to photorefraction, it is spatially phase shifted by up to $\pi/2$ (a quarter of a grating spacing $\Lambda/4$) with respect to the intensity distribution that induced it. Energy transfer between the two beams becomes possible. This is explained by the fact that a $\pi/2$ phase shift exists between the zero order and first order diffracted signals on a phase grating. On a grating spatially shifted by a quarter wavelength ($\Lambda/4$), an additional shift of $+\pi/2$ is imposed on one of the diffracted beams and $-\pi/2$ on the other. Hence, for one of the transmitted beams, the interference of the zero order beam and the first order diffracted beam is constructive while for the other transmitted beam, it is destructive. It is also possible to have phase shifts between 0 and $\pi/2$ depending on the magnitude of the applied electric field.

In practice, the sample is mounted on a piezoelectric stage, the grating is written, and the sample translated across the writing beams in the direction of the grating vector. The translation time should be significantly smaller than the grating writing time. The translation of the sample causes a modulation of the diffracted beams which manifests itself as an ac ripple on the photodetected signals. Because both beams automatically satisfy the Bragg diffraction condition, part of beam 1 is diffracted into beam 2 and vice versa. The key to the experiment is the piezoelectric stage which is used to translate the grating in the direction indicated by the arrow. This is the same direction as the grating vector which is normal to the grating planes. A mathematical treatment [29] (based on Kogelnick's coupled wave analysis) of the detected intensities of beams 1 and 2 from a sinusoidal grating yields the following expressions:

$$I^{(1)} = I_0 \exp\left[\frac{-\alpha d}{\cos \theta}\right] \left[1 - 2A \cos\left(\phi_A + \frac{2\pi\xi}{\Lambda}\right) - 2P \sin\left(\phi_P + \frac{2\pi\xi}{\Lambda}\right) \right] \quad (13)$$

$$I^{(2)} = I_0 \exp\left[\frac{-\alpha d}{\cos \theta}\right] \left[1 - 2A \cos\left(\phi_A + \frac{2\pi\xi}{\Lambda}\right) + 2P \sin\left(\phi_P + \frac{2\pi\xi}{\Lambda}\right) \right] \quad (14)$$

where $P = \frac{\pi \Delta n d}{\lambda \cos \theta}$, and $A = \frac{\Delta \alpha d}{4 \cos \theta}$. In these equations, I_0 = incident intensity, d = sample thickness, α = absorption coefficient, θ = angle of incidence, ϕ_A = phase shift from amplitude grating, ϕ_P = phase shift from index grating, Λ = grating spacing, ξ = grating displacement, Δn = refractive index change, and $\Delta \alpha$ = absorption coefficient change. The angle of incidence with

respect to the surface normal is q for both beams. The modulation of these signals depends on the magnitudes of P and A which are functions of Δn and $\Delta\alpha$ respectively. If the above two equations are added and subtracted, the results are given by [29]:

$$I^{(+)} = I^{(1)} + I^{(2)} = I_0 \exp\left[\frac{-\alpha d}{\cos\theta}\right] \left[2 - 4A \cos\left(\phi_A + \frac{2\pi\xi}{\Lambda}\right)\right] \quad (15)$$

$$I^{(-)} = I^{(1)} - I^{(2)} = I_0 \exp\left[\frac{-\alpha d}{\cos\theta}\right] \left[-4P \sin\left(\phi_P + \frac{2\pi\xi}{\Lambda}\right)\right] \quad (16)$$

The above two equations can be analyzed using nonlinear least squares regression to yield values for A , P , ϕ_A , and ϕ_P . Equations (13)–(16) above have been modified by Walsh and Moerner [30] to account for the geometry employed in their study. Their results were used to analyze the data obtained using P2ANS in this work.

An 8 μm sample of 50/50 P2ANS/MMA was metallized and poled at 100 V/ μm for 5 minutes at 140°C. The sample was placed in the two beam coupling set up of Figure 42, an external field of 50 V/ μm was applied, and a grating was written in the material for about two minutes at 637 nm. A close up schematic view of the geometry of the write beams with respect to the test sample is shown in Figure 43. Initial attempts to read gratings written parallel to the long dimension of the sample were not successful. This would have the advantage that the space charge field, E_{sc} , would be in the poling direction thereby maximizing the index modulation. With the chosen geometry shown in Figure 43, the effective field was given by:

$$E_{eff} = E_{sc} \cos\theta = E_{sc} \cos 67.4^\circ = 0.385 E_{sc} \quad (17)$$

The writing intensity was 56 mW/cm² in each beam. The piezoelectric driver was translated in the direction of the grating vector at a velocity of 3.1 $\mu\text{m}/\text{sec}$. The detector outputs are shown in Figure 44. The energy interchange is readily seen from the fact that the beam intensities are 180° out of phase as energy is transferred back and forth between them. It is also critical to observe that the initial data points are located at or near the extrema of the sinusoids. This indicates that the index grating is shifted by approximately $\pi/2$ with respect to the absorption grating. If the gratings were in phase, the initial data points would begin midway between the maximum and minimum. Analysis of the sum and difference curves of the two beams yielded a relative phase difference between the index grating and the absorption grating in the sample of 0.44π and an amplitude of the index grating that was 16 times greater than that of the absorption grating. The grating spacing based on the writing geometry was calculated to be 1.83 μm which compared quite well with the measured value of 1.76 μm .

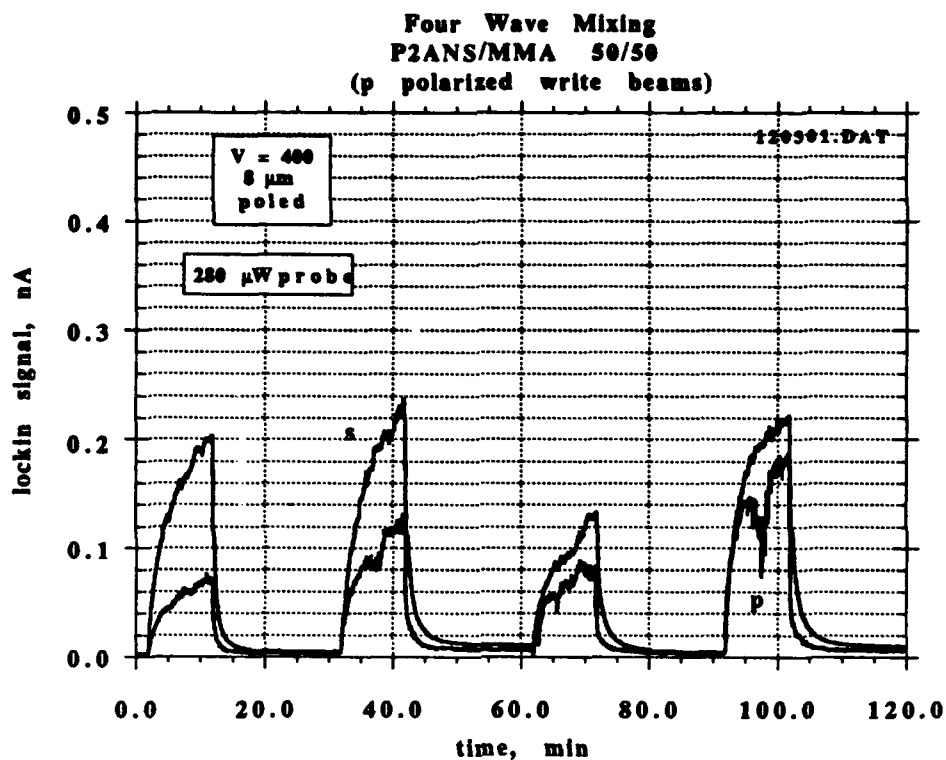


Figure 41. Four wave mixing using *p* writing beams and *s* & *p* reading beams.

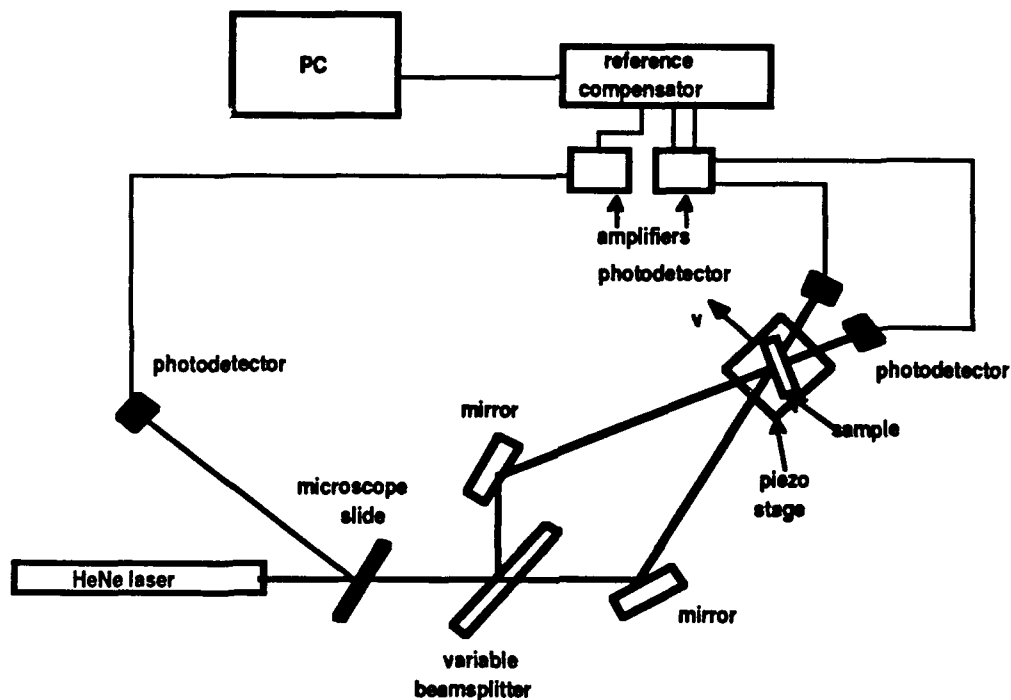


Figure 42. Experimental setup for two beam coupling.

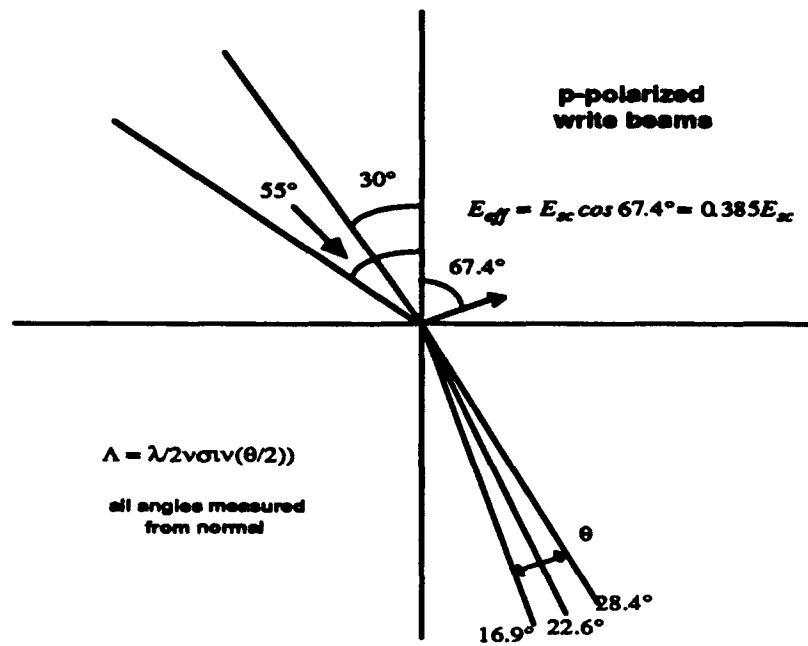


Figure 43. Beam geometry employed in the two beam coupling measurement.

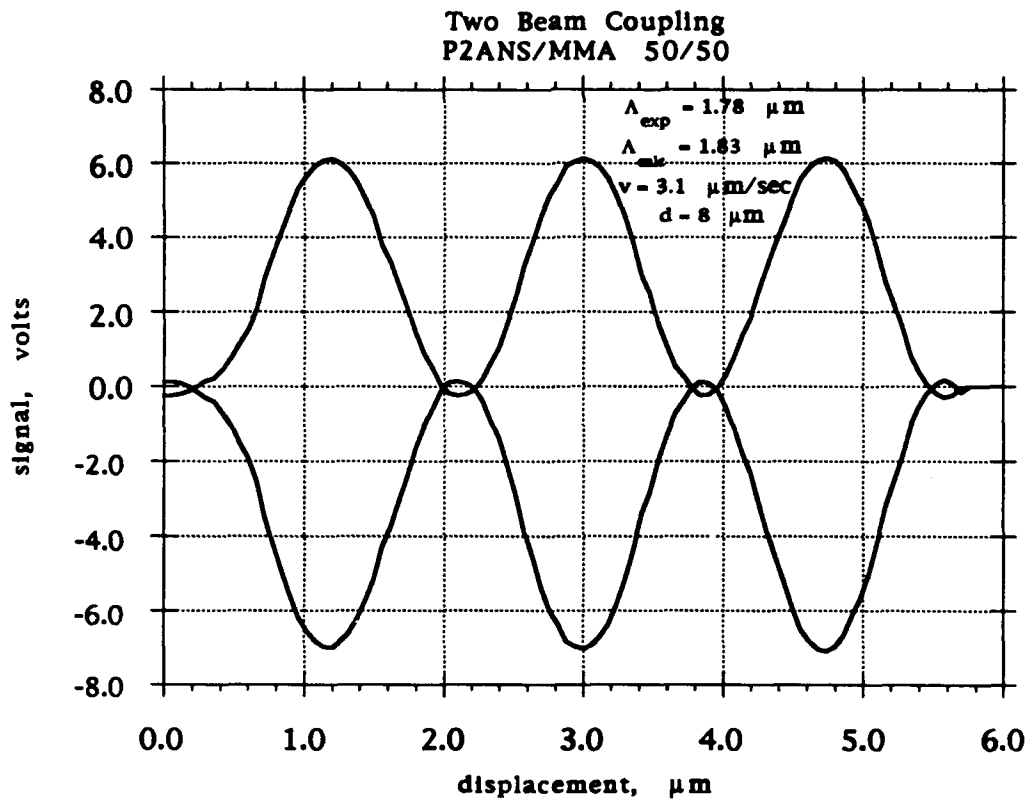


Figure 44. Two beam coupling result showing energy transfer between the beams.

5. Summary

Photoconductive behavior of our materials was characterized by photoinduced discharge and by steady state measurement. The former method was predominantly employed because of its speed and simplicity. It provided a semi-quantitative estimate of both the dark current and the photo current as well as an estimate of the quantum efficiency.

Photorefractive behavior has been demonstrated in an electrooptic aminonitrostilbene methacrylate based copolymer without the addition of photoconductive compounds. Using four wave mixing, photorefractive gratings were written in P2ANS/MMA using *s*-polarized and *p*-polarized writing beams and probed using orthogonally polarized probe beams. When the probe beam is orthogonally polarized with respect to the write beams, well behaved, field dependent, stable responses which we are ascribing to the photorefractive effect were observed. Diffraction efficiencies of 10^{-4} – 10^{-5} were obtained in 8 μm thick films under an applied field of 50 V/ μm with response times of 1.5 – 2 minutes. Increasing the sample thickness to 100 μm could result in a diffraction efficiency of 1% - 3%. Increasing the intensity to 1 W/ cm^2 (a typical value) could reduce the time constant by a factor of 20. Two beam coupling experiments confirmed the photorefractive nature of the gratings.

Photorefractive behavior was also observed in the tricyanovinyl-carbazole substituted siloxane polymer (TCV-CBZ/PSX) but was one order of magnitude lower than that observed in P2ANS/MMA. TCV-CBZ/PSX had much higher photoconductivity and a lower dark current than P2ANS but unfortunately also had a lower electrooptic coefficient. The trade off between electrooptic activity and photoconductivity to yield an optimized photorefractive material must still be determined.

6. References

- [1] A. Buckley, G. Calundann and A. J. East; Multifunctional Materials: SPIE Proc., Vol 878, 1988, pp 94-101.
- [2] H. Goldberg, A. J. East, R. Johnson and I. Kalnin; Multifunctional Macromolecules, AFOSR Final Report, Contract F49620-87-C-0109, May 1991
- [3] M. J. Sansone, K. Blatter, G. Breckenridge, A. J. East, H. Goldberg, M. Kwiatek, C.F.Shu; "Multifunctional Macromolecules: Photorefractive Polymers, "Presentation made to the 4th Annual OGAMMs Review, Ilkley, Yorkshire, England, on 8-21-91.
- [4] C. I. Simionescu, V. Percec; Polym. Bull., Vol 2, 1980, p 427
- [5] C. I. Simionescu and M. Grigoras; Prog. Polym. Sci., Vol 16, 1991, pp 907-976
- [6] O. Y. Webster, W. R. Hertler, D. Y. Sogah, W. B. Farnham and T. V. RajanBabu; J. Macromol. Sci-Chem., A21(8&9), 1984, pp 943-60
- [7] B. R. Hsieh and M. H. Litt; Macromolecules, Vol 19(3), 1986, pp 516-20
- [8] V. Percec; Polym. Bull., Vol 5, 1981 pp 651-7
- [9] H. Finkelmann, G. Rehage; Adv. Polym. Sci., 60/61, 1984, p 99
- [10] P.G. Pape; Dow Chemical Corporation (private communication)
- [11] P. Strohmriegl, Makromol. Chem., Rapid Commun. 7, 1986, pp 771-5
- [12] J. Chatt, L. M. Vallarino, L. M. Venanzi; J. Chem. Soc., 1957, p 2496
- [13] "Vogel's Textbook of Practical Organic Chemistry" 5th Edition, Publ: Longman Scientific and Technical, 1989, pp 1161-2
- [14] P. Strohmriegl; Mol. Cryst. Liq. Cryst., Vol 183, 1990, pp 261-7
- [15] H. Nishi, H. Kohno and T. Kano; Bull. Soc. Chem. Japan, Vol 54, 1981, pp 1897-8
- [16] P. J. Melz; J. Chem. Phys., Vol 72, 1972, pp 1694-99
- [17] M.A.Mortazavi (HCRD Summit); unpublished work.
- [18] W. W. Limburg (Xerox Corporation); U.S.Patent 3,978,029; published 8-31-76
- [19] K. Tamura, A. Padias, H.K.Hall and N. Peyghambarian; CLEO meeting, 1992
- [20] B. C. McKusick, R. E. Heckert, T. C. Cairns, D. D. Coffman and H. F. Mower; J. Amer. Chem. Soc., 1958, Vol 80, pp 2806-15
- [21] Org Syntheses Coll. Vol IV, pp 331-3
- [22] C. R. Walton, B. B. Marr and A. J. East; U.S.Patent 5,171,803; published 12-12-92
- [23] R. A. Hann; J. Chem. Soc. Perkin I, 1974, pp 1379-80
- [24] T. Kurihara, H. Kanbara, H. Kobayashi, K. Kubodera, S. Matsumoto and T. Kaino; Optics Commun., Vol 84(3,4), 1991, pp 149-154
- [25] V. Percec: see ref [8]
- [26] V. L. Tweedie and J. C. Allabashi; J. Org. Chem., Vol 26, 1961, pp 3676-81

- [27] D. Drew and J. R. Doyle: *Inorganic Syntheses*. Vol XIII, 1972, pp 47-55
- [28] H. Kogelnik, *Bell Syst. Tech. J.*, 48 (9), p. 2909-2947 (1969)
- [29] K. Sutter and P. Günter, *J.Opt.Soc.Am.*, 7 (12), p2274-2278 (1990)
- [30] C. A. Walsh and W. E. Moerner, *J. Opt. Soc. Am. B*, 9 (9), p1642-1647 (1992)

7. Subcontractor Final Report (University of Leeds)

Multifunctional Macromolecules

"Poling, Drawing, and Orientation in Side Chain Polymers"

Final Subcontract Report

(1991-1993)

Prepared by

P. L. Carr, G. R. Davies, V. Rogers, and I. M. Ward

IRC in Polymer Science and Technology

University of Leeds, Leeds, LS2 9JT

United Kingdom

INTRODUCTION

In the period 1991-1992, the fourth year of the project on multifunctional macromolecules, the principal aim of the Leeds research was directed at further improvement in the orientation of the NLO mesogens in a methacrylate polymer with electroactive side chains in order to optimise the electroactive properties for device applications in optical signal processing. The optimum mesogen concentration in the copolymers investigated was shown in the previous period to be approximately 30% and at this concentration the poled films were very brittle. Therefore, we sought to improve the mechanical properties of the poled films by using drawing techniques developed for brittle samples. Poling experiments involved optimising corona and contact poling and varying cooling rates to improve the long term stability of the poled orientation. Corona poling either concurrent with or consecutive to mechanical drawing of the solution cast polymer films was also investigated to see if this gave improved dipole orientation as well as a reduced tendency to brittle behaviour.

Pyroelectric coefficient measurements were used as before to provide a rapid assessment of poling and the activity of the poled films. The independent method of obtaining dipole orientation functions from IR spectroscopy was investigated further to study the effect on extinction coefficients of the internal field produced by the oriented dipoles themselves. This was modelled by applying a large external field from a corona discharge to unpoled 10% MO6ONS copolymer films in the IR spectrometer at room temperature.

In the period 1992-1993 the objectives of the Multifunctional Materials project were extended to investigate methods of producing highly poled thick films of P2ANS for photo refractive devices with potential applications for beam steering and image enhancement. Initial studies were undertaken on solvent cast samples to compare this material with the MO6ONS material. The pyroelectric coefficients were obtained after poling, the α and β relaxations were obtained from TSC data and the stability of the poled orientation was investigated as before. Thicker samples were then hot pressed and various methods were tried to orient these samples and improve their toughness. Corona poling hot pressed samples highlighted problems with shrinkage, surface roughness and micro voids and some work was directed to improve the quality of these thick films, including a short investigation of blends with PMMA.

Having demonstrated the effect of the local field on the extinction coefficient a method was developed for evaporating interdigitated electrodes on to thin MO6ONS polymer films so that more accurately known fields could be applied to films in the IR spectrometer. Preliminary results are described and publications are listed later in this report.

Acknowledgement

This research was sponsored by SDI/IST and managed by AFSOR

Technical Achievements 1991-1992

1. We have investigated the pre-drawing of 10% MO6ONS films as an aid to obtaining better mesogen orientation during poling. This was not found to have a significant effect.
2. The drawn (unpoled) films produced above allowed comparison of IR dichroism measurements using both an aromatic ring band and the NO₂ symmetric stretch band. Similar mesogen orientation functions were deduced for both bands, improving our confidence in the use of the NO₂ band.
3. Equipment has been designed and constructed for the simultaneous drawing and corona poling of the 10% MO6ONS films. An apparent improvement in poling efficiency is primarily due to the reduction in film thickness during drawing which increases the corona field.
4. Mechanical alignment of brittle films has been achieved by a novel compression technique whereby the brittle material is sandwiched between two deformable plates which are allowed to extend in one direction only when compression is applied perpendicular to the film. When applied to a 70% MO6ONS copolymer film a highly birefringent material was produced with a birefringence Δn up to 0.3, showing that the mesogens are aligned in the direction of maximum extension. The increased orientation improves the optical clarity of the films and renders the material less brittle. Low deformation ratio samples are negatively birefringent implying a perpendicular alignment of the mesogens to the partially oriented main chains.
5. We have substantially extended our IR studies of mesogen alignment to investigate the effects of internal fields on the molecular extinction coefficients in poled samples. Equipment has been designed and constructed which allows the application of corona fields to films in the IR spectrometer at room temperature. We have shown that the absorbance is reduced by the application of an external field. The effect is anisotropic, however, with the absorbance for the IR field perpendicular to the corona field hardly changing whereas the absorbance for the parallel case is greatly reduced.
6. The knowledge gained above explains the problem found last year where normal incidence and tilted film techniques gave different results for the orientation of mesogens in poled films. The normal incidence method, using IR fields perpendicular to the local field is hardly affected by the local field dependence of the extinction coefficient. The tilted film method, which uses data from the absorbance with a component of the IR field parallel to the internal local field is greatly affected by the change in extinction coefficient with the increasing local field in poled samples. Using a Langevin model for the alignment of mesogens in the poling field we conclude that the maximum value obtained for $\langle \cos \theta \rangle$ is 0.5 and for $\langle \cos^3 \theta \rangle$ is 0.3. (NLO coefficients are proportional to $\langle \cos^3 \theta \rangle$).

DRAWING, POLING AND MEASURING ORIENTATION IN SIDE CHAIN POLYMERS

REPORT TO HOECHST-CELANESE JULY 1992

The effect of Local Fields on the Extinction Coefficient

As shown in figure 1, measurements of mesogen orientation using unpolarised normal incidence IR and polarised tilted film IR assuming no local field effect show a significant difference in the deduced values of $\langle P_2(\cos\theta) \rangle$. If the tilted film data are processed to yield an equivalent 'isotropic' coefficient then this appears to decrease with poling field indicating that the molecular properties are changing. Basically, although no external field is applied, the local field from the oriented mesogens changes the complex refractive index as expected for a second order NLO material.

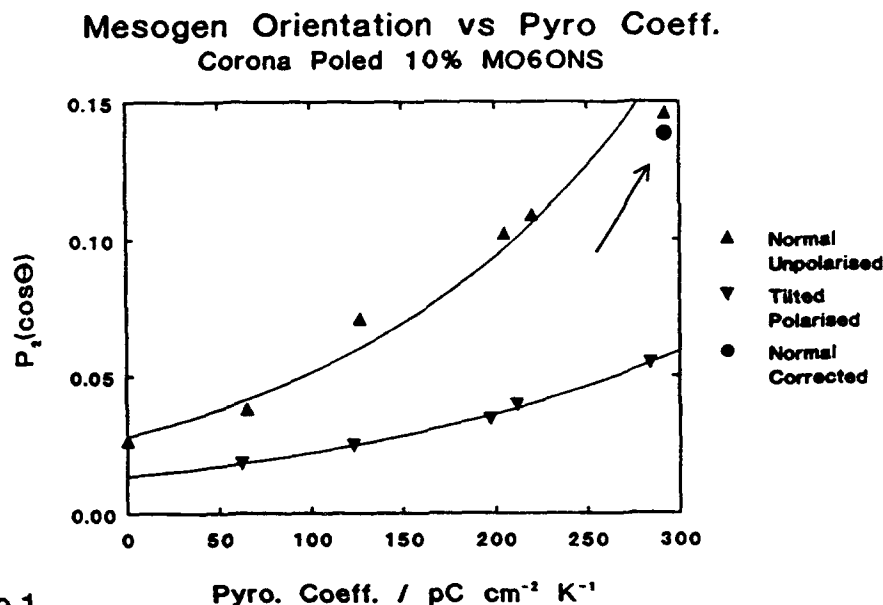


Figure 1.

Experiments have been carried out to investigate the effect of the local field by applying a large external field to unpoled 10%MO6ONS copolymer films in the IR spectrometer at room temperature. At this temperature mesogen re-orientation will not occur and changes in absorbance should reflect the field dependence of the extinction coefficients without the additional complication of molecular re-orientation. In the initial experiments the absorption at 1345 cm^{-1} has been analysed (NO_2 symmetric stretch). Corona fields have been applied to free films between two needles, and IR measurements have been made both at normal incidence and with the film tilted to give an angle of incidence of 60° . (This gives an angle of refraction in the film of 34°). Since free films were used, reflectivity was high and the incident radiation was therefore unpolarised to maximise the incident intensity as the effect of the field was otherwise too small to distinguish from instrument noise.

The effective electric field across the film was derived from a separate calibration experiment in which the same equipment was used to pole the films at T_g . From the resulting pyroelectric coefficients and previous experience the effective poling field could then be deduced for various needle voltages.

The results are shown in figure 2. These show that the absorbance is reduced in both normal incidence and tilted film configurations but that the effect is much larger in the tilted film case when the IR field has a component perpendicular to the film, i.e. parallel to the corona field. The unpolarised tilted film data is a complicated average of the in-plane and perpendicular absorption coefficients. We can readily deduce, however, that the change in the perpendicular absorption coefficient is even greater.

This implies that the normal incidence method of measuring $\langle P_2(\cos\theta) \rangle$ is relatively little affected by local field effects since this uses only the in-plane absorption coefficients. The tilted film method uses the perpendicular absorption coefficient which is much more affected by the local field. The highest value of $\langle P_2(\cos\theta) \rangle$ measured in normal incidence unpolarised IR and shown in figure 1, was corrected from the data of figure 2, at the estimated value of the local field and shown by the solid circle. The correction can be seen to be small showing that the upper curve in figure 1 is nearly correct.

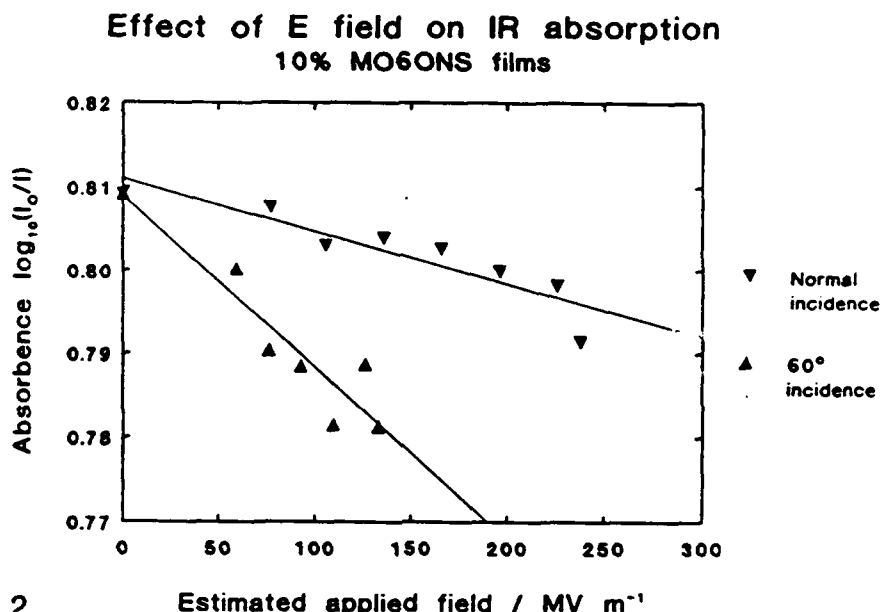


Figure 2.

The corresponding values of $\langle P_1(\cos\theta) \rangle$ will be slightly lower than 0.5 as previously reported. The largest NLO response in highly oriented systems is proportional to $\langle \cos^3\theta \rangle$ and we estimate this to be about 0.3 at most. It is clear that there is much to be gained from further improvements in poling.

Poling Pre-Drawn Samples.

A 10% MO6ONS copolymer film was drawn to a draw ratio of 2.5 and held to length while poling at various poling fields. The pyroelectric coefficient measurements showed that the stilbene mesogen was not more readily oriented in the drawn sample.

Concurrent Poling and Drawing.

10% MO6ONS copolymer films have been corona poled while being drawn to draw ratios up to 3 over a heated plate. To facilitate drawing with the poling field on, a thin film of oil was applied to the plate. Since this made the poling field difficult to estimate, a constant needle voltage of 6 kV was used throughout and the resulting pyroelectric coefficient was plotted against the reciprocal of the film thickness. Three

spacer and six spacer copolymers were compared with results from undrawn films poled in the same apparatus.

The solid line in figure 3 is fitted to the undrawn data. The results for simultaneously drawn and poled films, also shown in this graph, suggest that there is little or no advantage in drawing the films during the poling process.

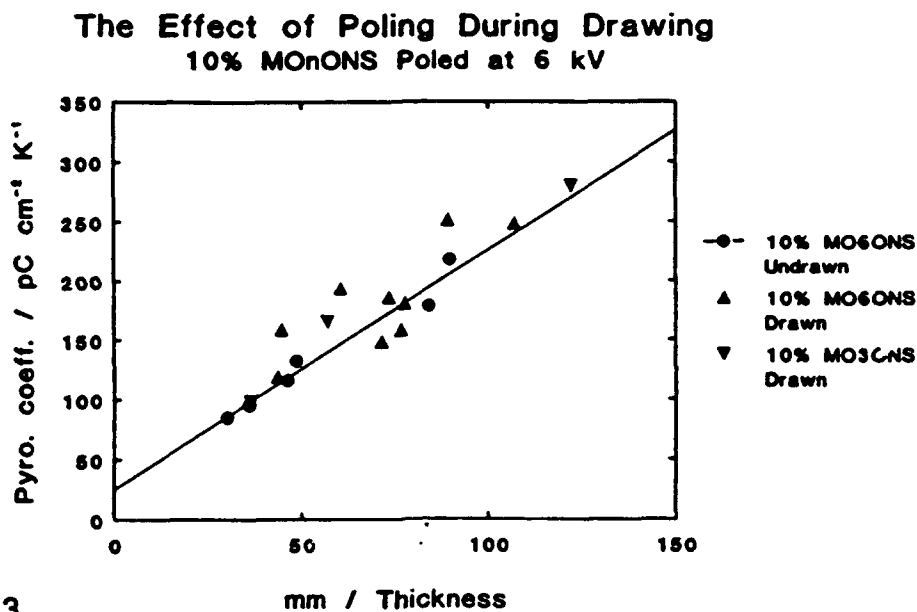


Figure 3.

Birefringence and Mesogen Orientation Produced by Drawing

The birefringence of the 10% copolymer film samples drawn to various draw ratios is shown as a function of draw ratio in figure 4. The birefringence of the drawn copolymer was at least an order of magnitude larger than that of the drawn PMMA and also of opposite sign showing that the side chain mesogens were being progressively aligned in the draw direction by the orientation of the main chain network.

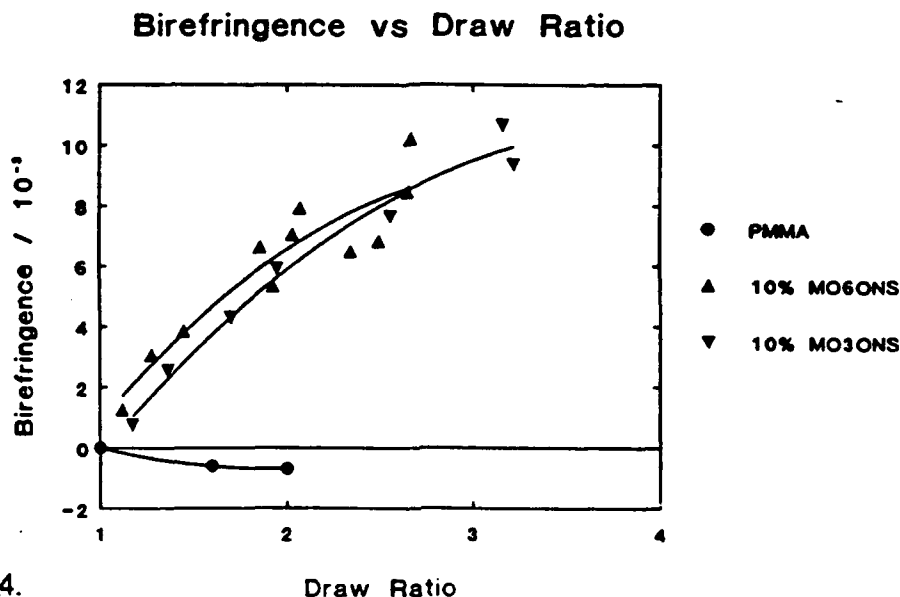


Figure 4.

IR spectroscopy measurements were made on the drawn film samples and values of $\langle P_2(\cos\theta) \rangle$ were derived and compared with the birefringence. The

symmetric stretch of the NO_2 group at 1345 cm^{-1} was used and results calculated from the ring breathing vibration at 1595 cm^{-1} have also been included. There was a good correlation between $\langle P_2(\cos\theta) \rangle$ calculated from both these vibrations and the birefringence measurements, as shown in figure 5. This suggests that the symmetric stretch at 1345 cm^{-1} does give valid results although the anti-symmetric stretch at 1515 cm^{-1} again gave an anomalous result.

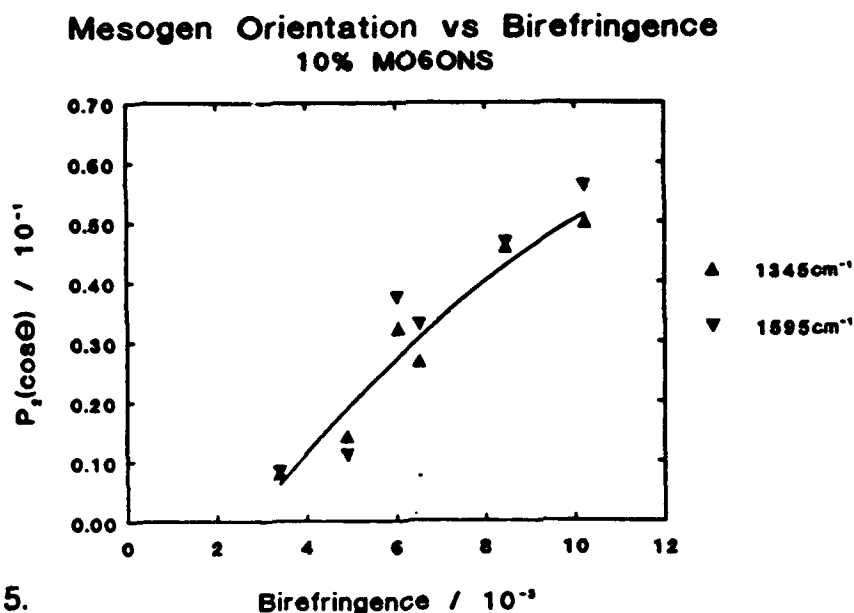


Figure 5.

Additional Experiments to Produce Mesogen Alignment

Drawing and poling experiments have, of necessity, been confined to the 10% copolymer, since this is the highest concentration which can be drawn as a free film. The more brittle copolymers of MO6ONS can be mechanically oriented, however, if they are held at a high hydrostatic pressure and deformed near to T_g . For example, quite high molecular alignment can be achieved in these brittle films by hot pressing between suitable deformable plates of PMMA or PVC.

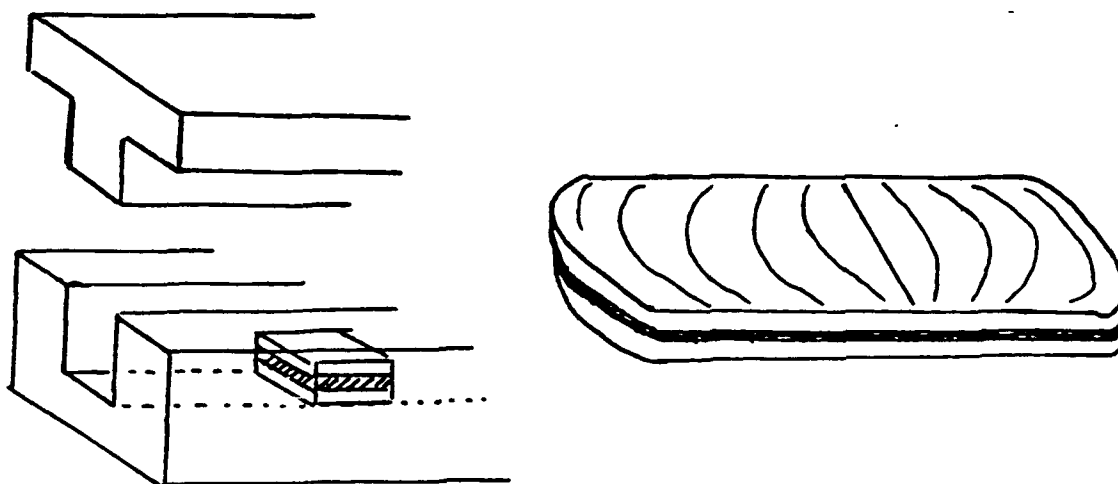


Figure 6. Mould with undrawn sample.

Drawn sample.

Samples are pressed in a special mould so that the width remains fixed and elongation can only take place in the length direction. The mold and typical flow profiles in the sample are shown in the diagram above.

This method produces predominantly uniaxial orientation with a small biaxial component which is difficult to quantify. However quite high orientations in the side chain mesogens have been achieved and in plane birefringence > 0.3 have been measured.

Although subject to fibrillation, this new structure in the material is optically transparent and can be more easily handled. It may be possible to perform poling and orientation experiments on such samples

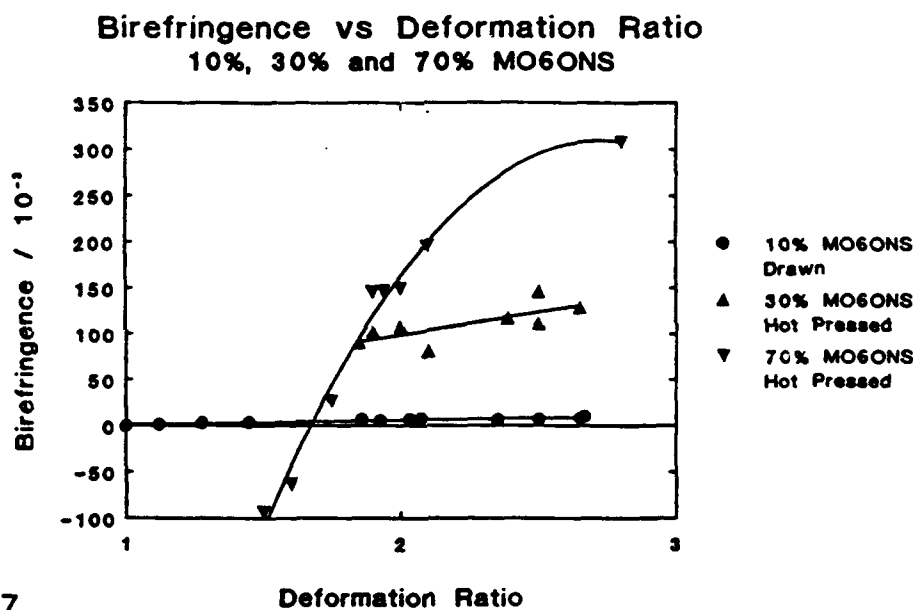


Figure 7.

Figure 7. shows some in plane birefringence measurements made on films oriented by hot pressing. The negative values at low draw ratios have to be confirmed but a high side chain orientation is clearly achieved in the 70% MO6ONS copolymer film. Cooling the mould before removing the pressure takes at least an hour and therefore some annealing must occur. Some low draw ratio samples may therefore relax to give perpendicular orientation of the mesogens in a similar manner to the experiments reported by Windle. The mesogen orientation in the draw direction is reduced but not destroyed by heating to T_g and the film shrinkage is less than that which occurs in drawn PMMA.

POLING AND ORIENTATION IN SIDE CHAIN POLYMERS

Technical Achievements 1992-93

1. We have solvent cast films of a 50/50 copolymer of P2ANS on to glass substrates, poled them over a range of poling fields and compared the resulting pyroelectric activity with MO6ONS. The P2ANS copolymer has a pyroelectric coefficient 30% greater than the 50/50 MO6ONS copolymer when poled at the same poling field.
2. Poled orientation in the P2ANS films was significantly more stable than in MO6ONS films. After one week the pyroelectric coefficient dropped approximately 5% compared with a drop of 20% for the MO6ONS films. When the cooling rate during poling was reduced from 10°C/min. to 1°C/min., to densify the material, the P2ANS films showed no appreciable decay after two months.
3. The P2ANS copolymer gave a TSC relaxation spectrum in which no discernable β relaxation was present near room temperature. This is similar to the 100% MO6ONS material.
4. Samples up to 0.5mm thick have been pressed from the powder material at 135°C and in low field poling experiments show the same activity as the thin films cast from solution. Corona poling roughened the film surface and allows uneven film shrinkage. This was not improved by clamping the thick samples to the earth plate. We have tried poling using one plate of a press as the poling electrode but high fields have not been obtained due to early breakdown.
5. The radial orientation obtained from pressing thick samples gives a small qualitative reduction in the brittle nature of the P2ANS films. However, this cannot be retained during corona poling. Blends with a small percentage of PMMA reduced brittleness but problems were encountered with phase separation and reduced clarity. Sandwich composites of P2ANS between thin films of PMMA also reduced brittleness but again suffered from reduced clarity. The most promising approach seems to be a pressing and slow cooling step followed by a second pressing and poling stage.
6. A method has been developed for evaporating interdigitated electrodes with 150 μm spacing on to 7 μm free films of the 10% MO6ONS copolymer and insulating the array with a second thin MO6ONS film. In this way the change in absorption coefficient parallel and perpendicular to an externally applied electric field has been determined using a Bomem FTIR spectrometer. The effect of the internal field on the extinction coefficient has been confirmed and the simple geometry allows quantitative measurements to be made. IR methods of measuring dipole orientation in side chain polymers can therefore be made with more confidence.
7. The following paper has been published:
P.L.Carr, G.R.Davies and I.M.Ward, Polymer, 1993, Vol 34, 1, p5. "The alignment of polar mesogens in electroactive polymers".
A paper " The measurement of mesogen orientation in side chain polymers using IR spectroscopy" by the same authors is ready for submission to Polymer.

POLING AND ORIENTATION IN SIDE CHAIN POLYMERS

REPORT TO HOECHST-CELANESE JUNE 1993

IR Measurement of Dipole Orientation and the Effect of Local Fields on the Extinction Coefficient

Evidence for this effect, which introduces an error in the IR measurement of orientation, has been described previously.

First, direct measurement of poled dipole orientation obtained from tilted film measurements gave a lower value of the absorption coefficient than measurements at normal incidence which effectively measure the dipoles remaining in the plane of the film and which lie normal to the internal field. Second, if the tilted film data are processed to yield an equivalent 'isotropic' coefficient, $\phi_0 = \phi_z + 2\phi_x$, then this appears to decrease with poling field indicating that the molecular properties are changing. Finally, the result of applying a high field from a corona discharge to an unpoled film in the spectrometer showed that the absorbance is reduced in both the normal incidence and tilted film configurations but that the effect is much larger in the tilted film case when the IR field has a component perpendicular to the film, i.e. parallel to the corona field. The unpolarised tilted film data is a complicated average of the in-plane and perpendicular absorption coefficients. However, the change in the perpendicular absorption coefficient is likely to be greater than the effect measured so far.

We have now developed a technique for evaporating interdigitated electrodes on to thin free films of the 10 % MO6ONS copolymer. Initially, photo resist techniques were tried but clean edges on the electrodes could not be obtained on a microscopic scale. Finally, wire grids were hand wound on a support using screw thread guides and wire thickness to give a suitable electrode size and spacing, approximately 150 μm . The interdigitating electrode array was then obtained on a thin MO6ONS film in a two stage evaporation. The array had then to be insulated. The best method devised so far has been to float a second thin polymer film over the first using a thin film of Nujol to exclude the air.

The electroded films were mounted in a Bomem FTIR spectrometer and measurements were made with the polarised IR beam parallel and perpendicular to the applied external electric field as shown in Fig.1. The results are shown in Fig.2.

The samples suffered from electrical breakdown at fields above 16v/ μm and improved methods of insulating the surface electrodes are being sought. However, using 100 scans on the FTIR instrument to give accurate values of peak height, and adjusting for base line changes, a significant effect was obtained even at low fields. Curve fitting may further improve accuracy. The reduction in absorption coefficient with the IR polarisation direction parallel to the direction of the applied field was greater than that obtained using the corona discharge to apply an external field to the tilted films. At these low fields a reduction in the perpendicular direction could not be detected. Measurements at higher fields will be attempted and curve fitting used to obtain quantitative data on this effect. IR methods of measuring dipole orientation in poled side chain polymers can then be made with confidence.

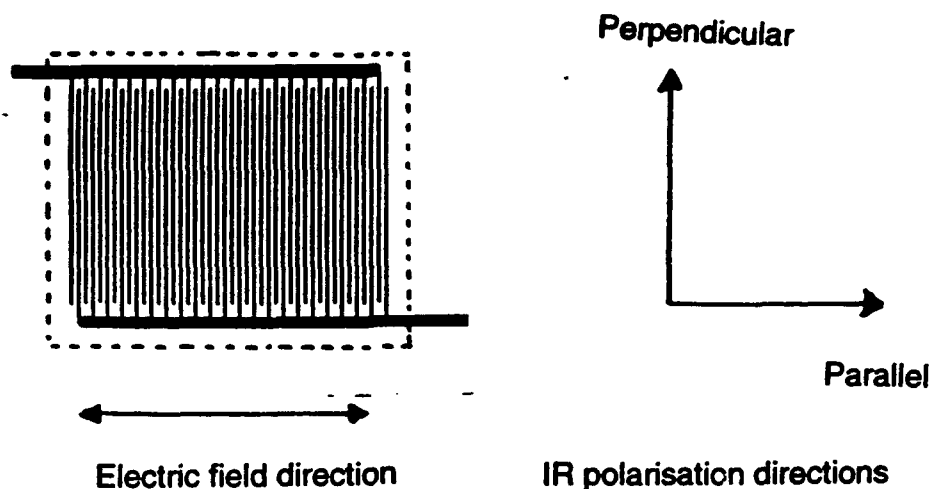


Fig. 1.

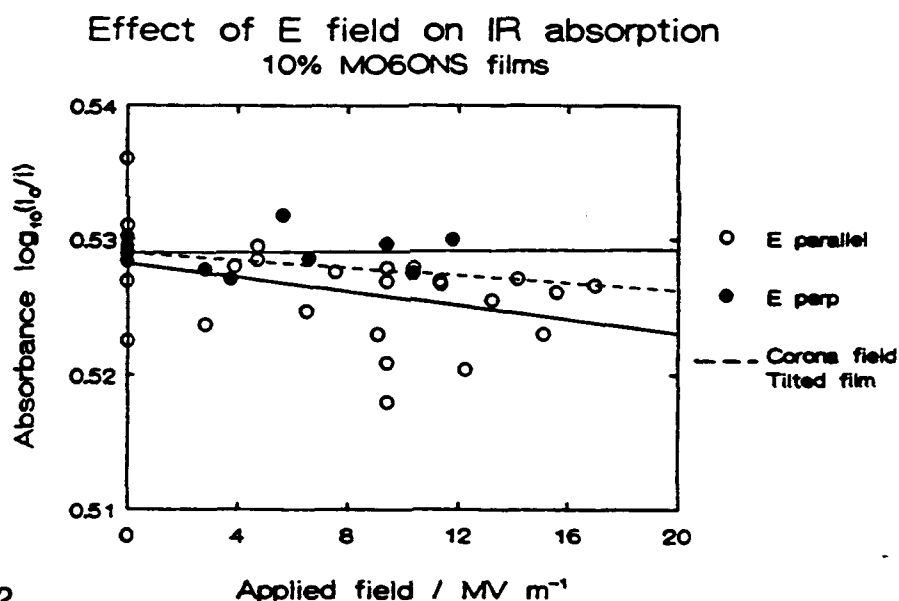


Fig.2.

Poling Experiments on Solvent cast and Hot Pressed Samples of P2ANS

Solvent cast films of the 50/50 copolymer of P2ANS with PMMA have been poled on glass substrates over a range of poling fields up to $40\text{v}/\mu\text{m}$. Fig.3 shows that the P2ANS copolymer has a pyroelectric coefficient 30% greater than the 50/50 MO6ONS copolymer when poled at the same poling field.

It has also been found that the P2ANS copolymer is significantly more stable than the MO6ONS homopolymer. This is shown in Fig.4. Also shown in Fig.4 are the results for P2ANS films cooled at $1^\circ\text{C}/\text{min}$. instead of the usual $10^\circ\text{C}/\text{min}$. In this case no appreciable decay occurred in two months. This is thought to be due to improved densification of the material.

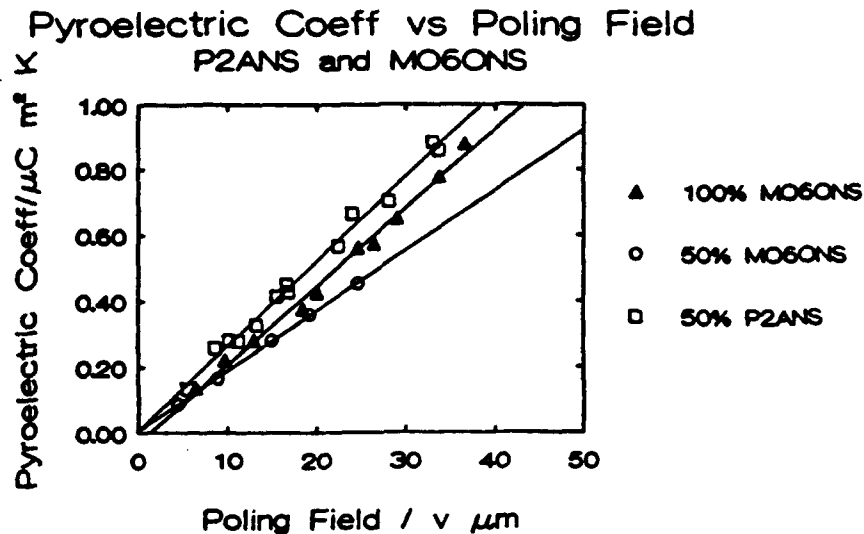


Fig.3.

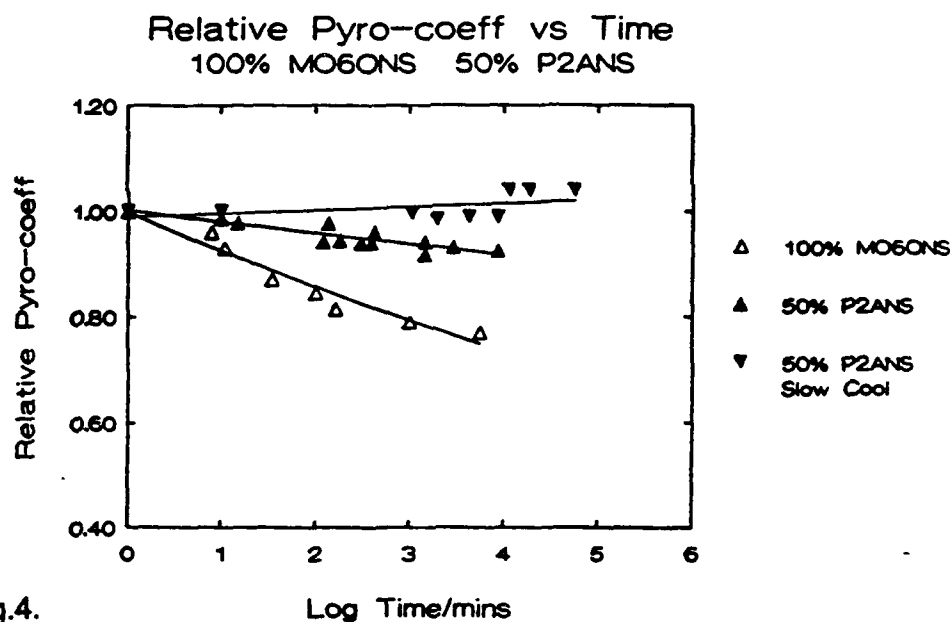


Fig.4.

Fig.5. shows an IR spectrum for P2ANS. A solvent cast thin film can be floated off a substrate and mounted for IR measurements but is too brittle to pole and handle further. In the IR spectrum the symmetric NO_2 stretch absorption peak has shifted slightly from 1342.5cm^{-1} in MO6ONS to 1335cm^{-1} in this case. The 1515cm^{-1} anti-symmetric stretch peak is also more clearly a double peak.

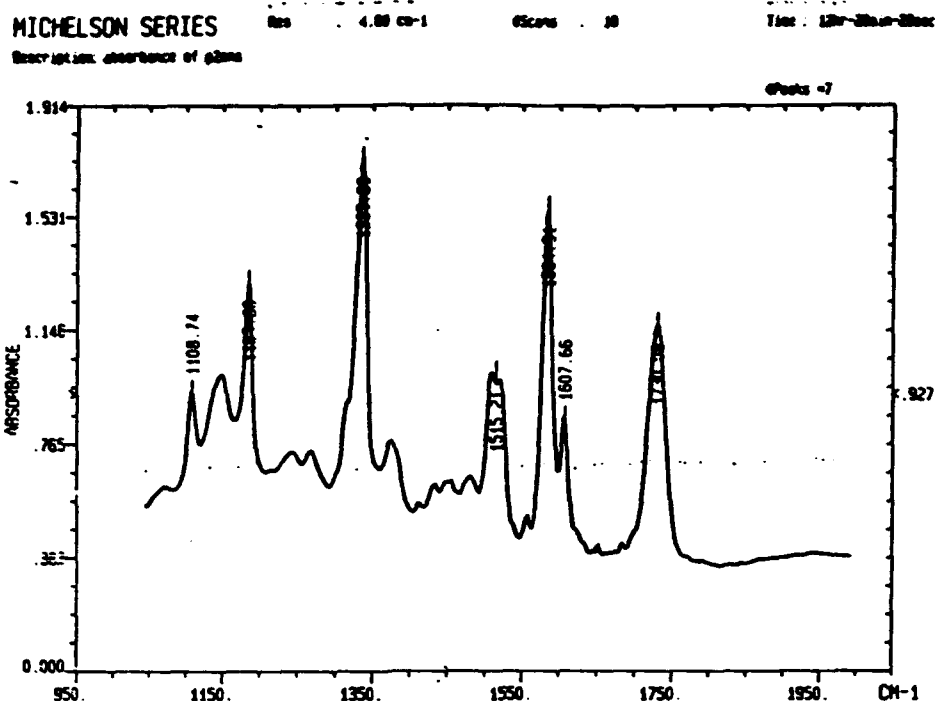


Fig.5.

The TSC spectrum shown in Fig.6 has little evidence of any β relaxation peak near room temperature which also suggests that interactions between the side chains in the two spacer P2ANS material impede side chain mobility.

Thermally Stimulated Current Data P2ANS

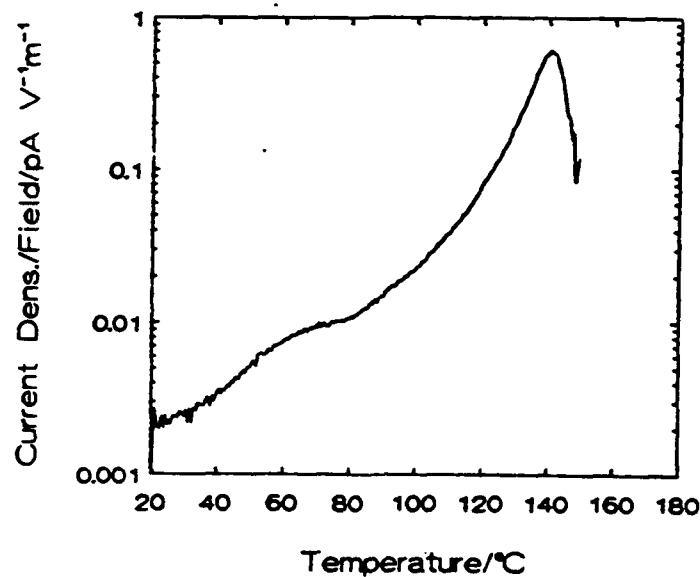


Fig. 6.

Thick film samples up to 0.5mm have been pressed from the powder material at 135°C and in low field poling experiments show the same pyroelectric activity as the thin films cast from solution. Corona poling these thicker samples tended to result in rougher surfaces than before and differential stresses in film pressing resulted in uneven shrinkage after poling. This was not improved by clamping the thick samples to the earth plate during the corona poling step. We have also made a small press which uses one plate of the press to contact pole during the pressing stage but high fields have not yet been obtained due to faults in the material. A multi-stage press/anneal/press and pole process may be more successful.

The radial orientation obtained from pressing thick samples gives a small qualitative reduction in the brittle nature of the P2ANS films which is not retained after corona poling. Blends with a small percentage of PMMA reduced brittleness substantially but problems were encountered with phase separation and reduced clarity. Sandwich composites of P2ANS between thin films of PMMA also made the films quite robust but we have not yet obtained and poled clear films.

GPC results at Leeds confirm that the P2ANS copolymer has much lower molecular weight than the MO6ONS copolymers. Therefore orienting the material would not be expected to improve the mechanical properties. However, given a higher molecular weight, the pressing and poling process may give satisfactory results.

8. Subcontractor Final Report (University of Bayreuth)

Multifunctional Macromolecules

"Nonlinear Optical Properties of Side Chain Polymers"

**Final Subcontract Report
(1991-1993)**

Prepared by

R. Fischer, H. M. Graf, O. Zobel, and D. Haarer

**University of Bayreuth
Physics Institute
P.O. Box 1101251
D-95440 Bayreuth
Germany**

R.Fischer, H.M.Graf, O. Zobel, D. Haarer
University of Bayreuth, Physics Institute ¹
P.O.Box 10 12 51, D-95440 Bayreuth
phone 49/921/55-3240

September 2, 1993

1 Introduction and review

Materials exhibiting the photorefractive effect were studied intensely in the past. Their most attractive feature in data processing and data storage is due to the capability of storing transient holograms. The research of leading groups has, in the past years, focussed on new polymeric materials consisting of both photoconductive units and molecular groups with electrooptic response. In this respect polymers have some important advantages over most inorganic systems.

Our first approach to these class of materials was to investigate the nonlinear optical properties independent of the photoconductive properties of various side-chain polymers.

In order to understand the macroscopic $\chi^{(2)}$ behavior we have to look at both the microscopic origin of the nonlinearities and the electric poling behavior.

For the special application of $\chi^{(2)}$ devices organic polymer films have to be poled in order to remove the inversion symmetry of the randomly oriented nonlinear chromophores of the pristine material³.

The anisotropy created this way affects both the linear and the nonlinear optical properties. The anisotropy of the absorption coefficient can be used as probe of the degree of orientation of the pertinent molecular polar groups. Since for most $\chi^{(2)}$ materials the lowest electronic singlet state is thought to be mainly responsible for the nonlinear response, the lowest-lying optical band in the UV is investigated.

We treated the poling process in the framework of a simple thermodynamic model which considers only the interaction of the dipoles with the external poling field.

A two-level model for the electronic states is applied as well as assumptions which arise from the linear shape of the studied NLO

¹ Research is sponsored by SDIO/IST and managed by e.g., DNA, AFOSR, ONR.

chromophores.

Both the poling field dependence and the wavelength dependence of higher order susceptibilities is taken as a proof of our model assumptions. Also different nonlinear coefficients (such as $\chi^{(2)}$ (SHG), $\chi^{(2)}$ (EO), $\chi^{(3)}$ (EO), and $\chi^{(3)}$ (THG)) are measured and compared to the theoretical equations.

The orientational order of the poled samples is described in terms of order parameters which are obtained from SHG and PAS measurements. Again these values are compared to the theoretical results.

From our studies we can conclude that our models and assumptions mentioned above are in a good qualitative agreement with the experimental data.

2 Materials

The materials are polymers containing the nonlinear optically active chromophores as covalently attached side-groups. The polymer backbone is PMMA and the dyes are ONS, ANS, and AZO.

3 Basic models and assumptions

First of all the local electric fields are assumed to be related to the macroscopic fields by local field factors of the well-known Lorenz-Lorentz or Onsager type.

In case of the quasi-one-dimensional chromophore under investigation the so-called β_{zzz} -approximation can be applied. That is only the zzz-component of the hyperpolarizabilities is assumed to be nonzero. The reason for this is that the transition dipole moments perpendicular to the molecular axes are small as compared to the transition dipole moment along this axis.

Both the linearity of the dye molecule and the geometry of the poling setup yield an orientational distribution function f of the chromophores which depends solely on the angle θ between the molecular axis and the poling field direction. Thus the distribution function $f(\theta)$ can be expanded in terms of so-called order parameters C_i with

$$C_i = \int d(\cos \theta) f(\cos \theta) \cos^i \theta \quad (1)$$

The first and second order susceptibility can thus be written as:

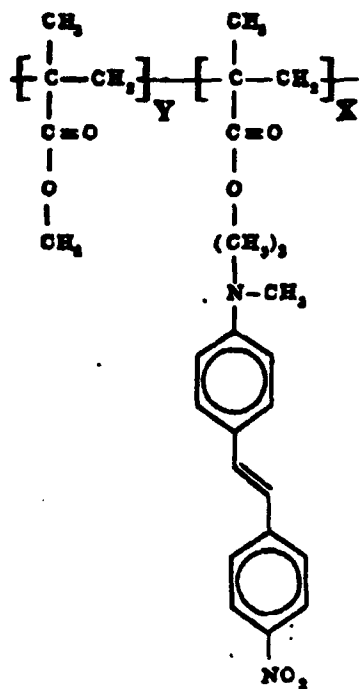


Figure 1: Molecular structure of the DANS-containing polymer

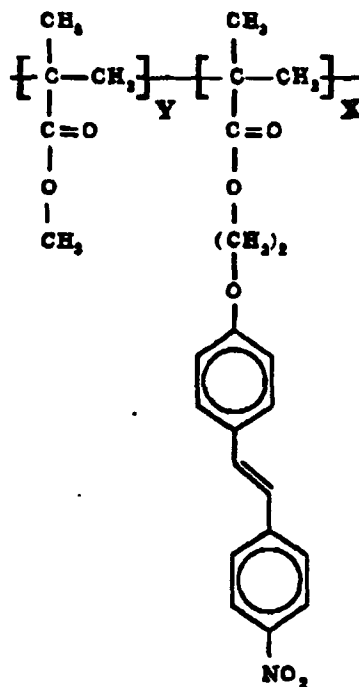


Figure 2: Molecular structure of the ONS-containing polymer

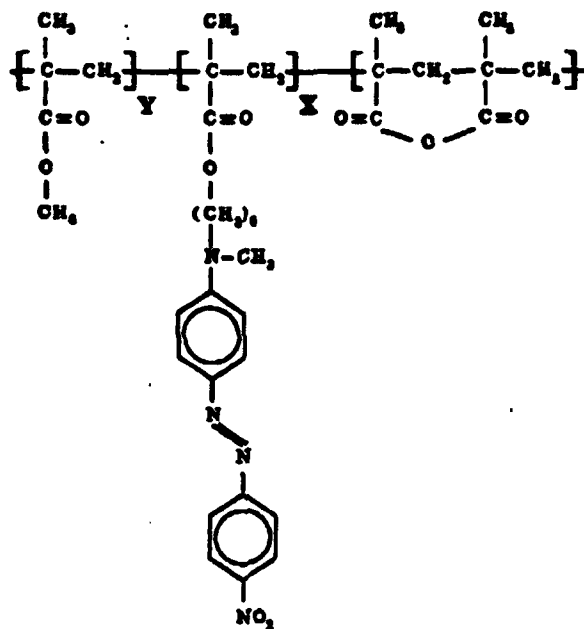


Figure 3: Molecular structure of the AZO polymer

$$\chi_{zzz}^{(2)} = N f^2 f^0 \langle \beta_{zzz} \rangle C_3 \quad (2)$$

$$\chi_{zz}^{(1)} = N f^0 \langle \alpha_{zz} \rangle C_2 \quad (3)$$

where N is the number density of the NLO chromophores, f stands for the local field factors and C_3 describes the orientational order obtained by the poling process. Here $\langle \beta \rangle$ denotes the hyperpolarizability corrected for the inhomogeneous line broadening.

The calculation of $\chi^{(2)}$ requires the knowledge of the order parameter C_3 which cannot be measured separately. Hence we have to apply a model for the orientational distribution. The simplest model takes only into account the interaction of the dipole moment of the chromophore with the external poling field: The statistics are governed by the factor $\exp[-\mu f^0 E_p / kT]$, where μ is the ground state dipole moment of the dye and f^0 is the local field factor for the poling field E_p .

For most ab-initio calculations of β only the two lowest-lying electronic states of the dye molecule are considered (two-level model). The resonance enhancement of the nonlinear coefficients at the wavelengths used in the experiments was calculated. This calculation takes the inhomogeneous absorption line into account.

Using the above-mentioned model assumptions yields the following dependencies :

- $\chi^{(2)}$ varies linearly with the poling field:

$$\chi_{sss}^{(2)} = N f^{2\omega} f^\omega f^\omega \langle \beta_{sss} \rangle \frac{\mu f^0 E_p}{kT} \quad (4)$$

- The order parameter A_2 which is related to C_2 by $A_2 = \frac{1}{2}(3C_2) - 1$ depends quadratically on the poling field:

$$A_2 = \frac{1}{15} \left(\frac{f^0 \mu E_p}{kT} \right)^2 \quad (5)$$

- The nonresonant value of the nonlinear coefficients d_{33} for the electro-optic effect is four times larger than the d_{33} coefficient for second harmonic generation.
- The order parameters C_3 and A_2 are related as

$$C_3 = \frac{1}{5} \sqrt{15 A_2} \quad (6)$$

4 Sample preparation

The various copolymers were dissolved in cyclohexanone and filtered with a $0.6\mu m$ filter. The polymer solutions were subsequently spun onto an indium-tin-oxide (ITO) coated glass substrate and dried for several hours in a vacuum oven at the glass transition temperature. The resulting films had a thickness of about $1\mu m$ and an optical density of about two to three in the investigated wavelength regime.

5 The poling procedure

The chromophore alignment is achieved by electric field poling. The samples are heated to their glass transition temperature. An electric field is applied perpendicular to the film surface and the samples are subsequently cooled down to room temperature with the poling field still on so that the chromophore alignment is frozen in.

Two poling techniques are employed: the corona-poling technique and poling by parallel electrodes.

- In the setup for corona-poling a high voltage of about 6kV is applied to two parallel wires with a mutual distance of 1.5cm to induce corona discharge. The distance between the poling wires and the sample is 1cm.
- In order to obtain a very homogeneous macroscopic electric poling field in the sample we have to use the poling technique with parallel electrodes. As top electrode a 30nm thick Al layer is used. This top electrode can be removed for optical measurements after poling.

6 Second-harmonic generation experiments

In order to determine second-order nonlinear coefficients, the transmitted second-harmonic intensity is recorded as a function of the angle of incidence of the fundamental beam on the sample ². The parameters which enter into the evaluation of the nonlinear coefficient are the sample thickness, the wavelength, and the refractive indices at both the fundamental and the second-harmonic wavelengths. The incident light intensity is eliminated by means of a reference measurement using a standard material with known nonlinear coefficients (e.g. a quartz crystal). Measuring the thickness and the refractive indices separately, one obtains the unknown nonlinear coefficient in arbitrary units by fitting the theoretical angular dependence to the experimental data. This fit has to be performed with both the sample and the standard material to obtain the absolute values for the sample.

The experimental setup used is shown in figure 6. The applied laser system consists of a 35 ps both actively and passively mode-locked Nd:YAG laser (Continuum) suitable for pumping a commercial Raman shifter (Quanta Ray RS-1, Spectra Physics), thus providing several wavelengths in the near infrared (fundamental: 1064 nm, shifted wavelength with pump wavelength 532 nm: 954 nm, 995 nm, 1579 nm with hydrogen and methane, respectively, as active gases). The output is split into two beams, one of which is focused onto the sample, and the other is guided onto a 'reference' sample (poled polymer film at fixed angle) to correct for pulse-to-pulse fluctuations. The pulse energy supplied by the Nd:YAG laser at 1064 nm after passing the optical components is about 1 mJ. Focussing the beam onto the sample by means of lens L3 leads to a light intensity on the sample surface of about

²J. Jerphagnon, S.K. Kurtz, J. Appl. Phys. 41, 1887 (1970)

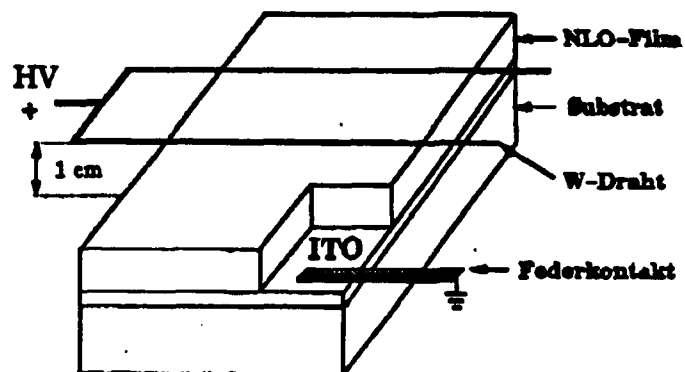


Figure 4: Scheme of the corona-poling setup

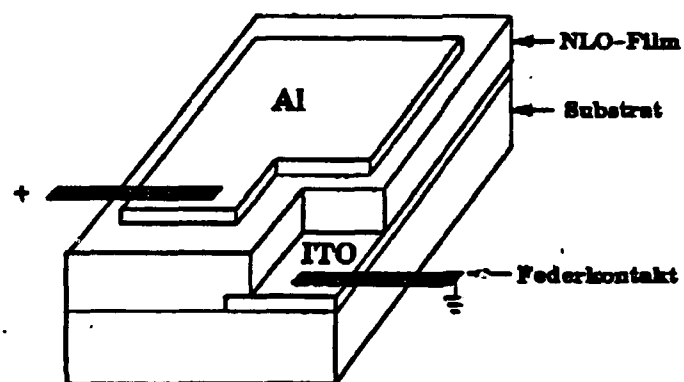


Figure 5: Scheme of the poling setup with plane-parallel electrodes

10 GW/cm². The second-harmonic signals of both the sample and the 'reference' material were fed into separate boxcar integrators (Stanford Research Systems). After performing an A/B division, the averaged signals were stored on a minicomputer for further data processing.

7 PAS experiment

The method, which is generally used to investigate the alignment of the chromophore molecules, compares the absorption behavior of an unoriented and an oriented sample using unpolarized light at normal incidence. The oriented samples usually show less absorbance than the unoriented ones. The reason for the decrease in absorption is the alignment caused by the poling process which leads to an orientation of the transition dipole moments of the respective chromophores. In this alignment process the permanent dipole moments of the molecules tend to orient in field direction. If one assumes that the molecular permanent dipole moment is parallel to the transition dipole moment, and if the poling field is perpendicular to the plane of the thin film $\chi^{(2)}$ -material, the molecular absorption decreases and would be zero for perfect alignment and for a non-divergent light beam. Thus a comparison of the absorption spectra of an oriented sample with the spectrum of an unoriented sample yields the degree of orientation⁴. This method will be referred to as NI method (normal-incidence method, NIM).

Here we present a variation of this method for determining the degree of orientation which has several advantages: The Polarized Absorption Spectroscopy (PAS). Light polarized parallel to the plane of incidence is used to study the absorption as a function of the angle of incidence. This angular dependence of the absorption spectrum (dichroism) is used to evaluate the degree of orientation. Since the absolute value of the absorbance of the unpoled sample does not enter into the numerical data evaluation, a potential error can be eliminated and more information on the molecular anisotropy prior to the poling procedure can be extracted.

7.1 Theory

The optical anisotropy of the respective samples is given by the two components of the complex susceptibility parallel ($\chi_{\parallel}^{(1)}$) and perpendicular ($\chi_{\perp}^{(1)}$) to the surface normal of the sample. These can

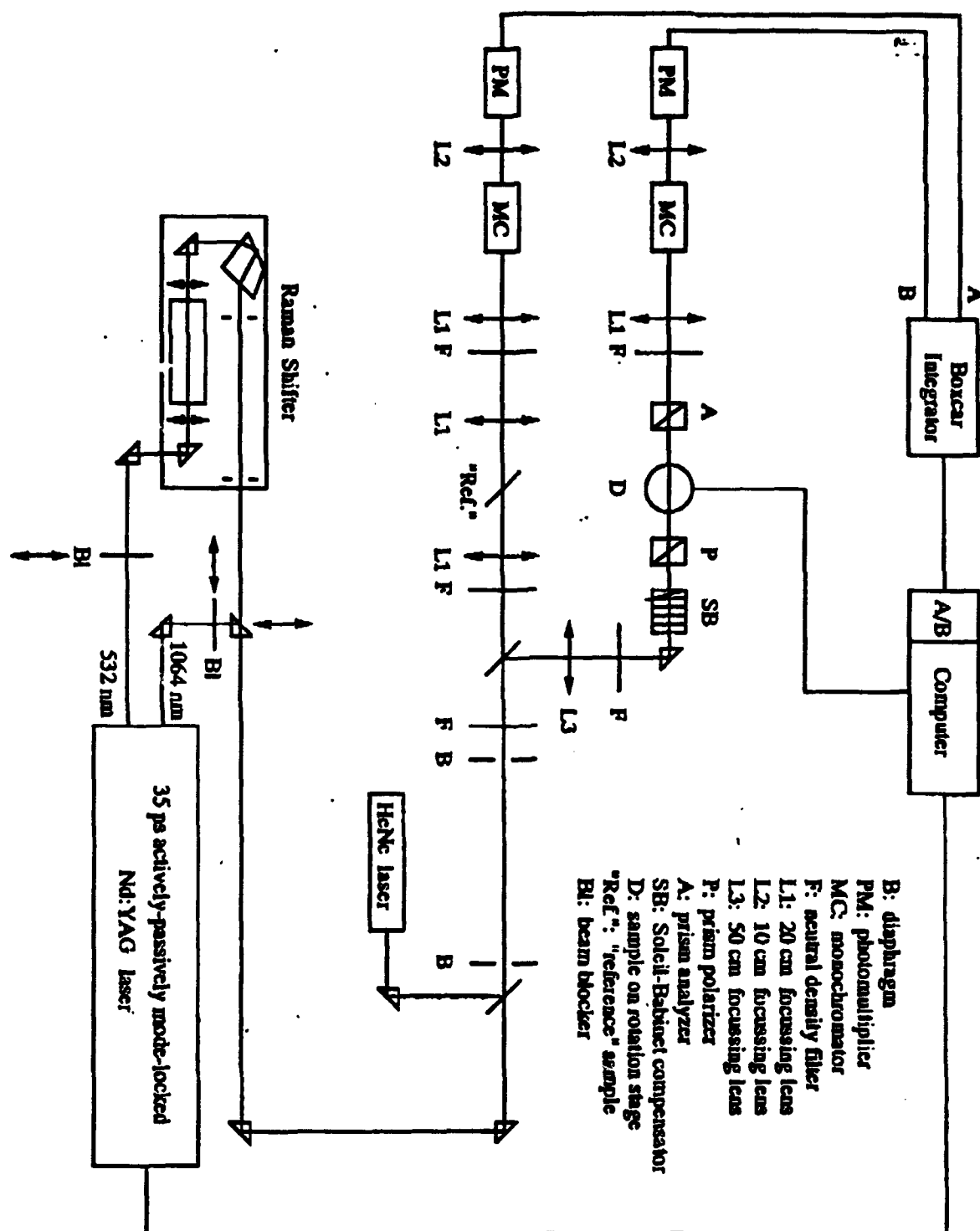


Figure 6: Setup for the SHG experiment

be calculated from the complex molecular polarizabilities parallel to the molecular axes by using an averaging procedure with respect to the angular distribution function $f(\cos \theta)$. The imaginary parts of $\chi^{(1)}$, which describe the absorption behavior, can be expressed in terms of the order parameter A_2 :

$$\chi_{\parallel}^{(1)''} = \text{const} \int \cos^2 \theta f(\cos \theta) d \cos \theta = \text{const} \frac{2A_2 + 1}{3} \quad (8)$$

$$\chi_{\perp}^{(1)''} = \text{const} \int \frac{1}{2} \sin^2 \theta f(\cos \theta) d \cos \theta = \text{const} \frac{1 - A_2}{3} \quad (9)$$

The electric field of the incident light will be described with plane waves:

$$\mathbf{E} = \mathbf{E}_0 \exp[i(\mathbf{k} \cdot \mathbf{r} - \omega t)] \quad (10)$$

The boundary conditions for the oscillatory fields¹² yield the complex wave vector \mathbf{k} for absorbing media:

$$\mathbf{k} = (k_{\parallel}, k_{\perp} + i\frac{\alpha}{2}) \quad (11)$$

where k_{\perp} is the real part of the wave vector perpendicular to the sample surface and where the imaginary part $\alpha/2$ describes the light absorption.

By solving Maxwell's wave equations with the above boundary conditions and taking into account the *comm*-symmetry of the poled sample a system of equations can be found which can be solved exactly for normal incidence only. Assuming low absorbance

$$\alpha^2 \ll k_{\perp}^2 \quad (12)$$

(e.g. for DANS the fraction α^2/k_{\perp}^2 is less than 5%) and neglecting the birefringence, the system of equations can be solved for all directions of light propagation in the sample. The absorption coefficient $\alpha(\Psi)$ calculated in this fashion is found to be

$$\alpha(\Psi) = \frac{2\omega}{c_0 n \cos(\Psi)} (\chi_{\parallel}'' \sin^2 \Psi + \chi_{\perp}'' \cos^2 \Psi) \quad (13)$$

where Ψ is the angle of propagation in the sample and n is the refractive index of the sample. Taking into account equation 8 a linear relation between the absorption coefficient and the order parameter A_2 can be derived as:

$$\alpha(\Psi) \cos \Psi = \frac{2\omega \text{const}}{c_0 n} \frac{1}{3} (1 + A_2(2 - 3 \cos^2 \Psi)) \quad (14)$$

The absorption coefficient α must be determined from optical density (OD) measurements. The transmitted intensity of the incident light is given by

$$I_{transmitted} = I_{incident} T_{Fresnel} e^{\alpha(\Psi) d_{sample}} \quad (15)$$

where $T_{Fresnel}$ is the calculated Fresnel transmission factor for the interfaces air-film, film-substrate and substrate-air and d_{sample} is the thickness of the sample. The direction of propagation in the sample, given by the angle Ψ , can be calculated from Snell's law, since n can be measured independently. Therefore the measured optical density can be expressed as:

$$OD(\phi) = -\log_{10} T_{Fresnel}(\phi) + \alpha(\phi) d_{sample} \log_{10} e \quad (16)$$

where ϕ is the angle of incidence.

Thus, for each wavelength, a plot of the absorption coefficient $\alpha(\Psi) = (OD + \log_{10} T_{Fresnel}) \cdot \cos \Psi$ versus $\cos^2 \Psi$ should yield a linear dependence as predicted by equation 14 which can be rewritten in the following form

$$\alpha(\Psi) = C \cdot (1 + S \cdot \cos^2 \Psi) \quad (17)$$

where $C \cdot S$ is the slope and C the intercept of the linear function. Various experimental dependencies are given in figure 7.

The order parameter A_2 can then be expressed by the following equation:

$$A_2 = \frac{-S}{2S + 3} \quad (18)$$

7.2 Experimental setup

The optical density was measured in a commercial spectrometer with a polarizing filter installed in a position to provide light which was polarized parallel to the plane of incidence. The samples were mounted on a rotation stage whose axis of rotation was in the plane of the film and perpendicular to the axis of light propagation. The optical density OD was measured as a function of the angle of incidence ϕ in steps of five degrees.

Samples with inversion symmetry (see figure 9) do not show any dichroism, the increase of the optical density with increasing angle ϕ is solely determined by the increase of the optical path and a decrease of the reflectivity. Oriented samples usually show dichroism and therefore a much stronger dependence on the angle ϕ as is shown in figure 10).

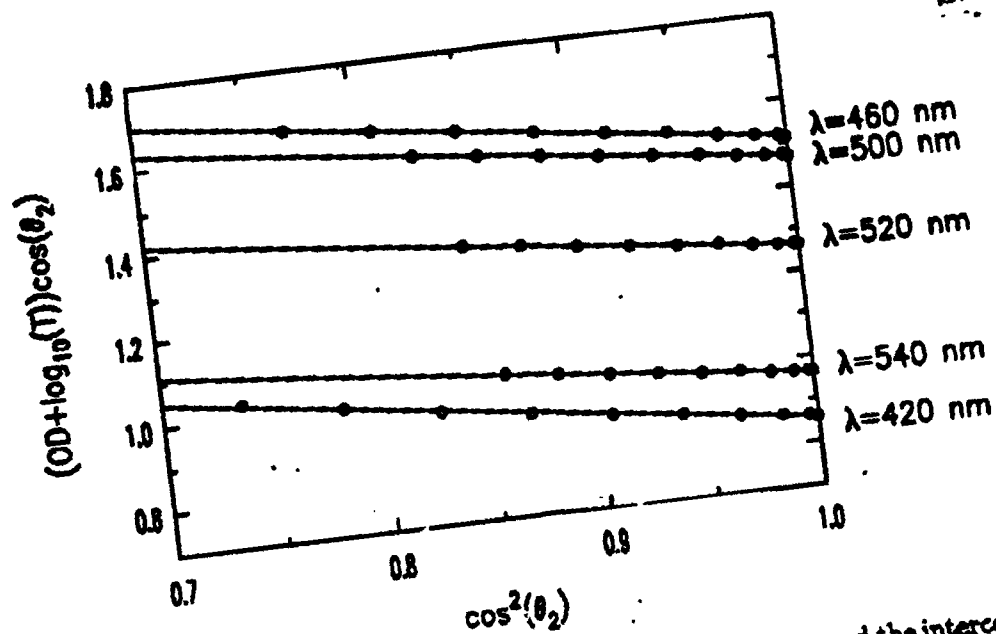


Figure 7: The order parameter A_2 is derived from both the slope and the intercept of a plot of $OD \cdot \cos \Psi$ versus $\cos^2 \Psi$

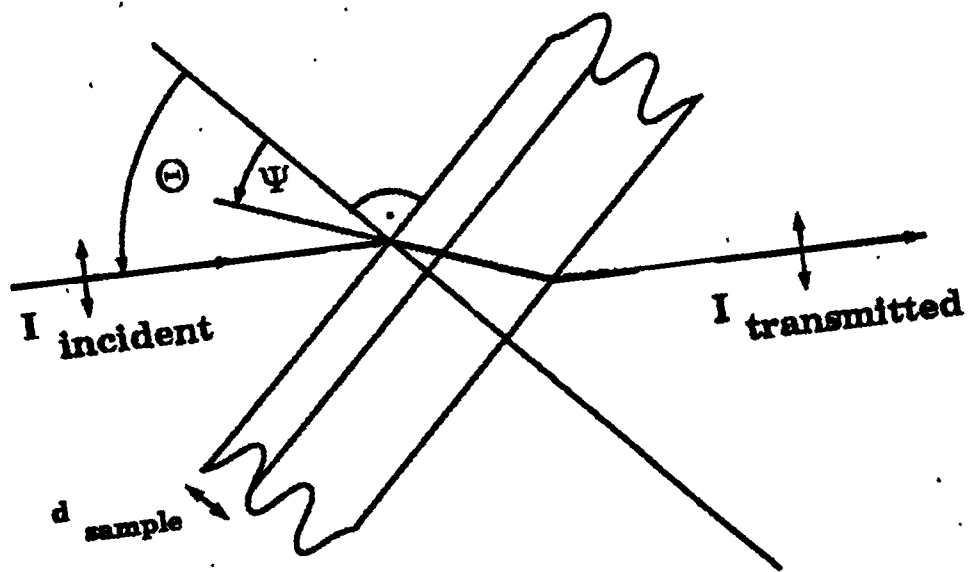


Figure 8: Geometry of the PAS experiment

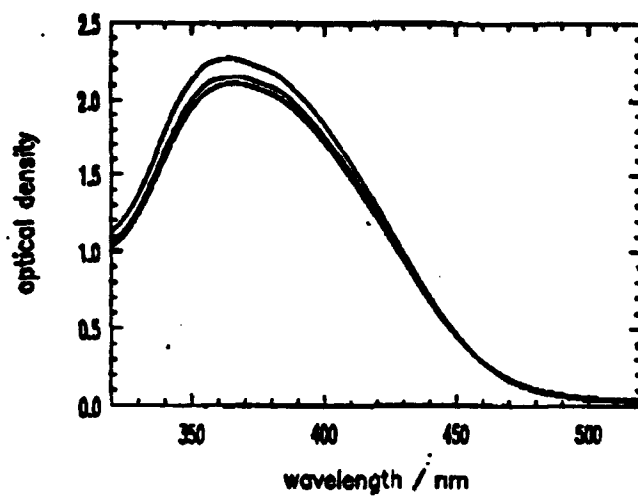


Figure 9: Angular dependence of the absorption spectra of an unpoled ONS sample

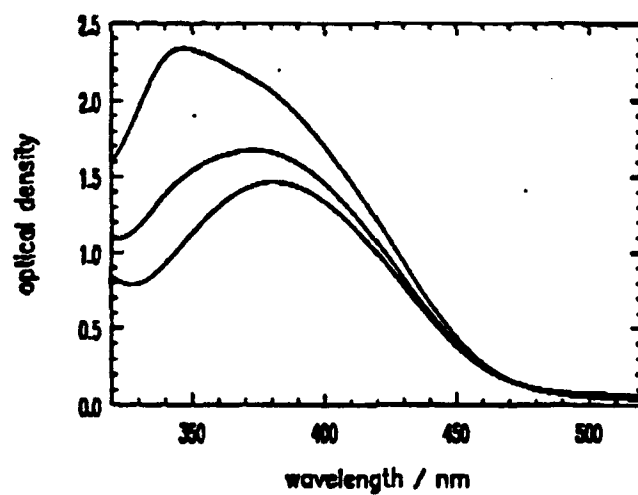


Figure 10: Angular dependence of the absorption spectra of a poled ONS sample

For evaluating the data, the index of refraction must be known precisely as can be seen by inspection of equation 14. The refractive index data in the wavelength regime studied are obtained from measurements of the respective Brewster angles.

8 Values of d_{33}

Typical values for the nonresonant nonlinear coefficient are summarized in table 8. They are comparable to those of inorganic nonlinear crystals such as $LiNbO_3$ ($d_{33} = 40 pm/V$). The order parameters C_3 corresponding to these d_{33} values (see equation 3, $C_3 \leq 0.15$), however, are small as compared to those determined for systems exhibiting inherent order such as Langmuir-Blodgett films ($C_3 \sim 0.7$).

System	$d [pm/V]$
P2ANS/MMA 25:75	20
AZOC6OH/MMA 37:50	40
MO3ONS/MMA 30:70	5

Table 1: Typical values of the nonresonant nonlinear coefficient

9 Poling field dependence of $\chi^{(2)}$

We poled different samples with increasing electric poling field. The nonlinear coefficient was measured immediately after poling and a month later. The measurements were carried out at wavelengths well off resonance (for both the fundamental and the second harmonic signal; fundamental wavelength 1579 nm) and at wavelengths at which resonance enhancement is expected (1064 nm).

The experimental findings are as follows: The dependence of d_{33} on the poling field is linear within the experimental error. The shape of the curve is independent of both the fundamental wavelength and the time after poling.

Both of these results are in a good agreement with the theoretical predictions of equation 4. However, if values for the hyperpolarizability (β), the ground state dipole moment μ_p , and the number density N are taken from the literature, the calculated value of d_{33} exceeds the experimental value by at least a factor of two.

Also, if we calculate the order parameter C_3 corresponding to the SHG signal from the order parameter A_2 corresponding to linear absorption (see the following section), the calculated C_3 value is larger than the experimental value by a factor of about two.

This deviations of the experimental values from the calculated ones are very likely due to an incomplete evaluation of the Maker fringe data since the sample birefringence is neglected herein ³.

So we can conclude that our model for the molecular distributions functions is valid at least qualitatively.

10 Wavelength dependence of the EO and SHG nonlinear coefficients

Usually, for characterizing poled polymer systems non-resonant second-order nonlinear coefficients are determined by applying the so-called Maker fringe technique ⁴ at fundamental wavelengths, for which the material under investigation is transparent for both the fundamental and the second harmonic wave. However, hardly any data exist on resonance enhancement and on the wavelength dependence of second-order nonlinear coefficients in general, and of polymeric systems in particular. This may be due to the higher theoretical and experimental effort required for a proper evaluation of nonlinear coefficients in the case when absorption occurs

10.1 Theory

In order to evaluate this nonlinear coefficient under resonant conditions for the second harmonic wavelength by means of the Maker fringe technique, the so-called 'free wave' occurring in the frequency doubling process is assumed to be modified by an exponential damping factor. The bound wave, however, is taken to be unchanged by the second-harmonic resonance effect. We attempted to explain the data obtained this way by a rather straightforward model based on the two-level approximation for the nonlinear system and found a reasonable agreement of this theoretical approach with the experiment.

We tried to determine the electronic contribution to the electro-optic coefficient r_{33} for the DANS system. This was achieved by comparing the second-order nonlinear coefficients $d_{33}(-\omega; \omega, 0)$ for

³N.Okamoto et al., J.Opt.Soc.Am.B, 9, 2083 (1992)

⁴J. Jerphagnon, S.K. Kurtz, J. Appl. Phys. 41, 1667 (1970)

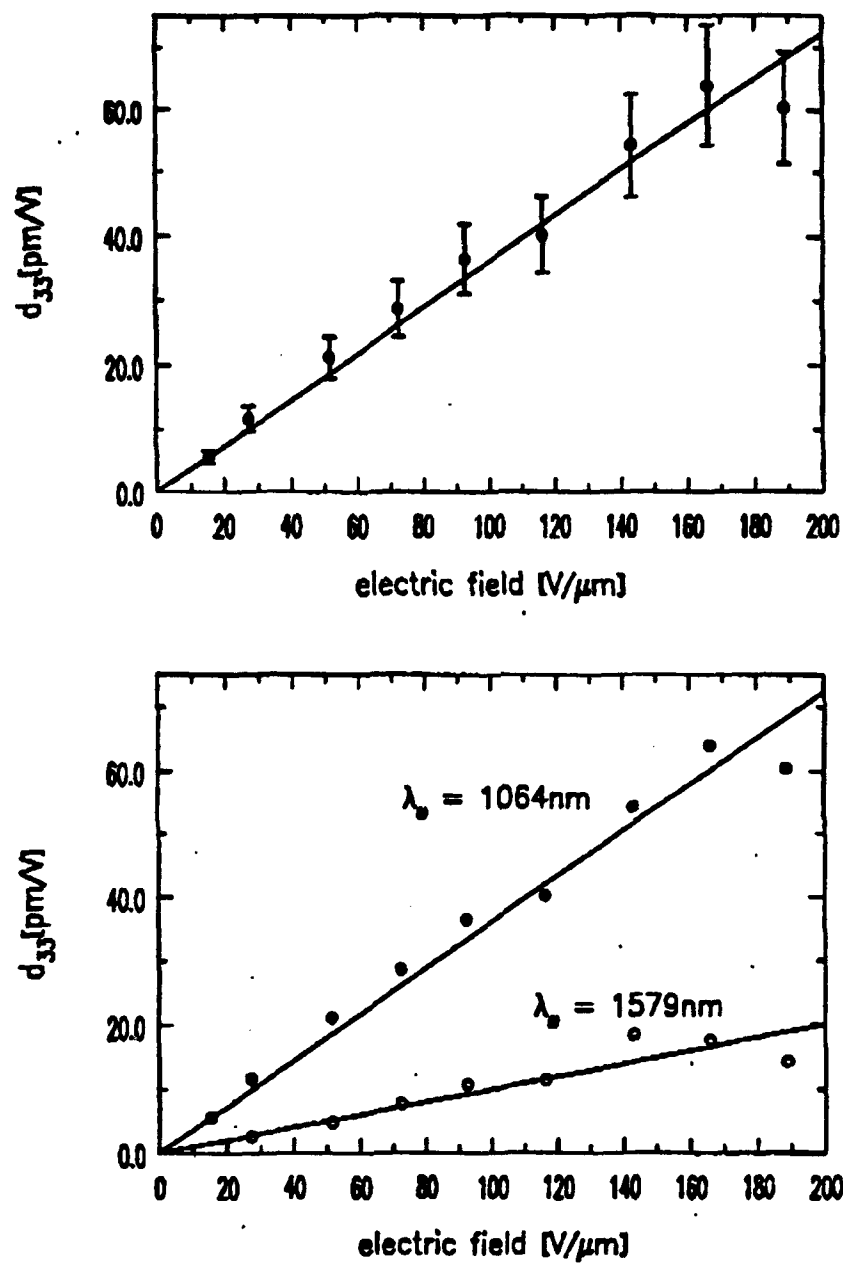


Figure 11: Poling field dependence of P2ANS/MMA 25:75

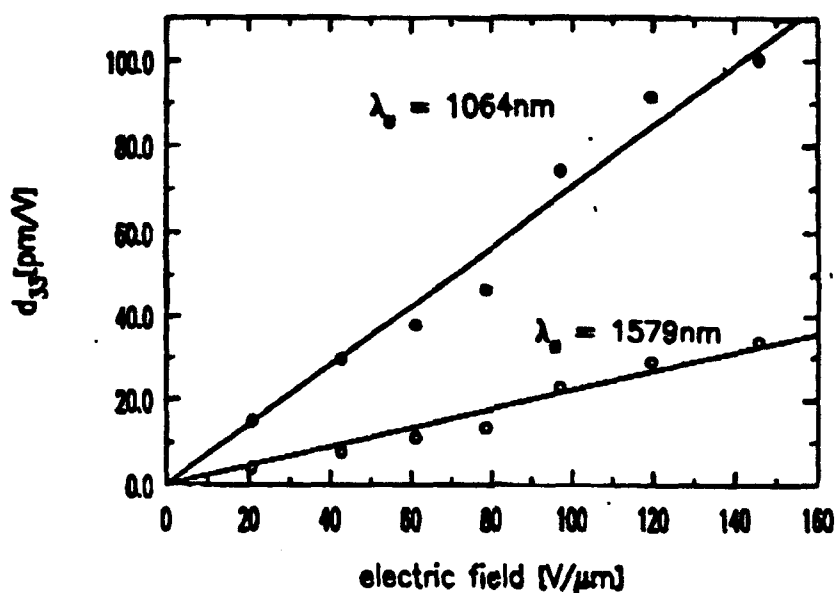


Figure 12: Poling field dependence of AZOC6OH/MMA 37:50

the linear electro-optic effect (LEOE) as obtained by an electro-optic method⁵ and by a calculation from the experimental SHG value $d_{33}(-2\omega; \omega, \omega)$. This procedure yielded only a slight discrepancy of about a factor of 1.2, which can in our opinion be largely related to the neglect of the birefringence in the polymer film in both evaluation techniques.

The determination of the nonlinear coefficient d_{33} from the experimental Maker fringes is based on the theoretical treatment of *Jerphagnon* and *Kurtz*, which has been performed for the non-resonant case only. Starting from the wave equations for the fundamental and the second-harmonic wave, and considering the boundary conditions for the tangential components of the electric and magnetic fields at the air-substrate, the substrate-film and the film-air interfaces, the second-harmonic intensity can be calculated as a function of the angle of incidence. In an extension of this approach we assumed the free wave (solution of the corresponding homogeneous wave equation) to be damped by absorption, whereas the bound wave (partial solution of the inhomogeneous wave equation) is not affected by these conditions. The evaluation procedure as outlined above does not take into account the effect of (poling-induced) birefringence. This fact may cause errors of the absolute d_{33} coefficients determined this way, as has recently

⁵P.Röhl et al., *Appl Phys Lett*, 59, 2793 (1991)

been pointed out by Okamoto et al.⁶ They argued that typical birefringence values for organic polymers of the kind we investigated generally lead to an underestimation of the coefficient d_{33} . A rough estimation of this effect in the case of our DANS system yielded a factor of about 1.2, assuming a reasonable value for the birefringence. A proper treatment of this problem would imply a very exact determination of birefringence in our polymer systems, i.e. measuring refractive indices with a relative accuracy of clearly less than one percent. The techniques we have applied so far, however, i.e. reflectometry and measurement of Brewster's angle, do not satisfy this requirement.

In the following section it will be shown that the wavelength dependence of the macroscopic nonlinear coefficient $d_{33}(-2\omega; \omega, \omega)$ can be calculated from linear optical quantities such as optical density (OD) and refractive index (n) spectra, when certain approximations are made and a two-level model is assumed for the microscopic nonlinear system.

First, the treatment of a two-level model for a molecular system will be outlined. Provided that contributions to the nonlinear polarizability arise along the molecular axis (z) only, the microscopic second-order hyperpolarizability tensor β reduces to the component β_{zzz} , which, in the molecular frame (indicated by a prime), is given by⁷

$$\beta'_{zzz}(-2\omega; \omega, \omega) = (\mu'_z)^2 (\mu'_z{}^{11} - \mu'_z{}^{00}) \frac{3\omega_0^2}{2\hbar^2(\omega_0^2 - \omega^2)(\omega_0^2 - 4\omega^2)} \quad (19)$$

If the local field factors are taken to be independent of wavelength in a first approach, the wavelength dependence of $\chi^{(2)}$ is determined by the following term:

$$\chi_{zzz}^{(2)}(\omega) \propto \langle \beta_{zzz}(\omega) \rangle_{\omega_0} \propto \int_{\text{inhom. line}} g(\omega_0) r(\omega, \omega_0) d\omega_0, \quad (20)$$

$r(\omega, \omega_0)$ representing the resonance term from eq. 19, i.e.

$$r(\omega, \omega_0) = \frac{\omega_0^2}{(\omega_0^2 - \omega^2)(\omega_0^2 - 4\omega^2)} \quad (21)$$

and $g(\omega_0)$ describing the inhomogeneous line distribution.

⁶N.Okamoto et al., J.Opt.Soc.Am.B, 9, 2083 (1992)

⁷see e.g. S.J.Lalaa, A.F.Garito, Phys.Rev. A 20, 1179 (1979)

The following steps are made to express $g(\omega_0)$ as a function of quantities which are accessible by experiment. If we assume horizontally polarized light at normal incidence (neglecting anisotropy and considering small damping losses only), the following relation can be derived for the dependence between the absorption coefficient α , the (real part of the) refractive index $n(\omega) = \sqrt{\epsilon'(\omega)}$ and the imaginary part of the dielectric function, $\epsilon''(\omega)$:

$$\alpha \propto \frac{\epsilon''(\omega) \cdot \omega}{n(\omega)} \quad (22)$$

Neglection of the reflection losses then leads to the relation

$$\epsilon''(\omega) \propto \frac{OD(\omega)n(\omega)}{\omega}, \quad (23)$$

where OD denotes the optical density. Writing $\epsilon''(\omega)$ as a convolution of the homogeneous and inhomogeneous line shapes $h(\omega)$ and $g(\omega)$, i.e.

$$\epsilon''(\omega) \propto \int_{\text{inhom. line}} h(\omega, \omega_0) g(\omega_0) d\omega_0, \quad (24)$$

and considering the narrow homogeneous line width (compared to the inhomogeneous line) as a delta function, one obtains the relation

$$g(\omega) \propto \frac{OD(\omega)n(\omega)}{\omega}. \quad (25)$$

Thus it is possible to calculate the frequency dependence of $\chi_{zzz}^{(2)}$ numerically from the absorption spectrum $OD(\omega)$ and the refractive index dispersion $n(\omega)$ via the relation

$$\chi_{zzz}^{(2)}(-2\omega; \omega, \omega) \propto \int_{\text{inhom. line}} \frac{OD(\omega_0)n(\omega_0)}{\omega_0} r(\omega, \omega_0) d\omega_0. \quad (26)$$

Results for the stilbene copolymers will be discussed in the following section.

10.2 Wavelength dependence of $\chi^{(2)}$

The evaluation procedure outlined in the previous section yields the results shown in figs. 13 and 14 for the second-order nonlinear coefficients d_{33} . The solid lines correspond to the wavelength dependence obtained from a numerical calculation according to eq. 26.

For this purpose, absorption and refractive index spectra were recorded. Refractive indices over a broad wavelength range (300 nm up to 2000 nm) were obtained using a reflectometry method (Lambda UV-VIS-NIR Spectrophotometer, Perkin Elmer) and measurement of Brewster's angle, yielding an accuracy of about one percent.

In order to perform the calculations, one has to take the resonance term including the damping parameter Γ instead of that in eq. 21, i.e. the complex expression $r(\omega, \omega_0) = r'(\omega, \omega_0) + ir''(\omega, \omega_0)$, where

$$\begin{aligned} r'(\omega, \omega_0) &= \frac{1}{(\omega_0 - \omega)(\omega_0 + \omega)} + \frac{(2\omega - \omega_0)/\omega}{(\omega_0 - 2\omega)^2 + \Gamma^2} + \\ &\quad + \frac{(2\omega + \omega_0)/\omega}{(\omega_0 + 2\omega)^2 + \Gamma^2} \quad \text{and} \quad (27) \\ r''(\omega, \omega_0) &= \frac{\Gamma/\omega}{(\omega_0 - 2\omega)^2 + \Gamma^2} + \frac{\Gamma/\omega}{(\omega_0 + 2\omega)^2 + \Gamma^2} \end{aligned}$$

The parameter Γ was chosen to be 0.02 (in units of 10^{15} s^{-1}), yielding optimum agreement between calculated and measured wavelength dependence. In fact, the parameter Γ represents the inhomogeneous line width. The choice of its value is more or less arbitrary, since it does not affect the result of the integral to a great deal. The only reason for introducing a finite Γ is to avoid singularities in the resonance term, which cause problems with the computer program. As can be seen from figs. 13 and 14, the description given by the two-level model seems to be reasonable for both stilbene systems.

10.3 Determination of the electronic contribution to the nonlinear coefficient d_{33} of the linear electro-optic effect (LEOE)

Assuming that a two-level model is appropriate for describing the second-order nonlinear optical properties of our stilbene copolymer systems, we made an attempt to estimate the electronic contribution to the coefficient $d_{33}(-\omega, \omega, 0)$ of the LEOE in the DANS system. For this purpose it was necessary to measure first the second-harmonic nonlinear coefficient $d_{33}(-2\omega; \omega, \omega)$ of a corona-poled sample using the Maker fringe technique. This quantity is related to the electronic contribution d_{33}^e of the coefficient d_{33} for the LEOE via the following equation

$$d_{33}^e(-\omega; \omega, 0) = d_{33}^e(-2\omega'; \omega', \omega') \cdot \frac{F^2(\omega)F(0)}{F(2\omega')F^2(\omega')} \cdot \frac{\beta_{zzz}(-\omega; \omega, 0)}{\beta_{zzz}(-2\omega'; \omega', \omega')} \quad (28)$$

In eq. 28 $f(\omega)$ and $f(2\omega)$ are local field factors of the Lorentz-Lorenz type and $f(0)$ represents the Onsager expression for the static or low frequency field. The ratio of the β values for SHG experiments and LEOE experiments approaches 4 in the long wavelength limit. Here the resonance enhancement of both values is taken into account by the averaging procedure over the inhomogeneous line as described previously.

The nonlinear coefficient for the LEOE can be measured by means of an electro-optic method, e.g. that developed by Röhl et al.⁸ This technique was applied to our sample⁹ and yielded a value of 70 pm/V, whereas the SHG experiment yielded a value of 10 pm/V, which could be used to calculate $d_{33}(-\omega; \omega, 0)$ as 65 pm/V by applying eq. 28. For this purpose values of 1.56, 1.54, 1.56, and 1.52 (obtained by reflectometry) were assumed for $n(\omega)$, $n(\omega')$, $n(2\omega)$, and $n(\infty)$. The static dielectric constant $\epsilon(0)$ was set to 3.7, which is the experimental result for PMMA¹⁰. In organic systems we would expect that the experimental and the calculated $d_{33}(-\omega; \omega, 0)$ are identical, since the origin of the nonlinearity in these systems should be of pure electronic nature. Indeed we found (neglecting birefringence) a very good agreement between both values.

⁸P. Röhl et al., Appl. Phys. Lett., 59, 2793 (1991)

⁹M. Herold, diploma thesis, University of Bayreuth (1992)

¹⁰R. Altmann, Ph.D. thesis, University of Bayreuth (1992)

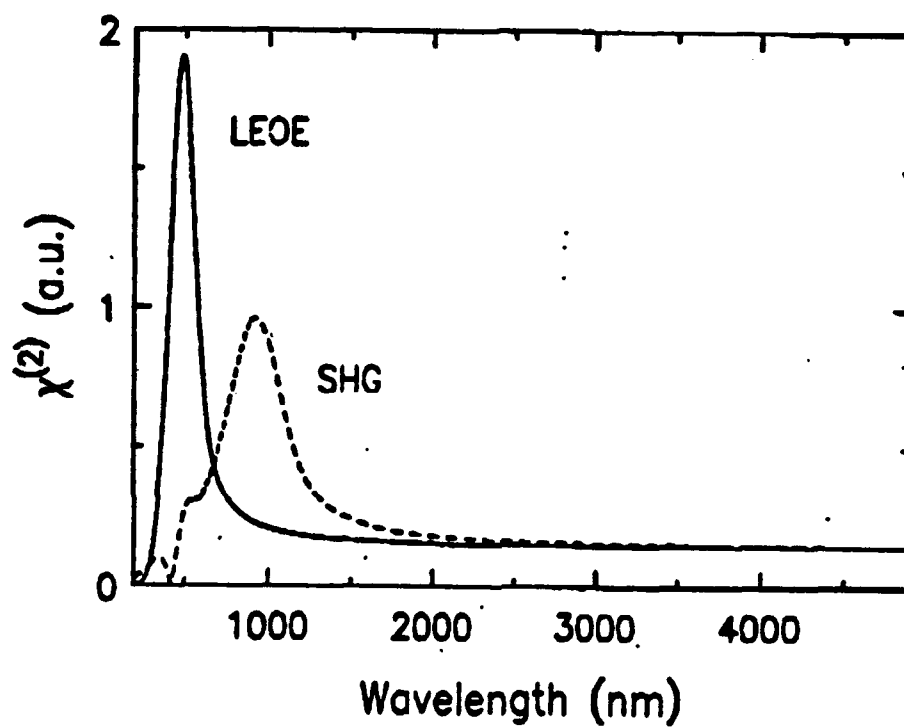


Figure 15: Calculated wavelength dependence of both the LEOE and SHG non-linear coefficients

11 The order parameter A_2

11.1 General

Typical values of A_2 for corona-poled films containing different chromophores are given in Table 2. All the measurements were carried out immediately after poling the samples. The error of these A_2 values is about 0.01 due to uncertainties in the refractive index. The numerical A_2 values show that, compared to liquid crystals exhibiting order parameters A_2 of about 0.6, the order parameters of our poled polymers are rather low. This is also a consequence of the limitation of the feasible electric field strengths used during the poling procedure. Nevertheless poled polymers exhibit $\chi^{(2)}$ values which are comparable to values characteristic of crystals such as LiNbO_3 .

11.2 Relaxation of the molecular orientation

After poling the molecular orientation decreases due to various relaxation processes. The decrease of the order parameter A_2 for two different polymers stored at room temperature is shown in Figure 5. For the copolymer containing the ONS dye the order parameter decreases to 75% of its initial value within one month. Since the glass transition temperature of the AZO-containing polymer, $T_G = 86^\circ\text{C}$, exceeds the T_G value of the ONS containing polymer by 15 degrees centigrade the relaxation of the AZO polymer is only about 15%.

The experimental data for both materials can be fitted empirically to a double exponential function. This behavior is in agreement with SHG-measurements which have been performed in order to get information about order parameters¹³. The first relaxation was interpreted as being due to space charges, the second relaxation is believed to be due to real reorientation processes of the involved chromophores.

12 Comparison of PAS results with the NI method and SHG measurements

Values for A_2 as obtained by the PAS method and the NI method for different corona voltages are summarized in Table 2 for samples containing the DANS chromophore. The table also lists values of

the second-order nonlinear optical coefficient d_{33} . These were measured by second-harmonic generation (SHG) at two fundamental wavelengths. The experimental error of the PAS values is about 0.01. The error of the NI data is difficult to estimate and is, in our opinion, considerably larger. The relative uncertainty of the nonlinear coefficient is about 15%.

Assuming a Boltzmann-like distribution function for the chromophore orientation¹⁴ the nonlinear coefficient d_{33} is expected to increase with increasing order parameter A_2 . While both the PAS and the SHG results do not show an appreciable dependence on the corona voltage the NI data increase drastically. Furthermore the measured A_2 values obtained by the NI method exceed those obtained by the PAS method.

So, the PAS values agree much better with the results of the nonlinear coefficient d_{33} obtained from SHG measurements than the corresponding NI values (see below).

13 A_2 values of unpoled samples

PAS measurements carried out on unpoled samples show that these samples have a slight orientation parallel to the film surface, i.e. $A_2^{\text{unpoled}} < 0$. We found $A_2^{\text{unpoled}} = -0.01$ for the azo dye and $A_2^{\text{unpoled}} = -0.04$ for the stilbene chromophore. We would like to emphasize that the negative A_2 values for unpoled samples are indicative of a molecular orientation in the plane of the film. Such an orientation can only be detected by the PAS method.

14 Conclusions

We measured the second-order nonlinear coefficient $d_{33}(-2\omega; \omega, \omega)$ in various stilbene and azo side-chain polymers at several wavelengths in the long-wavelength tail of the UV-VIS absorption band. We attempted to explain the observed wavelength and poling field dependence with the aid of a two-level model for the microscopic second-order nonlinear properties and a simple thermodynamic model for the orientation behavior of the dyes during poling respectively.

The wavelength dependence was studied by deriving a procedure, which allows us to calculate the wavelength dependence numerically from linear optical properties such as absorption spectrum and refractive index dispersion. For this purpose some major

simplifications have to be made. Among them are neglect of poling-induced birefringence and dispersion in the local field factors. On the basis of the two-level-model description we tried to estimate the electronic contribution to the electro-optic coefficient in another stilbene side-chain copolymer. This estimation is based on a comparison of experimental results for the second-order nonlinear coefficients as obtained from an SHG measurement and the corresponding value as obtained by an electro-optic technique. For a more quantitative treatment of these optical parameters more experimental data and a more quantitative theory is required.

As a second part of our work a novel method for determining the order parameter A_2 was developed which along with SHG-measurements gives information on the orientational order obtained by the poling process. This method is based on polarized absorption spectroscopy (PAS) at different angles of incidence. The experimental values are found to be smaller than those obtained by previously used setups (NI-methods). The agreement with SHG experiments, however, is much better for the values obtained by the PAS method. Moreover it is now possible to obtain order parameters for unpoled samples and it is shown that spin-cast films exhibit a non-vanishing order parameter in spite of the fact that they are unpoled.

corona voltage (kV)	A_2		d_{33} (pm/V)	
	PAS	NI	$\lambda =$ 1064nm	$\lambda =$ 1579nm
5	0.06	0.13	77	17
7	0.06	0.16	79	17
9	0.06	0.24	68	18

Table 3: Order parameter A_2 and second-order nonlinear coefficient d_{33} for corona-poled films with the *DANS* chromophore

9. Subcontractor Final Report (Cambridge University)

Multifunctional Macromolecules

"Structural Characterization of Side Chain Polymers"

Final Subcontract Report

(1991-1993)

Prepared by

Alan Windle

Department of Material Science

Pembroke Street

Cambridge, CB2 3QZ

United Kingdom

MULTI FUNCTIONAL MACROMOLECULES

Final Report

Alan Windle,
Department of Materials Science,
Pembroke Street,
Cambridge,
UK, CB2 3QZ

1 Introduction

1.1 This Report The work sponsored under this grant has lead to the publication of four papers, one still in press, with a further one in preparation. These papers, which form an appendix to this report, together with the numerous progress reports submitted to Hoechst Celanese form a definitive statement of what has been achieved by the Cambridge component of the project.. This final report, while highlighting some of the major conclusions which can be drawn from the research, focuses on the general principles which have been established by the programme. Some of the insights were won as the result of particular experiments, while others gradually developed as the synergy of the multi laboratory programme began to take effect.

1.2 Collaboration The 'M³' collaborating venture was managed by the team at Hoechst Celanese, where the molecular synthesis was carried out. The quality of the synthetic work was outstanding, with molecules of high purity and high molecular weight, providing an ideal basis for the structural, processing and property studies carried out in the UK. The Cambridge group concentrated on structural characterisation of the polymers and the development of electrical field routes for the generation of order in the molecular examples which were liquid crystalline. The research group at Leeds, under the leadership of Professor Ian Ward, concentrated on the development of order in the isotropic members of molecule set. They examined the degree of order achievable under poling fields by means of electrical measurements.

1.3 The Molecules The primary effort centred on a series of side-chain polymers based on methacrylate backbones. with oxynitrostilbene NLO active side groups attached through flexible alkane spacers. The molecular variables were the length of the flexible spacers, most work being carried out with three and six CH₂ groups respectively, and the degree of substitution on the methyl methacrylate backbones. Some characterisation was carried out on an earlier series in which the active side-group was oxynitrobiphenyl. These molecules were available in a molecular weight series, and enabled confirmation that the molecular weights achieved were sufficiently high to avoid being a factor in the transitional behaviour of the materials. Measurements were also made on the component monomers, and the full crystal structures were measured (in US) for two of these to demonstrate the natural packing characteristics of the active components.

1.4 The Central Issues The major remit of the Cambridge group, in addition to providing a structural characterisation resource to the complete programme, has been to explore the degree to which liquid crystallinity can be exploited in the achievement of the levels of orientational order necessary to the creation of a successful NLO polymer. As will be apparent below, the presence of liquid crystallinity, while providing a route to easy orientation of the active molecular components also has some serious limitations where an optical material is required.

2. Control of Transitions through Molecular Structure

2.1 Why Polymers ? The active groups do not need to be attached to a polymer backbone, in order to transmit their properties to a bulk material. However, distinct advantages accrue from the use of polymers. These are:

- (i) The polymer backbone enables the material, after processing, to be cooled into a non-crystalline solid state. The material is thus durable and free from the gross light scattering which crystallisation usually brings.
- (ii) The polymeric material opens up the possibility of processing to give thin, comparatively tough films, without the need for encapsulation.
- (iii) Attachment of the active groups to a backbone means that their concentration can be controlled and different types of active component introduced without the risk of phase separation, with its attendant light scattering. It is thus a key in the development of multifunctionality.

2.2 The Glass Transition The substitution of the active side groups, with their incorporated flexible spacers, onto the methyl methacrylate backbone, reduced the glass transition temperature of the polymer. The reduction was very noticeable in the case of C6 spacers, less so with C3. For the case of 100% substitution of C6 active stilbene groups, the T_g was reduced from 110°C to 61°C, and slightly more in the case of the oxy nitro biphenyl derivative. The T_g of a 50/50 random copolymer of C3 and C6 spaced units was midway between that of the two homopolymers. A glass transition in the range of 60° to 70° was seen as most appropriate for the type of NLO materials envisaged as it was sufficiently low to permit processing above it without undue risk of degradation while high enough to give a good prospect of long term microstructural stability in use under ambient conditions.

2.3 Liquid Crystallinity The liquid crystallinity observed was smectic in nature. It was only obtained in molecules with spacers of C4 or longer, and where the degree of substitution of the active groups was 100% or in the case of the C6 material 70% and 100%. None of the monomer units, with or without the methacrylate group, showed liquid crystallinity with the exception of C3 ONS unit terminated with just a hydroxyl group which gave a nematic melt above its crystal melting point.

Two competing effects have to be considered to understand the influence of substitution onto a backbone on liquid crystallinity. On the one hand, the attachment of a mesogenic group will reduce the stability of the isotropic melt phase

on account of the reduced freedom of motion of the groups. Set against this, must be the fact that a polymer backbone in a random coil conformation, will tend to disrupt the order of the attached side groups, especially if these are close coupled. It is for this reason that flexible spacers are necessary to achieve liquid crystallinity at all in side chain polymers. Increasing spacer length will, within limits, enhance the stability of the mesophase.

3. Liquid Crystallinity, Advantages and Drawbacks for NLO Materials.

3.1 Advantages Liquid crystalline materials show long range orientational order in a mobile phase. The efficiency with which the intrinsic second order NLO activity of the chemical group is transferred into a bulk property, is determined by:

- (i) the quality of the alignment of the groups
- (ii) the polarity of this alignment.

Liquid crystalline phases provide an excellent vehicle for the attainment of component (i), while the achievement of polarity in this alignment (strictly parallel rather than anti-parallel) will require the application of a DC poling field.

3.2 Disadvantages

- (i) Liquid crystallinity, especially of the smectic variety, tends to produce highly scattering textures which would be totally inappropriate for any optical material.
- (ii) Detailed structural analysis showed that, over the range of molecules examined, the smectic phase was interdigitated. That is the side groups from neighbouring chains adopted an anti parallel structure. Hence, any poling field would have to oppose the inherent thermodynamic stability of the structure.

4 Achievement of Monodomains

4.1 The Quench Route. Initial work, showed that it was possible to avoid strongly scattering smectic textures by quenching from the isotropic state. The glasses obtained appeared quite clear although no quantitative optical measurements were made. However, the approach is intrinsically flawed because:

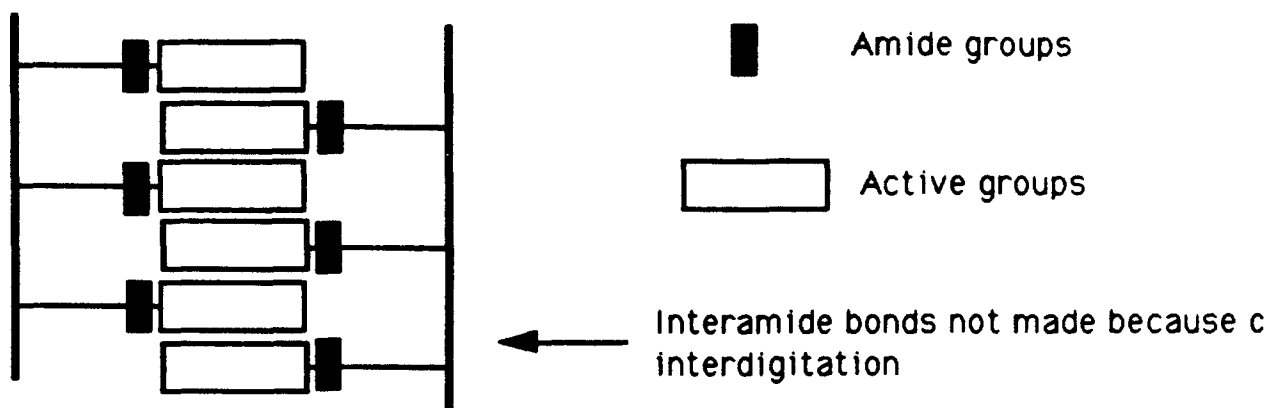
- (i) If one wishes to avoid a liquid crystalline phase, it would be better to do it through molecular design, using material with a shorter flexible spacer or lower degree of substitution into the methyl methacrylate backbone.
- (ii) The glass would only be metastable in that it would be susceptible to developing opacity with time particularly if subjected to temperatures approaching T_g , even for short times.

4.2 AC Induced Monodomains. Transparency was achieved in the smectic polymers by creating a monodomain through orientation in an AC field between ITO coated glass. The orientation was only induced at the point at which the sample was

cooled through the isotropic to smectic transition. The threshold voltage for the C6 homopolymer was of the order of 4 V per μm at 33kHz, the exact figure depending on cooling rate. While full details are given in the attached literature, one other aspect is worthy of mention. The plots of threshold voltage against sample thickness, showed an intercept on the thickness axis at 10 μm . The implication is that a very thin film would achieve monodomain orientation, without the need for any field at all, presumably as a consequence of homotropic alignment on the ITO. It was considered that this effect accounted for the clarity of spin-coated samples. It must be emphasised that the induced polarization which is the basis of the AC orientation provides no polar component to the alignment. Thus AC monodomains, would need further poling treatment in a DC field before they might be expected to show second order NLO activity.

5. Poling Response

- 5.1 DC Fields.** Cooling through the isotropic to smectic transition, in the presence of a DC field was not successful in forming a monodomain. Instead, the observation of a pretransitional instability was observed, which led to a highly scattering structure. The electrohydrodynamic instability (electrical stirring) was only observed near to the transition temperature, and was not accompanied by any change in the steady decline in specimen current observed during the experiment. It is thus not thought to be due to charge injection, which is further attestation to the high purity of the Summit material.
- 5.2 DC - AC Combined Fields.** Samples cooled through the transition in a combination of DC and AC fields, did show a monodomain, although its transparency was degraded in proportion to the size of the DC component. Nevertheless a small poling effect was observed, with a Pockels coefficient for a 71 μm sample cooled in 800V AC (5kHz) and 400V DC fields was $r_{33} - r_{13} \sim 70\text{fmV}^{-1}$.
- 5.3 Poleability of Smectic Polymers.** Parallel work in Leeds, in which a series of C6 and C3 polymers were poled below their glass transition temperatures, showed an increasing polar anisotropy, measured as pyroelectric coefficients, with increasing content of the active ONS groups, up to the composition just prior to the onset of smectic liquid crystallinity. Beyond that point the effect decreased. It appears that this observation is further evidence that the smectic structures involve interdigitation of the side groups which thus leads to antiparallel packing, and thus a degradation of second order NLO activity. We consider that interdigitation is the major reason which precludes the exploitation of liquid crystalline routes in the achievement of high activity in this range of polymers.
- 5.4 Modifications to Molecular Design.** A molecular design modification was proposed as a route to discourage antiparallel packing of the side groups. The idea is to position a group, such as an amide, which has strong interaction potential with neighbouring, similar groups, just inboard of the active element of the side chain. Antiparallel packing in which the amide groups were opposite each other would be discouraged by the fact that the aromatic, stilbene, component of one side chain would be alongside the aliphatic flexible spacer of the next, and so on.



The synthesis necessary to test this concept was not completed before the conclusion of the project.

6. Current Studies

6.1 Mechanical Orientation. The final part of the project has focused on the orientation of the side chains in mechanical fields, both below and above T_g . The orientation is measured using both X-ray diffraction and birefringence measurements. Orientation can be achieved equally in the 50% substituted PMMA and in the 70% and 100%, samples even though the first is not liquid crystalline. Smectic liquid crystallinity thus does not appear to have any influence on the response of side group orientation to an applied deviatoric, mechanical field.

6.2 Orientational Effects of Relaxation. The mechanically induced orientation of the side groups is initially in the same direction as that of the backbone. However, when the liquid crystalline examples of the series are annealed in the mesophase region, the side groups turn through 90° to orient normal to the mean direction of the backbone. The reason for this behaviour is not clear, although it may be that the smectic packing is more efficient with the mesogenic units normal to the backbone which can thus be positioned mainly between the ordered layers. It is hoped to continue some of this work as a student project.

7. Conclusion

Whatever the future of NLO active polymeric materials in competition with inorganics and small-molecule organics, the work undertaken under the multifunctional macromolecular materials programme, has advanced our understanding of such side chain systems. The quality standards were set by the high level of synthetic expertise at the Summit laboratory, has meant that the polymers fed into the programme were always excellent, with respect to molecular weight, purity and reproducibility.

The Cambridge component of the work has explored fully the possible benefits of processing and aligning in the liquid crystalline phase. *On balance, liquid crystallinity is probably more of a liability than a benefit in this type of application.*

Other signposts for the future, are:

(i) The need to avoid poling under conditions where hydrodynamic instabilities can occur, and the importance of achieving a polymeric state in which rotational diffusion of the active groups is easy in comparison to the viscous shear processes. The investigation of central attachment of the active groups to the backbone and also cross linking as means of achieving poleability above T_g , could be significant new steps.

(ii) The need to achieve film processibility of polymers with significant levels of active side group substitution. The investigation of networks cross linked under a field, to produce elastomeric monodomains, is also an important pointer for the future.

(iii) The mechanisms of side chain orientation open up general questions of orientation of substituted rod-like species in monomeric matrices. The basic question is that if the rod molecules respond to a mean field, then it should be possible to achieve higher levels of orientation in the rods than in the surrounding (conventional) polymer. If this is the case, it could have important implications for guest/host systems.

10. Subcontractor Final Report (GEC-Marconi Research Center)

**Multifunctional Macromolecules
"Investigation of Photorefractive Polymers"**

**Final Subcontract Report
(1991-1993)**

Prepared by

M. Worboys

**GEC-Marconi Research Center
West Hanningfield Road
Great Baddow, Essex
United Kingdom**

ABSTRACT

Applications for photorefractive materials have been widely discussed in the literature but it has yet to be shown that many of these are viable. The limiting factor which governs the practical implementation of these applications is the performance of available materials. Traditionally, photorefractive materials have been doped inorganics of one type or another. Such materials have been widely studied but, on the whole, do not exhibit the overall qualities required of a practical photorefractive. Recently, a new class of organic photorefractive materials has emerged. The properties of these materials are more amenable to tailoring and this raises the possibility of 'engineering' a photorefractive with properties which are optimised for a given application.

In this study we look at the mechanisms involved in the photorefractive effect, examine the figures of merit which can be used to compare the performances of different classes of materials, and review the materials themselves. A review of eleven potential photorefractive applications is presented and the feasibility of each of these for practical implementation is examined.

INTRODUCTION

Inorganic materials have been widely studied since the photorefractive effect was first observed. During this time, most work has been carried out using either oxygen-octahedra ferroelectrics or semiconductors (see Section 4.1). However, whilst these materials are suitable for demonstrating many photorefractive applications in the laboratory they are not, on the whole, suitable for use in practical devices. Reasons for this include inadequate sample size or quality, excessive optical power requirement or slow response time.

A new class of materials has recently emerged and this is attracting a growing level of interest among the photorefractive community. These are organic materials and work on both crystals and polymers has been reported (see Section 4.2). Such materials have been heavily studied in recent years for applications in nonlinear optics and promising materials have been identified. An important feature of these materials is the ability to tailor their properties to favour a given application. Such an approach to 'engineering' a material is not so readily achievable with inorganic materials. A photorefractive polymer is the archetypal multifunctional material, combining the properties of electro-optic response with photoconductivity.

In this report we review the applications which have been proposed for photorefractive materials and critically examine the requirements for the materials needed to implement these. Some applications are shown to be only possible in the laboratory (where excessive optical power is required) while others could be implemented with only small improvements in material performance. In many cases we found that applications which have been proposed for photorefractives could be implemented, often more successfully, using an alternative technology (such as electronic processing). Our work on comparing the performance of different materials in these applications was severely hampered by the variability of data which is reported throughout the literature. This was especially true for different groups working with nominally 'identical' materials. Reports from a single group rarely contain a full set of parameters for the material studied and therefore results from different groups are almost impossible to compare. In many cases this is probably because the exact composition and quality of the sample being studied is unknown.

Finally, the report draws together some conclusions on the potential of organic materials for practical implementation of photorefractive applications and indicates the direction to be taken in evaluating present generation materials.

2 MECHANISMS OF PHOTOREFRACTION

2.1 Definition of Photorefraction

The scope of this programme has been deliberately limited to the study of materials in which the origin of the photorefractive effect is a combination of two specific properties, photoconductivity and electro-optic modulation. Under this definition, materials in which the refractive index modulation occurs as a result of photothermal or photochemical changes on exposure to light (e.g. atomic displacement, photo bleaching, phase change or crosslinking) are not considered here.

2.2 Mechanisms

The photorefractive effect is widely documented and the principle is shown in Figure 1. When two incident coherent light beams interfere in a photorefractive material, photons in the bright parts of the interference fringes are absorbed and free carriers created. These free carriers move within the material by diffusion (or drift under the influence of an external applied field) until they are trapped in the dark parts of the interference fringes. The net result is a periodic spatial charge pattern. This charge pattern generates an electric field which, via the Pockels effect, causes a change in the refractive index which has the same spatial frequency Λ as the optical interference pattern. The induced refractive index pattern can exhibit a spatial phase shift ϕ relative to the interference fringes, where ϕ can be of the order of $\pi/2$.

The photorefractive effect is essentially a combination of four separate physical processes. These are:

- (i) Photogeneration - photons are absorbed and free carriers generated.
- (ii) Photoconduction - the free carriers move through the material by diffusion, by drift (when an external electric field is applied) or by the photovoltaic effect.
- (iii) Trapping - the free carriers are trapped to produce a static charge distribution.
- (iv) Electro optic effect - the electric field generated by the trapped charge produces a variation in the refractive index of the material.

The efficiency of the photorefractive effect is determined by the efficiencies of each of the above processes. Likewise, the response time of the photorefractive effect is a combination of the response times of all the above processes.

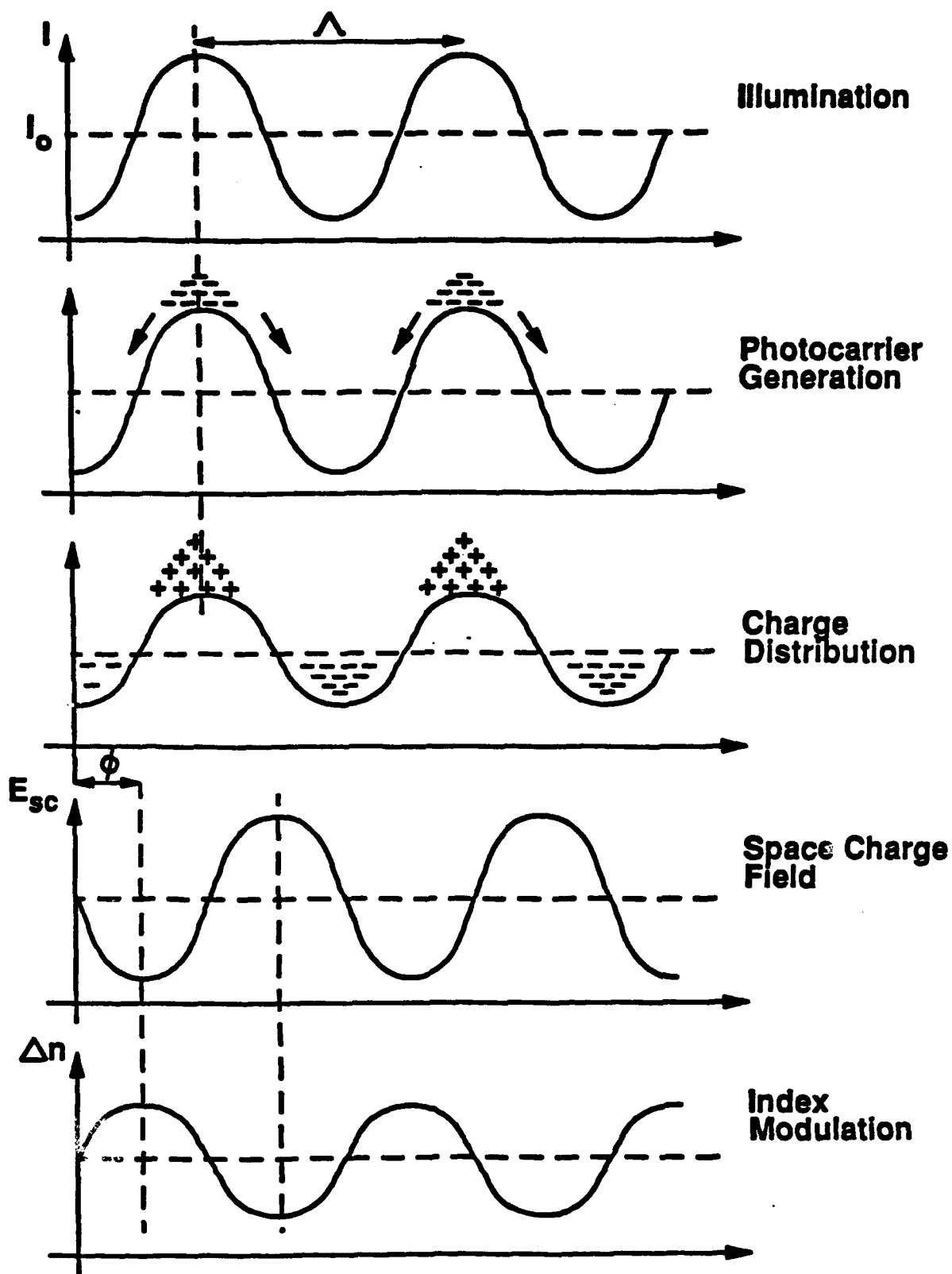


Figure 1: Schematic diagram of the photorefractive effect

2.2.1 Charge Generation

Photons arriving at dopant (or impurity) centres within a photorefractive material photoionise these species so that charge carriers (electrons or holes) are generated. The efficiency of this process is dependent upon the nature of the charge generation species and the wavelength of incident light.

2.2.2 Photoconduction

Once generated, the charges will move within the photorefractive material by one of three processes; diffusion, drift or the photovoltaic effect. These processes are described in more detail below but each process involves repeated trapping and re-excitation of the carriers. Charges are trapped within the dark regions so, as they diffuse away from the regions of high intensity, they will accumulate in regions of lower intensity. Each charge that moves inside the crystal leaves behind a less mobile charge of the opposite sign.

(i) Diffusion

Charges diffuse from regions of high carrier density to regions of low carrier density, corresponding to a movement from light regions in the material to dark regions. As a result, a space charge distribution is established which is modulated in phase with the light intensity. However, the resulting space charge electric field is shifted by 90° from the light intensity modulation, as shown in Figure 1.

(ii) Drift

Applying a dc electric field to the photorefractive material causes a stronger space charge distribution to be established than is obtained by diffusion alone. However, in this case the electric field (and consequently the refractive index grating) is shifted away from the optimal quarter phase shift. Such a phase shift can be avoided by applying an external ac electric field to the material. In this case the resulting internal electric field is larger than that produced by diffusion alone and the refractive index grating has the same $\pi/2$ phase shift as if no drift field were present.

(iii) Photovoltaic Effect

In electro optic crystals, such as LiNbO_3 , a photocurrent can be produced without an applied voltage. Photoelectrons are excited into the charge transfer band with a preferential direction of electron motion along the polar axis direction. The photovoltaic effect produces a shift in the spatial distribution of the carriers and immobilised charges in a similar way as an applied dc field.

In different materials, depending on the electronic properties and experimental conditions, any one of the transport processes described above can dominate.

2.2.3 Charge Trapping

Trapping of the mobile charge carriers occurs at defect centres in the photorefractive material. These defect centres are often the ionised species which remain stationary in the matrix after photoexcitation has occurred.

2.2.4 Grating Formation

The full mathematical description of grating formation has been derived by Kukhtarev et al [1]. The space charge field arising between the ionised donor centres and the trapped charges modulates the refractive index of the material via the electro-optic effect. The index modulation at saturation is given by [2]

$$\Delta n = 2n_0^3 r \frac{\beta^{\frac{1}{2}}}{1 + \beta} \left(\frac{E_0^2 + E_D^2}{(1 + E_D/E_q)^2 + (E_0^2/E_q^2)} \right)^{\frac{1}{2}} \times \frac{1}{2} \quad \text{..... (1)}$$

and the spatial shift ϕ between the incident fringe pattern and the photo-induced index modulation by

$$\tan \phi = \frac{E_D}{E_0} \left(1 + \frac{E_D}{E_q} + \frac{E_0^2}{E_D E_q} \right) \quad \text{..... (2)}$$

where r is the electro-optic coefficient, n_0 is the background refractive index of the medium, β is the incident intensity ratio of the two interfering beams, E_0 is an externally applied field, E_D is the diffusion field and E_q is the maximum field which would correspond to a complete separation of the positive and negative charges by one grating period. These fields are given by

$$E_D = \frac{2\pi k_B T}{e \Lambda} \quad ; \quad E_q = \frac{e N_A \Lambda}{2\pi \epsilon_0 \epsilon} \quad \text{..... (3, 4)}$$

where N_A is the trap density in the material volume, Λ is the fringe spacing, ϵ is the relative static dielectric constant, T is the temperature, e is the electron charge and ϵ_0 is the permittivity of free space.

3 FIGURES OF MERIT

3.1 Diffraction Efficiency

The diffraction efficiency η of a thick phase transmission grating with a peak to peak index modulation $2\Delta n$ is given by [2]

$$\eta = \exp\left(\frac{-\alpha d}{\cos\theta}\right) \sin^2\left(\frac{\pi d \Delta n}{\lambda \cos\theta}\right) \quad \text{..... (5)}$$

where α is the absorption coefficient, d is the crystal thickness, θ is the Bragg angle in the crystal and λ the incident wavelength.

From Equation 1 it can be seen that the larger the electro-optic coefficient, the larger the photo-induced index change. This in turn results in an increase in the diffraction efficiency η . Thus materials such as barium titanate and strontium barium niobate which have high electro-optic coefficients ($r \sim 1000 \text{ pm.V}^{-1}$) will have large values of Δn ($\sim 2 \times 10^{-5}$) and therefore high diffraction efficiencies. In materials with small electro-optic coefficients (such as bismuth silicon/germanium oxide and gallium arsenide) the refractive index modulation can be enhanced with an externally applied electric field E_o .

3.2 Response Time

The time constant for the build-up of a phase grating is given by [2]

$$\tau = \tau_{di} \frac{(1 + \tau_R/\tau_D)^2 + (\tau_R/\tau_E)^2}{[1 + (\tau_R \tau_{di}/\tau_D \tau_i)] (1 + \tau_R/\tau_D) + (\tau_R/\tau_E)^2 (\tau_{di}/\tau_i)} \quad \text{..... (6)}$$

where τ_{di} is the dielectric relaxation time of the material and is given by

$$\tau_{di} = \epsilon \epsilon_o / n_o \mu e \quad \text{..... (7)}$$

and where n_o is the free carrier concentration due to the incident illumination I_o , given by

$$n_o = \tau_R \alpha \phi I_o / h\nu \quad \text{..... (8)}$$

μ is the mobility of the photocarriers and ϕ is the quantum efficiency. The charge recombination time τ_R can be written as

$$\tau_R = (\gamma_R N_A)^{-1} \quad \text{..... (9)}$$

where γ_R is the recombination coefficient. The drift time τ_E of the charges is given by

$$\tau_E = \frac{1}{K \mu E_o} \quad \text{..... (10)}$$

and the diffusion time τ_D of the charges is given by

$$\tau_D = \frac{1}{\mu k_B T K^2}$$

..... (11)

where $K = 2\pi/\Lambda$. Finally, τ , the inverse sum of photogeneration rate s/I_0 and ion recombination rate $\gamma_R n_0$, is given by

$$\tau = (s/I_0 + \gamma_R n_0)^{-1} \quad \text{..... (12)}$$

The time dependence of the space-charge field during grating recording is

$$\Delta E_{sc} = m E_{sc} (1 - \exp(-t/\tau)) \quad \text{..... (13)}$$

and, during erasure by uniform illumination, the photo-induced space-charge field decreases as

$$\Delta E_{sc} = m E_{sc}^{-\exp(-t/\tau)} \quad \text{..... (14)}$$

where E_{sc} is the initial amplitude of the field and m the incident modulation.

The response times of various materials are plotted against incident intensity in Figure 2, and the experimental parameters associated with each material are summarised (where known) in Table 1.

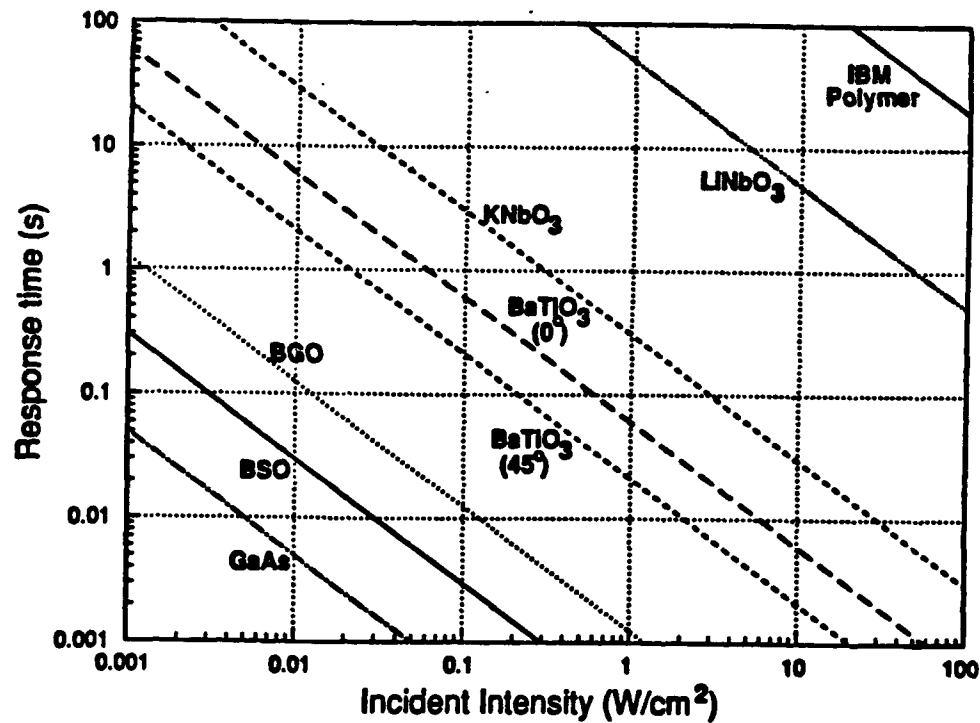


Figure 2: Response time as a function of incident intensity for various photorefractive materials (see Table 1)

Material	Wavelength $\lambda/\mu\text{m}$	Interaction Length $l/\mu\text{m}$	Absorption Coefficient α/cm^{-1}	Grating Wavelength $\lambda/\mu\text{m}$	Intensity $I/\text{W}/\text{cm}^2$	Beam Ratio β	Gain Coefficient Γ/cm^{-1}	Applied Field $E_A/\text{KV}/\text{cm}^{-1}$	Energy Density J/cm^2	Response Time μs	Doping Concentration N_A/cm^{-3}	Reference	Label in Figure 2
Bismuth Silicon Oxide	514.5	-	2.3	5	-	-	-	6	300×10^4	-	-	[3]	[a]
Barium Titanate (45° cut)	514.5	0.87	-	-	1	800	38.7	-	0.021	21×10^3	-	[4]	[b]
Bismuth Germanium Oxide	514.5	-	2.1	5	-	-	-	6	1.25×10^4	-	-	[3]	[a]
Barium Titanate (0° cut)	514.5	-	-	-	300×10^3	-	-	-	0.06	200×10^3	-	[5]	[c]
Lithium Niobate	514.5	10	-	-	-	-	-	-	50	-	-	[6]	[d]
Gallium Arsenide	1060	-	4	-	-	-	0.5	0	0.5×10^4	-	1×10^{17}	[7]	[d]
Potassium Niobate	488	-	1.5	-	0.5	-	-	-	0.3	0.6	-	[8]	[a]
IBM Polymer	647.1	0.35	-	1.6	13	1	-	126	1900	150	1.9×10^{18}	[9]	[c]

Table 1: Summary of parameters for materials shown in Figure 2

3.3 Photorefractive Sensitivity

The photorefractive sensitivity of a material is defined as the refractive index change Δn per unit absorbed energy density

$$S = \frac{\Delta n}{\alpha I_0 \tau} \quad \dots (15)$$

where α is the absorption coefficient at recording wavelength λ , I_0 is the incident power density and τ is the crystal response time. Since the response time τ is the dielectric response time multiplied by a function of different parameters such as E_0 , Λ , drift and diffusion lengths (r_E and r_D respectively) then the sensitivity is usually expressed as

$$S = \frac{n_0^3 r}{2\epsilon\epsilon_0} F(E_0, \lambda, r_E, r_D) \quad \dots (16)$$

It can be seen from equation (16) that, since n_0 and r/ϵ are usually approximately constant for a given class of materials, the photo-refractive sensitivity is mainly determined by the recording conditions and the relative lengths of r_E and r_D compared to the grating spacing. The sensitivity reaches a maximum value when $r_E, r_D \geq \Lambda$ and, for a beam ratio of 1 and unit quantum efficiency

$$S_{\max} = \frac{n_0^3 r e \Lambda}{4\pi\epsilon\epsilon_0 h\nu} \quad \dots (17)$$

In materials such as bismuth silicon/germanium oxide and gallium arsenide, this optimum sensitivity can be achieved and can be estimated to be $100 \text{ cm}^3 \cdot \text{kJ}^{-1}$ at a recording wavelength of 500 nm.

Equation (17) shows that the sensitivity is inversely proportional to the dielectric constant of the material, ϵ . This benefits organics since the dielectric constants of these materials can be much lower than those of inorganic materials.

The photosensitivity of various inorganic crystals is plotted against wavelength in Figure 3. The experimental parameters associated with each point on the plot are summarised in Table 2. All the photosensitivities are based on reported experimental results.

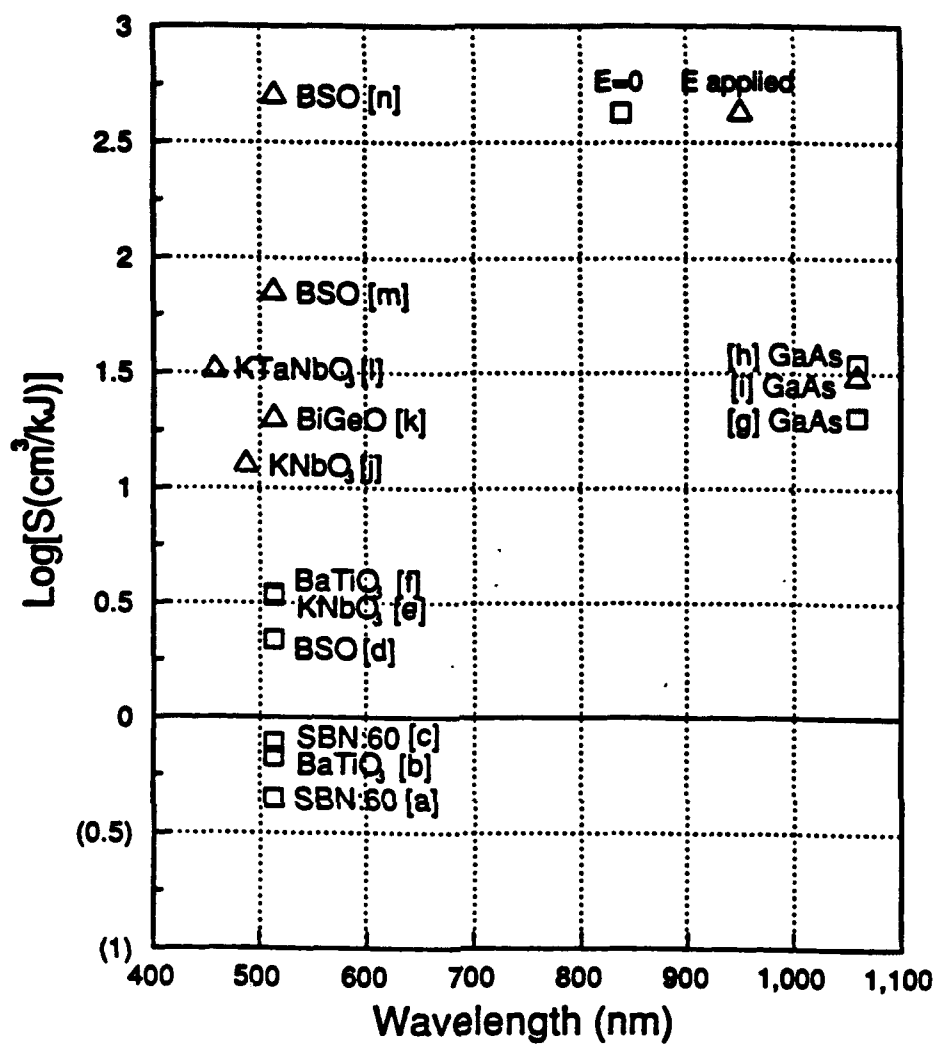


Figure 3: Log sensitivity as a function of wavelength for various materials (see Table 2)

Label in Figure 3	Material	Dopant/ imp density N/cm ³	Wavelength λ/nm	Photo- Sensitivity S/cm ² J ⁻¹	Absorption Coefficient α/cm ⁻¹	Gain Coefficient Γ/cm ⁻¹	Response time τ/nms	Incident Intensity I/W/cm ²	η ^a (kJ/cm ²)	Hall Angle θ/°	Grating Wavelength λ/nm	Applied Field E/kV/cm ⁻¹	Index Modulation Δn	Interaction Length l/nm	Beam Width μm	Refractive Index	Reference
(a)	SBN:60	.011 wt% Co	514.5	0.44*	1	36	333	0.8		18.7	0.8		15 × 10 ⁻⁴	.63	2.5	2.35	[10]
(b)	BaTiO ₃ (0%cat)	N = 10 ¹⁸	514.5	0.68*	3	10			2 × 10 ³				4.1 × 10 ⁻⁴				[7]
(c)	SBN:60	Co N = 10 ¹⁸	514.5	0.77*	2	15			4 × 10 ³				6.2 × 10 ⁻⁴			2.35	[7]
(d)	BSO	N = 10 ¹⁸	514.5	2.2*	1.6	1.4			1.6 × 10 ⁻⁴				0.6 × 10 ⁻⁴			2.5	[7]
(e)	KNbO ₃	Fe	514.5	3.41*			3	1.0								2.22	[10]
(f)	BaTiO ₃ (45° cat)	20 ppm Co	514.5	3.44*	2.2	38.7	21	1.0		25.4	0.6		16 × 10 ⁻⁴	0.87			[10]
(g)	GaAs	Cr N = 10 ¹⁷	1060	20.6*	4	0.5			5 × 10 ⁴				0.42 × 10 ⁻⁴				[7]
(h)	GaAs	N = 10 ¹⁸	1060	35*	1.2	0.4			8 × 10 ⁴				0.3 × 10 ⁻⁴				[7]
(i)	GaAs	Cr N = 10 ¹⁷	1060	30.7*	4	0.9			6 × 10 ⁴			6	0.76 × 10 ⁻⁴				[7]
(j)	KNbO ₃		488	12.5	3.8	2.6					10	7					[11]
(k)	BiOxO		514.5	20	2.1						5	6		1.0			[11]
(l)	KTaNbO ₃		458	33						3.2		10		13.0		2.4	[11]
(m)	BSO		514.5	71	2.3						5	6		1.0		2.5	[11]
(n)	BSO		514.5	490*	2	12			5 × 10 ⁴			10				2.5	[7]

*Photosensitivity calculated using the formula $S = \Gamma \lambda / 4 \pi \alpha l \tau$ [27]

Table 2: Summary of experimental parameters for materials shown in Figure 3

4 CLASSES OF MATERIALS

4.1 Inorganics

Photorefractives are defined as electro-optic materials in which refractive indices are altered by photo-induced space charge fields via the electro-optic effect [11]. The group of materials which show the largest electro-optic effects are the oxygen-octahedra ferroelectrics, and therefore most of the reported work has been undertaken using these materials.

Early work on these materials identified the importance of dopants (originally Fe^{2+} impurities present in the raw materials used for crystal growth) in observing the photorefractive effect. However, whilst many types of dopant have been added in precise concentrations to maximise the photorefractive properties, none have yet been able to match the performance achieved by Fe, as shown in Figure 4.

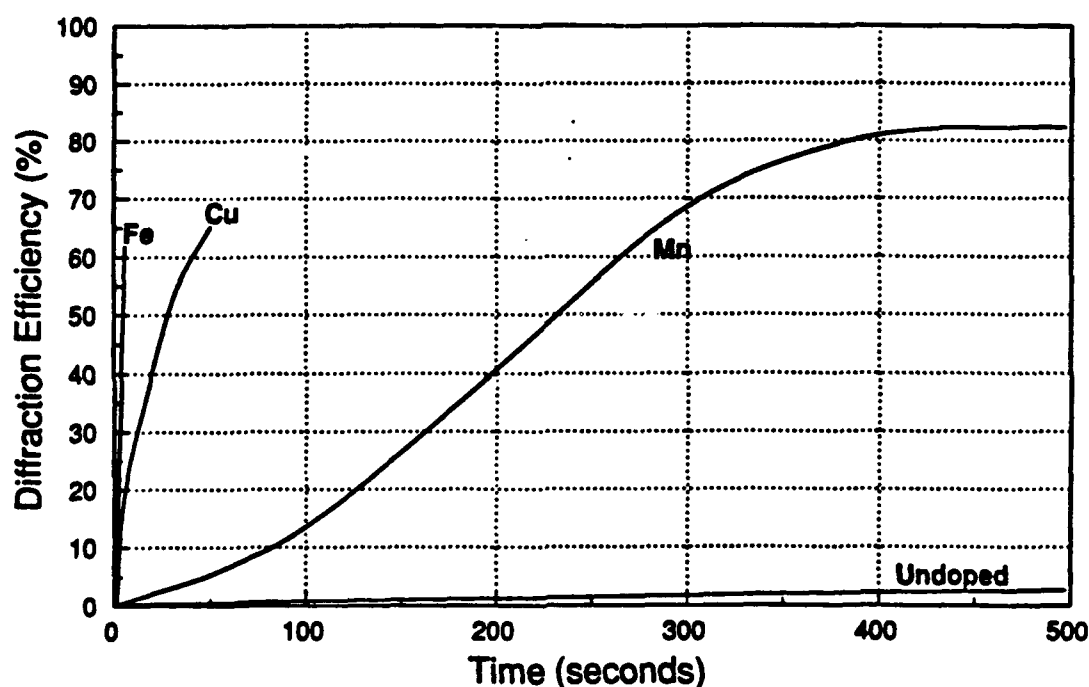


Figure 4: Diffraction efficiency as a function of grating writing time in LiNbO_3 with different dopants [11]

A summary of the most important parameters for a selection of inorganic photorefractive materials is given in Table 3. Much of the literature data is incomplete and in many cases the magnitude of parameters reported by different groups can differ significantly. Every effort has been taken to ensure the data shown in Table 3 is consistent.

Material	Type	Absorption Coefficient/cm ⁻¹	Δn_{max}	λ_{nm}	Trap Density/cm ⁻³	n	ϵ	r_g (pm.V ⁻¹)
SBN:75 (Ce)	Oxide	0.5 [7]		514 [7]	-	2.37 [13]	3400 [13]	1340 [13]
SBN:60 (Ce)	Oxide	2.0 [7]		514 [7]	1×10^{16} [7]	2.36 [13]	880 [13]	235 [13]
BaTiO ₃	Oxide	3.0 [7]	5×10^{-5} [12]	514 [7]	1×10^{16} [7]	2.365 [12]	168 [12]	80 [12]
BSO ($E_g = 0$)	Oxide	1.6 [7]		514 [7]	1×10^{16} [7]	2.5 [14]	56 [14]	5 [14]
BSO ($E_g = 10 \text{ kV.cm}^{-1}$)	Oxide	2.0 [7]		514 [7]	1×10^{16} [7]	2.5 [14]	56 [14]	5 [14]
BGO	Oxide				1×10^{16} [7]	2.55 [12]	47 [12]	3.4 [12]
LiNbO ₃ :Fe	Oxide		1×10^{-5} [12]			2.259 [12]	29 [12]	31 [12]
KNbO ₃	Oxide	3.8 [7]	1×10^{-5} [12]			2.227 [14]		64 [14]
GaAs ($E_g = 0$)	Semiconductor	1.2 [7]		1060 [7]	1×10^{16} [7]	3.5 [15]		1.2 [15]
GaAs: Cr ($E_g = 0$)	Semiconductor	4 [7]		1060 [7]	1×10^{17} [7]	3.5 [15]		
GaAs: Cr ($E_g = 6 \text{ kV.cm}^{-1}$)	Semiconductor			1060 [7]	1×10^{17} [7]	3.5 [15]		
PLZT ($E_g = 10 \text{ kV.cm}^{-1}$)	Ceramic		1×10^{-5} [12]					

Table 3: Important parameters for selected inorganic photorefractive materials
(references shown in square brackets)

4.1.1 Lithium Niobate

The photorefractive effect (originally known as optical damage) was first observed in LiNbO_3 [16]. However, despite being heavily studied since that time, LiNbO_3 is by no means one of the best photorefractive materials; grating formation requires high incident light intensities and is relatively slow. This means that many of the applications discussed in Section 6, such as convolution or those using two or four wave mixing, are not possible using lithium niobate.

Despite these problems the material does have some attractive properties. High quality crystals up to 15 cm long can be grown using the Czochralsky growth technique. These can then be poled to give large, single domain crystals. The dark conductivity is extremely low (typically of the order of $10^{-20} (\Omega\text{cm})^{-1}$) which means that grating storage times of up to 10 years are possible [11]. This, coupled with the fact that the Fe concentration can be chosen to select an appropriate absorption coefficient (α can range from 0.1 cm^{-1} to 100 cm^{-1} [11]) and the size of the refractive index modulation Δn_{max} (as shown in Figure 5), makes lithium niobate a suitable material for holographic storage.

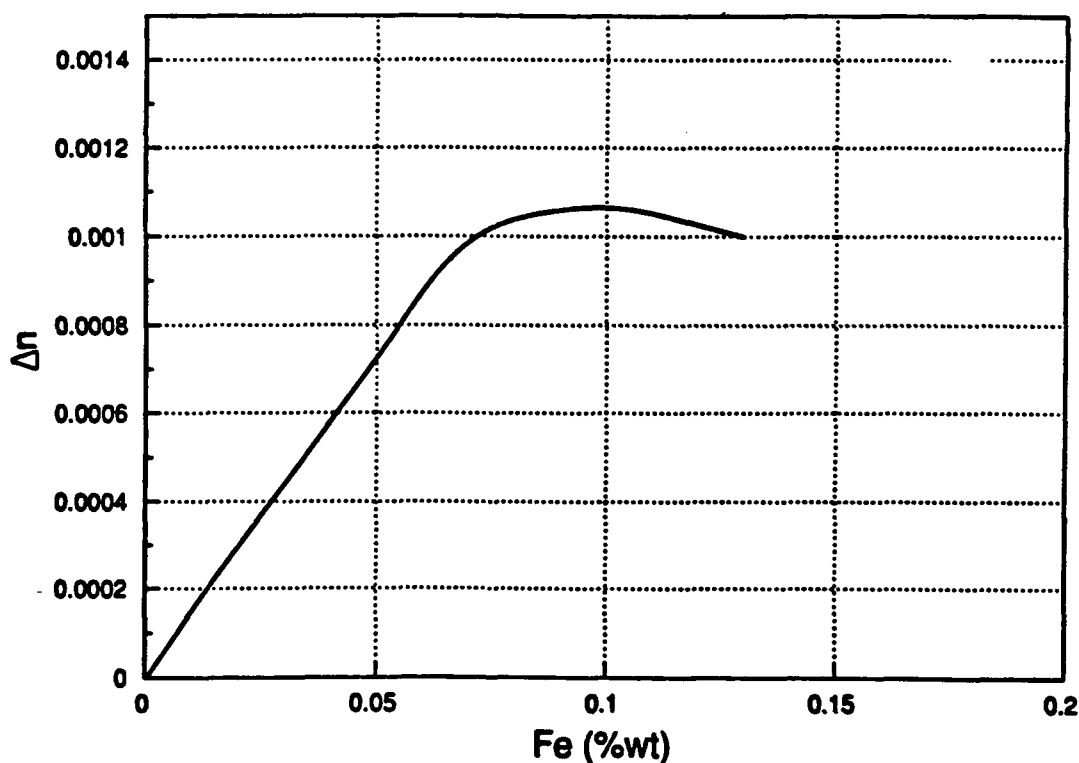


Figure 5: Refractive index modulation as a function of dopant concentration in $\text{LiNbO}_3:\text{Fe}$

4.1.2 Potassium Niobate and Barium Titanate

Both potassium niobate (KNbO_3) and barium titanate (BaTiO_3) have sensitivities several times larger than lithium niobate[17]. These sensitivities can be increased further by applying high voltages to the crystal and therefore allowing charge migration by drift rather than diffusion. However, the sensitivity will only be increased if the period of the grating being written is $\geq 3 \mu\text{m}$. If the grating period is $\leq 1 \mu\text{m}$, diffusion will still dominate and, between $1 \mu\text{m}$ and $3 \mu\text{m}$, both migration processes will contribute. Since the refractive index modulation varies proportionally to fringe spacing for drift, and inversely proportional to fringe spacing for diffusion, it leads to a fairly complicated relationship between refractive index modulation and fringe spacing when both diffusion and drift contribute (see Figure 6) [11]. This applies in general for all photorefractive materials (except lithium niobate, which is not affected by applied fields) and occurs because of the relative magnitudes of grating spacing and charge migration lengths.

These properties make potassium niobate and barium titanate particularly suitable for applications involving phase conjugation or two wave mixing (where good sensitivity is required) such as optical tracking, novelty filtering or associative memory.

Both of these materials are very difficult to grow, with crystal sizes of 1 to 20 cm^3 being the present limit[17]. The dark conductivities are relatively high (of the order of $10^{-13} (\Omega\text{cm})^{-1}$ [11]) so grating storage times are shorter than those in lithium niobate. This means that holographic storage applications are not viable using these materials.

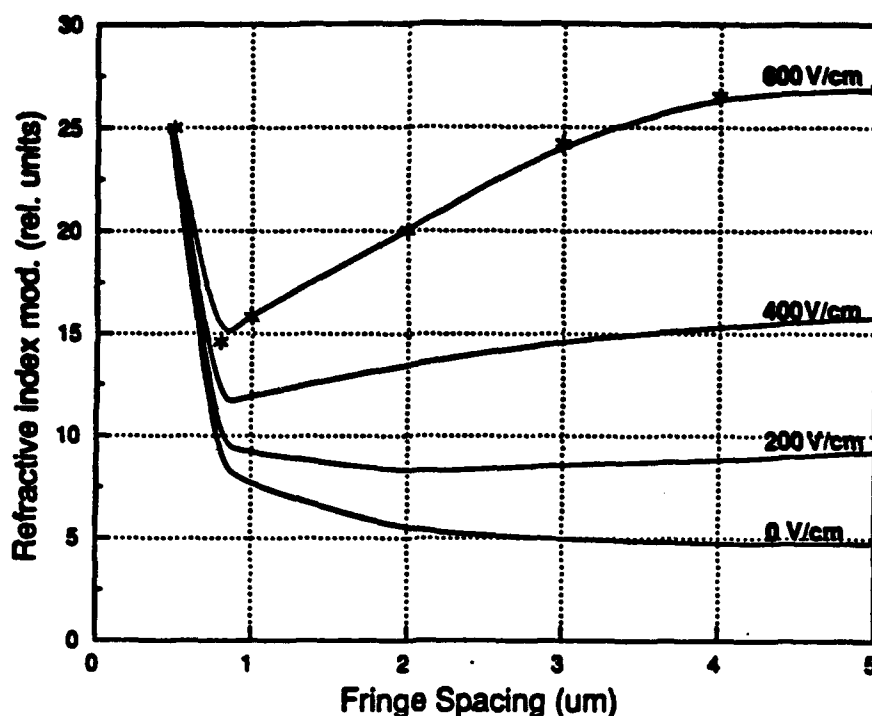


Figure 6: Refractive index modulation as a function of fringe spacing in BaTiO₃ for several different applied field strengths

4.1.3 Barium Sodium Niobate and Strontium Barium Niobate

Barium sodium niobate (BSN) is rarely used since its photorefractive sensitivity is fairly poor. However, strontium barium niobate (SBN) can exhibit a much higher sensitivity. The stoichiometry ($\text{Sr}_x\text{Ba}_{1-x}\text{Nb}_2\text{O}_6$) and the dopant concentration (CeO_2) of SBN dramatically affect both the broadband absorption coefficient and the photorefractive response time, as shown in Figure 7 [18]. Only SBN:60 ($x = 0.60$) and SBN:75 are shown in these graphs (including undoped SBN for comparison), since among the materials investigated to date, these two show the best results.

Although the rate of grating formation in undoped SBN:60 is faster than that of doped SBN:75 (see Figure 7(a)), SBN:75 is still a useful material as it exhibits good sensitivity. Both doped SBN:60 and doped SBN:75 have very high electro-optic coefficients (SBN:60(Ce) has r_{13} of 47 pm.V⁻¹ and r_{33} of 235 pm.V⁻¹, SBN:75(Ce) has r_{13} of 67 pm.V⁻¹ and r_{33} of 1310 pm.V⁻¹ [13]) and this helps to increase the photorefractive sensitivity but they also have low dark conductivities which, whilst resulting in long grating storage times, can reduce the sensitivity. However, these

materials have large quantum efficiencies and this can compensate for the low dark conductivity, increasing the sensitivities to the extent that the performance of these materials approaches that of barium titanate. Thus many trade-offs are involved in determining the overall performance of these materials.

The advantage these materials have over barium titanate is that large single crystals are relatively easy to grow, and to some extent the properties of the crystal can be tailored to meet individual requirements.

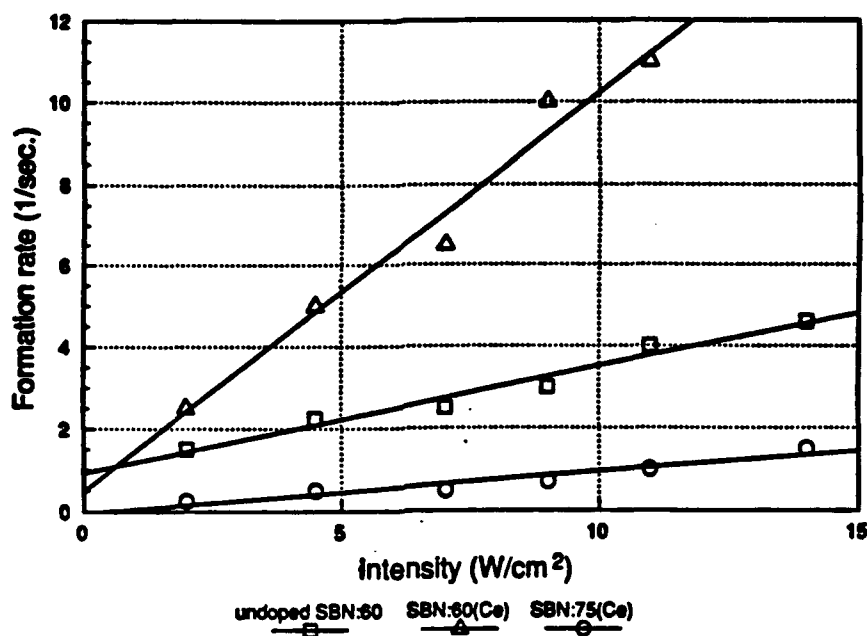


Figure 7(a): Rate of grating formation as a function of incident intensity in SBN

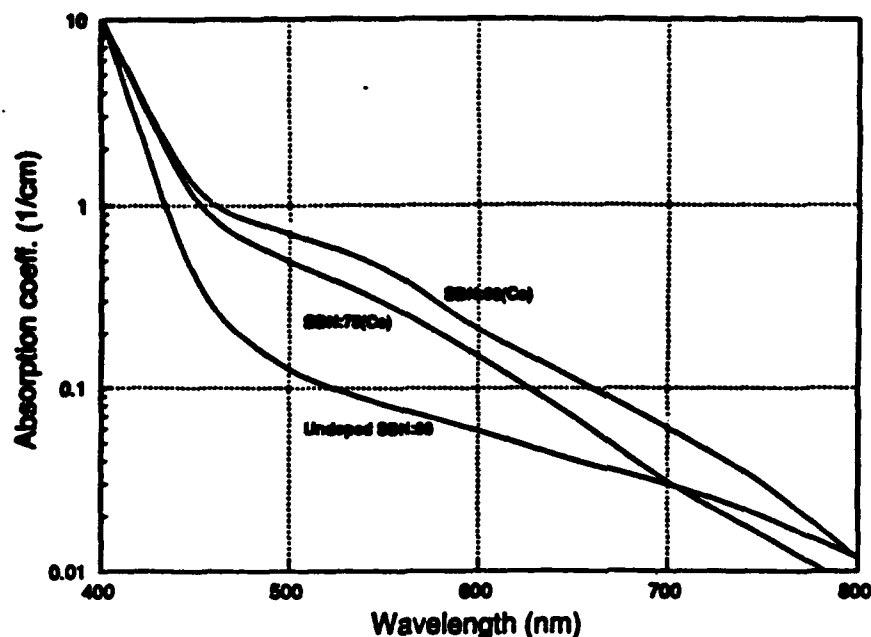


Figure 7(b): Change in absorption coefficient as a function of wavelength in SBN

4.1.4 Bismuth Silicon Oxide and Bismuth Germanium Oxide

Bismuth silicon oxide (BSO) and bismuth germanium oxide (BGO) exhibit strong optical activities, therefore the polarisation states of the incident, diffracted and scattered light are all different. This means that unwanted beams and noise can be removed by using polarisers. However, the photorefractive response of these materials can be optimised by altering the orientation of the input optical beams with respect to the crystallographic orientation of the photorefractive material.

The electro-optic coefficients ($\sim 5 \text{ pm} \cdot \text{V}^{-1}$) and the dark conductivities are small, but the response times are fast and this means that the materials have high sensitivities. However, because the electro-optic coefficients are small the peak diffraction efficiencies are relatively small ($\sim 20\%$). However, diffraction efficiencies of almost 100% can be achieved if an external field is applied under optimised conditions. Applying an external field also enhances the gain coefficient of the material and values as high as 10 cm^{-1} have been reported [19] but, in order to achieve these values, a piezo mirror is required (as detailed in Section 5.1.1) to generate a 90° phase shift between the intensity distribution and the phase grating formed in order to maximise the beam coupling. When diffusion dominates, this 90° spatial phase shift of the phase grating with respect to the incident intensity distribution is a feature of the photorefractive process but, when an external field is applied, the phase shift is moved from the optimised 90° case.

4.1.5 Gallium Arsenide

Chromium doped gallium arsenide (GaAs) has been most widely studied of the group III - V semiconductors. Carrier mobilities in semiconductors are very large and, coupled with good photosensitivities, these materials show fast recording speeds (up to two orders of magnitude faster than BSO [29]) for wavelengths in the region of 0.95 - 1.35 μm . However, the electro-optic coefficients are small and so the magnitude of Δn which can be achieved is small.

Oxygen-octahedra ferroelectrics are generally transparent to approximately 5 μm and so, in theory, they could be used for applications in the infra-red region. However, the quantum efficiency of these materials in the IR is very low because of their large bandgaps [11].

Gallium arsenide has a much smaller bandgap (~ 1.46 eV) and so is much more useful for applications in the infra-red region. This small bandgap does mean that the dark conductivity of gallium arsenide is high (of the order of $10^{-9} (\Omega\text{cm})^{-1}$ [11]) so it cannot be used for applications requiring long storage times, such as holographic memory. The gain coefficient of doped GaAs is still quite small ($\Gamma \sim 1 \text{ cm}^{-1}$ [21]) and only just compensates for the small absorption coefficient of the material in beam coupling experiments. As in BSO and BGO, this gain coefficient can be enhanced by applying an electric field (gain coefficients of 7 cm^{-1} have been reported [15]) but, as in BSO and BGO, a piezo mirror is then required to optimise the spatial phase shift of the grating.

4.2 Organics

Although research into organic photorefractive materials is at an early stage it is already apparent that they could, potentially, offer advantages over inorganic materials. Firstly, organic polymers can have large electro-optic coefficients (up to $\sim 200 \text{ pm.V}^{-1}$) and their dielectric constants are much lower than those of inorganic photorefractives. Bulk samples of polymer can be prepared by standard polymer processing techniques with good uniformity and high optical clarity.

However, to date only four materials have been investigated and reported in the literature. None of these materials have exhibited very large photorefractive effects although results have been encouraging.

The most important parameters of these materials are shown in Table 4, although, as with the inorganic materials, much of the data is incomplete.

Material	Type	Absorption Coefficient/cm ⁻¹	Δn_{max}	λ/nm	Trap Density/cm ⁻³	n	c	$r_f/\mu\text{m}\cdot\text{V}^{-1}$	$n^2 r_f c$ $\mu\text{m}\cdot\text{V}^{-1}$
BisA-NPDA (IBM) [9]	Polymer	32.1		647.1	1.9×10^{15}	1.63	2.9		
COANP:TCNQ [22, 23]	Crystal		$\sim 2 \times 10^{-6}$			1.7	~ 3.4	~ 10	~ 14.0
Kodak [24]	Polymer					1.7	3.9	~ 2	~ 2.5
Arizona University [30]	Polymer			830		1.68	3.9	~ 6	7.4

Table 4: Important parameters for organic photorefractive materials
(references shown in square brackets)

4.2.1 IBM Polymer (bisA-NPDA)

The polymer reported by IBM[9] is formed by reacting bisphenol-A-diglycidylether with the nonlinear chromophore 4-nitro-1,2-phenylenediamine. As a dopant, diethylamino-benzaldehyde diphenylhydrazone (DEH) is then added to form connecting pathways in the polymer for the hopping motion of the holes.

As Figure 8 shows, the diffraction efficiency of this polymer is very low (approximately 10^{-6}) but can be enhanced to some extent by applying an external electric field. The low values of the diffraction efficiency are not unexpected since the electro-optic coefficient of the polymer is very low.

Preliminary results for a different polymer with a higher electro-optic coefficient (also doped with DEH) suggest a diffraction efficiency of 10^{-3} is possible although no details of this material are given.

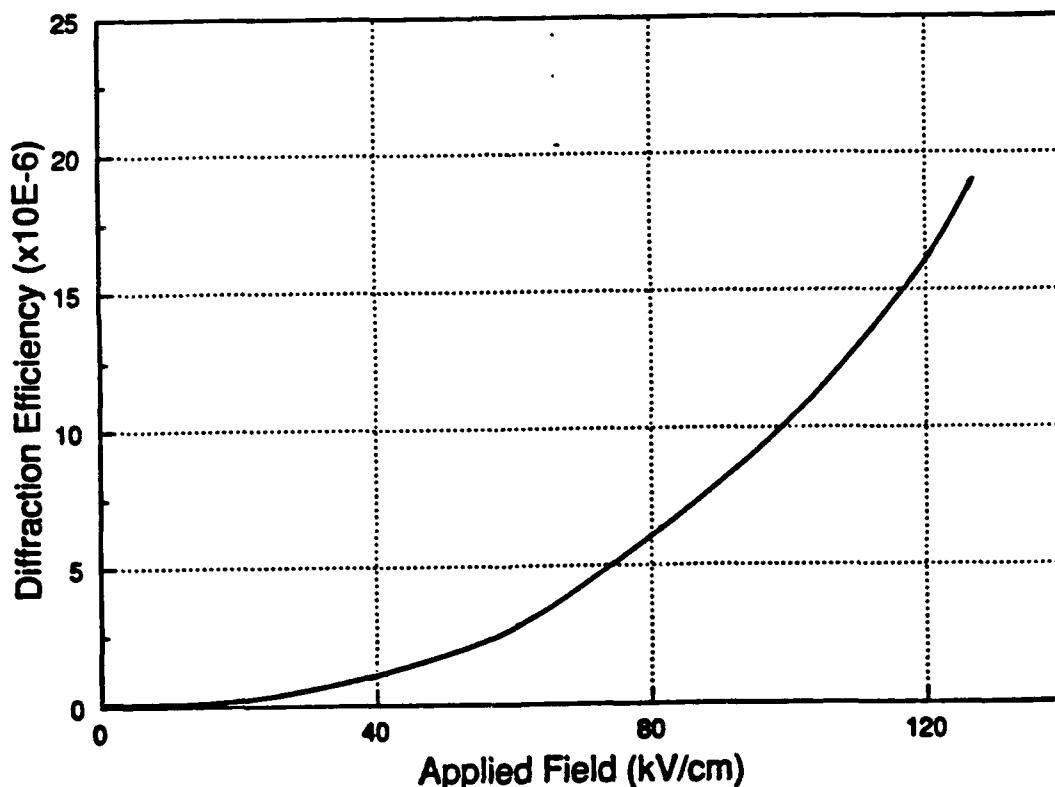


Figure 8: Diffraction efficiency as a function of applied field in bisA-NPDA [9]

4.2.2 COANP:TCNQ

The composition of this material is 2-cyclooctylamino-5-nitropyridine doped with 0.1 wt% 7,7,8,8-tetracyanoquinodimethane [22]. It is worth noting that, unlike the other organic photorefractives in this section, COANP:TCNQ is a crystal rather than a polymer. The maximum diffraction efficiency achieved to date is only 10^{-4} and grating writing times are approximately 20 to 100 minutes [23]. The dark conductivity is $\sim 2 \times 10^{-14} (\Omega\text{cm})^{-1}$ which, although not nearly as low as in lithium niobate, is considerably lower than in many inorganic photorefractives.

4.2.3 Kodak Polymer

This polymer[24] has an acrylic backbone with a 4-dialkylamino-4-methylsulphonyl stilbene side chain. It is sensitized with N,N-bis(2,5-di-tert-butylphenyl)-3,4,9,10- perylene-dicarboximide and doped with 1,1-bis(4-di-p-tolyaminophenyl)cyclohexane. To date, very little information is available concerning this material other than that the electro-optic coefficient is 2.5 pm.V^{-1} . This low value suggests that the diffraction efficiency is likely to be even lower than that of the IBM polymer.

4.2.4 Arizona University Polymer

The most recent report of an organic photorefractive material comes from Arizona University [30]. This is the first report of a polymer which has intrinsic photoconductive (based upon carbazole moities) and electro-optic properties. All previous reports have used the guest-host approach to incorporate a carrier transport agent and/or sensitiser. No direct evidence of a photorefractive effect is reported although the authors' claim that the effect is large enough to observe by direct measurement. Results for electro-optic poling stability, quantum efficiency and photoconductivity are presented. An electro-optic coefficient r_{33} of 6.2 pm.V^{-1} at 830 nm was achieved from one of the samples.

All photorefractive effects require a grating to be formed in the material so that diffraction can occur. This requires the presence of a minimum of two beams (the second beam can either be discrete or a reflection of the first beam). In this section the two key optical configurations on which all the applications are based (two and four wave mixing) are examined in detail. The special case of self pumped phase conjugation is also discussed as this serves to clarify the later discussion on applications.

5.1 Two-Wave Mixing

The recording of phase volume gratings in a photorefractive material results in a stationary energy exchange between the two coherent beams. This occurs as a result of self-diffraction of the reference pump beam by the dynamic phase grating which is produced. As the diffracted wave experiences a $\pi/2$ phase delay with respect to the read beam, maximum energy transfer is achieved when the incident fringe pattern and induced index modulation are shifted by $\phi = \pi/2$. This situation arises when the induced grating is created by the diffusion of charge carriers with no external applied field, as shown in Figure 9.

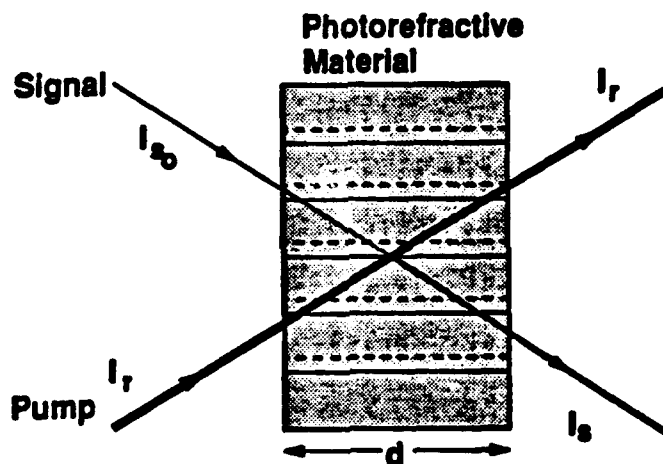


Figure 9: Degenerate two-wave mixing in a photorefractive material showing the maxima of (i) the illumination (continuous line), and (ii) the index modulation (dashed line) with a phase shift ϕ of $\pi/2$.

Applying coupled wave equations to the $\pi/2$ phase shifted component of the induced index modulation, then the coherent interaction between two waves of respective amplitude R and S is given by [2]

$$\frac{dS}{dz} = \frac{1}{2}\Gamma \frac{R^2 S}{R^2 + S^2} - \frac{1}{2}\alpha R \quad ; \quad \frac{dR}{dz} = \frac{1}{2}\Gamma \frac{R S^2}{R^2 + S^2} - \frac{1}{2}\alpha S \quad \dots (18)$$

and the transmitted signal beam intensity which results from the dynamic two beam coupling is given by

$$I_s = I_{s0} \frac{\beta + 1}{\beta + \exp(\Gamma d)} \exp [(\Gamma - \alpha)d] \quad \text{..... (19)}$$

where Γ is the exponential gain coefficient of the interaction and is related to the maximum amplitude of the photo-induced index modulation Δn , by

$$\Gamma = \frac{4\pi\Delta n}{\lambda \cos \theta} \sin \phi \quad \text{..... (20)}$$

where ϕ is the spatial phase shift of the grating (Γ is a maximum when $\phi = \pi/2$). For negligible pump depletion, the transmitted beam intensity reduces to

$$I_s = I_{s0} \exp [(\Gamma - \alpha)d] \quad \text{..... (21)}$$

Thus, when $\Gamma > \alpha$, the incident signal exhibits gain. The magnitude of the energy transfer can be determined experimentally by measuring the effective gain γ_0 where

$$\gamma_0 = \frac{I_s \text{ with pump beam}}{I_s \text{ without pump beam}} \quad \text{..... (22)}$$

which, for the undepleted pump case, can also be written as

$$\gamma_0 = \exp(\Gamma d) \quad \text{..... (23)}$$

Hence the value of Γ can be determined experimentally. In materials where charge carriers move by diffusion the index modulation phase shift ϕ is $\pi/2$, Δn can be large and so Γ can be large ($\sim 20 \text{ cm}^{-1}$). However, in materials where an external electric field is applied and the charge carriers drift, the phase shift ϕ can be less (or more) than the optimum $\pi/2$ and so only very low beam coupling ($\Gamma \sim 1 \text{ cm}^{-1}$) is achieved. However, as described below, this phase shift can be restored to the optimal $\pi/2$ value by moving the fringe pattern in the photorefractive at a constant velocity, a technique referred to as nearly degenerate two-wave mixing.

5.1.1 Nearly Degenerate Two-Wave Mixing

A schematic diagram of a typical arrangement for nearly degenerate two-wave mixing is shown in Figure 10. The reference pump beam is reflected off a piezo mirror driven by a saw-tooth voltage. As a result the frequency is shifted a small amount $\delta\omega$ and a moving fringe pattern results. The speed is adjusted so that the index modulation is recorded in the material at all times, but with a spatial phase shift with respect to the interference fringes. The flyback time of the piezo mirror must be

significantly shorter than the grating response time. Also, to ensure the grating remains coherent, the mirror must flyback to a well defined position with respect to the grating.

The optimum fringe velocity depends on the recording time constant τ , and when an interference pattern moving at velocity v is introduced into the coupled wave equations, the resulting gain coefficient Γ is given by

$$\Gamma = \frac{4\pi\Delta n}{\lambda \cos \theta} \frac{Kv\tau}{(1 + K^2v^2\tau^2)} \quad \dots (24)$$

The optimum fringe velocity required to achieve efficient energy transfer is $v_0 = \Lambda(2\pi\tau)^{-1}$ which corresponds to a frequency shift of the reference beam by $\delta\omega = \tau^{-1}$.

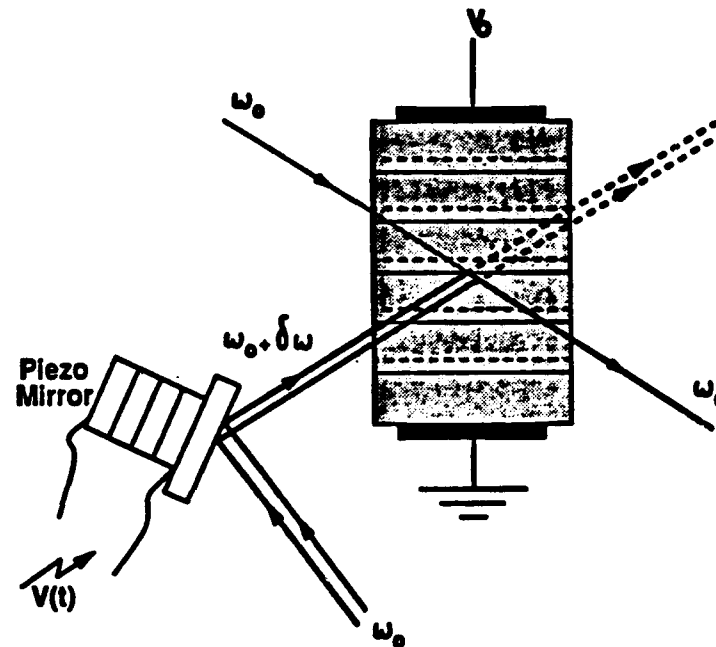


Figure 10: Schematic diagram of nearly degenerate two-wave mixing

An alternative technique for achieving an optimal $\pi/2$ spatial shifting of the grating is to apply an ac field to the photorefractive material. The charges preferentially drift in one direction for the first half cycle of the applied field and in the opposite direction for the next half cycle. Thus the build-up of the space charge field is intensified over that achieved by diffusion alone but the refractive index grating has the same average $\pi/2$ phase shift as if no drift field were present.

5.2 Four-Wave Mixing

As the name suggests, four-wave mixing involves the interference of four beams in a medium. Three of these are input beams; one of which is the object beam and the other two are reference beams. The reference beams usually travel in opposite directions to

each other and have the same frequency as the object beam. The object beam may enter the photorefractive material from any direction. The fourth beam, which is an output beam, is the phase conjugate of the object beam and emerges along the same line as the object beam but with a reversed direction of propagation. This situation is shown schematically in Figure 11.

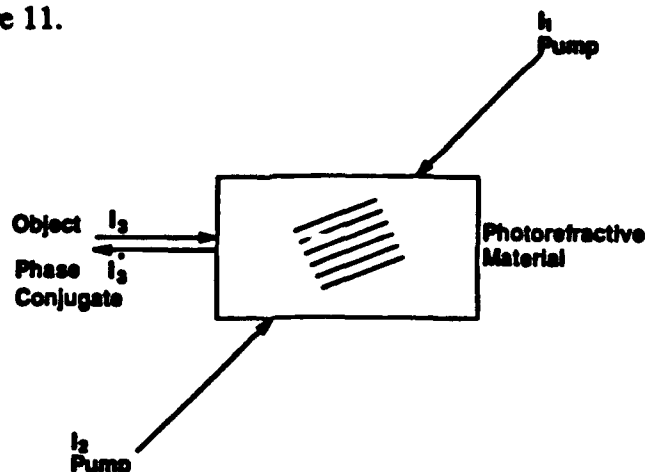


Figure 11: Schematic diagram of four-wave mixing

The conjugate (fourth) beam is produced by perturbations in the medium due to interference of the object beam with one of the reference beams. All the information about the phase of the object beam is stored as an interference pattern. The second reference beam is reflected by the interference pattern and reads the stored phase information. As the second reference beam comes from a direction opposite to that of the first one, the reflected beam is the phase conjugate of the signal beam.

Phase conjugate mirrors have many applications in 'cleaning up' beams of light which have passed through distorting media - the phase distortion can be removed by allowing the wavefront to travel back through the same medium. Amplification of the phase conjugate signal can also be achieved by energy transfer with one of the pump beams. This occurs in the same way as described earlier for two-wave mixing.

5.2.1 Nearly Degenerate Four-Wave Mixing

This process employs a moving grating and is very similar to that of nearly degenerate two-wave mixing described in Section 5.1.1. However, two extra parameters are of interest in four wave mixing;

- (i) the pump beam ratio $\beta = I_{P2}/I_{P1}$, and
- (ii) the polarisation of the "reading" beam I_{P2} .

The conjugate beam reflectivity is dependent upon both of these factors. For example, higher reflectivities are obtained in GaAs with an asymmetric pump beam ratio ($\beta < 1$) and crossed polarisation of the pump beams.

5.3 Self-Pumped Phase Conjugation

In 1982 Feinberg [25] observed that with an image bearing beam incident on a crystal of barium titanate, the two counter propagating pump beams could be blocked off without any deleterious effect on the intensity of the phase conjugate beam. On investigation it was found that the pump beam which was required to form the phase conjugate signal was generated via amplified scattering and total internal reflections from the crystal-air interfaces.

The image quality of the self-pumped phase conjugate beam can be far better than that generated using external pump beams. Theory suggests that to reconstruct a high quality phase-conjugate replica of an incident image beam the pumping beams must be phase conjugates of each other. In practice this can be difficult to achieve since the surface quality of the crystal can distort the quality of the pump beam. No such problem is encountered when self-pumping occurs and reflectivities up to 0.7 can be achieved on materials such as BaTiO_3 .

6 APPLICATIONS

Photorefractive materials have potential for many applications in the field of coherent optics. Each class of materials has strengths and weaknesses, and therefore careful selection of the appropriate material for a given application is necessary.

In this section several of the most important applications are discussed. Some have been successfully demonstrated in a laboratory, whereas others are still far from being realised.

6.1 Coherent Beam Excisor

As coherent light travels through a photorefractive material, some of that light is scattered by defects in the lattice [26]. This scattered light then interferes with the main body of light and produces self-enforcing phase gratings in the crystal via the photorefractive effect. Normally, the diffraction efficiencies of these gratings remain very small since the percentage of the light scattered by defects is very small, and the effect these gratings have on the main body of light is negligible. However, if the wavelength of the light is close to an absorption peak (i.e. high quantum efficiency) and the material has a high sensitivity the diffraction efficiency of the induced gratings can become relatively large so that they diffract a significant proportion of the incident light.

This effect will occur at defect sites throughout the crystal, causing the incident light to fan out over a wide area.

One possible application of this effect [26] is in laser protection for optical sensors (including the eye) since, while coherent light is diffracted in the material and fans out, incoherent light passes straight through with little effect (see Figure 12).

The response time of the effect depends on the intensity of the incident light and on the sensitivity of the material being used at the irradiance wavelength. From laser hazard classification charts we can estimate that an intensity of approximately $1 \text{ mW.cm}^{-2} \text{ cw}$ represents a laser hazard to the eye, and hazardous effects will be seen with an exposure of a few microseconds. This means that for this application to be viable a photorefractive material with a response time of $1 \mu\text{s}$ at 1 mW.cm^{-2} incident intensity would be required. However, even bismuth silicon oxide which is one of the most sensitive materials (and therefore has one of the fastest response times) can only theoretically achieve response times of 0.1 ms at 1 W.cm^{-2} incident intensity [4]. Since response rate scales linearly with incident intensity, it can be seen that this is equivalent to a response time of approximately 0.1 seconds at 1 mW.cm^{-2} incident intensity, which is five orders of magnitude too slow for this application.

However, in many systems requiring laser protection there is an image plane in the optics, through which all the light entering the system must pass before reaching the sensor (for example, night vision viewers have such a configuration). At this point, light from a collimated source (i.e. a laser) will be focussed down to a very small area so, if the initial aperture is $1 \times 1 \text{ cm}^2$ (say), and in the focal plane this light is focussed down to $10 \times 10 \text{ }\mu\text{m}^2$ this will increase the power density by a factor of 10^6 . Thus 1 mW.cm^{-2} entering the system will become 1 kW.cm^{-2} in the focal plane and so a photorefractive material placed in this plane would only be required to respond in $1 \text{ }\mu\text{s}$ at incident intensities 1 kW.cm^{-2} . This is theoretically possible in materials such as bismuth silicon oxide or gallium arsenide, although gallium arsenide is opaque at visible wavelengths and could therefore only be used for IR systems.

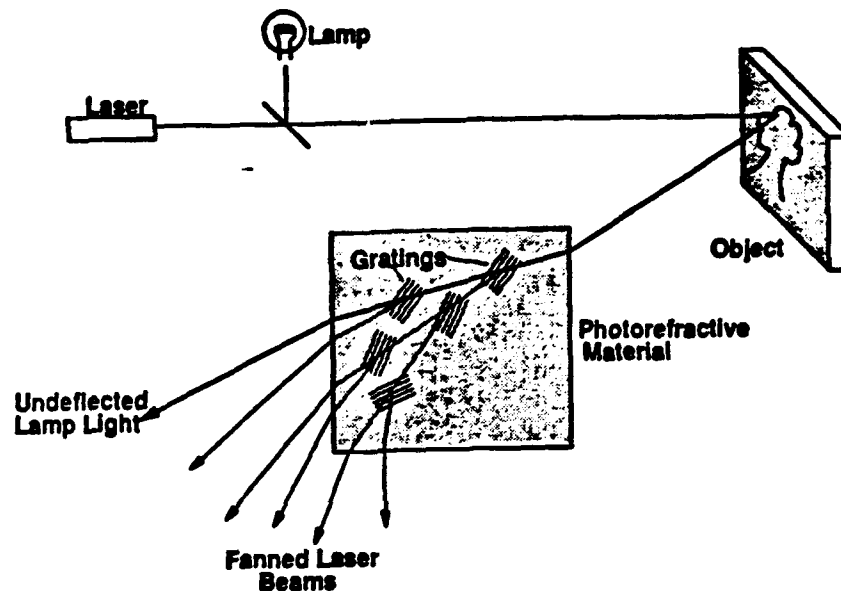


Figure 12: Coherent beam excisor

6.2 Novelty Filter

In a two wave mixing system the spatial phase shift of the refractive index modulation with respect to the intensity distribution of the incident light means that it is possible for energy to be transferred between the beams[2]. If the gain coefficient Γ of the material is large enough, and if both incident beams are approximately the same intensity, almost all of the energy from one beam can be drawn into the other.

Figure 13 shows a configuration which makes use of this two beam interaction. The liquid crystal display (LCD) is arranged as a phase modulating device, receiving real time image information from a camera. The LCD phase modulates beam 2 which continues on

and interferes with beam 1 in the photorefractive material, setting up a phase grating. The grating couples the two beams together and allows energy transfer from beam 2 to beam 1.

The system is configured so that under steady state conditions all of the energy in beam 2 will be transferred to beam 1, and the CCD camera placed in the path of beam 2 will detect nothing. However, if any of the information on the LCD changes, the phase modulation of beam 2 will change and when this interferes with beam 1 in the photorefractive material the intensity distribution will be different to the original distribution. This means that a new phase grating (corresponding to the altered intensity distribution) will be written in the photorefractive. However, since the photorefractive has a finite response time, for the period of time during which the altered phase grating is being written those parts of beam 2 which have changed will not be coupled to beam 1 and so will be detected by the CCD array. Thus only moving objects will be detected by the CCD array. In effect, the novelty filter performs the time derivative of an image in parallel.

The slowest material response time required for this application is of the order of 100 ms. This can be achieved using undoped KNbO_3 and illuminating with an incident intensity of 1 W.cm^{-2} . However, this novelty filter function can also be fairly easily implemented using conventional digital electronics, for example, a frame-store and a computer.

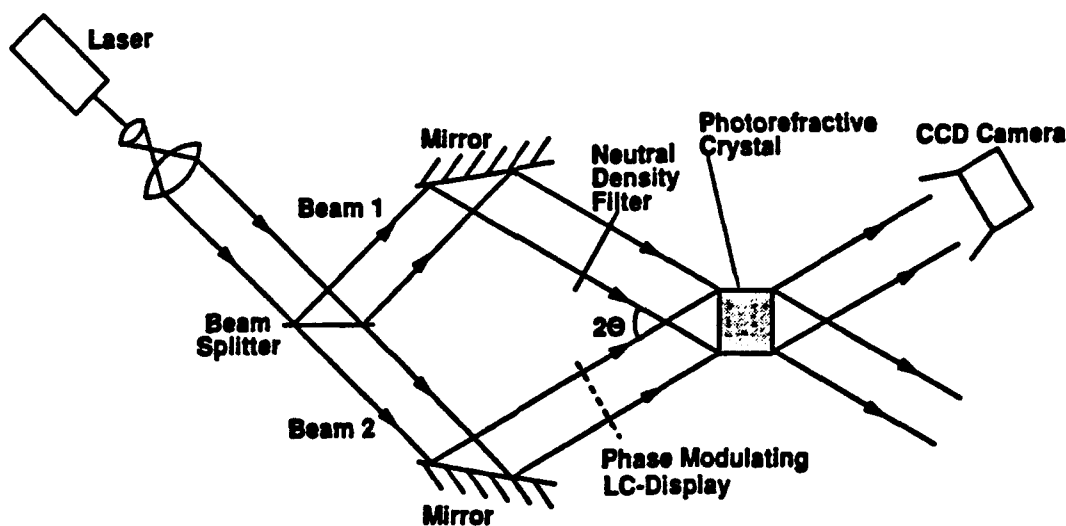


Figure 13: Novelty filter

6.3 Convolution and Correlation

Mathematically, the multiplication of two functions in the Fourier plane is exactly equivalent to the convolution of the two functions in the real plane. Therefore convolution is realisable by using a lens to Fourier transform two images (U_1 and U_2 , say) and coherently interfering their two Fourier transforms. If the intensity distribution generated is recorded in a photorefractive material it can then be read out by another laser (non-coherent with the writing light), inverse Fourier transformed and imaged to give convolution information. Figure 14 shows a setup which could be used to implement convolution, where images can be fed into the system using two spatial light modulators to encode the incident beams with the image information U_1 and U_2 , and convolution information read out in parallel. The blocking filter is a simple dichroic mirror which reflects strongly at 514 nm but is transmissive at 633 nm. This then stops U_1 and U_2 from being imaged at the output plane and obscuring convolution information.

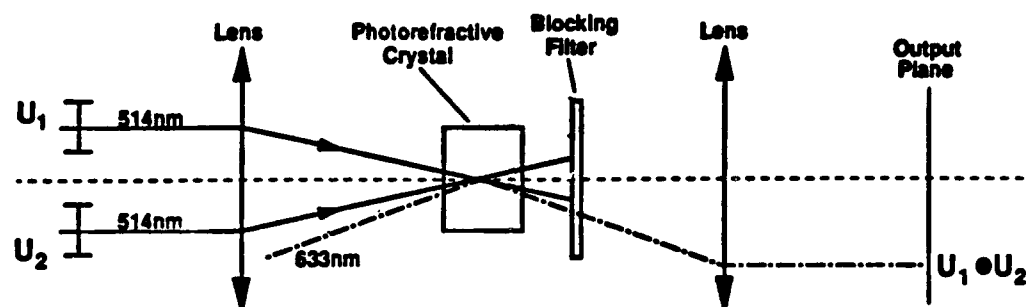


Figure 14: Schematic diagram of an optical correlator

The speed of the system will be limited by the frame rate of the spatial light modulators which encode the write beams in fast photorefractive materials. Currently, state of the art 176×176 electrically addressed spatial light modulators have a frame rate of 1 kHz which is equivalent to 1 ms per comparison. However, there is a much simpler method of performing correlation (using two spatial light modulators (SLMs)) which does not require a photorefractive material. This is known as a Vander Lugt correlator and is shown in Figure 15. An image (equivalent to U_1 in the previous system) is displayed on SLM1 which is interrogated by coherent light and encodes that light with image information. This is then Fourier transformed by the lens and presented to SLM2 which is displaying the Fourier transform of the image to be correlated with U_1 (this is equivalent to $F(U_2)$). The second lens then inverse Fourier transforms the reflected light giving the correlation of U_1 with U_2 in the plane of the detector array.

The disadvantage of this system is that the alignment of the two SLMs is critical, whereas in the system containing the photorefractive material it is not. The system containing the photorefractive material does still have alignment problems since the read beam must enter the photorefractive material at the Bragg angle for efficient diffraction from the phase grating. Therefore there is little point in making a correlator system more complex by adding a photorefractive material when it does not solve the alignment problems of simpler systems.

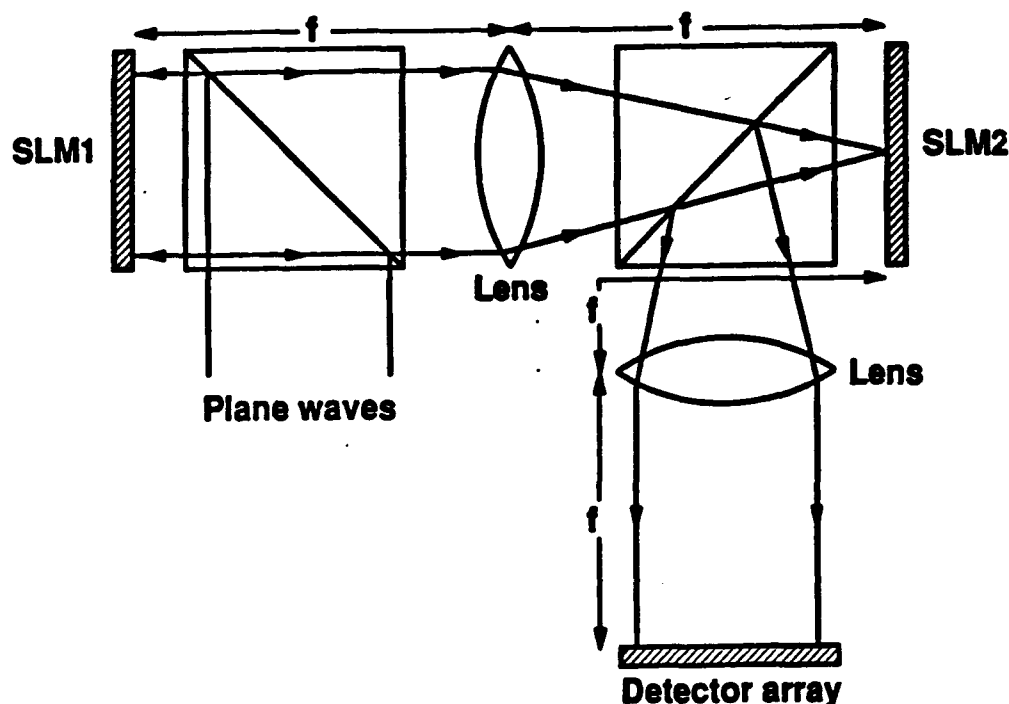


Figure 15: Vander Lugt correlator

6.4 Phase Conjugate Optical Tracking

The principle of this system is to lock a laser beam onto an object and follow it as it moves, either to track it or to focus a substantial quantity of laser power onto it. The potential advantage of using a phase conjugate mirror to do this is that it is self-targeting and compensates for phase aberrations which would normally be induced in the laser beam by the amplifying medium.

Figure 16 shows a system which could theoretically be used for optical tracking [27]. The low power laser illuminates the object, causing light to be scattered from it. Some of this scattered light is captured by the focussing element and directed through the amplifying medium to the phase conjugate mirror (a photorefractive material set up for

four wave mixing). On the first pass through the amplifying medium the reference wavefront will be aberrated by imperfections in the medium, then will be "time reversed" by the phase conjugate mirror and as the wavefront passes back through the amplifying medium the aberrations will be removed. This amplified beam now travels back along the path of the scattered light to the object. If the gain of the amplifier and the reflectivity of the target are sufficiently high it is possible to set up a resonant cavity where the target acts as one reflector and the phase conjugate mirror acts as the other. In this mode the beam will track the target as it moves, as long as the response time of the photorefractive material is sufficiently fast and the transmission losses (including divergence) are sufficiently low.

One method of attempting nuclear fusion (inertial confinement) is to direct many very high power lasers at polymer pellets containing small amounts of deuterium and tritium as they drop through a vacuum chamber. The high optical input powers explosively compress the pellet and produce extremely high temperatures, causing fusion of the nuclei. At present, all of these lasers have to be directed towards each pellet simultaneously but, if each laser was replaced with a phase conjugate tracking system, then the lasers would be self targeting on the pellets dropping through the chamber.

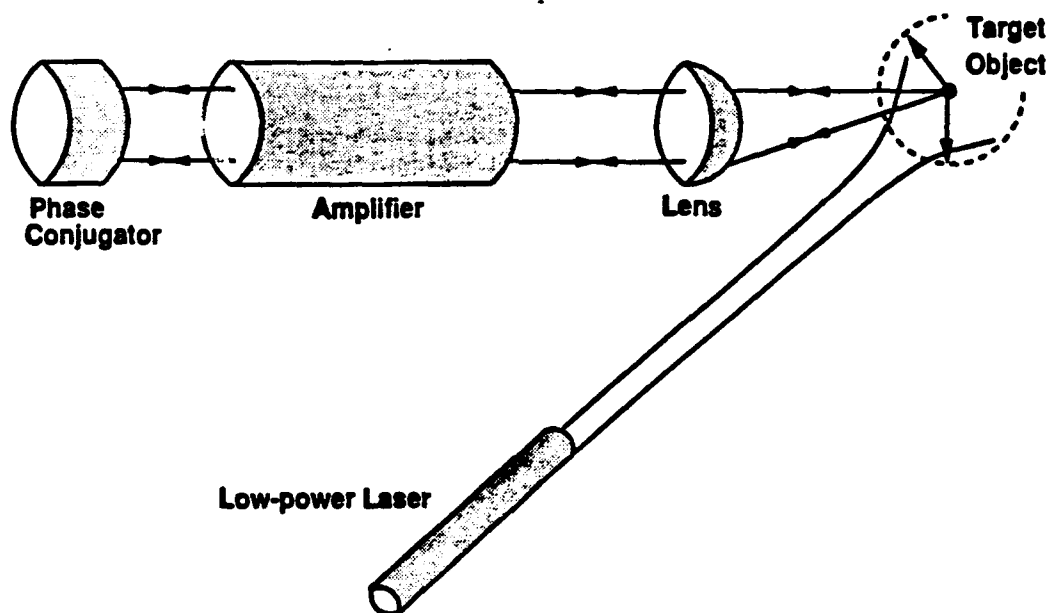


Figure 16: Phase conjugate optical tracker

6.5 Frequency Locking of Lasers

Phase-locking lasers enables a single output mode to be obtained where coherence can be achieved despite large differences in amplifier characteristics and optical path lengths [28]. A basic optical configuration which can be used to lock several independent laser sources is shown in Figure 17. The master laser supplies the two counter-propagating pump beams necessary for four wave mixing in a photorefractive material. The beams from the slave lasers intersect the pump beams in the material, causing it to act as a phase conjugate mirror with gain, and resonant cavities are set up between the phase conjugate mirror and the mirror's M1. Because of the phase conjugating properties of photorefractive materials in this configuration, any phase aberrations caused by inhomogeneities in the laser amplifying media and differences in optical path lengths are compensated for.

The number of lasers that can be locked together using this method is limited by the gain of the photorefractive material since each individual beam entering the material should have a phase conjugate reflectivity close to unity. Another factor limiting the system is the maximum laser power the photorefractive will accept before optical damage occurs.

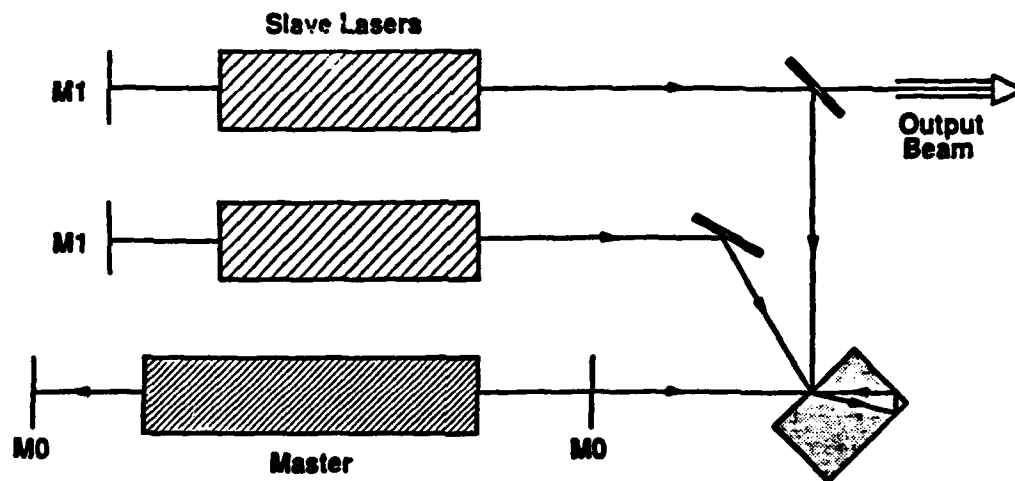


Figure 17: Optical setup for mode locking lasers

6.6 Holographic Storage

Holography, in general, is just a method of encoding and storing information. Its advantage over electronic storage methods is its ability to store very large quantities of information in a small area. For example, according to Rajbenbach et al [2], a thin holographic material (one where the holographic fringe spacing is large relative to the

recording medium thickness) with dimensions $1 \text{ mm} \times 1 \text{ mm}$ can store approximately 10^4 bits of information in a single hologram. In thick holographic materials, light will only be diffracted if it is incident at the Bragg angle so angular encoding of information can be introduced and up to 500 holograms can be stored in a 1 mm^2 area. This gives a storage capability of 0.5 Gbits.cm^2 [2].

Figure 18 shows a possible arrangement for a holographic memory [11]. The beam deflector is fed by a laser and is able to optically address each individual segment of the fly's eye lens separately. The optics of the system are configured so that each segment of this lens, when addressed, will focus the light onto a different area of the storage medium. This light illuminates a binary, electrically addressed spatial light modulator (SLM) on its path towards the storage medium and is spatially encoded with data (shown in a simplified form as "data in" in Figure 18). The encoded beam interferes with the reference beam in the storage medium to produce a hologram. Hence many different, spatially distinct holograms can be written in the storage medium by addressing different segments of the fly's eye lens.

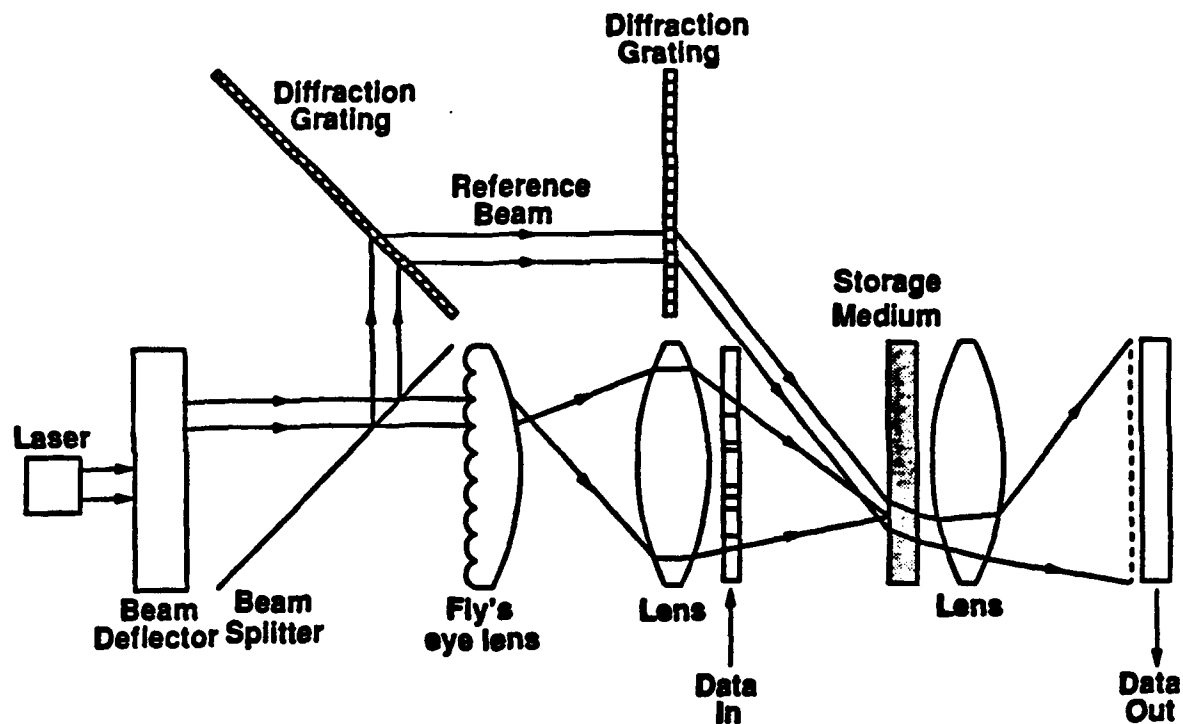


Figure 18: Implementation of holographic storage

To read out any of the data blocks, the hologram can be illuminated by the relevant reference beam alone, and the diffracted light imaged onto a CCD array, shown here as "data out". This diffracted light will be a replica of the data originally displayed on the SLM.

The arrangement in Figure 18 would be suitable if either thin or thick holographic materials were being used as the storage medium. However, in the case of thick holographic materials many holograms could be recorded at each spatial position by varying the angle of the reference beam (as discussed previously), significantly increasing the storage capacity.

To date, the main disadvantage of this type of memory has always been the read-only nature of conventional holographic materials once the information has been stored. However photorefractive materials are erasable, and therefore have the potential to become a viable alternative to electronic storage systems.

6.7 Associative Memory

A system configured to perform as an associative memory is one where information presented to the system is compared to several sets of stored information, and on successive iterations converges towards one stored information set.

This system can be realised using phase conjugate mirrors and a holographic memory element, as shown in Figure 19. The information sets (in this case images) to be stored as memory are recorded in the holographic medium as described in Section 6.6, where angular encoding of the reference beam during recording separates the different images [2]. This hologram can now be placed in the configuration shown in Figure 19.

A corrupted or partial image presented to the system passes through the holographic memory and generates diffracted beams which correspond to the angularly separated reference beams used to store the original images. The relative intensities of these beams will depend on how close the corrupted image is to each of the stored images. These reference beams are amplified by phase conjugate mirror 2 and reflected back through the hologram to generate complete reconstructions of their relative images which, after reflection from phase conjugate mirror 1, pass back through the holographic memory and regenerate the reference beams. This cycle iterates with the most intense reference beam and reconstruction, gradually drawing all of the power from the others until it is the only one left.

Although this system may not be able to outperform correlators (optical or electronic) without using very high power lasers to decrease the response time of the phase conjugate mirrors, it does have one major advantage. By replacing the hologram with a photorefractive material configured as a holographic memory, real time modification would be possible, in effect introducing the potential for learning to the system.

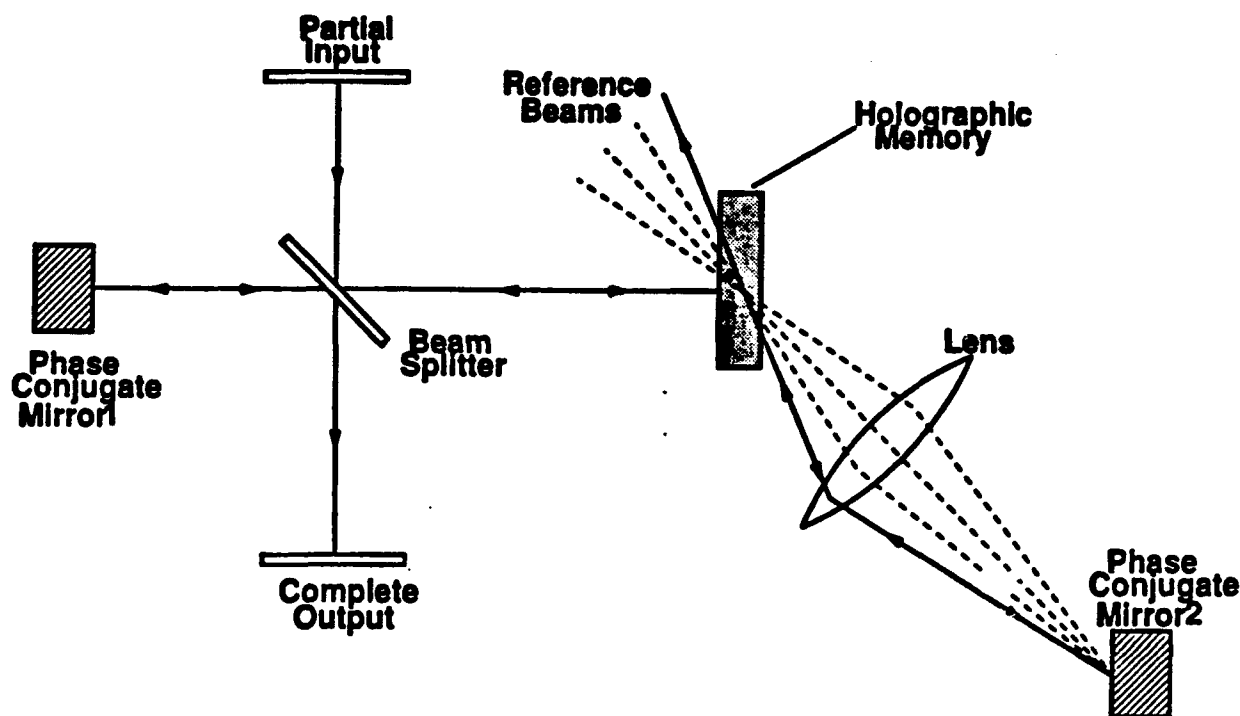


Figure 19: Implementation of associative memory

6.8 Beam Steering

When a photorefractive material is being pumped by two counter-propagating laser beams it will act as a phase conjugate mirror with gain. However, defects in the lattice will scatter some of the light from the pump beams in all directions. If any of the scattered light hits a reflective surface and returns to the photorefractive material it will be amplified and phase conjugated, sending a more intense beam back to the point it was reflected from. This process will continue until the system reaches a steady state and a resonant cavity has been set up between the photorefractive material and the reflecting surface.

If a spatial light modulator is added to this system (see Figure 20) individual pixels can be made to absorb or reflect light and therefore set up resonant cavities[2]. With the

phase conjugate reflectivity of the photorefractive less than unity some of the light in the resonant cavities will pass through the crystal and out the other side. The deflection angle will depend on which SLM pixel it originated from.

One possible application for photorefractive beam steering is for the scanning element in a laser radar system. Possible requirements for such a system are given below.

- Laser wavelength - cw : 10.6 μm , 1.06 μm , 830 nm.
- pulsed 10.6 μm , 1.06 μm , 830 nm.
- Laser power - cw : ~kW
- pulsed ~100 mJ over 10 ns (1.06 μm).
Pulse rate 10 kHz.
- Frame size : 100 \times 100 pixels.
- Frame rate : ~1 Hz
- Scanning range : ~40° \times 20°

Conventional scanners for laser radar include moving galvanometers, spinning polygons and flapping mirrors. These generally scan in a set pattern and do not allow scanning back to regions of interest. If a Bragg cell (acousto-optic deflector) is employed, the scan can take any form but these devices have low scanning ranges (typically 5-10°). In order to increase the range to 40°, a telephoto lens (e.g. $\times 4$) would need to be added to the system. This would decrease the linearity of the system and reduce the cross-sectional area of the scanning beam.

Since a fast photorefractive material which is sensitive at 10.6 μm does not currently exist, photorefractive beam steering at 10.6 μm is not an option at present.

However a practical system could be achieved for a pulsed laser radar operating at 1.06 μm . At this wavelength the system could employ a GaAs photorefractive with a field applied and nearly degenerate mixing to form the grating. The 100 mJ pulse over 10 ns corresponds to a peak power of ~10 MW. From Figure 2, the response time of GaAs at this intensity is picoseconds. Therefore there is sufficient time for the grating to be set-up in each pulse.

SLM used. If a ferroelectric liquid crystal SLM is employed, the response time of each pixel would be $\sim 100 \mu\text{s}$. For a 64×64 pixel array, with each pixel sequentially addressed, this would correspond to a frame rate of 2.5 Hz. While this is an acceptable rate, a faster frame rate could be achieved if a faster SLM was employed.

The scanning angle available will depend on the size and separation of the SLM from the crystal but could potentially be higher than the $40^\circ \times 20^\circ$ required.

If the laser radar is to be "eye safe", a wavelength of $\sim 2 \mu\text{m}$ would be preferable. While it is possible that GaAs could be used as a photorefractive at this wavelength there is not enough information to predict its performance.

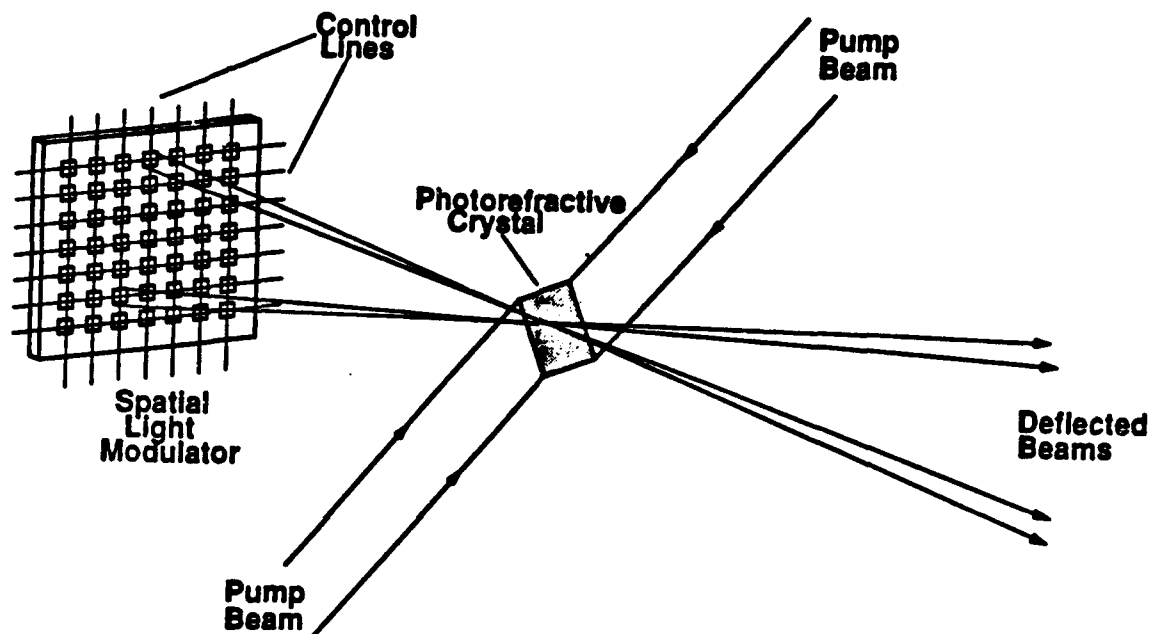


Figure 20: Beam steering using an SLM

6.9 Edge Enhancement

In the straightforward four wave mixing configuration, edge enhanced images are produced if the image-bearing beam is much more intense than the two pump beams [11]. This occurs because the amplitude of the refractive index modulation in the photorefractive material (and therefore the diffraction efficiency of the phase grating) is directly proportional to the amplitude of the intensity modulation caused by the interference of the image bearing beam with the pump beams. Therefore, if the pump beams are weak, the interference patterns they form with both bright and dark areas of the image bearing beam will have only small intensity variations (due to the inequalities of the beam strengths) and so will form phase gratings with low diffraction efficiencies.

Only areas of the image where there are dark to light transitions (so that the image beam intensity is equal to the pump beam intensity) will form gratings with large diffraction efficiencies. This results in an edge enhanced phase conjugate image.

The only real drawback with this application is that it can also be implemented electronically using nearest neighbour comparison routines.

6.10 Beam/Image Amplification

In principle this is perhaps the simplest application of photorefractive materials and therefore has the potential to be developed into a useful system. Essentially, beam/image amplification is degenerate two-wave mixing (as described in Section 5.1) with a few minor alterations. For beam amplification, if the pump beam is much more intense than the probe beam, energy transfer from the pump beam to the probe beam can be used to amplify the probe beam many times over. In this way an intense beam with a very messy wavefront can be used to amplify a weak beam with a planar wavefront giving an intense beam with a planar wavefront. Or, if the probe beam is encoded with image information, this image will be amplified by the pump beam.

In practice, the system is likely to be less straightforward to implement since in many of the faster, more sensitive photorefractive materials (such as BSO and GaAs) external fields must be applied to give high beam-coupling coefficients. This in turn alters the spatial phase shift of the index modulation which means that a piezo mirror is needed to recreate the required phase shift (i.e. nearly degenerate two-wave mixing).

6.11 Waveguide Applications

The applications of photorefractive waveguides can be split into two. Firstly there are those applications which have traditionally been investigated using thick bragg gratings formed by either acousto-optics or electro-optics. To form the grating in planar waveguides, two beams are symmetrically arranged relative to the normal to the polar axis. An interference pattern will be formed along the polar axis, which should lead to the formation of a phase grating. To interrogate the grating, a third beam is coupled in at the bragg angle (see Figure 21). This beam should have a different wavelength (where the photorefractive sensitivity will be much less) and be of low intensity. Alternatively, the grating can be written by two external beams with a waveguided probe beam, as shown in Figure 22[16].

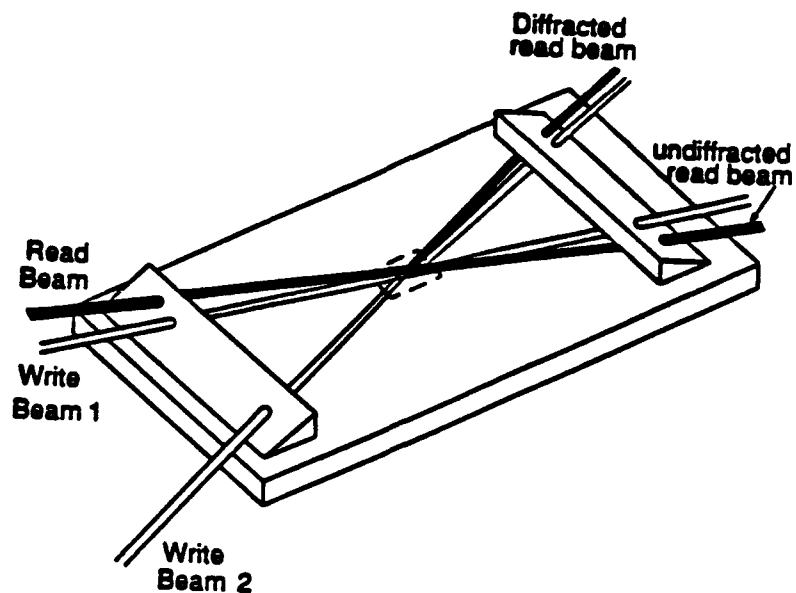


Figure 21: Formation of phase grating with two guided beams

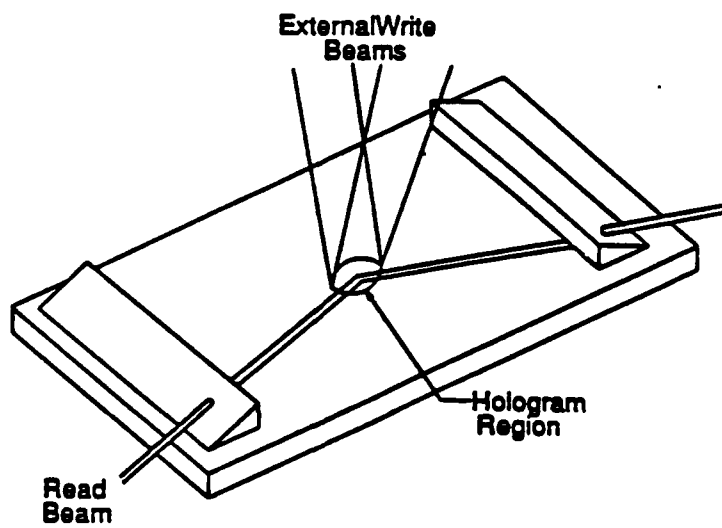


Figure 22: Formation of phase grating with two external beams

Photorefractive gratings offer the following advantages over alternative waveguide technologies:

- (i) The grating spacing can be small, enabling large diffraction angles to be obtained.
- (ii) The refractive index changes produced can be quite large, giving rise to high diffraction efficiencies.
- (iii) No external structures are required and there are no operating power requirements.

Some experimentation has been carried out on photorefractive gratings in LiNbO_3 waveguides. The information is summarised in Table 5. From the table it can be seen that while high diffraction efficiencies (50%) can be obtained, the grating formation times are rather large. If practical formation times are to be realised, the guide must be formed in materials with higher sensitivities, such as GaAs, BaTiO_3 or BSO.

The gratings can be used as switches, modulators, beam splitters and mirrors. While these applications can all be conveniently undertaken using conventional waveguide technology (such as Mach Zehnder interferometers, directional couplers, etc.) the volume holograms become much more attractive for large scale networks, such as $1 \times n$ switches or $n \times n$ interconnection networks, etc. A holographic interconnection in photorefractive LiNbO_3 waveguides has been demonstrated[6], and many types of devices have been proposed.

All of the interaction processes discussed in Section 5 can be carried out in an optical waveguide, and many of the applications discussed in this section can also be implemented in waveguides.

To-date, the papers reviewed on photorefractive waveguides deal solely with two-wave mixing [29], however there is no fundamental reason why four-wave mixing cannot be achieved.

One possible application which has not been discussed in the literature to-date is wavelength division multiplexing. Implementation of this process using a Bragg grating is complicated because any incident beam of wavelength λ must attend the grating at the specific Bragg angle for that wavelength. If an incident beam contains a number of wavelength components, there must be an equal number of wavelength components in the write beams to write a Bragg grating for each of them.

The multiple wavelength nature of the write beams will give rise to intermodulation products, which in turn will cause cross-talk. It is possible to carefully configure the interactions to reduce the cross-talk for small numbers of wavelength components, but the task becomes more difficult for larger sets. Since wavelength multiplexing is already possible with conventional waveguide technology (although difficult), the suitability of a photorefractive grating for this application seems to be limited.

Type of Guide	Write			Read			Diffraction Efficiency	Grating Formation Time	Grating Period λ_{gr}
	Wavelength /nm	Polarisation	Power Level/W.cm ⁻¹	Wavelength /nm	Polarisation	Power Level/W.cm ⁻¹			
LiNbO ₃	488	TE	~1	488 633	TE TE	~0.5 Low	52% 28%	1 - 10 min	1 - 2
Ti in-diffused	633	TE		633	TE		50%		6
Ti in-diffused (LiNbO ₃ :Fe)	633	TE	1 - 12	633	TE	Half write power	45 - 90%	2 - 8 min	1 - 8
Fe in-diffused	633	TM	3	633	TE	1	55%		12

Table 5: Summary of LiNbO₃ waveguide grating experiments [16]

Figure 23 shows a summary of required response times and intensity ranges for the applications discussed in this report. It should be noted that in many cases there are no definite limits on the maximum intensity which could be used and in these cases reasonable estimates have been made.

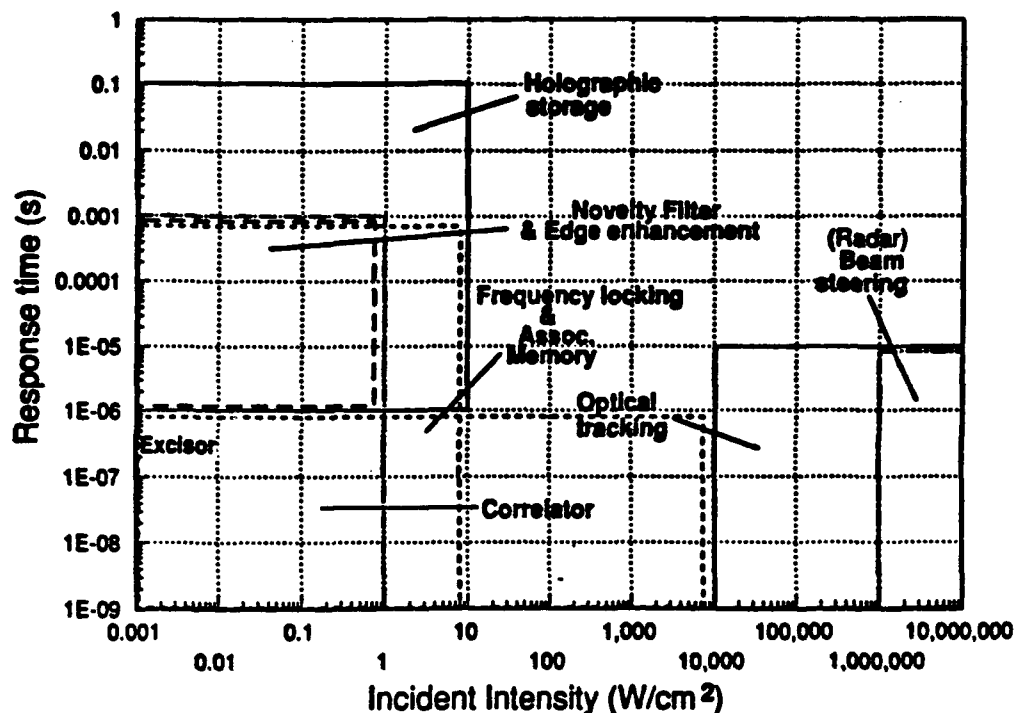


Figure 23: Response time and intensity limits required for a selection of applications

Figure 24 shows the data from Figure 23 with materials performance data overlayed. This material data is taken from Figure 2 and extrapolated for higher incident intensities. However, it should be noted that many of the materials may suffer permanent optical damage at the higher intensities shown, depending on the exposure time and therefore the energy density.

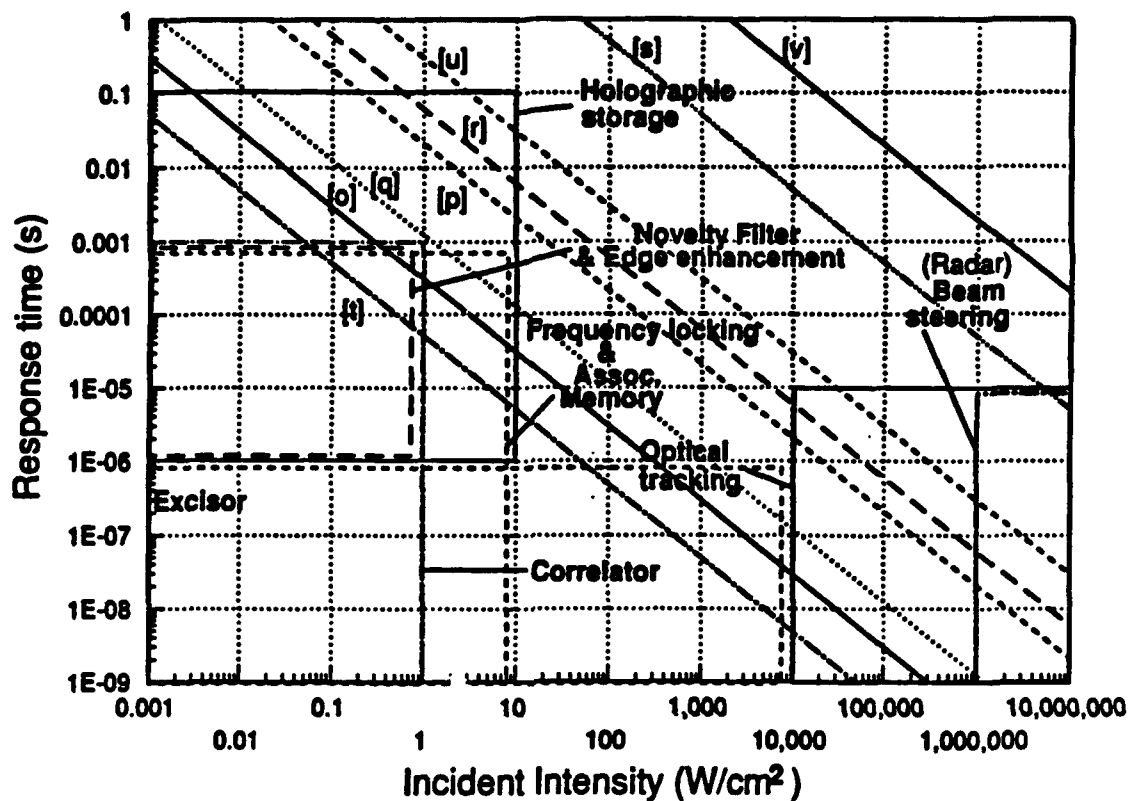


Figure 24: Comparison of applications response time and intensity requirements (from Figure 23) with materials performance (from Figure 2). Letters shown in square brackets refer to materials, as shown below.

[o] BSO	[s] LiNbO_3
[p] BaTiO_3 (45°)	[t] GaAs
[q] BGO	[u] KNbO_3
[r] BaTiO_3 (0°)	[v] IBM Polymer

7 CONCLUSIONS

Organic materials could offer a number of advantages over inorganic materials for photorefractive applications. For example, their properties may be tailored and large area films or shaped parts could be produced with novel configuration. However, the performance of organic materials which are currently available is not promising (e.g. low sensitivity and slow response speed) and it is easy to conclude that significant design and synthetic work will be required to improve their performance.

The performance of the currently available inorganic materials still falls far short of what would be optimum for many of the applications discussed in this report, making other means of implementation (such as electronic processing) an attractive alternative. Inorganic photorefractives still have a number of significant problems (e.g. fragility, availability (small size), high cost, uniformity, etc.) and these limit their use in systems.

For the best current photorefractive materials, the most accessible applications (when characteristics needed to outperform any more conventional implementations are taken into account) may be placed in two groups:

- (i) Beam steering, laser radar and optical tracking.
 - In these applications wavelengths are (to a great extent) set by external systems needs, power levels are high (up to MW.cm^{-2}) and response times short (ms-ns).
- (ii) Holographic storage, with possibly image processing and image identification being useful 'add-ons' (i.e. relaxing constraints of electronic competition because the storage medium is already optical).
 - In these instances the wavelengths can often be selected to suit the photorefractive material, power densities are modest (W.cm^{-2}) and millisecond to second response speeds acceptable.

To be of practical significance, a write energy of $<1 \text{ J.cm}^{-2}$ is required. To compete with the best inorganics, $<1 \text{ mJ.cm}^{-2}$ is required.

This study can be used as the basis for a practical investigation of organic photorefractive materials. Until intrinsically photoconductive materials become available within the Multifunctional Macromolecules Programme it is proposed that a guest-host approach be used. The advantage of such an approach is that a wide combination of materials can be scanned for suitability without the need for significant synthetic effort. However, this approach is not without its problems as the guest molecules are likely to plasticise the host polymer (reducing T_g) and may sublime during processing. Despite these

drawbacks (which are well understood from early organic nonlinear optical work) the guest-host approach can provide a useful insight at this time. We propose to undertake a study to determine the best method for poling a photoconductive material and to carry out simple experiments to determine the best technique for achieving high carrier mobility. Techniques for preparing bulk polymer samples (and poling these) must also be identified. Using this knowledge and the most promising materials, it should be possible to demonstrate simple two or four-wave mixing in a guest/host organic polymer.

8 REFERENCES

- [1] Kukhtarev, N.V., Markov, V.B., Odulov, S.G., Soskin, M.S. and Vinetskii, V.L., *Ferroelectrics*, **22**, p949 (1979).
- [2] Rajbenbach, H., Huignard, J.P. and Günter, P., *Springer Series in Electronics and Photonics*, **30**, p151 (1990).
- [3] Peltier, M. and Micheron, F., *J. Appl. Phys.*, **48**(9), p3683 (1977).
- [4] Wood, G.L. and Neurgaonkar, R.R., *Opt. Lett.*, **17**(2), p94 (1992).
- [5] Vainos, N.A. and Gower, M.C., *J. Opt. Soc. Am. B.*, **8**(11), p2355 (1991).
- [6] Brady, D.J. and Psaltis, D., *Appl. Opt.*, **30**(17), p2324 (1991).
- [7] Kyuma, K., *Nonlinear Optics*, **1** (1), p42 (1991).
- [8] Voit, E., Zaldo, C. and Gunter, P., *Opt. Lett.*, **11**(5), p309 (1986).
- [9] Ducharme, S., Scott, J.C., Twieg, R.J. and Moerner, W.E., *Phys. Rev. Lett.*, **66** (14), p1846 (1991).
- [10] Garnet, M.H., Chang, J.Y., Jenssen, H.P. and Worde, C., *Optics Letters*, **17** (2), p103 (1992).
- [11] Günter, P., *Phys. Rev.*, **93** (4), p199-299 (1982).
- [12] Günter, P. and Huignard, J.P., *Topics in Appl. Phys.*, **61**, p51-53 (1988).
- [13] Vazquez, R.A., Ewbank, M.D. and Neurgaonkar, R.R., *Optics Comms.*, **80** (3,4), p253 (1991).
- [14] Günter, P. and Eichler, H.J., *Springer Proceedings in Phys.*, **18**, (1987).
- [15] Imbert, B., Rajbenbach, H., Mallik, S., Herriau, J.P. and Huignard, J.P., *Opt. Lett.*, **13** (4), p327 (1988).
- [16] Huignard, J.P. and Günter, P., *Springer-Verlag Topics in Applied Physics*, **62**, (1989).
- [17] Klein, M.B., *Topics in Applied Physics*, **61**, p196 (1988).
- [18] Ewbank, M.D., Neurgaonkar, R.R. and Cory, W.K., *J. Appl. Phys.*, **62** (2), p374 (1987).

- [19] Renegar, P.H., Solymar, L., Rajbenbach, H. and Huignard, J.P., *Journal of Applied Physics*, **58**, p45 (1985).
- [20] Cheng, J.T. and Gheen, G., *Applied Optics*, **27** (20), p1236 (1988).
- [21] Imbert, B., Rajbenbach, H., Mallick, S., Herriau, J.P. and Huignard, J.P., *Optics Letters*, **13** (4), p327 (1988).
- [22] Sutter, K., Hullinger, J. and Günter, P., *Topical Meeting on Photorefractive Materials, Effects and Devices II*, PD1-1 (January, 1990).
- [23] Sutter, K., Hullinger, J. and Günter, P., *Solid State Comms.*, **74** (8), p867-879 (1990).
- [24] Schildkraut, J.S., *Appl. Phys. Lett.*, **58** (4), p340 (1991).
- [25] Feinberg, J., *Opt. Lett.*, **7**, p486 (1982)
- [26] Pepper, D.M., Feinberg, J. and Kukhtarev, N.V., *Sci. Amer.*, p34 (10/1990).
- [27] O'Meara, T.R., Pepper, D.M. and White, J.O., *Optical Phase Conjugation* p544 (1985).
- [28] Huignard, J.P. and Günter, P., *Topics in Applied Phys.*, **62**, p268, (1989).
- [29] Nakao, O., *Appl. Phys. Lett.*, **60** (7), p793 (1992).
- [30] Tamura, K., Padias, A.B., Hall, H.K. and Peyghambarian, N., *Appl. Phys. Lett.*, **60**(15), 1803 (1992).